Contents

The bistatic radar cross-section of a large size body embedded in a random medium

Z. Q. Meng
Fukuoka University
Fukuoka, 814-0180, Japan

M. Tateiba
Kyushu University
Fukuoka, 812-8581, Japan

1 Abstract

We have found that a radar cross-section (RCS) of a body embedded in a random medium may be nearly twice as large as that in free space, under the condition that the body size is smaller than the spatial coherence length of incident wave. If the condition does not hold, the RCS may oscillate with the size of the body and becomes much larger than that in free space in some cases.

This paper shows numerical results of bistatic RCS of a larger size circular cylinder in a random medium. We can see the complicated oscillation of the RCS, i.e., enhancement and depression, in different directions, and discuss the new scattering characteristics with change in the size of the body in a fixed random medium for E-wave incidence.

2 Introduction

When a body is embedded in a random medium, the radar cross-section (RCS) of the body may be remarkably different from that in free space. This special phenomenon is called backscattering enhancement, and has been one of important subjects for radar engineering, remote sensing, astronomy and bioengineering [1–7].

We have investigated the phenomenon by numerically analyzing the RCS of a body embedded in a continuous random medium, such as air turbulence, for more than ten years [8–16]. Our approach is based on general results of both independent studies on the surface current on a conducting body in free space and on the wave propagation and scattering in a random medium. A non-random operator, called current generator, is introduced to get the surface current from any incident wave. The operator depends only on the body surface and can be constructed by Yasuura's method. On the other hand, the wave propagation in a random medium is expressed by use of Green's function in the medium. Here, a representative form of the Green's function is not required but the moments are done for the analysis of average quantities concerning observed waves. At first we made use of a simple approximation of the moments in the backward direction, and obtained many numerical results of monostatic RCS. We have found that the RCS in a random medium may be nearly twice as large as that in free space, under the condition that the body size is smaller than the spatial coherence length of incident wave. If the condition does not hold, we shows that the RCS oscillates with the size of the body and becomes more than one hundred times as large as that in free space, on the assumption that the twice backscattering enhancement occurs for small size bodies. We also reveal that there is a depression of the RCS of small size bodies outside the backscattering enhancement peak. All the numerical results agree with the law of energy conservation. Moreover, we find that a second enhancement peak exists outside the depression in some cases, which peak is lower and wider than the peak in the backward direction.

In this paper, we discuss the bistatic RCS of a larger size circular cylinder embedded in a random medium for E-wave incidence without the aforementioned limitations.

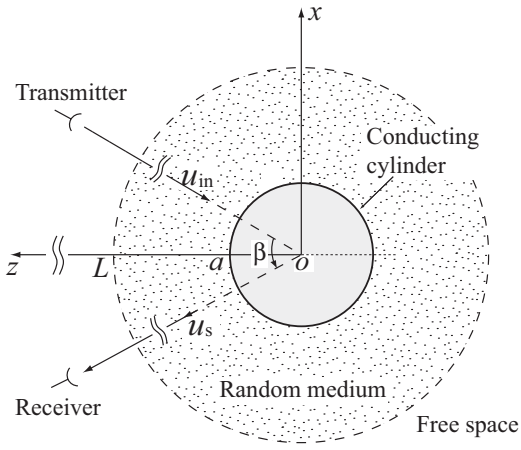

Figure 1: Geometry of the scattering problem from a conducting cylinder surrounded by a random medium.

3 Formulation

Consider a two-dimensional problem of electromagnetic wave scattering from a perfectly conducting circular cylinder embedded in a continuous random medium, as shown in Fig.1. Here L is the thickness of the random medium layer surrounding the cylinder and is assumed to be larger enough than the size of the cylinder cross-section. The random medium is assumed to be described by the dielectric constant ε, the magnetic permeability μ and the electric conductivity σ, which are expressed as

$$\varepsilon = \varepsilon_0[1 + \delta\varepsilon(\boldsymbol{r})] \ , \quad \mu = \mu_0 \ , \quad \sigma = 0 \ , \tag{1}$$

where ε_0, μ_0 are constant and $\delta\varepsilon(\boldsymbol{r})$ is a random function with

$$\langle \delta\varepsilon(\boldsymbol{r}) \rangle = 0 \ , \tag{2}$$

$$\langle \delta\varepsilon(\boldsymbol{r}_1) \cdot \delta\varepsilon(\boldsymbol{r}_2) \rangle = B(\boldsymbol{r}_1 - \boldsymbol{r}_2) \ . \tag{3}$$

Here the angular brackets denote the ensemble average and $B(\boldsymbol{r}_1 - \boldsymbol{r}_2)$ is the correlation function of the random function. For numerous cases, it can be approximated as

$$B(\boldsymbol{r}_1 - \boldsymbol{r}_2) = B_0 \exp\left[-\frac{|\boldsymbol{r}_1 - \boldsymbol{r}_2|^2}{l^2}\right] \ , \tag{4}$$

$$B_0 \ll 1 \ , \quad kl \gg 1 \ , \tag{5}$$

where B_0, l are the intensity and scale-size of the random medium fluctuation, respectively, and $k = \omega\sqrt{\varepsilon_0\mu_0}$ is the wavenumber in free space. Under the condition (5), depolarization of electromagnetic waves due to the medium fluctuation can be neglected; and the scalar approximation is valid. In addition, the forward multiple scattering approximation is valid, and hence the backscattering by the random medium becomes negligible. In the present analysis, consequently we do not need to consider the re-incidence of backscattered waves by the random medium on the cylinder[8, 9].

Suppose that the current source with the time factor $\exp(-j\omega t)$ suppressed throughout this paper is a line source, located at $\boldsymbol{r}_\mathrm{T}$, far from and parallel to the cylinder. Then the incident wave is expressed by Green's function in a medium containing the random medium and free space $G(\boldsymbol{r}, \boldsymbol{r}_\mathrm{T})$ whose dimension coefficient is understood. Using the current generator Y that transforms any incident wave into the surface current on the cylinder, we can give the average intensity of scattered waves u_s for E-wave incidence as follows[8, 9]:

$$\begin{aligned} \langle |u_\mathrm{s}|^2 \rangle \quad = \quad & \int_S \mathrm{d}\boldsymbol{r}_1 \int_S \mathrm{d}\boldsymbol{r}_2 \int_S \mathrm{d}\boldsymbol{r}_1' \int_S \mathrm{d}\boldsymbol{r}_2' \Big\{ Y_\mathrm{E}(\boldsymbol{r}_1; \boldsymbol{r}_1') Y_\mathrm{E}^*(\boldsymbol{r}_2; \boldsymbol{r}_2') \\ & \big\langle G(\boldsymbol{r}; \boldsymbol{r}_1) G(\boldsymbol{r}_1'; \boldsymbol{r}_\mathrm{T}) G^*(\boldsymbol{r}; \boldsymbol{r}_2) G^*(\boldsymbol{r}_2'; \boldsymbol{r}_\mathrm{T}) \big\rangle \Big\}, \end{aligned} \tag{6}$$

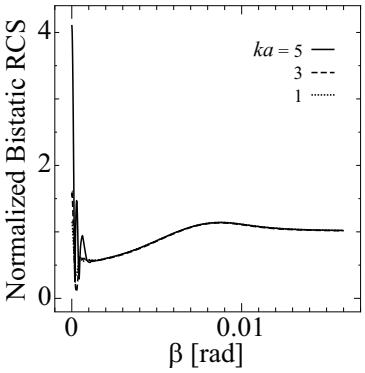

Figure 2: The bistatic RCS of the cylinders.

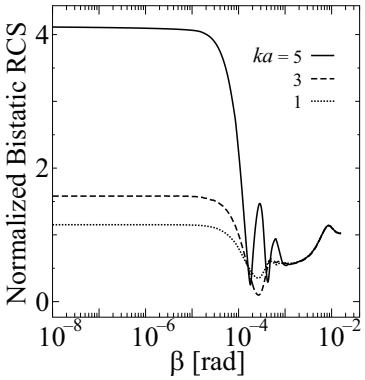

Figure 3: As in figure 2, but for change in the scale of β.

where S denotes the cylinder surface, and the asterisk does the complex conjugate. The $Y_{\rm E}$ can be calculated by Yasuura's method[8, 9] and expressed in an infinite series for a circular cylinder[11]:

$$Y_{\rm E}(\boldsymbol{r};\boldsymbol{r}') = \frac{\mathrm{j}}{\pi^2 a^2}\sum_{n=-\infty}^{\infty}\frac{\exp\{\mathrm{j}n(\theta-\theta')\}}{J_n(ka)H_n^{(1)}(ka)}\,, \tag{7}$$

where J_n is the Bessel function of order n and $J_n(ka)\neq 0$; that is, the internal resonance frequencies are excepted. The $H_n^{(1)}$ is the Hankel function of first kind.

The fourth moment of Green's functions in (6) can be written as

$$\langle G(\boldsymbol{r};\boldsymbol{r}_1)G(\boldsymbol{r}_1';\boldsymbol{r}_{\rm T})G^*(\boldsymbol{r};\boldsymbol{r}_2)G^*(\boldsymbol{r}_2';\boldsymbol{r}_{\rm T})\rangle = G_0(\boldsymbol{r};\boldsymbol{r}_1)G_0^*(\boldsymbol{r};\boldsymbol{r}_2)G_0(\boldsymbol{r}_1';\boldsymbol{r}_{1\rm T})G_0^*(\boldsymbol{r}_2';\boldsymbol{r}_{2\rm T})\cdot m_{\rm s}\,, \tag{8}$$

where G_0 is Green's function in free space[4]. The $m_{\rm s}$ includes multiple scattering effects of the random medium and can be obtained by two-scale method [6, 7, 12, 15]; as a result, it is

$$m_{\rm s} = \frac{k}{2\pi z}\iint_{-\infty}^{\infty}\mathrm{d}\eta\mathrm{d}\rho\exp\left\{-\frac{jk}{z}\eta[\rho-(x-x_{\rm T})]\right\}P(\rho,\eta)\,, \tag{9}$$

where

$$\begin{aligned}P(\rho,\eta) = \exp\Big\{&-\frac{\sqrt{\pi}k^2 lz}{8}\int_0^{L/z}\mathrm{d}t\Big(\,D[a(\sin\theta_1'-\sin\theta_2')t+\eta t]+D[a(\sin\theta_1-\sin\theta_2)t+\eta t]\\ &-D[a(\sin\theta_1'-\sin\theta_1)t-\rho(1-t)+\eta t]-D[a(\sin\theta_2'-\sin\theta_2)t-\rho(1-t)-\eta t]\\ &+D[a(\sin\theta_1'-\sin\theta_2)t-\rho(1-t)]+D[a(\sin\theta_2'-\sin\theta_1)t-\rho(1-t)]\Big)\Big\}\,,\end{aligned} \tag{10}$$

$$D(x) = 2B_0\left[1-\exp\left(-\frac{x^2}{l^2}\right)\right]\,. \tag{11}$$

4 Numerical results

We calculated the bistatic RCSs of three conducting circular cylinders ($ka=1,3,5$) embedded in a random medium ($k^2B_0lL=2\pi^2\times10^3$) for E-wave incidence by using (6) , normalized them to those in free space, and illustrated the numerical results in figures 2 and 3 to study the effects of body size.

We find that there are backscattering enhancement peaks at $\beta=0$ and depressions outside the peaks where σ/σ_0 is less than one. For all the cases, σ/σ_0 tends to one if β is large enough, and the integral value of σ/σ_0 with respect to β becomes almost one. This fact means that the results agree with the law of energy conservation.

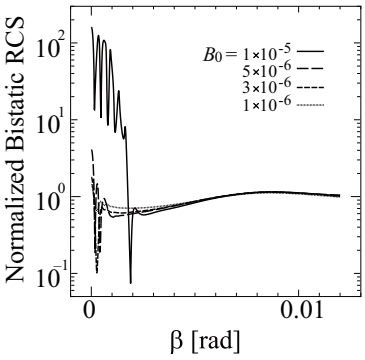

Figure 4: The bistatic RCS of the cylinders.

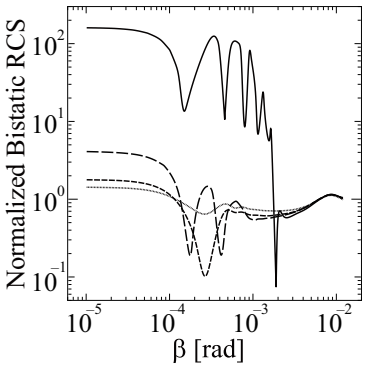

Figure 5: As in figure 4, but for change in the scale of β.

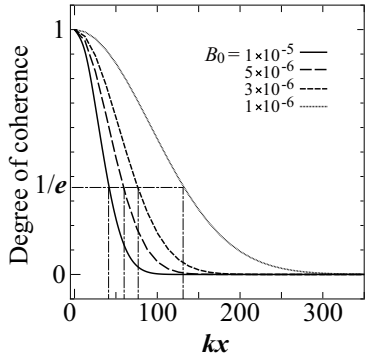

Figure 6: The degree of spatial coherence for different fluctuation intensities.

As ka increases, the oscillation of the RCS becomes much complicated about the backward direction. In the case of $ka = 5$, the backscattering peak value is about 4.1, much larger than the well-known level that is nearly twice as large as that in free space.

To study the fact moreover, we calculate the RCS of the cylinder of $ka = 5$ for four cases of $B_0 = 10^{-6}, 3 \times 10^{-6}, 5 \times 10^{-6}, 10^{-5}$, where $k^2 lL = 4\pi^2 \times 10^8$, and plot the results in figures 4 and 5. As shown in [13], we find again that the RCS in a random medium becomes more than one hundred times as large as that in free space.

The oscillation of bistatic RCS may be caused by an interference of incident and scattered waves. To study the interference, we analyze the degree of spatial coherence Γ:

$$\Gamma(x,z) = \frac{\langle G(\boldsymbol{r}_1;\boldsymbol{r}_\mathrm{t}) G^*(\boldsymbol{r}_2;\boldsymbol{r}_\mathrm{t})\rangle}{\langle |G(\boldsymbol{r}_0;\boldsymbol{r}_\mathrm{t})|^2\rangle}\ , \tag{12}$$

where $\boldsymbol{r}_1 = (x,0)$, $\boldsymbol{r}_2 = (-x,0)$, $\boldsymbol{r}_0 = (0,0)$, $\boldsymbol{r}_\mathrm{t} = (0,z)$. Figure 6 shows Γ for B_0 used in Figures 4 and 5. Then the spatial coherence length (SCL) is defined as double the kx at which $|\Gamma| = \mathrm{e}^{-1} \approx 0.37$. We note that the SCL for $B_0 = 1 \times 10^{-5}$ becomes almost the same order as the cylinder diameter, which means the scattering of spatially partially-coherent incident wave. This scattering leads to interesting results compared with the case of perfectly coherent wave: that is , ordinary incident wave.

5 Conclusions

We discussed the scattering characteristics of a conducting circular cylinder embedded in a random medium by changing the cylinder size and the fluctuation intensity of the medium. The numerical results of bistatic radar cross-section (RCS) show that the RCS in the neighborhood of backward direction may sometimes become much larger than that in free space, when the spatial coherence length and the body size are in the

same order. The complicated oscillation of the RCS is considered to be caused by statistical interference of incident and scattered waves. For all numerical results, the integral value of the bistatic RCS with respect to β is almost equal to that in free space, which fact shows that the results agree with the law of energy conservation.

REFERENCES

1. de Wolf D A 1971 Electromagnetic reflection from an extended turbulent medium: cumulative forward-scatter single-backscatter approximation *IEEE Trans.* **AP-19** 254-262
2. Y.A.Kravtsov, and A.Saichev: "Effect of double passage of waves in randomly inhomogeneous media", Sov. Phys. Usp., Vol.25, pp.494-508(1982).
3. Kuga Y and Ishimaru A 1984 Retroreflectance from a dense distribution of spherical particles *J. Opt. Soc. Am. A* **1** 831-835
4. Y.M.Lure, C.C.Yang, and K.C.Yeh: "Enhanced backscattering phenomenon in a random cotinuum", Radio Science, Vol.24, pp.147-159 (1989).
5. C.E.Mandt,L.Tsang,and A.Ishimaru: "Copolarized and depolarized backscattering enhancement of random discrete scatterers of large size based on second-order ladder and cyclical theory", J. Opt. Soc. Am. A,Vol.7,pp.585-592(1990)
6. R.Mazar: "High-frequency propagators for diffraction and backscattering in random media", J. Opt. Soc. Am. A, Vol.7, pp.34-46 (1990).
7. R.Mazar, and A.Bronshtein: "Double passage analysis in random media using two-scale random propagators", Waves in Random Media, Vol.1, pp.341-362 (1991).
8. M.Tateiba, and E.Tomita: "Theory of scalar wave scattering from a conducting target in random media",IEICE Trans. on Electronics, Vol.E75-C, pp.101-106 (1992).
9. M.Tateiba, and Z.Q.Meng: "Wave scattering from conducting bodies embedded in random media — theory and numerical results", in PIER 14: Electromagnetic Scattering by Rough Surfaces and Random Media, ed M.Tateiba, and L.Tsang, EMW Pub, Cambridge, pp.317-361 (1996).
10. Z.Q.Meng, and M.Tateiba: "Radar cross section of conducting elliptic cylinders embedded in strong continuous random media", Waves in Random Media, Vol.6, pp.335-345 (1996).
11. M.Tateiba, and Z.Q.Meng: "Infinite-series expressions of current generators in wave scattering from a conducting body", Research Reports on Information Science and Electrical Engineering of Kyushu University, Vol.4, pp.1-6 (1999).
12. Z.Q.Meng, N.Yamasaki, and M.Tateiba: "Numerical analysis of bistatic cross-sections of conducting circular cylinders embedded in continuous random media", IEICE Trans. on Electronics, Vol.E83-C, pp.1803-1808 (2000).
13. H.El Ocla, and M.Tateiba: "Strong backscattering enhancement for partially convex targets in random media", Waves in Random Media, Vol.11, pp.21-32 (2001).
14. H.El Ocla,and M.Tateiba: "Analysis of backscattering enhancement for complex targets in continuous random media for H-wave incidence",IEICE Trans. on Communications,Vol.E84-B,pp.2583-2588(2001).
15. M.Tateiba, and Z.Q.Meng: "Radar cross-sections of conducting targets surrounded by random media" (invited paper), IEICE Trans. on Electronics, Vol.J84-C, pp.1031-1039 (2001) (in Japanese).
16. M.Tateiba, Z.Q.Meng and H.El Ocla: "Scattering by Conducting Bodies in Random Media" (invited paper), IEEJ Trans. FM, Vol.124, pp.1094-1100 (2004).

Properties of Metallic Photonic Band Gap Prism at microwave frequencies: calculation and experimental verification

S. Massaoudi [1,2], A. de Lustrac [1] , I. Huynen [2],

1. Institut d'Électronique Fondamentale, Université Paris-Sud, France.
2. EMIC, Université Catholique de Louvain, Belgium.

Submitted for possible publication in Journal of Electromagnetic Waves and Applications.

Abstract – In this paper, the properties of a Metallic Photonic Band Gap Prism (MPBGP) with and without defects are studied. The PBG prism is made of metallic rods disposed in an isosceles right-angled triangle. The commercial software HFSS based on the finite element method is used to study the behavior of the Metallic Photonic Band Gap Material by means of three-dimensional dispersion diagrams, iso-frequency curves, radiation patterns and the carthography of electric field. Results show that the MPBGP without defects behaves like a homogeneous and ultrarefractive medium in the first allowed frequency band, and that the addition of defects on the surface of the prism does not modify the propagation of electromagnetic waves through the MPBGP. In the forbidden frequency bands, the presence of surface defects leads to anomalous transmission through the MPBGP. These predictions are successfully validated by experiment carried out in the frequency range [7 - 16 GHz].

Index Terms – Photonic band gap materials, periodic structures, ultrarefractive effect, surface defects and directive antennas.

1. Introduction

Since their invention by S. John and E. Yablonovitch, photonic band gap (PBG) materials have attracted much attention from the optical community [1], [2]. Basically, PBG materials are dielectric or metallic periodic structures whose spatial periods are of the order of magnitude of the considered wavelengths. These periodical structures produce a set of allowed and forbidden (gap) frequency bands. One of the most interesting properties of metallic photonic band gap materials is the emergence of an ultrarefractive effect [3-5] in the allowed frequency band and localized defect modes in their bandgap [6-7]. These properties may be explored for applications in antennas and wave length multiplexers or for lenses with very short focal length. In view of this, this paper investigates numerically and experimentally some properties of a two-dimensional Metallic PBG **P**rism (MPBG**P**) at microwave frequencies. The MPBGP is made of a 2-dimensional periodic lattice of metallic rods (Fig.1a) disposed into an isosceles right-angled triangle. An ultrarefraction phenomenon in the allowed band, the anomalous transmission in the bandgaps are predicted between 6 GHz and 16 GHz, using the Finite Element Method implemented in the HFSS commercial software, applied first to the infinite two-dimensional Metallic Photonic Band Gap **M**aterial (MPBG**M**), then to the prism of finite extent. The choice of the prism geometry enables to easily point out experimentally ultrarefraction and anomalous transmission. We show that the MPBGP with or without defects behaves like a homogeneous medium with effective refractive index between 0 and 1 in its first allowed frequency band. In the bandgaps, the addition of surface defects increases the anomalous transmission. Theoretical predictions are successfully validated by measurements in the frequency range 7-16 GHz. The choice of the microwave range is related to several applications, such as high directivity antennas, high impedance surfaces and tuneable antennas [8-9].

2. Properties of metallic photonic band gap material in the first allowed frequency band.

Our approach aims to predict the behavior of the finite structure from the knowledge of the properties of infinite structure. The FEM method implemented in HFSS is adequate for this, because it enables to compute the electric field patterns, the radiation pattern and the transmission diagram of finite structures. We first study the properties of a perfect MPBGPrism that is without defects. For this structure the transmission diagram has been calculated for a given number of layers and from the three dimensional dispersion diagrams for an infinite 2D-Metallic PBG Material (MPBGM) having same inclusions and periodicity as the MPBGP. Then we insert the defects in the MPBGP and study the propagation properties, keeping the number of defects constant, and changing only their distributions inside the structure.
Fig.1a shows the picture of the Metallic PBG Prism (MPBGP). It consists of copper rods disposed in an isosceles right-angled triangle. The diameter of each rod is d = 2mm, and the period $a = 15$ mm. As

mentioned above, the prism geometry enables us to identify two different regions for the refraction at output interface of MPBGM, illustrated in Fig. 1b: zone I corresponds to ultrarefraction with refractive index n<1, while zone II corresponds to usual refraction (n>1). We first calculate and measure the transmission diagram of the infinite MPBGM depicted in the inset of Fig. 1c, consisting of a square lattice of metallic rods having the same diameter *d* and periodicity *a* as the MPBGP of Fig. 1a. This enables to identify the allowed and forbidden frequency bands, as shown in Fig. 1c. In this graph the transmission factor respectively measured using a Vector Network Analyser-VNA (solid curve) and calculated with HFSS (dashed curve) are superimposed. Simulation is performed between 1 and 20 GHz. The measurement was taken between 7 and 16 GHz using the VNA in transmission mode and two identical horns. Teflon lenses are placed in front of the emitting and receiving horns to focus the incident wave on the material. Two allowed and forbidden bands are observed. The first allowed band lies between 6.54 GHz and 10 GHz. The second one appears above 13.5 GHz. The first forbidden band lies between 0 GHz and 6.5 GHz and the second one is between 10.5 and 13.5 GHz.

Fig. 2a shows the 3-dimensional dispersion diagram of the MPBGM calculated with HFSS following the method reported in [10]. The horizontal plane gives the Bloch wave vector $\vec{K}$ and the vertical axis gives the frequency in GHz. The projection of the dispersion diagram in the plan (k_x, k_y) for a particular frequency between 6.6 and 10 GHz gives the corresponding iso-frequency curve, which is a circle. Fig. 2b indeed shows the iso-frequency curves at 6.6 GHz (just above the plasma frequency located at 6.54 GHz). For the MPBGP structure, it corresponds to the circle with the smaller radius: in the vicinity of plasma frequency, the iso-frequency curve has a circular form with radius close to zero. The larger circle shown on Fig. 3.b is the iso-frequency curve calculated for vacuum at the same frequency. $\vec{K}_0$, represents the incident wave vector in vacuum. $\vec{K}_c$ and $\vec{K}_t$ are transmitted wave vectors through the MPBGP and at its output in the vacuum respectively. These waves vectors are obtained from the imposed continuity of their tangential component at each interface of photonic band gap material. From the results of Fig. 2.a it can be verified that the dispersion curves of the MPBGM are circles for all frequencies located in the first allowed band (Fig. 2c), i.e. between 6.54 and 10 GHz, having radius smaller than radius of vacuum. Thus the metallic photonic band gap material behaves like a homogenous and ultrarefractive medium in this frequency band: its refractive index *n* is less than unity, so that transmission should occur preferably in zone I of Fig. 1b.

Figure 3 shows the corresponding radiation patterns in output plane of MPBGPrism for 3 frequencies located in the first allowed band, respectively simulated using HFSS, and measured using a VNA in transmission mode as for Fig. 1c. The measurements are taken in TM polarization [10]. Fig. 3 (b) and (c) show simulated radiation patterns at 8 and 9 GHz, respectively, while Fig. 3 (d), (e), (f) show corresponding radiation patterns measured at 7.4, 8 and 9 GHz respectively. Measurements are in good agreement with the theoretical prediction. These patterns confirm that the MPBGP structure of Fig. 1a behaves like a homogenous and ultrarefractive medium for all frequencies between 6.54 GHz and 10 GHz, that is in the first allowed band. The main lobe of output radiation pattern is located in zone I of Figure 1b, meaning a refractive index n < 1. In particular, Figure 3(a) shows the iso-frequency curve calculated for the PBGM and the vacuum at 7.4 GHz, as well as the wave vector $\vec{K}_c$ inside the PBG and $\vec{K}_t$ at the output interface: the direction of $\vec{K}_t$ is in perfect agreement with the main lobe of radiation in Fig. 3d.

Figure 4 represents the measured near field radiation patterns at 8 GHz (in allowed band) for the MPBGP (a) without defect (identical to Fig. 3f), (b) with three defects consisting of missing metallic rods placed on the surface (their location is marked by red crosses) and (c) with three defects placed inside the structure. It is concluded that the presence of defects does not influence the propagation of electromagnetic waves through the MPBGP: it still behaves like a homogeneous and ultrarefractive medium.

3. Numerical calculations and experimental verifications in the second forbidden frequency band.

In the first forbidden frequency band, i.e. when the frequency is lower than the plasma frequency, the PBG material behaves like a perfect reflector medium. Only evanescent modes can exist in the structure [12]. Therefore we focus our study on the second forbidden band, i.e. between 10.5 and 13.5 GHz, which is characteristic of a stopband associated to a Photonic Crystal behavior. We have indeed verified by simulations that in this band, increasing the number of periodic layers increases the attenuation level in the stopband, while in the first forbidden band, below 6.54 GHz, the attenuation is unsensitive to the number of layers.

Fig. 5 gives the carthography of electric field calculated with HFSS at 12 GHz (in the bandgap range) for a perfect MPBGP without defects (a) and for the same prism with three surface defects consisting of missing rods (b). It is observed that in this bandgap the electromagnetic wave is quite completely reflected by the crystal in the case of the prism without defects while inside the prism the wave is evanescent (Fig. 5a). On the other hand, when we introduce the surface defects, the electromagnetic waves propagate through the MPBGP (Fig. 5b), behaving like Bloch propagating modes.

For better understanding the physical origin of transmission occurring in zone I, we have calculated the dispersion relation of the MPBGM as shown on Fig. 5c. On this figure, the frequency is represented as a function of the Bloch wave vector $\vec{K}$ in the first reduced Brillouin zone. This diagram enables us to visualize the whole set of solutions for all directions of propagation, as well as the variation of the group velocity according to the frequency. At 12 GHz there are no Bloch modes in $\Gamma \rightarrow X$ direction corresponding to normal incidence, and the electromagnetic wave is reflected by the structure, as confirmed by Fig. 5a. But in the vicinity of M point (direction $\Gamma \rightarrow M$ corresponding to normal to output interface) the Bloch modes exist (Fig. 5c). The physical origin of the transmission occurring in zone I at the output of the prism on Fig. 5b is related to diffracted waves on the photonic band gap material which lead to the excitation of Bloch modes in the structure.

Experimental results confirm the numerical and theoretical predictions. Fig. 6 represents the measured near field radiation pattern at 12 GHz. On Fig. 6a (prism without defect) we observe several lobes but with a normalised transmission which doesn't exceed 9% in zone I. These solutions are related to evanescent modes in the finite structure. When we introduce the defects on the surface of the prism (Fig. 6b) anomalous transmission appears at 308 degree, i.e. due to electromagnetic Bloch modes excited on the vicinity of M point. When the defects are placed inside the structure (Fig. 6c), anomalous transmission decreases very quickly, because we do not have a sufficient coupling between incident waves and Bloch modes, due to strong evanescence of waves over depth of prism [8], as can be seen from Fig. 5a.

4. Conclusion

In this paper, the microwave properties of a photonic band gap material made of periodic metallic rods have been studied. In its first allowed frequency band the so-called Metallic Photonic Band Gap Material (MPBGM) with and without defects behaves like a homogeneous and ultrarefractive medium (effective index lies between 0 and 1). In the bandgap the surface defects could improve the coupling of an incident wave to the propagating modes of MPBGMaterial. The numerical calculations are validated by experiments on a MPBGPrism topology, which enables to point out ultrarefractive phenomena occurring in the MPBGM.

References:

[1] S. John, Strong Localization of Photons in Certain Disordered Dielectric Superlattices, Phy. Rev. Lett. Vol. 58, 2486, 1987.

[2] E. Yablonovitch, Inhibited spontaneous emission in solid-state physics and electronics, Phys. Rev. Lett., Vol. 58, 2059, 1987.

[3] H. Kosaka et al, "Photonic crystals for micro lightwave circuits using wavelength-dependent angular beam steering," App. Phys. Lett., Vol. 74, No. 10, 1370-1372, 1999.

[4] W. Jiang, R.T. Chen, X. Lu, "Theory of light refraction at the surface of a photonic crystal," Phys. Rev. B, 71 245115 1-12, 2005.

[5] M.J. Steel et all, "Analytic properties of photonic crystal superprism parameters," Phys. Rev. E, Vol. 71 , 056608 1-9, 2005.

[6] S. Massaoudi, A. de Lustrac, T. A. Denidni, "Study of Dielectric and Metallic Photonic Band Gap Material at Micro-Waves Frequencies: Calculation and Experimental Verification", IEEE AP-S Int. Symp. on Ant. Prop., New Mexico, USA, July 9 - 15, 2006.

[7] S. Massaoudi, A. Ourir, A. de Lustrac, ''Effect of Surface Defects on the Amplification of Anomalous Transmission in Dielectric and Metallic Photonic Band Gap Materials: Calculation and Experimental Verification'', Progress in Electromagnetics Research Symposium (PIERS 2006), Cambridge, USA, March 2006.

[8] N. Guérin, S. Enoch, G. Tayeb, P. Sabouroux, P. Vincent, and H. Legay, "A Metallic Fabry–Perot Directive Antenna", IEEE Trans. Ant. Prop., Vol. 54, No. 1, 2006.

[9] D. F. Sievenpiper, J. H. Schaffner, H. Jae Song, ,R.Y. Loo, G. Tangonan, "Two-Dimensional Beam Steering Using an Electrically Tunable Impedance Surface, "IEEE Trans. Ant. Propag., Vol. 51, No. 10, 2003.

[10] S. Massaoudi, PhD Thesis, Institut d'Électronique Fondamentale, Université Paris-Sud, France, 2005.

[11] Pendry J.B, Holden A.J., Robnins D.J., Stewart W.J., Magnetism from conductors and enhanced nonlinear phenomena, IEEE Trans. Microwave Theory Tech., Vol. 47 No. 11, 2075-2084,1999.

[12] F. Gadot, E. Akmansoy, S. Massaoudi, A. De Lustrac, ''Amplification of anomalous refraction in photonic band gap-prism'', ELECTRON. LETT. vol. 39, n. 6, 2003.

[13] S. Massaoudi, A. de Lustrac, I. Huynen, T. Rachid., Properties of Metallic Photonic Band Gap Materials with Defects at Microwave Frequencies: Calculation, Experimental Verification and Application in Wireless Communications, abstract accepted for presentation at the Progress in Electromagnetics Research Symposium (PIERS 2006), Tokyo, on 2-5 August 2006.

[14] Lourtioz (J. M), H. Benisty, V. Berger, J.M. Gérard, D. Maystre, A. Tchelnokov, Les cristaux photoniques ou la lumière en cage, collection technique et scientifique des télécommunication, Lavoisier(2003).

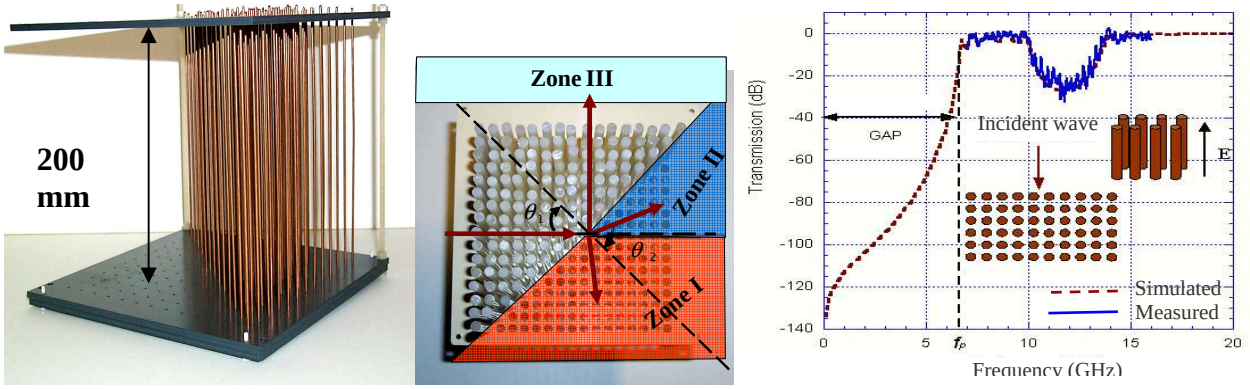

(a) (b) (c)

Fig. 1: a) 3-dimensional picture of Metallic PBG-Prism (MPBGP) made of copper rod having diameter d = 2 mm. The rods are placed in an isosceles right angle triangle arranged with period $a = d_1 = d_2 = 15$ mm. b) Top view of MPBGP, showing 2 zones for propagation after MPBGP: zone I corresponds to ultrarefractive transmission (refractive index n < 1), while zone II corresponds to n > 1 c) Simulated (red colour) and measured (blue colour) of transmission through 2-D square lattice material (MPBGM) having same parameters as MPBGP of Fig. 1ab. Polarization is TM.

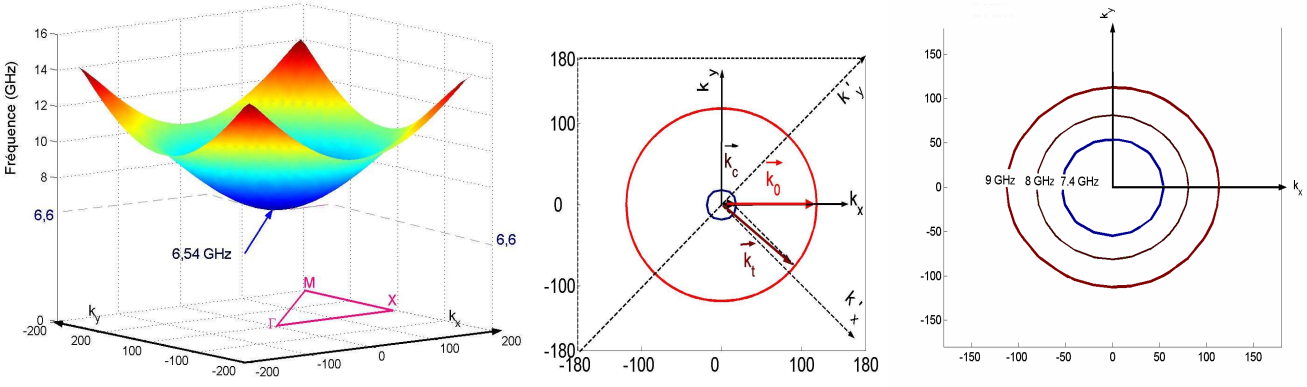

(a) (b) (c)

Fig. 2 (a) Three-dimensional dispersion diagram of MPBGM of Fig. 1c, calculated between 1 and 14GHz with Finite elements method. (b) iso-frequency curves of MPBGM (blue curve) and vacuum (red curve) calculated at 6.6 GHz; wave vectors in vacuum, and at input and output of photonic crystal are depicted in plane (k_x, k_y). (c) iso-frequency curves of MPBGM at 7.4, 8 and 9 GHz. Calculations are in TM polarization.

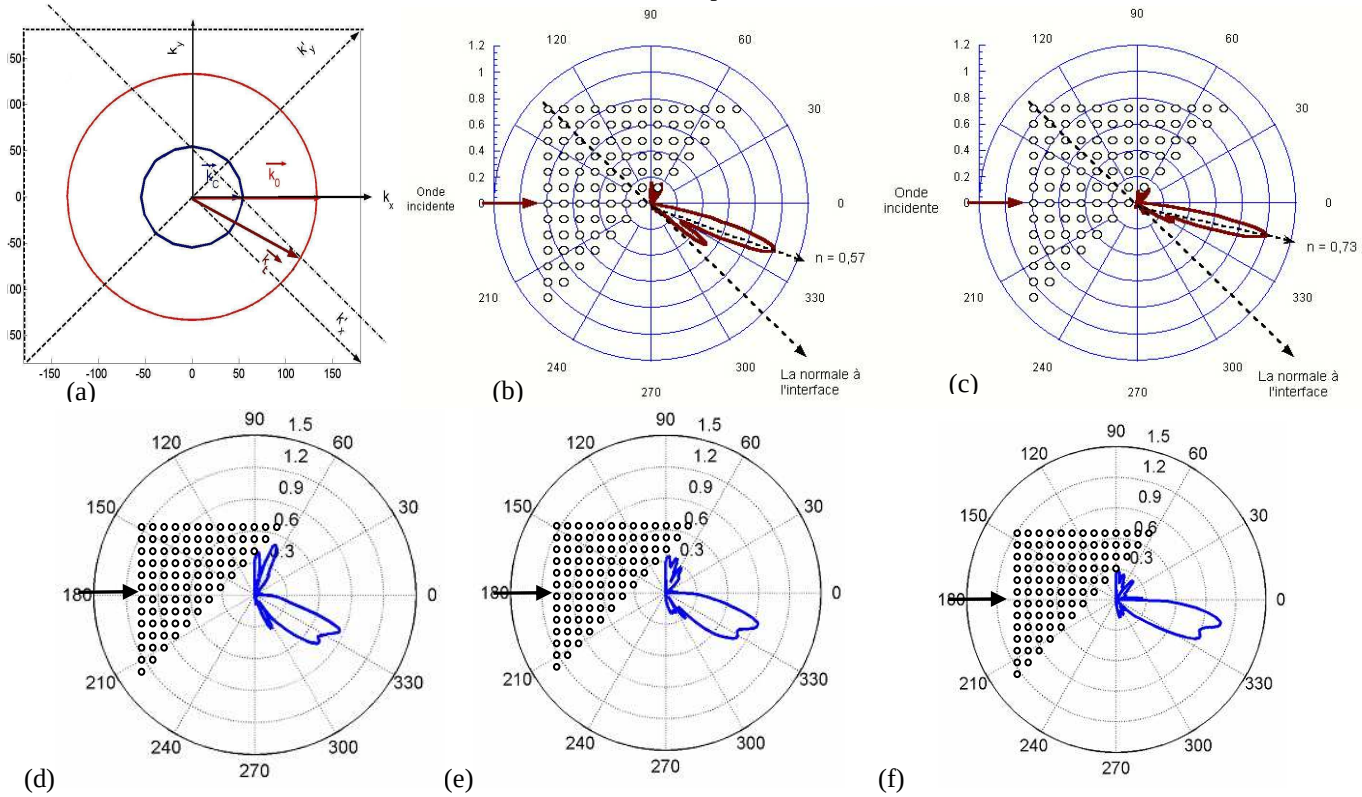

(a) (b) (c)

(d) (e) (f)

Fig. 3 (a) Iso-frequency curves for MPBGM and vacuum at 7.7 GHz (b) (c) Simulated radiation pattern of MPBGP at 8 and 9 GHz respectively (d), (e), (f) measured radiation pattern of MPBGP at 7.4; 8 and 9 GHz respectively.

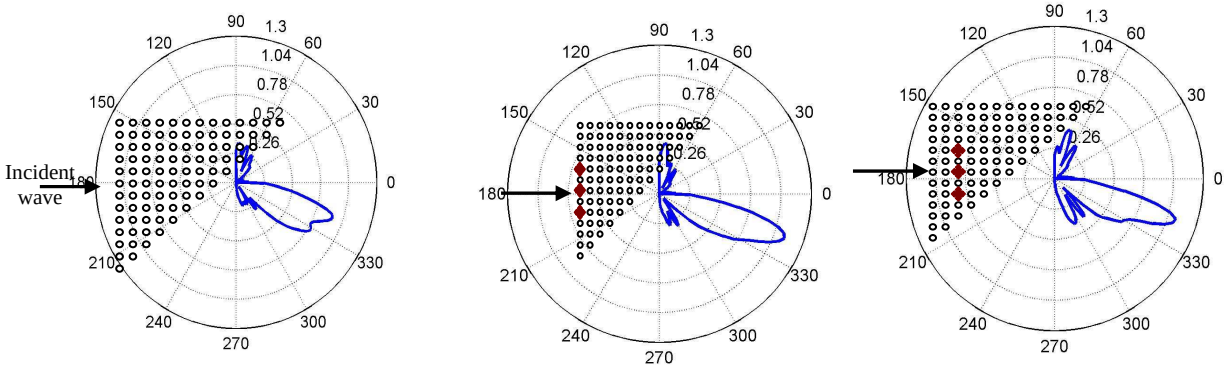

Fig. 4 Measured near field radiation patterns of metallic PBG prism at 8 GHz. (a) Perfect PBG-prism. (b) PBG-prism with three defects (missing rods located as indicated by red crosses) placed on the surface. (c) PBG-prism with three defects placed inside the structure. The polarization is transverse magnetic (TM).

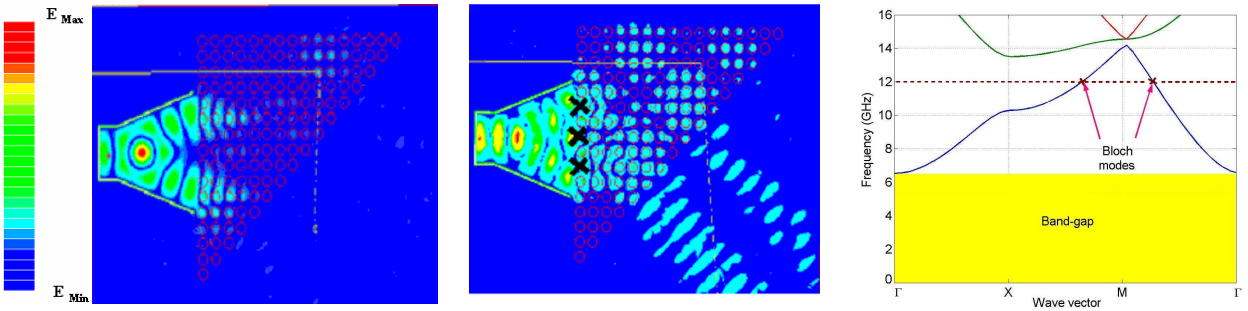

Fig. 5 2-D Cartographies of electric field calculated with HFSS for the MPBG at 12 GHz. (a) without defect (b) with three defects marked with black crosses. The red colour corresponds to the maximal amplitude, the blue colour to the minimal amplitude**.** (c) Dispersion diagram of the metallic 2-D square lattice depicted in the inset of Fig. 1c with *r = 1/15*a*. The polarization is transverse magnetic (TM).

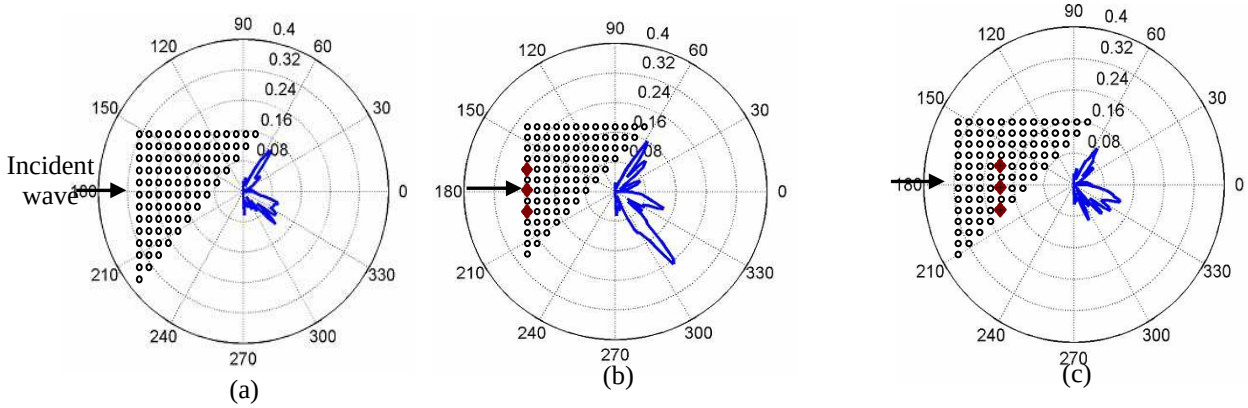

Fig. 6 Measured near field radiation pattern at 12 GHz for the MPBGP (a) without defects (b) with three defects on the surface (location marked in red) (c) with three defects inside.

Analysis of Thin Sinusoidal Metallic Gratings in Conical Diffraction

Hideaki Wakabayashi and Jiro Yamakita
Okayama Prefectural University, Japan

1. Introduction

Electromagnetic wave scattering by metallic gratings is one of fundamental problems in engineering of radio and optical waves. In most of the analyses of the metallic gratings, the grating is usually so thin electrically compared to a wavelength that thickness is neglected and calculations are carried out so that surface resistance and surface current distribution satisfy the boundary condition [1]. By neglecting the thickness, two-dimensional grating in addition to one-dimensional grating can be analyzed. Therefore, an investigation into the limits of the thickness of metallic gratings which can be neglected during analysis is very important in antennas engineering. In our previous work, thin metallic gratings with rectangular thickness profile placed in conical mounting were analyzed. By defining metallic grating as lossy dielectric gratings, the limit of thickness was investigated [2]. However, the analyses of the gratings whose thickness profile is not uniform along the boundary have not reported so far. In this paper, we demonstrate that a thin metallic grating with sinusoidal thickness profile placed in conical mounting can be approximated by a plane grating with surface resistance as a function of the position parameter parallel to the boundary. As for the method of analysis for thin sinusoidal metallic gratings, by partitioning the grating layer into multilayers having rectangular profiled gratings, the matrix eigenvalue calculations and the flux densities expansion approach [2][3] are applied. As for the method of analysis for plane gratings with thickness of zero, the spectral Galerkin method is applied to the resistive boundary condition. From the comparison of the numerical results of thin metallic and plane gratings, the limit of the thickness is investigated.

2. Setting of the problem

Figure 1 shows a thin metallic grating with sinusoidal thickness profile placed in conical mounting. We consider the scattering problem by the grating with periodicity Λ and width W that is uniform in the y direction. Sinusoidal profile is defined as a function $f(z)$. The incident wave is given by a polar angle θ_i, an azimuthal angle ϕ_i and a polarization angle γ. Regions I and III, which have relative permittivity ε_1 and ε_3, are lossless materials. The grating layer in region II is described by relative permittivity $\varepsilon_2 = \varepsilon_2' - i\varepsilon_2'' = 1 - i\varepsilon_2''$ ($\omega\varepsilon_0 \ll \sigma \to \varepsilon_2' = \varepsilon_1 = 1$) and thickness $d(z) = d\ f(z)$. As the thickness $d(z)$ is very small and the conductivity σ varies in such a way that the product σd stay finite, the materials of a thin metallic grating can be approximated by a plane grating with surface resistance $R_s(z)$ as

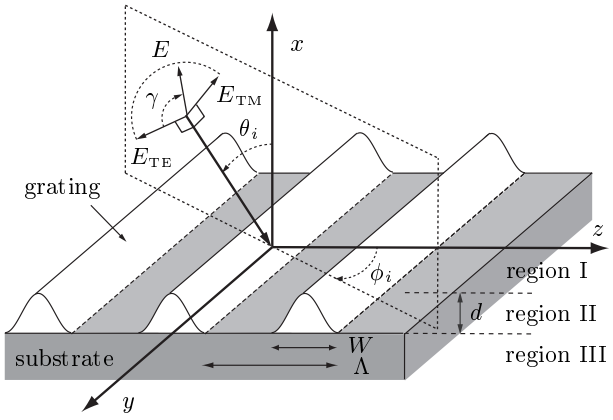

Fig. 1 Sinusoidal metallic grating.

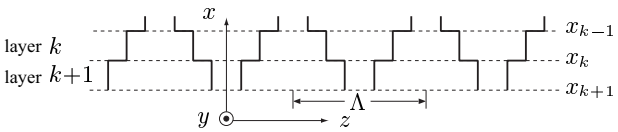

Fig. 2 Partitioning of grating layer.

$$R_s(z) = \frac{1}{\sigma\, d(z)} = \frac{1}{(1/Z_0)\,\varepsilon_2''\,k_0\,d\,f(z)} = R_{s0}\frac{1}{f(z)} \tag{1}$$

where R_{s0} is the resistance value in the maximum thickness on the thickness profile and ε'' is given by

$$\varepsilon_2'' = \frac{\sigma}{\omega\varepsilon_0} = \frac{1}{(R_{s0}/Z_0)\,k_0\,d}\ . \tag{2}$$

In the following formulations, the space variables are normalized by the wave number in vacuum $k_0 = \omega\sqrt{\varepsilon_0\mu_0}$ such that $k_0 x \to x$, $k_0 y \to y$, $k_0 z \to z$. Using the normalized space variables, Maxwell's equations can be

written in dimensionless form as

$$\overline{\mathrm{curl}}\sqrt{Y_0}\boldsymbol{E} = -i\ \mu\sqrt{Z_0}\boldsymbol{H}, \quad \overline{\mathrm{curl}}\sqrt{Z_0}\boldsymbol{H} = i\ \varepsilon\sqrt{Y_0}\boldsymbol{E} \tag{3}$$

where $Z_0 = 1/Y_0 = \sqrt{\mu_0/\varepsilon_0}$ and $\overline{\mathrm{curl}}$ is the rotation of the normalized space variables.

3. Method of analysis for sinusoidal metallic gratings

3.1 The differential equations

The grating region is approximated by partitioning into stratified $(L-2)$ multilayers having rectangular profile and the cross-sectional profile is set to the x-z plane, as shown in Fig. 2. Since the relative permittivity and permeability in each layer can be expressed by $\varepsilon(z)$ and $\mu(z)$ as a periodic function, respectively, the relative permittivity $\varepsilon(z)$ and its inverse $1/\varepsilon(z)$, and the relative permeability μ and its inverse $1/\mu(z)$ in the grating layer are expanded as a Fourier series of N_f terms with Fourier coefficients, respectively :

$$\left\{\begin{array}{c} \varepsilon(z) \\ \dfrac{1}{\varepsilon(z)} \\ \mu(z) \\ \dfrac{1}{\mu(z)} \end{array}\right\} = \sum_{m=-N_f}^{N_f} \left\{\begin{array}{c} \tilde{\varepsilon}_m \\ \left(\dfrac{1}{\tilde{\varepsilon}}\right)_m \\ \tilde{\mu}_m \\ \left(\dfrac{1}{\tilde{\mu}}\right)_m \end{array}\right\} \exp\left(i\ msz\right), \quad s = \lambda/\Lambda\ . \tag{4}$$

The electromagnetic fields $\sqrt{Y_0}E_i$, $\sqrt{Z_0}H_i$ $(i = x, y)$ and the flux densities $\sqrt{Y_0}D_z$, $\sqrt{Z_0}B_z$ are continuous in the grating region along the z axis. Since the structure is periodic, $\sqrt{Y_0}E_i$, $\sqrt{Z_0}H_i$, $\sqrt{Y_0}D_z$ and $\sqrt{Z_0}B_z$ are expressed in terms of spatial harmonics with the expansion coefficients e_{im}, h_{im}, d_{zm} and b_{zm} :

$$\left\{\begin{array}{c} \sqrt{Y_0}E_\ell \\ \sqrt{Z_0}H_\ell \\ \sqrt{Y_0}D_z \\ \sqrt{Z_0}B_z \end{array}\right\} = \sum_{m=-M}^{M} \left\{\begin{array}{c} e_{\ell m}(x) \\ h_{\ell m}(x) \\ d_{zm}(x) \\ b_{zm}(x) \end{array}\right\} \exp\left\{-i(q_0 y + s_m z)\right\} \tag{5}$$

$$q_0 = \sqrt{\varepsilon_1\mu_1}\sin\theta_i\sin\phi_i, \quad s_m = s_0 + m\ s, \quad s_0 = \sqrt{\varepsilon_1\mu_1}\sin\theta_i\cos\phi_i\ . \tag{6}$$

Substituting Eqs. (4) and (5) into Maxwell's equations (3), the differential equations for the y and z field components can be derived as

$$\frac{d}{dx}\boldsymbol{F} = i\,[C]\,\boldsymbol{F}, \quad [C] = \left[\begin{array}{cc} [0] & [C_{hb}] \\ [C_{ed}] & [0] \end{array}\right], \quad \boldsymbol{F} = [\boldsymbol{e}_y \quad \boldsymbol{d}_z \quad \boldsymbol{h}_y \quad \boldsymbol{b}_z]^t \tag{7}$$

$$[C_{hb}] = \left[\begin{array}{cc} -[q]\,[\varepsilon]^{-1}\,[s] & [q]\,[\varepsilon]^{-1}\,[1/\mu]\,[q] - [1] \\ -[1/\varepsilon]^{-1}\left([s]\,[\varepsilon]\,[s] - [\mu]\right) & [1/\varepsilon]^{-1}\,[s]\,[\varepsilon]^{-1}\,[1/\mu]\,[q] \end{array}\right] \tag{8}$$

$$[C_{ed}] = \left[\begin{array}{cc} [q]\,[\mu]^{-1}\,[s] & -[q]\,[\mu]^{-1}\,[1/\varepsilon]\,[q] + [1] \\ [1/\mu]^{-1}\left([s]\,[\mu]\,[s] - [\varepsilon]\right) & -[1/\mu]^{-1}\,[s]\,[\mu]^{-1}\,[1/\varepsilon]\,[q] \end{array}\right] \tag{9}$$

$$[\varepsilon] = [\tilde{\varepsilon}_{n-m}], \quad [1/\varepsilon] = \left[(1/\tilde{\varepsilon})_{n-m}\right], \quad [\mu] = [\tilde{\mu}_{n-m}], \quad [1/\mu] = \left[(1/\tilde{\mu})_{n-m}\right]\ . \tag{10}$$

By using $4(2M+1)$-dimensional column vector $\boldsymbol{a}(x)$ with the complex amplitudes $a_m^{\pm}(x)$ for propagation in the $\pm x$ directions and transforming $\boldsymbol{F} = [T]\,[\boldsymbol{a}^+(x)\ \boldsymbol{a}^-(x)]^t = [T]\left[{}^{\mathrm{E}}\boldsymbol{a}^+(x)\ {}^{\mathrm{M}}\boldsymbol{a}^+(x)\ {}^{\mathrm{E}}\boldsymbol{a}^-(x)\ {}^{\mathrm{M}}\boldsymbol{a}^-(x)\right]^t$, Eq. (7) becomes $d\boldsymbol{a}(x)/dx = i[\kappa]\boldsymbol{a}(x)$ where $[\kappa]$ is a diagonal matrix expressed in terms of the eigenvalue κ_m of the matrix $[C]$. The superscripts E and M refer to TE and TM waves, respectively. $[T]$ is a diagonalization matrix for $[C]$ and consists of eigenvectors corresponding to κ_m which is numerically calculated by general subroutine. The solution of Eq. (7) is given by

$$\boldsymbol{F} = [T_k]\left[\begin{array}{cc} \left[\mathrm{EXP}_k^+(x-x_0)\right] & [0] \\ [0] & \left[\mathrm{EXP}_k^-(x-x_0)\right] \end{array}\right]\left[\begin{array}{c} \boldsymbol{a}_k^+(x_0) \\ \boldsymbol{a}_k^-(x_0) \end{array}\right] \tag{11}$$

$$\left[\mathrm{EXP}_k^{\pm}(x)\right] = \left[\delta_{pq}\exp\left(\mp i\kappa_{k,p}\ x\right)\right], \quad p, q = 1, \cdots, 2(2M+1)\ . \tag{12}$$

3.2 The uniform regions

Uniform regions I and III are described by the relative permittivity $\varepsilon(z) = \varepsilon$ and the relative permeability $\mu(z) = \mu$. The electromagnetic fields can be expanded in terms of spatial harmonics. From Maxwell's equations (3), the differential equations can be expressed in terms of the coefficient matrix $[C]$ as follows :

$$\frac{d}{dx}\boldsymbol{F} = i\,[C]\,\boldsymbol{F}, \quad \boldsymbol{F} = [\boldsymbol{e}_y \quad \boldsymbol{e}_z \quad \boldsymbol{h}_y \quad \boldsymbol{h}_z]^t\ . \tag{13}$$

The submatrices can be given by $[\varepsilon] = \varepsilon[1]$ and $[\mu] = \mu[1]$. Therefore, the coefficient matrix $[C]$ consists of diagonal submatrices. $[c_m]$ corresponding to the m-th mode can be written as

$$[C_m] = \begin{bmatrix} 0 & 0 & -s_m q_0/\varepsilon & q_0^2/\varepsilon - \mu \\ 0 & 0 & \mu - s_m^2/\varepsilon & s_m q_0/\varepsilon \\ s_m q_0/\mu & \varepsilon - q_0^2/\mu & 0 & 0 \\ s_m^2/\mu - \varepsilon & -s_m q_0/\mu & 0 & 0 \end{bmatrix} . \tag{14}$$

The eigenvalue κ_m of 4×4 matrix $[c_m]$ can be obtained in a closed form as follows :

$${}^{\mathrm{E}}\kappa_m^{\pm} = {}^{\mathrm{M}}\kappa_m^{\pm} = \mp\xi_m = \mp\sqrt{\varepsilon\mu - q_0^2 - s_m^2} \tag{15}$$

$$[T_m] = \begin{bmatrix} \dot{s_m}\sqrt{\mu^*} & \xi_m \dot{q_0}/\sqrt{\varepsilon} & -\dot{s_m}\sqrt{\mu^*} & \xi_m \dot{q_0}/\sqrt{\varepsilon} \\ -\dot{q_0}\sqrt{\mu^*} & \xi_m \dot{s_m}/\sqrt{\varepsilon} & \dot{q_0}\sqrt{\mu^*} & \xi_m \dot{s_m}/\sqrt{\varepsilon} \\ \xi_m \dot{q_0}/\sqrt{\mu^*} & -\dot{s_m}\sqrt{\varepsilon} & \xi_m \dot{q_0}/\sqrt{\mu^*} & \dot{s_m}\sqrt{\varepsilon} \\ \xi_m \dot{s_m}/\sqrt{\mu^*} & \dot{q_0}\sqrt{\varepsilon} & \xi_m \dot{s_m}/\sqrt{\mu^*} & -\dot{q_0}\sqrt{\varepsilon} \end{bmatrix} \tag{16}$$

$$\dot{q_0} = \begin{cases} q_0/\sqrt{q_0^2 + s_m^2} \\ 0 \end{cases}, \qquad \dot{s_m} = \begin{cases} s_m/\sqrt{q_0^2 + s_m^2} & (q_0^2 + s_m^2 \neq 0) \\ 1 & (q_0^2 + s_m^2 = 0) \end{cases} . \tag{17}$$

3.3 Boundary conditions

By using the transformation matrix $[M]$ defined from $\boldsymbol{e}_z = [1/\varepsilon]\,\boldsymbol{d}_z$ and $\boldsymbol{h}_z = [1/\mu]\,\boldsymbol{b}_z$, the continuity of the fields $\boldsymbol{e}_\ell$ and $\boldsymbol{h}_\ell$ $(\ell = y, z)$ requires that

$$[T_1] \begin{bmatrix} \boldsymbol{a}_1^+(d) \\ \boldsymbol{a}_1^-(d) \end{bmatrix} = [M_2][T_2] \begin{bmatrix} [\mathrm{EXP}_2^+(x_1 - x_2)] & [0] \\ [0] & [1] \end{bmatrix} \begin{bmatrix} \boldsymbol{a}_2^+(x_2) \\ \boldsymbol{a}_2^-(d) \end{bmatrix} \tag{18}$$

$$\begin{aligned} &[M_k]\,[T_k] \begin{bmatrix} [1] & [0] \\ [0] & \left[\mathrm{EXP}_k^-(x_k - x_{k-1})\right] \end{bmatrix} \begin{bmatrix} \boldsymbol{a}_k^+(x_k) \\ \boldsymbol{a}_k^-(x_{k-1}) \end{bmatrix} \\ &= [M_{k+1}]\,[T_{k+1}] \begin{bmatrix} \left[\mathrm{EXP}_{k+1}^+(x_k - x_{k+1})\right] & [0] \\ [0] & [1] \end{bmatrix} \begin{bmatrix} \boldsymbol{a}_{k+1}^+(x_{k+1}) \\ \boldsymbol{a}_{k+1}^-(x_k) \end{bmatrix} \end{aligned} \tag{19}$$

$$[M_{L-1}][T_{L-1}] \begin{bmatrix} [1] & [0] \\ [0] & \left[\mathrm{EXP}_{L-1}^-(x_{L-1} - x_{L-2})\right] \end{bmatrix} \begin{bmatrix} \boldsymbol{a}_{L-1}^+(x_{L-1}) \\ \boldsymbol{a}_{L-1}^-(x_{L-2}) \end{bmatrix} = [T_L] \begin{bmatrix} \boldsymbol{a}_L^+(0) \\ \boldsymbol{a}_L^-(0) \end{bmatrix} \tag{20}$$

$$\boldsymbol{a}_1^- = [\,0 \cdots 0\ \cos\gamma\ 0 \cdots 0\ \sin\gamma\ 0 \cdots 0\,]^t, \quad \boldsymbol{a}_L^+ = [\,0 \cdots 0 \cdots 0\,]^t$$

where $k = 2, \cdots, L-2$. Unknowns are $\boldsymbol{a}_1^+(d)$ and $\boldsymbol{a}_3^-(0)$. The diffraction efficiencies of the reflected and transmitted waves ${}^{\mathrm{E,M}}\eta_m^r$ and ${}^{\mathrm{E,M}}\eta_m^t$ are given for TE and TM waves as follows :

$${}^{\mathrm{E}}\eta_m^r = \frac{|\,Re\left\{{}^{\mathrm{E}}\kappa_{1,m}^+\right\}\,|\,|{}^{\mathrm{E}}\,a_{1,m}^+(d)\,|^2}{P_{in}}, \quad {}^{\mathrm{M}}\eta_m^r = \frac{|\,Re\left\{{}^{\mathrm{M}}\kappa_{1,m}^+\right\}\,|\,|{}^{\mathrm{M}}\,a_{1,m}^+(d)\,|^2}{P_{in}} \tag{21}$$

$${}^{\mathrm{E}}\eta_m^t = \frac{|\,Re\left\{{}^{\mathrm{E}}\kappa_{L,m}^-\right\}\,|\,|{}^{\mathrm{E}}\,a_{L,m}^-(0)\,|^2}{P_{in}}, \quad {}^{\mathrm{M}}\eta_m^r = \frac{|\,Re\left\{{}^{\mathrm{M}}\kappa_{L,m}^-\right\}\,|\,|{}^{\mathrm{M}}\,a_{L,m}^-(0)\,|^2}{P_{in}} \tag{22}$$

$$P_{in} = |\,Re\left\{{}^{\mathrm{E}}\kappa_{1,0}^-\right\}\,|\,|\cos\gamma\,|^2 + |\,Re\left\{{}^{\mathrm{M}}\kappa_{1,0}^-\right\}\,|\,|\sin\gamma\,|^2 \ . \tag{23}$$

4. Method of analysis for plane gratings

A resistive boundary condition can be characterized by using the tangential electric field $E_{\ell\tan}(y,z)$ at the interface $x = 0$, the surface resistance $R_s(z)$ expressed as a function of position parameter z parallel to the boundary, and the surface current density $J_\ell(y,z)$ $(\ell = y, z)$ as follows :

$$\sqrt{Y_0}E_{\ell\tan}(y,z) - (R_s(z)/Z_0)\sqrt{Z_0}J_\ell(y,z) = 0 \qquad (\ |\,z\,| \leq W/2\ ) \ . \tag{24}$$

The tangential electric field is expressed by the sum of the primary field and the scattered field which can be approximated to be spatial harmonics expansion and written as

$$\begin{aligned} \sqrt{Y_0} \begin{bmatrix} E_{y\tan}^{1st}(y,z) \\ E_{z\tan}^{1st}(y,z) \end{bmatrix} &= \begin{bmatrix} e_{y0} \\ e_{z0} \end{bmatrix} \exp\{-i\,(q_0 y + s_0 z)\} + \sum_{m=-M}^{M} \begin{bmatrix} e_{ym} \\ e_{zm} \end{bmatrix} \exp\{-i\,(q_0 y + s_m z)\} \\ &= \begin{bmatrix} e_{y0} \\ e_{z0} \end{bmatrix} \exp\{-i\,(q_0 y + s_0 z)\} + \sum_{m=-M}^{M} \begin{bmatrix} g_{1m}^{yy} & g_{1m}^{yz} \\ g_{1m}^{zy} & g_{1m}^{zz} \end{bmatrix} \begin{bmatrix} j_{ym} \\ j_{zm} \end{bmatrix} \exp\{-i\,(q_0 y + s_m z)\} \ . \end{aligned} \tag{25}$$

The surface current $J_\ell(y,z)$ can be expanded in terms of the spatial harmonics :

$$\sqrt{Z_0}J_\ell(y,z) = \sqrt{Z_0}J_\ell(z)\exp(-i\,q_0\,y) = \sum_{m=-M}^{M} j_{\ell m} \exp\{-i\,(q_0 y + s_m z)\} \ . \tag{26}$$

The current density $j_{\ell m}$ and $\sqrt{Z_0}J_\ell(z)$ can be approximated in terms of the basis function $\phi_{\ell mp}$ and $\Phi_{\ell p}$ of the expansion number K in the spectral and spatial domains, respectively, as

$$j_{\ell m} = \sum_{p=1}^{K} I_{\ell p}\ \phi_{\ell mp}\ , \quad \sqrt{Z_0}J_\ell(z) = \sum_{p=1}^{K} I_{\ell p}\ \Phi_{\ell p}(z)\ , \quad \phi_{\ell mp} = \frac{1}{\Lambda}\int_{-\Lambda/2}^{\Lambda/2} \Phi_{\ell p}(z)\ \exp\left(\, is_m z\right)\, dz\ . \tag{27}$$

Applying the Galerkin procedure to the condition (24), yields a system of linear equation as follows :

$$\sum_{p=1}^{K}\sum_{p'=1}^{K} \begin{bmatrix} Z^{yy}_{p'p} & Z^{yz}_{p'p} \\ Z^{zy}_{p'p} & Z^{zz}_{p'p} \end{bmatrix} \begin{bmatrix} I_{yp} \\ I_{zp} \end{bmatrix} = \begin{bmatrix} V_{yp'} \\ V_{zp'} \end{bmatrix} \tag{28}$$

$$Z^{yy}_{p'p} = \sum_m \phi^*_{ymp'} g^{yy}_{1m} \phi_{ymp} - \int_{-W/2}^{W/2} \Phi^*_{yp'}(z)\frac{R_s(z)}{Z_0}\Phi_{yp}(z)dz\ , \quad Z^{yz}_{p'p} = \sum_m \phi^*_{ymp'} g^{yz}_{1m} \phi_{zmp}, \tag{29}$$

$$Z^{zy}_{p'p} = \sum_m \phi^*_{zmp'} g^{zy}_{1m} \phi_{ymp}\ , \quad Z^{zz}_{p'p} = \sum_m \phi^*_{zmp'} g^{zz}_{1m} \phi_{zmp} - \int_{-W/2}^{W/2} \Phi^*_{zp'}(z)\frac{R_s(z)}{Z_0}\Phi_{zp}(z)dz \tag{30}$$

$$V_{yp'} = -\phi^*_{y0p'} e_{y0}, \quad V_{zp'} = -\phi^*_{z0p'} e_{z0}\ . \tag{31}$$

Using the method of analysis based on the matrix eigenvalue calculations described in section 3, e_{y0}, e_{z0} and g_m corresponding to the Green functions can be obtained numerically. Therefore, the diffraction efficiencies are expressed by using the complex amplitudes $a^{\pm}_m(x)$ as follows :

$${}^{\mathrm{E,M}}\eta^r_m = \frac{|\ Re\{{}^{\mathrm{E,M}}\kappa^+_{1,m}\}\ |\ |\ \sum\limits_{\ell=y,z}^{\mathrm{E,M}} a^+_{1,m\ell}(0)\ j_{\ell m} + {}^{\mathrm{E,M}}\ a^+_{1,0}(0)\ \delta_{0m}\ |^2}{P_{in}} \tag{32}$$

$${}^{\mathrm{E,M}}\eta^t_m = \frac{|\ Re\{{}^{\mathrm{E,M}}\kappa^+_{L,m}\}\ |\ |\ \sum\limits_{\ell=y,z}^{\mathrm{E,M}} a^+_{L,m\ell}(0)\ j_{\ell m} + {}^{\mathrm{E,M}}\ a^+_{L,0}(0)\ \delta_{0m}\ |^2}{P_{in}}\ . \tag{33}$$

5. Numerical examples

To show that a thin metallic grating with sinusoidal thickness profile placed in conical mounting can be approximated by a plane grating with surface resistance as a function of the position parameter. Calculations are performed under $\varepsilon_1 = 1$, $\varepsilon_3 = 2.5$, $\Lambda/\lambda = 0.5$, $W/\Lambda = 0.5$, $\gamma = 90\ ^\circ$. In using Galerkin procedure, step functions are used as the basis functions, the number of spatial harmonics is truncated to $M = 300$, and a current expansion number of $K = 100$ is used. In order to investigate the convergence, Fig. 3 shows the power transmission coefficients against the number of spatial harmonic expansion terms $2M + 1$ for $\theta_i = \phi_i = 30\ ^\circ$. When the terms are large, the solutions of metallic gratings are close to those of plane gratings. For TM-wave and small surface resistance, the speed of the convergence is slow. In the following analyses of metallic gratings with sinusoidal thickness profile, the spatial harmonic expansion terms and the number of partitioned layers are truncated to $2M + 1 = 201$ and $L = 42$, respectively, by the convergence of solutions and the computational time.

Figures 4(a) and 4(b) show the power transmission coefficients against thickness d/λ for $\theta_i = \phi_i = 30$ and $45\ ^\circ$. When surface resistance becomes large, the results of thin metallic gratings at a thickness of around $d/\lambda = 0.01$ are close to those of plane gratings. The results of thin metallic and plane gratings are in good agreement where θ_i and ϕ_i change. We can find that thin metallic gratings with sinusoidal thickness profile can be treated as plane gratings with surface resistance as a function of the position parameter.

The jump condition of tangential magnetic fields between the surface of the metallic grating and interface in region III is equivalent to electric current and is compared with the current distributions on plane gratings for $\theta_i = \phi = 30\ ^\circ$, as shown in Figs. 5(a) and 5(b). In Fig. 5(b) of z component, the difference of current distributions against thickness is small. When the thickness is $d/\lambda = 0.001$, the jump conditions are in good agreement with the current distributions.

6. Conclusions

We have shown that a thin metallic grating with sinusoidal thickness profile placed in conical mounting can be approximated by a plane grating with surface resistance as a function of position parameter parallel to the boundary. Methods of analyses for metallic and plane gratings are formulated for the same considered model. By comparing numerical results, a thin metallic grating can be analyzed by the numerical approach for a resistive plane grating. In the future, we will investigate various thickness profiles and compare with the case of planar mounting [4].

REFERENCES

1. K. Sumitani, H. Wakabayashi and H. Inai, "A study of uniform approximation of equivalent impedance sheet for parallel metallic gratings", IEEJ Trans. EIS., vol. 123, no. 11, pp. 1930–1935, 2003. (in Japanese)
2. H. Wakabayashi, J. Yamakita, M. Asai and H. Inai, "Availability of resistive boundary condition for thin metallic gratings in conical mounting", IEICE Trans. Electron., vol. E87-C, no. 9, pp. 1560–1567, 2004.
3. M. Komatsu, H. Wakabayashi and J. Yamakita, "Computational methods for surface relief gratings using electric magnetic flux expansions", IEICE Trans. Electron., vol. E88-C, no. 12, pp. 2192–2198, 2005.
4. H. Wakabayashi, M. Komatsu, J. Yamakita and M. Asai, "Improved convergence in the analysis of thin metallic gratings with thickness profile", American Geophysical Union, Radio Science, vol. 38, no. 6, pp. 8-1–8-10, 2003.

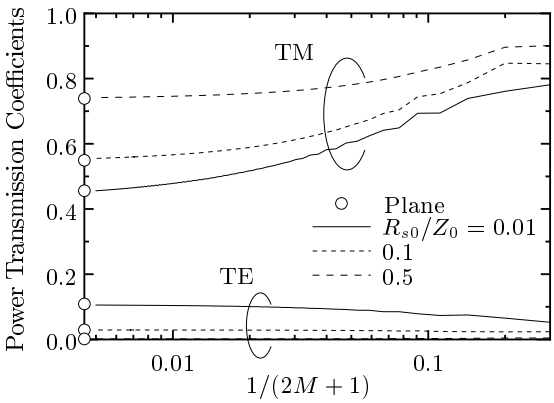

Fig. 3 The convergence against the number of spatial harmonic expansion terms.

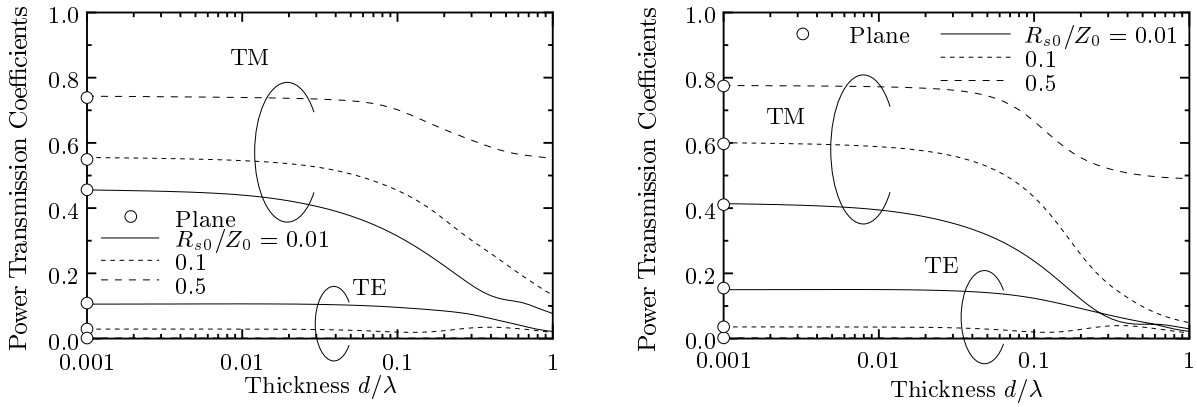

(a) $\theta_i = \phi_i = 30$ ° (b) $\theta_i = \phi_i = 45$ °

Fig. 4 The power reflection coefficients against thickness.

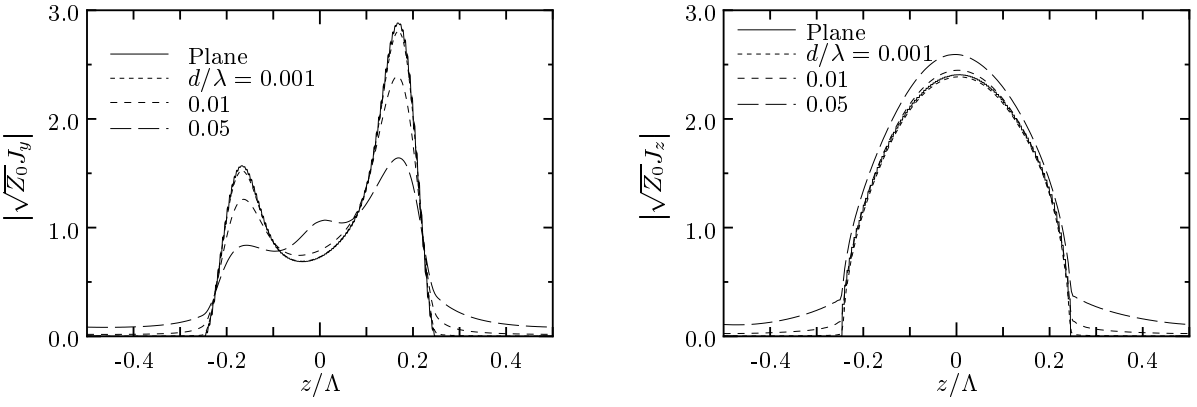

(a) y component (b) z component

Fig. 5 The current distributions of resistive gratings.

AN ANALYSIS OF THE TRANSFER MATRIX METHOD ON BAND STRUCTURE OF ONE DIMENSION GRADED–INDEX PHOTONIC CRYSTAL

[1]I-Chun Tsai, [2]Jin-Jei Wu, [3]Tzong-Jer Yang
([12]Department of electrical Engineer,Chung Hua University [3]Institute and Department of Electrophysics, National Chiao-Tung University [12]No.707, Sec.2, WuFu Rd., HsinChu, Taiwan 300, R.O.C., [3]1001 Ta Hsueh Road, Hsinchu, Taiwan 300, ROC. [1]Tel: 886-910652117 , [1]Email:m09301053@chu.edu.tw)

Abstract –The characteristics of guide-wave scattered by graded-index photonic crystal were investigated with an equivalent network method. By modulating a homogeneous layer's width, the higher order bandgap is suppressed by a parabolic-index profile in the other layer.

1 Introduction

The electromagnetic problem of a straight uniform periodic structure has been analyzed by the equivalent network method [1] and the transfer matrix. With these basic analyses, the one dimension multi-thin film can be considered to be well understood. In recent years, many authors have conducted work on different types of photonic crystal. The graded-index has benefit in optical fiber. Thus, it is mandatory to analyze a photonic crystal with a graded-index in each unit cell. Each unit cell in photonic crystal includes two layers: one is the homogeneous refraction index and the other is graded-index. In this letter, we will utilize the equivalent network method which is used to calculate both reflectivity and band gap diagrams. We expect this change can improve on many optical components.

2 Methods

As an illustration of this method, consider a structure as depicted in Fig. 1(a). This is a 1-D photonic crystal and its equivalent network. The transfer matrix of the equivalent network is expressed as equation (1).

$$T_i = \begin{bmatrix} \cos(\kappa_i W_i) & jZ_i \sin(\kappa_i W_i) \\ jY_i \sin(\kappa_i W_i) & \cos(\kappa_i W_i) \end{bmatrix} \quad (1)$$

For the normal incidence, the κ_i and Z_i is represented by equation (2) and (3)

$$\kappa_i = \frac{\omega}{c} n_i \quad (2)$$

$$Z_i = \frac{1}{Y_i} = \frac{377}{n_i} \quad (3)$$

As we decide the frequency of indicate light, the transfer matrix, equation (1), should also be knew.

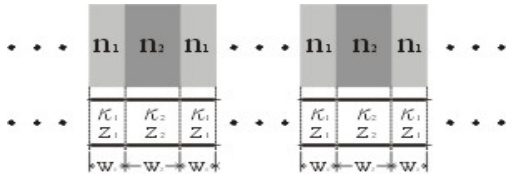

(a)

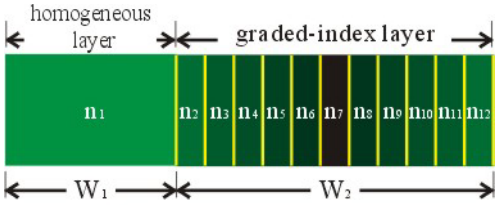

(b)

Figure 1 (a) multi-layer thin film and its equivalent network model
(b) a unit cell: a homogeneous layer in left side and a graded-index layer in right side.

Assume we consider a unit cell which include two layers: one is a homogeneous layer with the width W_1 and the other is a graded index layer with the width W_2. Based on the equivalent network method, the graded-index layer can be replaced by a sequence of basic units. The each unit has same width, 11nm, as shown in Fig. 1(b). The indexes of graded-index layer are decided by graded-index optical fiber's formula, equation (4).

$$n = n_7[1 - 2\Delta(\frac{r}{a})^{\alpha}]^{1/2} \qquad \alpha = 2 \qquad (4)$$

In our case, $n_1 = 1.38$、$n_7 = 2.35$、$a = 5$、$r = 1 \sim 5$ and $\Delta = 0.32$. The n_7 is the highest index value in graded-index layer. To calculate twenty-one periods and then consider half-illumining air layers in both sides of the structure, we obtain photonic crystals' reflectivity and energy gap as functions of normalized frequency. The frequency is normalized by fundamental frequency, ω_o, as equation (5) shows.

$$\omega_o = c\pi / \sum_i n_i \cdot W_i \qquad (5)$$

3 Result and Discussion

In the case of W_1 is 89nm. Figure 2(a) shows the reflectivity as a function of normalized frequency. Figure 2(b) shows the κd as a function of normalized frequency.

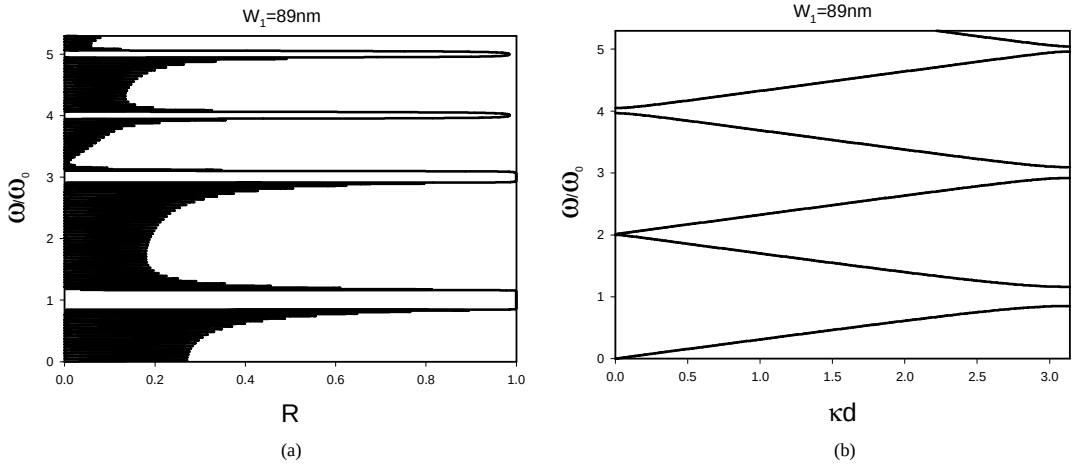

(a) (b)

Figure 2 (a) reflectivity diagram: R1=1.0000, R2=0.0988, R3=1.0000, R4=0.9846, R5=0.9846 (b) dispersion diagram: g1=0.308, g2=0.012, g3=0.176, g4=0.084, g5=0.084 . ω_o =2583.7(THz)

Fig. 2(b) shows that in the $2\omega_o$, the bandgap was eliminated. Its reflectivity is 0.0988 and bandgap is 0.012. This phenomenon would be understood by the dispersion equation of the structure. Based on S.T.

Peng (1989) found the trigonometric form of dispersion equation, we get the limiting equations, equation (6) and (7), of dispersion about our structure.

$$\begin{cases} -1<(T_{11}+T_{22})/2<1 & \text{no gap} \quad (6) \\ (T_{11}+T_{22})/2>1 \ or \ (T_{11}+T_{22})/2<-1 & \text{have gap} \quad (7) \end{cases}$$

while

$$\begin{bmatrix} T_{11} & T_{12} \\ T_{21} & T_{22} \end{bmatrix} = T_1 \cdot T_2 \cdot T_3 \cdot T_4 \cdot T_5 \cdot T_6 \cdot T_7 \cdot T_8 \cdot T_9 \cdot T_{10} \cdot T_{11} \cdot T_{12}$$

If $(T_{11}+T_{12})/2$ is between 1 and -1, the light will satisfied with the dispersion equation of this structure. The light will alive inside the structure and we will not find bandgap in that indicate frequency. Using twice fundamental frequency as indicate frequency and different W_1, we have different values of $(T_{11}+T_{12})/2$. Figure 3 shows W_1 vs. $(T_{11}+T_{12})/2$.

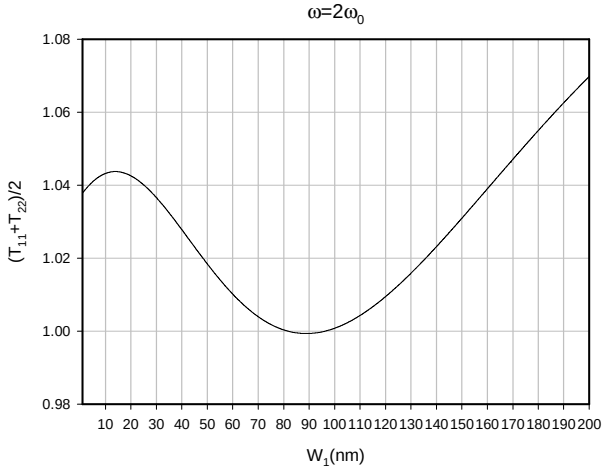

Figure 3 W_1 is from 1nm~100nm)

From figure 3, there is no bandgap as W_1 is a value between 82nm and 96nm. The value of 89nm (W_1) is between 82nm to 96nm.

To calculate the input impedance, from the left side of homogeneous layer,

$$Z_i = Z_o \frac{Z_L + jZ_o \tan(\kappa d)}{Z_o + jZ_L \tan(\kappa d)} \quad (8)$$

we can analize by electronic component

(Table 1) ω_o =2583.7(THz)

Indicate frequency	R	Z_{in}
5 ω_o	**0.9846**	**1.4895+51.0694i**
4 ω_o	**0.9846**	**11.259+977.01i**
3 ω_o	**1.0000**	**0.0043997+245.10i**
2 ω_o	**0.0988**	**202.00+52.792i**
1 ω_o	**1.0000**	**0.0000035591+956.94i**

Table 1, second row from the bottom, 0.967 is the normalized real part of input impedance by the input impedance's magnitude (208.785). In the same frequency, the normalized imaginary part of input impedance is 0.253. Compare with other frequencies, the structure with this special frequency is more like a resistance, others are inductive.

The reflectivity is decided by input impedance, as equation (9) shows and the values are listed on the second column of Table 1.

$$R = \left(\frac{Z - Z_{in}}{Z + Z_{in}}\right)\left(\frac{Z - Z_{in}}{Z + Z_{in}}\right)^{*} \tag{9}$$

To compare with the Fig 2(a), the reflectivity are the same values.

We do figure 3 again but use triple 、fourfold or fivefold fundamental frequency as indicate frequency. We have figure 4.

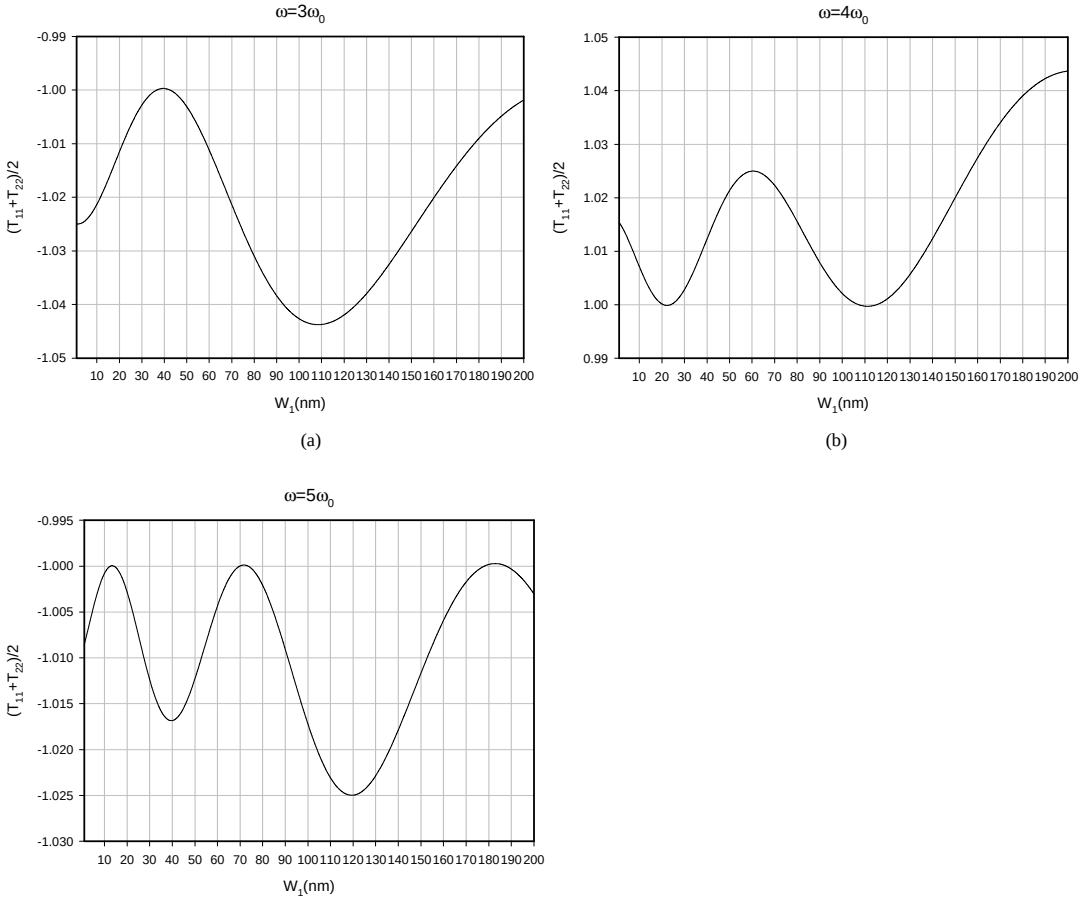

Figure 4 (a) one section, 37nm~42nm, no bandgap (b) two sections, 21nm~24nm and 108nm~115nm, no bandgap (c) three sections, 13nm~14nm 、70nm~73nm and 178nm~188nm, no bandgap

Using higher indicate frequency, we had more sections that make indicate light went pass this 1-D graded-index photonic crystal. By modulating the W_1 within a section value of no bandgap, we can let a light go pass the photonic crystal with special indicate frequency.

4 Conclusion

Numerical results show that we can decide a bandgap which is suppressed by modulating the width of homogeneous index layer. Therefore this type of periodic structures may provide another degree of freedom to design optical-frequency selector、filters and optical resonators.

5 References

1 S.T. Peng, “Rigorous formulation of scattering and guidance by dielectric grating waveguide: general case of oblique incidence”, J. Opt. Soc. Am. A, 1989, Vol,6 No. 12. pp.1869-1883.

2 J.M Lourtioz, H. Bensity and A. Chelnocov, ”Photonic Crystals and the real world of Optical Telecommunication", Annals of Telecommunications, 2003, T. 58, No, 9-10, pp.1191-1196.

Variable Frequency Shifting of a Continuous Light Wave Based on Multistage Phase Modulation

S. Hisatake and T. Kobayashi
Osaka University, Japan

Abstract—Frequency shifting of a continuous light wave based on multistage phase modulation with a relative phase control of sidebands has been investigated. The proposed frequency shifting process consists of three stages: (i) phase modulation and chirp compression to generate pulse train, (ii) Doppler shift of the pulse center frequency in a second phase modulation, and (iii) demodulation of the pulse train. The condition of the chirp compression in the stage (i) is optimized for maximizing the shifting efficiency. Shifting of a carrier frequency of signal data by the proposed shifting processes is also evaluated on the basis of cross-correlation diagram between the input signal and the demodulated output signal.

1. Introduction

Optical frequency shifters are of great potential interest as key components in various fields, including optical communication systems, optical frequency synthesis, and spectroscopy. Electrooptic (EO) frequency shifting or frequency conversion has a number of advantages compares with other methods of all-optical (not requiring light detection and retransmission) frequency conversion, such as cross-gain and cross-phase modulation in semiconductor optical amplifiers and four-wave mixing. EO methods require no second optical source, and provide high conversion efficiency and simple control of the shifting amount.

For a continuous light wave, a single-sideband frequency shifter based on Mach-Zehnder interferometers [1] provides over 10-GHz shifting with the maximum efficiency of 34%, corresponding to the square of the maximum value of the first-order Bessel function. Previously, we proposed highly efficient Bragg diffraction type EO frequency shifter and demonstrated the frequency shifting of 16.25-GHz with the efficiency of 82% [2]. In those methods, the amount of frequency shifting is exactly equal to the driving modulation frequency, therefore it is difficult to achieve dynamically controlling of the shift amount of over 1 THz.

As pioneering works, all-optical EO frequency shifter based on phase modulation of pulsed light with linear regions of time-varying refractive index change was proposed and demonstrated in the 1960s [3, 4]. Recently, frequency shifting of optical pulses by as much as 86 GHz in a polymer traveling-wave phase modulator was demonstrated [5]. The frequency shifting obtained by those pulse shifter is related to both the modulation frequency and modulation index, therefore output frequency (destination frequency) can be controlled simply by modulation power. We recently proposed quasi-velocity-matching (QVM) technique with periodic domain inversion that has spanned a 3-THz comb bandwidth at a 16.25-GHz modulation frequency [6]. The QVM technique compensates velocity mismatching between an optical group velocity and a microwave phase velocity in an EO crystal to realize large modulation index by periodically inverting the sign of the EO coefficient of the crystal. Pulse shifters with our QVM EO phase modulators (EOMs) can be one of the promising candidates for wavelength converter in wavelength division multiplexing (WDM) optical communication system, however, it can not apply to the continuous light wave.

In this paper, we propose, analyze, and optimize an efficient frequency shifter for a continuous light wave on the basis of multiple phase modulation with a relative phase control of the sidebands.

2. Frequency shifting process

Figure 1 schematically shows frequency shifting process. The shifting process consists of three stages: (i) phase modulation and chirp compression to generate pulse train, (ii) center frequency shifting of the pulse train

through the Doppler shift in a second phase modulation, and (iii) demodulation of the pulse train through the reverse process of the stage (i) to improve frequency shifting efficiency. In the figure, input and output waveforms for each stage are depicted in Fourier spectrum shown in units of the sideband number n. All EOMs are assumed to be driven at the same modulation frequency of f_m. Considering a plane continuous light wave with frequency of ν_0, the modulated light field just after the EOM1 is expressed as

$$\begin{aligned} E_1(t) &= \exp[j(\omega_0 t - \Delta\theta_1 \cos(\omega_m t))] \\ &= \sum_{n=-\infty}^{\infty} J_n(\Delta\theta_1) \exp[j(\omega_0 + n\omega_m)t], \end{aligned} \tag{1}$$

where $\Delta\theta_1$ is the modulation index, J_n is the nth Bessel function of the first kind, $\omega_m = 2\pi f_m$, $\omega_0 = 2\pi\nu_0$. The amplitude of the nth sideband component after the relative sideband-phase control of $\phi_1(n)$ can be written as

$$q_{1n} = J_n(\Delta\theta_1)\phi_1(n). \tag{2}$$

In our case, $\phi_1(n)$ is

$$\phi_1(n) = \exp\left(j\frac{\alpha}{2\Delta\theta_1}n^2\right) \times \exp\left(-j\frac{\pi}{2}n\right), \tag{3}$$

for achieving chirp compression. α is the bunching parameter to be optimized to improve frequency shifting efficiency. The pulsed output generated in the stage (i) is fed into the stage (ii) as shown in Fig. 1. The relative modulation phase between EOM1 and EOM2 is adjusted so that the chirp compressed pulses go through the medium of the EOM2 at times when the refractive index increases or decreases at the fastest rate. $\exp(-jn\pi/2)$ in (3) is such a delay factor to realize upshift. The amplitude $q_{2n'}$ of the component at frequency $(\nu_0 + n'f_m)$ just after the EOM2 is expressed as

$$q_{2n'} = \sum_{n=-\infty}^{\infty} q_{1n} J_{-(n-n')}(\Delta\theta_2). \tag{4}$$

Although the temporal intensity profile is not influenced by the second phase modulation, optical pulse spectrum seems to have shifted. This is explained in terms of Doppler shift in time domain [3]. Equation (4) shows that this effect can also be explained by the superposition of the sidebands. In the EOM2, each frequency $(\nu_0 + nf_m)$ generated by the EOM1 gives rise to a set of sidebands spaced by multiples of f_m from the original frequency $(\nu_0 + nf_m)$. Because EOM1 and EOM2 are driven at the same modulation frequency, each of these sidebands coincides in frequency of other sidebands of other input frequencies. Here we refer to the sideband number for a component having the maximum intensity as n'_{max}. The maximum frequency deviation in the EOM2 can be approximated as $f_m\Delta\theta_2$, hence n'_{max} can be expressed as $n'_{max} \approx \Delta\theta_2$. Filtering this n'_{max}th sideband component, we achieve continuous light wave whose frequency is shifted by $n'_{max}f_m$. The shifting amount is

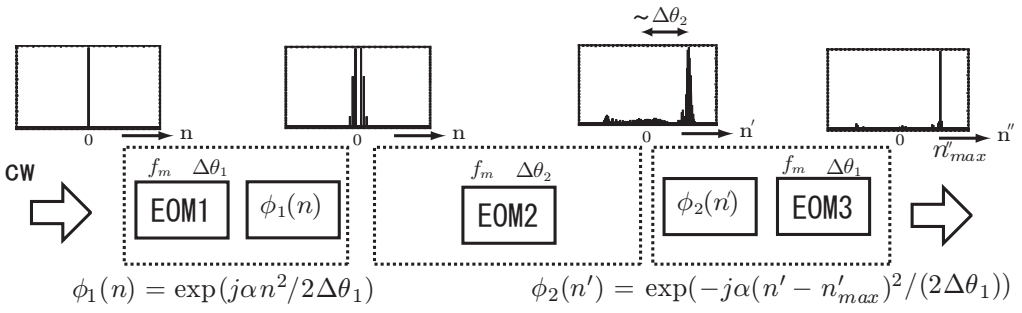

Figure 1: Schematics of the frequency shifting process. The frequency shifting process consists of three stages: (i) phase modulation and chirp compression, (ii) center frequency shifting of the pulse train, and (iii) demodulation of the pulse train.

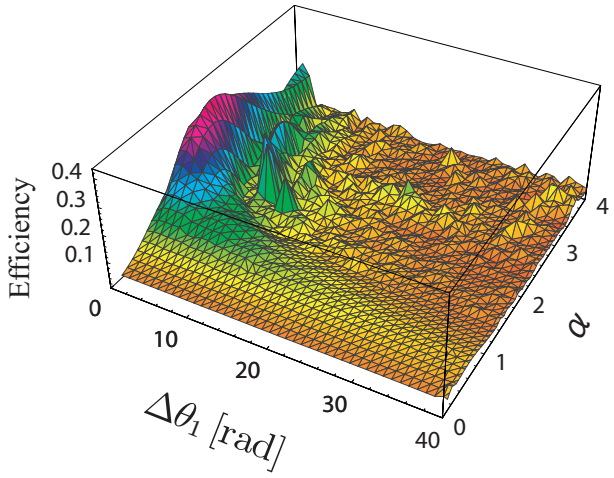

Figure 2: shifting efficiency as a function of ($\Delta\theta_1$, α).

about $n'_{max} \approx \Delta\theta_2$ times as large as that of the SSB method or our Bragg diffraction type frequency shifter, though the efficiency is about 10%. This shifting efficiency can be improved through the reverse process of the stage (i).

Using two EOMs operating at the same modulation frequency and the same modulation index of $\Delta\theta$, the resultant light signal can be made to have a modulation index anywhere between 0 and $2\Delta\theta$ by properly adjusting the relative phase of the modulation signal. Hence, if there is complete Doppler shift in the stage (ii) not by the sinusoidal but by ideally linear refractive index change, we can completely cancel the first phase modulation using third EOM. Although the Fourier spectrum of the pulse train is not completely shifted in our case, the shifting efficiency can be improved through the stage (iii). In the stage (iii), the relative sideband phase is controlled by $\phi_2(n')$ and then the phase is modulated by the EOM3. The EOM3 is driven π out of phase compared with the EOM1 with the same modulation index of $\Delta\theta_1$. Because center frequency of the pulse train has been shifted by $n'_{max}f_m$, the inverse phase control of $\phi_2(n')$ can be,

$$\phi_2(n') = \exp\left(-j\frac{\alpha}{2\Delta\theta_1}(n' - n'_{max})^2\right) \times \exp\left(-j\frac{\pi}{2}n'\right). \tag{5}$$

Note that the $\exp[-jn'\pi/2]$ is the delay factor for achieving a proper modulation phase shift. The amplitude $q_{3n''}$ of the component at frequency $(\nu_0 + n''f_m)$ just after the EOM3 is expressed as

$$q_{3n''} = \sum_{n'=-\infty}^{\infty} q_{2n'}\phi_2(n')J_{-(n'-n'')}(\Delta\theta_1). \tag{6}$$

Filtering the n''_{max}th component, we achieve frequency shifted continuous light wave efficiently.

In our frequency shifting process, the shift amount is determined by not only the modulation frequency, f_m, but also the modulation index of the EOM2, $\Delta\theta_2$. On the other hand, the shifting efficiency is influenced by the pulse characteristic generated in the stage (i). To maximize the shifting efficiency, we simply optimized the parameters ($\Delta\theta_1$, α).

Figure 2 shows relation between shifting efficiency and ($\Delta\theta_1$, α) numerically calculated using (6). In the calculation the modulation index of the EOM2 is fixed at $\Delta\theta_2 = 50$ rad. The optimized parameters are found to be ($\Delta\theta_1$, α)=($3\pi/4$ rad, 1.8) maximizing $|q_{3n''_{max}}|^2$.

3. Numerical simulation

Figure 3(a) shows numerically calculated output spectrum. Using (6), calculation is carried out with $\Delta\theta_2 =$ 50 rad. The relative modulation phase between the EOM1 and the EOM2 is set to be $-\pi/2$ for upshift. In the case of $\Delta\theta_2 = 50$ rad, about 40% of the total optical power is concentrated in the 48th component. Note that with the QVM technique, modulation index of 50 rad at the modulation frequency of 16 GHz can be realized [6].

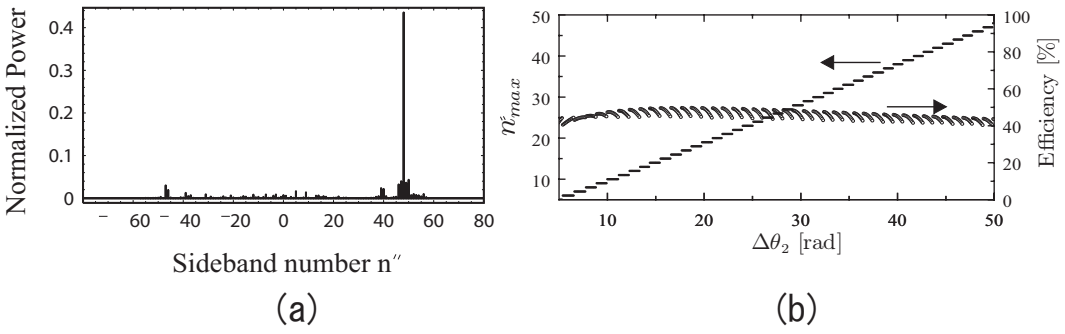

Figure 3: (a) Output spectrum. Modulation index of the EOM2 is 50 rad. n''_{max} is 48. (b) Conversion efficiency and n''_{max} characteristics as a function of $\Delta\theta_2$.

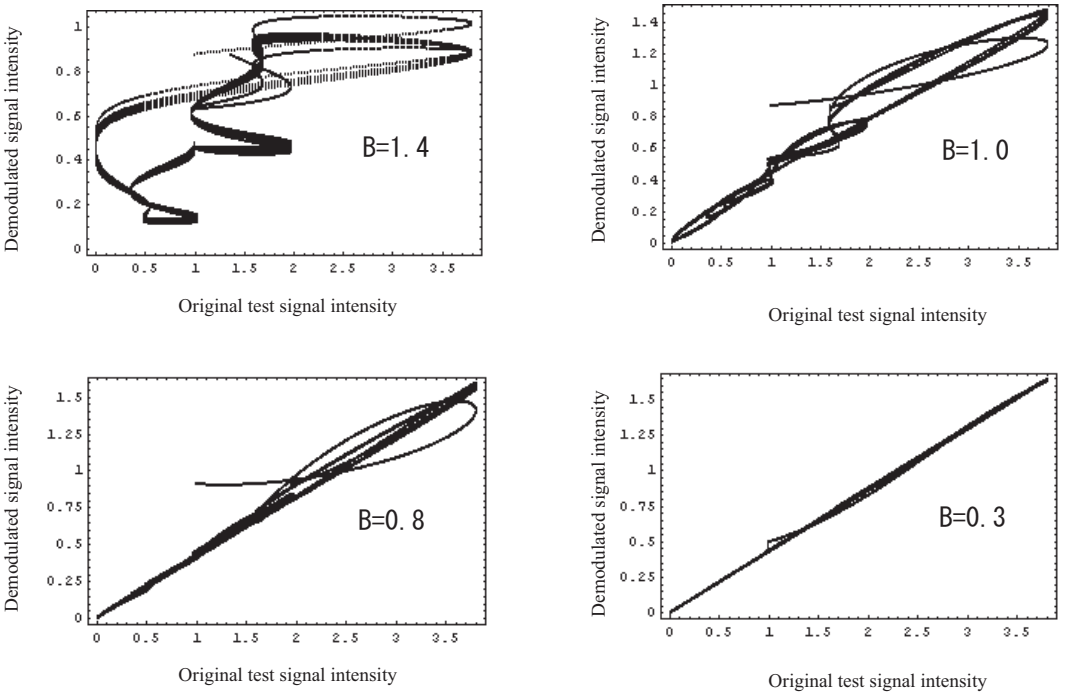

Figure 4: cross-correlation diagrams between the original test signal and the demodulated signal after carrier frequency shifting.B =(signal bandwidth)/(f_m).

Figure 3(b) shows the characteristics of the destination sideband number n''_{max} and the shifting efficiency as a function of the modulation index of the EOM2, $\Delta\theta_2$. The calculation was carried out with 0.1 rad steps of $\Delta\theta_2$ based on (6). n''_{max} increases discretely with the increase of $\Delta\theta_2$. The overall frequency shifting efficiency is about 40-50%. The shifting efficiency changes by $\sim 5\%$ with the change of the modulation index of 1 rad. The destination frequency which can be controlled by $\Delta\theta_2$ lies in the frequency grid spaced accurately by the modulation frequency. This characteristic is very useful for the frequency converter in the WDM optical communication systems, where the use of wavelengths separated by a few tens of gigahertzs is an important issue.

The proposed method can convert carrier frequency of any modulated signal occupying the signal bandwidth of less than f_m. Figure 4 shows the cross-correlation diagrams between the original test signal and the demodulated signal after carrier frequency shifting. B in the figure is normalized occupation bandwidth of the signal defined by B =(signal bandwidth)/(f_m). The simulation is carried out with the time-domain analysis using Fast Fourier Transform. The cross-correlation diagram for $B = 1.4$ is complicated because of the crosstalk

between the neighboring channels. For the carrier frequency shifter based on this technique in the WDM optical communication systems, B is required to be less than at least 0.8.

4. Conclusion

We have numerically demonstrated an efficient frequency shifting method for a continuous light wave on the basis of multistage phase modulation with a relative phase control of the sidebands. The destination frequency of the frequency shift, which can be controlled by the modulation power, lies in the frequency grid spaced accurately by the modulation frequency. With the optimized condition, frequency shifting efficiency of about 40% covering at least ±50-channel of the destination frequency in units of the modulation frequency has been numerically demonstrated. The carrier frequency shifting of the analog data stream has been also evaluated based on cross-correlation diagram.

Acknowledgment

This research was partially supported by the Ministry of Education, Science, Sports and Culture, Grant-in-Aid for Scientific Research on Priority Areas, 18040005, 2006.

REFERENCES

1. M. Izutsu, S. Shikama, and T. Sueta,"Gntegrated optical SSB modulator/frequency shifter," IEEE J. Quantum Electron., **17,** 2225 (1981).
2. k. Shibuya, S. Hisatake and T. Kobayashi, "10-GHz-order high-efficiency electrooptic frequency shifter using slant periodic domain inversion," IEEE Photon. Technol. Lett. **16,** 1939 (2004).
3. M. A. Duguay, L. E. Hargrove, and K. B. Jefferts, "Optical frequency translation of mode-locked laser pulses," Apll. Phys. Lett. **9,** 287 (1966).
4. M. A. Duguay and J. Hansen, "Optical frequency shifting of a modelocked laser beam," IEEE J. Quantum Electron., **4,** 477 (1968).
5. I. Y. Poberezhskiy, B. J. Bortnil, S.-K. Kim, and H. R. Fetterman, "Electro-optic polymer frequency shifter activated by input optical pulses," Opt. Lett. **28.** 1570 (2003).
6. A. Morimoto, M. Tamaru, Y. Matsuda, M. Arisawa, and T. Kobayashi, in Pacific Rim Conference on Lasers and Electro-Optics (Institute of Electrical and Electronics Engineers, 1995), p. 234.

Modified Range Migration Algorithm for Airborne Squint Mode Spotlight SAR Data Processing

Hee-Sub Shin and Jong-Tae Lim
Department of EECS and Radiowave Detection Research Center,
Korea Advanced Institute of Science and Technology, Korea

Abstract - To use the range migration algorithm (RMA) technique for squint-mode SAR, we introduce an approximated reference signal with phase compensation to a fixed point. The modified reference signal makes a squinted phase of scene center scatter into a broadside-mode case. Then, the presented formulation is analyzed by using the principle of the stationary phase. The effectiveness of the proposed method is tested with some numerical simulations via a pulsed spotlight SAR simulator.

1. Introduction

Spotlight synthetic aperture radar (SAR) is a powerful remote sensing technique that allows a fine resolution microwave imaging system mounted on airborne or spaceborne. Thus, several algorithms have been developed for the reconstruction of spotlight SAR data [1]-[3]. Each has its own advantages and drawbacks. Since conventional reconstruction methods like the polar format algorithm (PFA) typically employ the plane wave assumption, the algorithms have curvature errors and degraded images. The range migration algorithm (RMA) technique has the high image quality by modeling the actual spherical wave and the computation efficiency in the broadside-mode. However, the SAR with the squinted geometry produces crucial problems in the RMA technique. That is, since the RMA technique requires the phase compensation to a line unlike the PFA technique, the phase of scene center scatter is changed after motion compensation to a line [1]. Thus, the RMA technique cannot generate an acceptable performance in the squint-mode. If this problem is not properly compensated during the SAR data processing, the quality of the final image in the squint-mode SAR is degraded. Though several methods have been researched in the squinted stripmap-mode SAR, in the case of spotlight SAR with a squint angle, it is a still difficult task to obtain the images with high quality [4]-[5]. Thus, we introduce an extension of the original RMA technique to process the spotlight data with a squint angle. To use the RMA technique with squinted geometry, we introduce a reference signal with phase compensation to a fixed point based on the approximation to obtain the phase of scene center scatter like broadside-mode. Then, we use the principle of the stationary phase to analyze the terms added by the modified reference signal. Moreover, we test the proposed algorithm with some numerical simulations via a pulsed spotlight SAR simulator.

2. Signal Model of Airborne Squint Mode Spotlight SAR

As shown in Fig. 1, the SAR sensor travels a straight-line flight path parallel to the x-axis during a synthetic aperture length L. Also, the radar transmits and receives pulses at a fixed pulse repetition interval to maintain uniform spatial sampling along the flight path. Let a SAR sensor position along the flight path be (x_a, y_a, z_a) where x_a is an azimuth position, y_a is the constant ground range distance between the x-axis and the flight path, and z_a is the constant nominal altitude of airborne. Let the distance between the SAR sensor and the target be $R_t = \sqrt{(x_a - x_t)^2 + (y_a - y_t)^2 + (z_a - z_t)^2}$. Also, let a squinted scene center position be (x_c, y_c) and a squint angle be $\theta_s = \tan^{-1}(\frac{x_c}{y_a - y_c})$.

The linear FM (chirp) pulse with duration time T_p transmitted by the radar is

$$s_t(\tau) \quad = \quad e^{j(2\pi f_c \tau + \pi\gamma\tau^2)} \tag{1}$$

where τ is time, the quantity f_c represents the center transmit frequency, and γ is the FM chirp rate

[1]. The received signal is

$$s_r(n,\tau) = \rho(x_t,y_t,z_t)e^{j2\pi f_c(\tau-\frac{2R_t}{c})}e^{j\pi\gamma(\tau-\frac{2R_t}{c})^2} \quad (2)$$

where c is the speed of microwave, n is the pulse number, and $\rho(x_t,y_t,z_t)$ is the reflectivity function of the target.

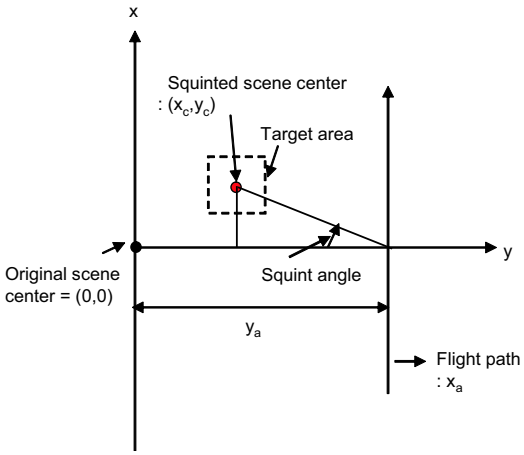

Figure 1: 2-D geometry model

3. Main Results

After motion compensation to a line in the original RMA technique, the partial phase of scene center scatter is

$$\phi_1 = \sqrt{x_a^2+y_a^2+z_a^2}-\sqrt{y_a^2+z_a^2} \quad (3)$$

However, the partial phase of scene center scatter for squint-mode is

$$\phi_2 = \sqrt{(x_a-x_c)^2+(y_a-y_c)^2+z_a^2}-\sqrt{y_a^2+z_a^2} \quad (4)$$

Thus, since the squint-mode changes the phase of scene center scatter, the original RMA technique is difficult to reconstruct the image for squint-mode SAR. To solve the problem of the RMA technique, we use a reference signal with motion compensation to a fixed point rather than to a line. That is, to make the phase of (3) in the squint-mode, we introduce the following compensation technique. To better approximate, we extend the Taylor series in the 2 variables (x_c,y_c). Thus, the first term of (4) can be simplified and rewritten as follows:

$$\begin{aligned}\sqrt{(x_a-x_c)^2+(y_a-y_c)^2+z_a^2} &\approx \sqrt{x_a^2+y_a^2+z_a^2} \\ &\quad -\sum_{k=1}^{m}\frac{1}{m}x_c\times\frac{(x_a-\frac{m-k}{m}x_c)}{\sqrt{(x_a-\frac{m-k}{m}x_c)^2+(y_a-\frac{m-k}{m}y_c)^2+z_a^2}} \\ &\quad -\sum_{k=1}^{m}\frac{1}{m}y_c\times\frac{(y_a-\frac{m-k}{m}y_c)}{\sqrt{(x_a-\frac{m-k}{m}x_c)^2+(y_a-\frac{m-k}{m}y_c)^2+z_a^2}} \\ &= \sqrt{x_a^2+y_a^2+z_a^2}+R \end{aligned} \quad (5)$$

where $R=\sum_{k=1}^{m}\frac{-\frac{1}{m}x_c(x_a-\frac{m-k}{m}x_c)-\frac{1}{m}y_c(y_a-\frac{m-k}{m}y_c)}{\sqrt{(x_a-\frac{m-k}{m}x_c)^2+(y_a-\frac{m-k}{m}y_c)^2+z_a^2}}$. From (3) and (4), using $R_a=R_s+R=\sqrt{y_a^2+z_a^2}+R$ as the reference, we can obtain the phase of scene center scatter like broadside-mode case, i.e., $\phi_1\approx\phi_2$.

Thus, to compensate the problem for squint-mode, we use the following reference signal

$$s_{ref}(n,\tau) = e^{j2\pi f_c(\tau-\frac{2R_a}{c})}e^{j\pi\gamma(\tau-\frac{2R_a}{c})^2} \quad (6)$$

If we mix the received signal (2) with the complex conjugated signal of (6), the resulting signal is

$$s(n,\tau;x_a,y_a,z_a) = \rho(x_t,y_t,z_t)e^{j\Phi(n,\tau;x_a,y_a,z_a)} \quad (7)$$

with $\Phi(n,\tau;x_a,y_a,z_a) = -\frac{4\pi\gamma}{c}(\frac{f_c}{\gamma}+\tau-\frac{2R_a}{c})(R_t-R_a)+\frac{4\pi\gamma}{c^2}(R_t-R_a)^2$
From the phase of (7), we obtain the following phase term

$$\Phi(n,\tau;x_a,y_a,z_a) = -\frac{4\pi\gamma}{c}(\frac{f_c}{\gamma}+\tau-\frac{2R_s}{c})(R_t-R_a)+\frac{8\pi\gamma}{c^2}(R_a-R_s)(R_t-R_a)+\frac{4\pi\gamma}{c^2}(R_t-R_a)^2 \quad (8)$$

Also, to remove the residual video phase terms $\frac{8\pi\gamma}{c^2}(R_a-R_s)(R_t-R_a)+\frac{4\pi\gamma}{c^2}(R_t-R_a)^2$, we use the range deskew [1]. We modify the original range deskew to remove an additional term $\frac{8\pi\gamma}{c^2}(R_a-R_s)(R_t-R_a)$.
The range deskew process is as follows:
Since the instantaneous frequency is $f=\frac{1}{2\pi}\frac{d\Phi}{d\tau}$, evaluating this derivative yields

$$f = -\frac{2\gamma}{c}R_\Delta(1-\frac{2}{c}\frac{dR_\Delta}{d\tau})-\frac{2\gamma}{c}(\tau-\frac{2R_a}{c}+\frac{f_c}{\gamma})\frac{dR_\Delta}{d\tau} \quad (9)$$

using $R_\Delta = R_t - R_a$ for convenience. Therefore, since the approximation $f \approx -\frac{2\gamma}{c}R_\Delta$ is adequate, we introduce the following phase compensation term

$$s_{com}(f_\tau) = e^{-j(\frac{\pi f_\tau^2}{\gamma}-\frac{4\pi(R_a-R_s)}{c}f_\tau)} \quad (10)$$

where f_τ is the frequency variable of τ while τ is the time variable.
After application of $s_{com}(f)$, the phase becomes

$$\Phi(n,k_r;x_a,y_a,z_a) = -k_r(R_t-R_a) \quad (11)$$

where $k_r = \frac{4\pi\gamma}{c}(\frac{f_c}{\gamma}+\tau-\frac{2R_s}{c})$.
Thus, we obtain the following phase term

$$\Phi(n,k_r;x_a,y_a,z_a) = -k_r(\sqrt{(x_a-x_t)^2+(y_a-y_t)^2+(z_a-z_t)^2}-f(x_a)) \quad (12)$$

where $f(x_a) = R_s + R$.
However, since the term R is added, we need to perform the following step.

Let $R_B = \sqrt{(y_a-y_t)^2+(z_a-z_t)^2}$. Then, the azimuth Fourier transform of $s(n,k_r;x_a,y_a,z_a)$ with respect to x_a yields

$$S(n,k_x,k_r) = \int \rho(x_t,y_t,z_t)e^{-jk_r(\sqrt{(x_a-x_t)^2+R_B^2}-f(x_a))-jk_xx_a}dx_a \quad (13)$$

To evaluate (13), using the method of stationary phase, we determine the stationary point of its phase. Also, the phase function φ corresponds to

$$\varphi(n,k_r;x_a,y_a,z_a) = -k_r\sqrt{(x_a-x_t)^2+R_B^2}+k_rf(x_a)-k_xx_a \quad (14)$$

Equating the first derivative of (14) to zero gives

$$\frac{\partial\varphi(n,k_r;x_a,y_a,z_a)}{\partial x_a}(x_a^*) = -\frac{k_r(x_a^*-x_t)}{\sqrt{(x_a^*-x_t)^2+R_B^2}}+k_r\frac{\partial f(x_a)}{\partial x_a}-k_x = 0 \quad (15)$$

Solving (15) for x_a^*, we obtain

$$x_a^* = -\frac{(k_x - k_r\frac{\partial f(x_a)}{\partial x_a})R_B}{\sqrt{k_r^2 - (k_x - k_r\frac{\partial f(x_a)}{\partial x_a})^2}} + x_t \tag{16}$$

as the stationary point. Also, since x_a is much smaller than y_a and z_a for airborne SAR, we obtain

$$\begin{aligned} f(x_a) &\approx \sum_{k=1}^{m} \frac{-\frac{1}{m}x_c(x_a - \frac{m-k}{m}x_c) - \frac{1}{m}y_c(y_a - \frac{m-k}{m}y_c)}{\sqrt{(y_a - \frac{m-k}{m}y_c)^2 + z_a^2}} + R_s \\ &= q_1 x_a + q_2 + R_s \end{aligned} \tag{17}$$

where $q_1 = \sum_{k=1}^{m} \frac{-\frac{1}{m}x_c}{\sqrt{(y_a - \frac{m-k}{m}y_c)^2 + z_a^2}}$ and $q_2 = \sum_{k=1}^{m} \frac{\frac{1}{m}\frac{m-k}{m}x_c^2 - \frac{1}{m}y_c(y_a - \frac{m-k}{m}y_c)}{\sqrt{(y_a - \frac{m-k}{m}y_c)^2 + z_a^2}}$. Moreover, since $\frac{\partial f(x_a)}{\partial x_a} \approx q_1 \approx 0$ for airborne SAR is satisfied, we approximate x_a^* using the first-order Taylor approximation in the variable $\frac{\partial f(x_a)}{\partial x_a}$. Thus, x_a^* is rewritten as follows:

$$x_a^* \approx -\frac{k_x R_B}{\sqrt{k_r^2 - k_x^2}} + x_t \tag{18}$$

Hence, substituting the value x_a^* for x_a in the phase of (12), after some manipulation and the Taylor approximation, we obtain the following phase term

$$\begin{aligned} \Phi(n, k_x, k_r) &\approx k_r f(x_a^*) - R_B\sqrt{k_r^2 - k_x^2} - k_x x_t \\ &\approx k_r(q_2 + R_s) - R_B\sqrt{k_r^2 - k_x^2} - k_x x_t \end{aligned} \tag{19}$$

Also, from $q_2 \ll R_s$, the phase matched filter can be defined as follows:

$$\Phi_{mf}(k_x, k_r) = -k_r R_s + \sqrt{k_r^2 - k_x^2}R_s \tag{20}$$

A change of variables, known as the Stolt interpolation is defined as $k_y = \sqrt{k_r^2 - k_x^2}$. Thus, after application of the matched filter and the Stolt interpolation, the phase term becomes

$$\Phi_{rma}(n, k_x, k_y) \approx -k_y(R_B - R_s) - k_x x_t \tag{21}$$

Thus, we obtain

$$S_{rma}(n, k_x, k_r) \approx \rho(x_t, y_t, z_t)e^{-jk_y(R_B - R_s) - jk_x x_t} \tag{22}$$

From (22), if we perform a 2-D inverse FFT for the distributed targets, we can obtain the SAR images. Finally, since the targets are not in their original position, we need a transformation.

4. Simulation Results

In order to test the validity and effectiveness of the proposed method, we simulate a radar imaging of 2-D five point targets. The basic simulation parameters are as follows: $f_c = 10$GHz, $L = 300$m, bandwidth $B = 250$MHz, PRF=1000Hz, platform velocity $v = 100$m/s, $T_P = 1\mu$sec, sampling frequency $F_s = 350$MHz, $y_a = 5000$m, $z_a = 2000$m. Also, we set $(x_c, y_c) = (1000, 200)$m and $(x_c, y_c) = (1500, 200)$m. As shown Figs. 2-5, the proposed method generates better results compared to the original RMA technique.

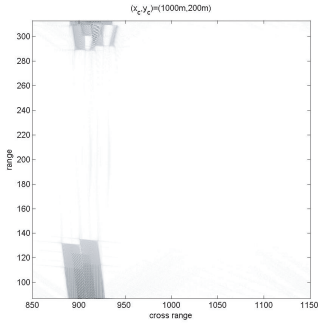

Figure 2: Target response via original RMA

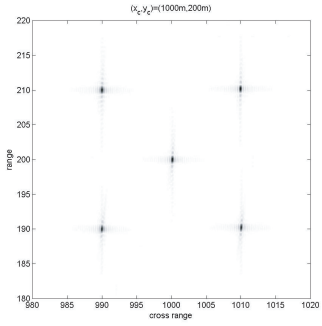

Figure 3: Target response via proposed method

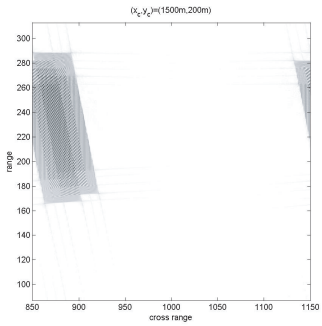

Figure 4: Target response via original RMA

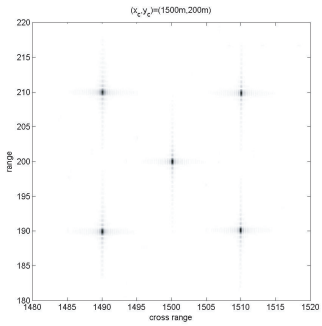

Figure 5: Target response via proposed method

5. Conclusion

To obtain SAR images with high quality for airborne squint-mode spotlight SAR data processing, we proposed an efficient compensation method. That is, we introduce the modified reference signal with phase compensation to a fixed point. Then, using the principle of the stationary phase, we formulated and analyzed the phase information. Further works are to increase the squint angle and the scene size. We will extend and apply the principle of the stationary phase in the modification of the stationary point induced by the compensation term.

Acknowledgement

This research was supported by the Agency for Defense Development, Korea, through the Radiowave Detection Research Center at Korea Advanced Institute of Science and Technology.

REFERENCES

1. CARRARA, W.G., GOODMAN, R.S., and MAJEWSKI, R.M., Spotlight synthetic aperture radar signal processing algorithms, Artech House, 1995.
2. SOUMEKH, M., Synthetic aperture radar signal processing with MATLAB algorithms, John Wiley & Sons, Inc., 1999.
3. CUMMING, I.G. and WONG, F.H., Digital processing of synthetic aperture radar data, Artech House, 2005.
4. DAVIDSON, G.W., CUMMING, I.G., and ITO, M.R., "A chirp scaling approach for processing squint mode SAR data," *IEEE Trans. Aerosp. Electro. Syst.*, Vol. 32, No. 1, 121-132, 1996.
5. YEO, T.S., TAN, N.L., ZHANG, C.B., and LU, Y.H., "A new subaperture approach to high squint SAR processing," *IEEE Trans. Geosci. Remote Sens.*, Vol. 39, No. 5, 954-968, 2001.

Weighted Singularity-Spreading Method to Unwrap Airborne Interferogram

Ryo Yamaki and Akira Hirose
Dept. Electron. Eng., The University of Tokyo, 7-3-1 Bunkyo-Ku, Tokyo, 113-8656, Japan
Phone: +81-3-5841-7494 Fax:+81-3-5841-7494
yamaki@eis.t.u-tokyo.ac.jp , ahirose@ee.t.u-tokyo.ac.jp

Abstract— How to process phase singular points (residues) is a di cult problem in 2D phase unwrapping. Though the minimum-cost network ow method is widely used for phase unwrapping, some problems still remain. That is, the method cannot process isolated singular points properly. It also takes long time to unwrap phase data that contains many residues. Previously, we propose a new unwrapping method, the singularity-spreading phase unwrapping (SSPU), which solves these problems. In this paper, we newly propose weighted SSPU. We explain how to utilize amplitude information in the weighted SSPU. It is found that the weighted SSPU obtains more precise result than the simple SSPU method. The calculation time is also evaluated.

1 Introduction

Interferogram generated in InSAR systems and other radars is used to generate accurate digital elevation maps (DEMs) that express landscape. Since the obtained phase data is wrapped into to , we need to unwrap the phase value to construct a DEM. However, the phase data contains many singular points (SPs or residues), which cause phase inconsistency. Therefore, various methods to estimate the unwrapped phase have been proposed[1][2]. Particularly, the minimum-cost network ow method that Costantini proposed in 1998 is now mainstream[3]. However, the method cannot process isolated SPs properly, and it takes long time to unwrap a phase image that contains many SPs.

In this paper, we explain our proposal[4], the singularity-spreading phase unwrapping to solve these problems and how to utilize amplitude information in the weighted singularity spreading. It is found that the weighted singularity-spreading phase unwrapping (SSPU) obtains more precise result than the simple SSPU. The calculation time in the simple or weighted SSPU is found less than in the network programming method.

2 Phase Singularity Spreading Method

2.1 Isotropic Phase-Singularity Spreading Method

We prepare a coordinate system as shown in Fig.1. We de ne the rotation $R(x, y)$ at (x, y) in the wrapped phase as

$$\begin{aligned} R(x,y) \equiv & \quad [\ {}_w(x+\Delta x, y) \quad {}_w(x,y)] \\ & +[\ {}_w(x+\Delta x, y+\Delta y) \quad {}_w(x+\Delta x, y)] \\ & \quad [\ {}_w(x+\Delta x, y+\Delta y) \quad {}_w(x, y+\Delta y)] \\ & \quad [\ {}_w(x, y+\Delta y) \quad {}_w(x,y)]\ /2 \end{aligned} \tag{1}$$

where ${}_w(x, y)$ denotes observed wrapped phase value and $[\bullet]$ means the principal value within (,]. At an SP, $R(x, y)$ has non-zero value, i.e., +1 or 1.

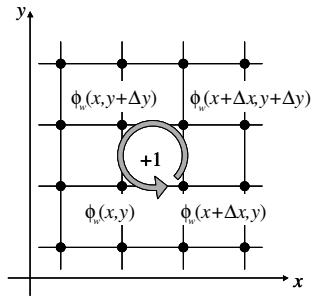

Figure 1: Coordinate

In the minimum-cost network ow method, we add integer multiple of 2 to one of four phase discrete derivatives around a singular point. With this process, an SP moves to one of the neighboring pixels. When positive and negative residues combine, phase inconsistency is canceled. However, the method often generates unnatural long cli s and sharp peaks, which do not exist in the real landscape, because of isolated residues.

We consider that the cause of emergence of phase singularity is phase distortion in electromagnetic wave propagation [5]. For example, in steep area, interference of re ecting waves causes phase distortion. In shadowed area, phase value is unreliable and containing relatively much noise. Therefore, the phase singularity should be compensated or eased in a continuous manner with their vicinity, instead of discrete 2 phase shift.

$$_{cx}(x,y) = 2\ R(x,y)/4 \quad (2)$$
$$_{cx}(x,y+\Delta y) = 2\ R(x,y)/4 \quad (3)$$
$$_{cy}(x,y) = 2\ R(x,y)/4 \quad (4)$$
$$_{cy}(x+\Delta x,y) = 2\ R(x,y)/4 \quad (5)$$

where $_{cx}$ and $_{cy}$ compensators to denote x- and y-directional phase derivatives, respectively.

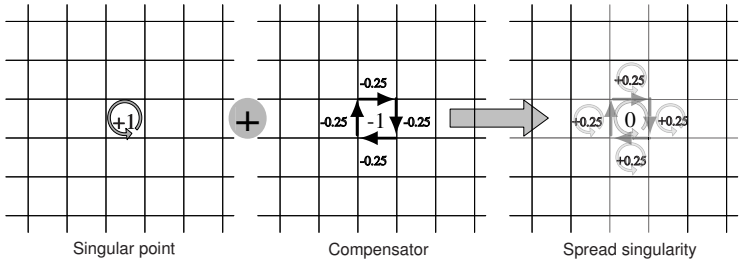

Figure 2: Isotropic phase-singularity spreading

Therefore, we have proposed the SSPU. In this method, we spread around and attenuate phase singularity by adding fractions of inverse rotation to respective four phase derivatives around the SP distributively as This spreading process is illustrated in Fig.2. After iterations (index : l) of this process over the whole image, compensators $_{cx}$ and $_{cy}$ are accumulated as

$$_{cx}(x,y) = \sum_{l} {}_{cx}(x,y) \quad (6)$$
$$_{cy}(x,y) = \sum_{l} {}_{cy}(x,y) \quad (7)$$

where $_{cx}(x,y)$ and $_{cy}(x,y)$ are the nal compensators. In the spreading process, the positive and negative residues combine loosely with each other and the phase inconsistency is cancelled. Then, we can unwrap the phase data simply by summing the phase di erences between neighboring pixels.

In Fig.2, we spread the singularity with evenly-fractional inverse rotation. We call this SSPU method the isotropic SSPU.

2.2 Anisotropic Phase-Singularity Spreading Method Utilizing Amplitude Value

In this paper, we present a modi ed SSPU, i.e., the weighted SSPU, by utilizing amplitude information. In this method, we weight the fractions of the inverse rotation depending on the absolute values of the amplitude derivatives. For example, we determine the weights as

$$_{cx}(x,y) = 2\ R(x,y)\frac{|\Delta_x a(x,y)|}{\sum_c |\Delta a(x,y)|} \quad (8)$$
$$_{cx}(x,y+\Delta y) = 2\ R(x,y)\frac{|\Delta_x a(x,y+\Delta y)|}{\sum_c |\Delta a(x,y)|} \quad (9)$$
$$_{cy}(x,y) = 2\ R(x,y)\frac{|\Delta_y a(x,y)|}{\sum_c |\Delta a(x,y)|} \quad (10)$$
$$_{cy}(x+\Delta x,y) = 2\ R(x,y)\frac{|\Delta_y a(x+\Delta x,y)|}{\sum_c |\Delta a(x,y)|} \quad (11)$$

where x-directional amplitude derivative is $\Delta_x a(x,y) \equiv a(x+\Delta x,y)\quad a(x,y)$, and y-directional one is $\Delta_y a(x,y) \equiv a(x,y+\Delta y)\quad a(x,y)$.

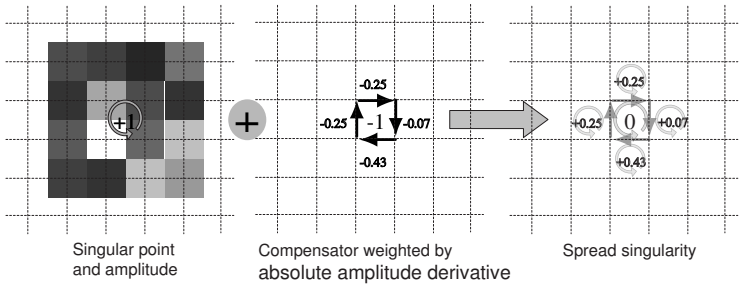

Figure 3: Amplitude-weighted phase singularity spreading

Note that $\sum_c |\Delta a(x,y)| \equiv |\Delta_x a(x,y)| + |\Delta_x a(x,y+\Delta y)| + |\Delta_y a(x,y)| + |\Delta_y a(x+\Delta x,y)|$. The phase singularity is spread ansiotropically as shown in Fig. 3. We call this SSPU method the anisotropic SSPU.

It is known that, in an amplitude image, the amplitude level is higher than the vicinity of layovers. In the same part in the phase image, the phase value is distorted by interference and should be corrected. Therefore, we enlarge compensators locally in the layover area by weighting the fractions with the absolute values of the amplitude derivatives. Then, the residues have less in uence over other areas. In this case, singularity in the shadowed area or lake, where the re ection is almost zero, are spread almost isotropically in consequence of random noise.

3 Experimental Results

3.1 Compensator Map and Obtained Unwrapped Phase

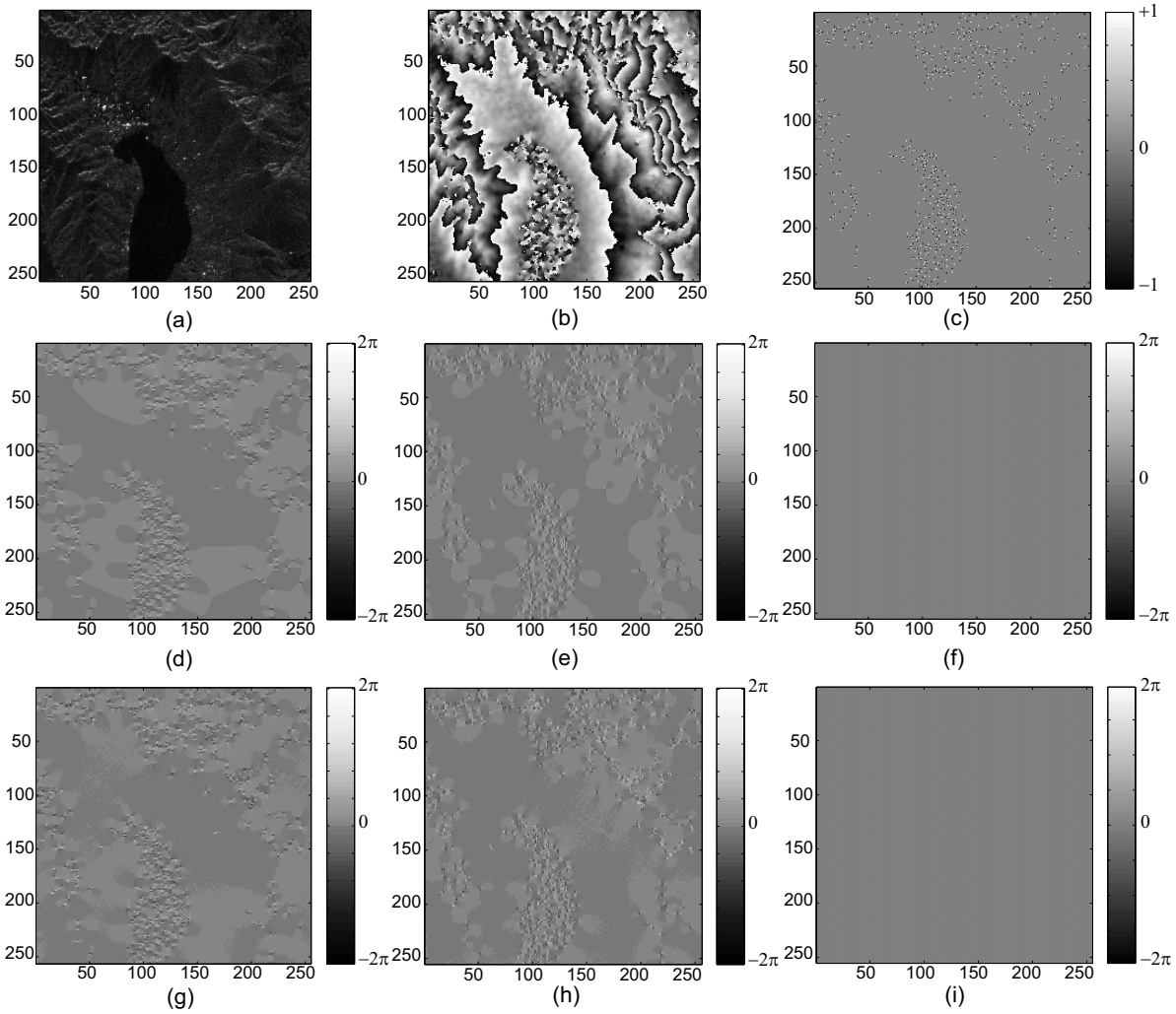

Figure 4: InSAR data and experimental results (a)amplitude image $a(x, y)$, (b)phase image $_w(x, y)$, (c)residue map $R(x, y)$, (d)x-directional compensator (isotropic spreading) $_{cx}(x, y)$, (e)y-diectional compensator (isotropic spreading) $_{cy}(x, y)$, (f)phase inconsistency after isotropic spreading, (g)x-directional compensator (anisotropic spreading) $_{cx}(x, y)$, (h)y-directional compensator (anisotropic spreading) $_{cy}(x, y)$, (i)phase inconsistency after anisotropic spreading.

Figure 4 shows InSAR data, residue map, and the result of singularity spreading. The amplitude image is shown in Fig.4(a). The wrapped phase image is shown in Fig.4(b) in gray scale where black means while white is . In a single phase-cycle, the brighter the color is, the higher the point is. Residue map is shown in Fig.4(c). Pixels where phase rotation is zero are shown in gray. Pixels where phase rotation is +1 are shown in white, while 1 in black. In (a) and (c), it is veri ed that many residues are observed where the layover occurs or where the amplitude is extremely low. We applied isotropic and anisotropic singularity-spreading to the data. Figures 4(d) and (e) show the x- and y-directional phase compensator maps, $_{cx}(x, y)$ and $_{cy}(x, y)$ in isotropic spreading. The resulting phase inconsistency shown in Fig.4(f) is almost zero. Since phase inconsistency is zero, the result of unwrapping is settled uniquely, independent of integration path. Figures 4(g) and (h) show the x- and y-directional phase compensator maps, $_{cx}(x, y)$ and $_{cy}(x, y)$ in anisotropic spreading. Phase inconsistency shown in Fig.4(i) is almost zero as it is in the result of isotropic spreading. It is veri ed that positive and negative residue pairs shown in Fig.4(c) combine each other with compensators shown in (d) and (e), or (g) and (h).

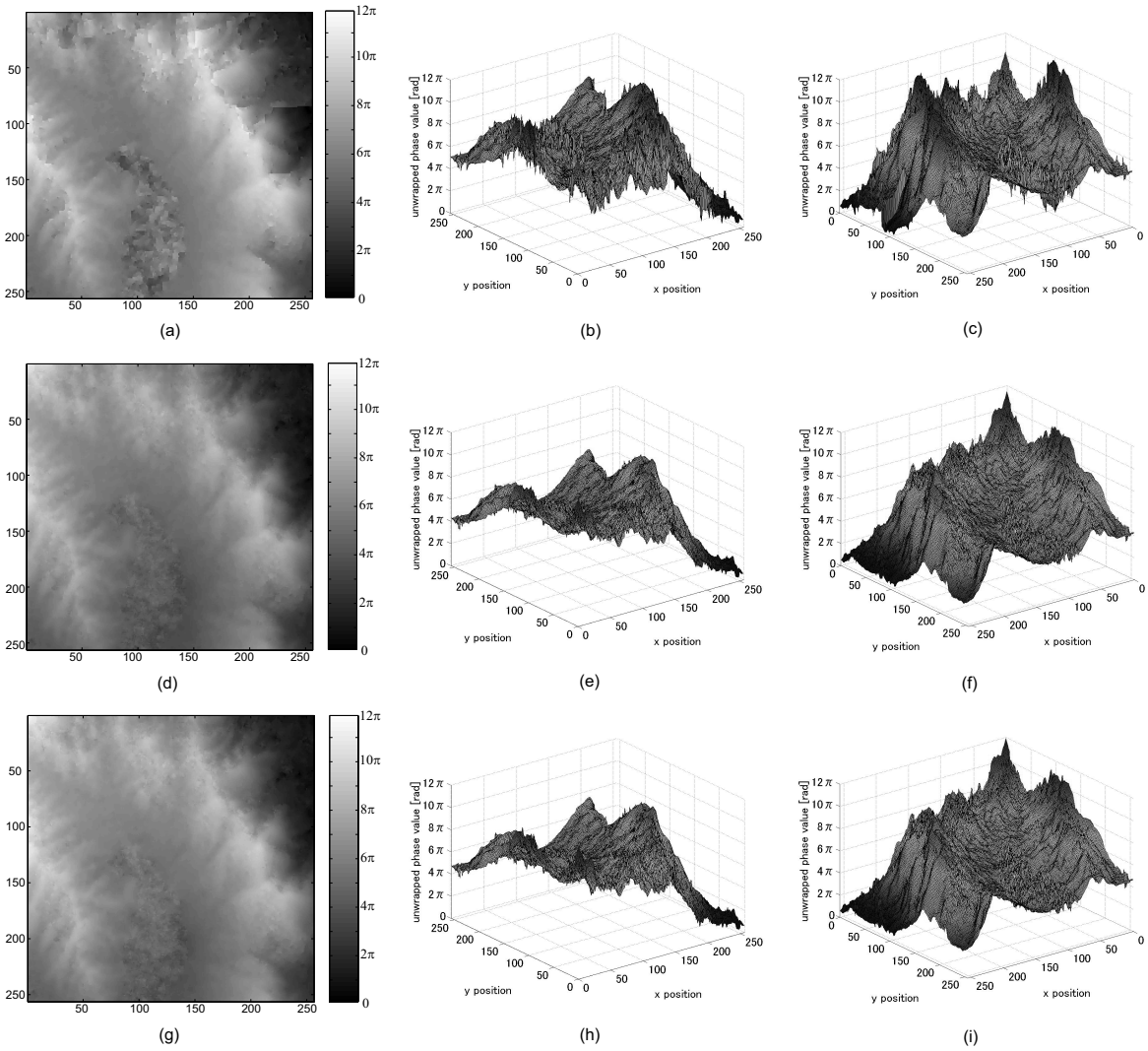

Figure 5: (a)Unwrapped phase obtained in the minimum-cost network ow method, (d)one in the isotropic phase singularity spreading method, and (g)one in the anisotropic phase singularity spreading method, (b),(e) and (h)three dimensional displays of (a),(d) and (g), (c),(f) and (i)displays of (b),(e) and (h) from the opposite viewpoint.

Method	MSE $10^3[m^2]$	Peak Value $10^3[m^2]$
Min. Cost Network Flow	1.659	60.6
Isotropic SSPU	1.463	41.7
Anisotropic SSPU	1.297	47.7

Table 1: MSE and Peak Value

Figure 5 shows the results of unwrapping in (a)the conventional method, (d)the isotropic SSPU, and (g)the anisotropic SSPU, respectively. Figures 5(b),(e) and (h) are the three dimensional displays of Figs.5(a),(d) and (g). Figures 5(c),(f) and (i) are the displays of Figs.5(b),(e) and (h) from the opposite view point.

In the result of the conventional method, for example, in the right top of Fig.5(a) or the left bottom of (c), we nd unnatural long cli s caused by the locus of the SP movement. Such a cli is generated, when a residue cannot nd another one with which it combines in its vicinity. We also nd sharp peaks in the ridges of hills, in particular, in the central top in (b), where the phase values are distorted by the interference. On the surface of the lake, unwrapped phase value is also found uctuating.

On the contrary, in the results of two proposed methods (Fig.5(d),(e) and (f) or (g),(h) and (i)),unnatural

cli s and sharp peaks, which we observed in the result of the conventional method, are reduced, and the phase value uctuation on the lake surface is almost invisible. The results show that the singularity-spreading methods function well.

After the transformation from unwrapped phase values to height maps, we evaluated the errors between the maps and the real terrain height data. Table 1 shows the mean square errors (MSEs) and peak values of the square errors in the respective methods. The squared height-range is 4.423 $10^5[m^2]$. As shown in Table 1, singularity spreading methods reduce both MSEs and error peak values in comparison with the conventional method. In particular, the reductions in peak values remove the sharp peaks on the ridges of the hills. Furthermore, MSE is lower in the anisotropic method than the isotropic one, and the DEM obtained in the anisotropic method is found more accurate than that in the isotropic one.

3.2 Calculation Time

We compared the calculation times these are required for the respective methods to unwrap some phase images (256 256 pixels), which have various density of residues. As shown in Figure 6, in the network programming approach, the more residue we have, the more calculation time is required. In the SSPU, contrarily, the calculation cost is very low and independent of residue density. In the isotropic SSPU, the calculation cost is lower than in the anisotropic SSPU.

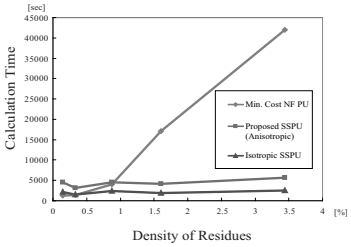

Figure 6: Calculation time

4 Discussion

4.1 E ect of Amplitude Weighted Compensation

With the anisotropic SSPU utilizing the absolute value of the amplitude derivatives, locally in the layover area, larger compensator is added than in other area. That is, the residues have less in uence over other areas. That e ect is veri ed from the reduction in MSE in the anisotropic spreading method as shown in Table 1.

4.2 Calculation Time

In the SSPU, the calculation cost is independent of residue density. Where the residues appear densely, they are close to each other. Then, the process of combining one positive and negative residue pair is completed with less iteration. Furthermore, in the isotropic SSPU, the calculation cost is lower than in the anisotropic SSPU. In the isotropic SSPU, the spreading is weighted equally with constants of 1/4. On the contrary, in the anisotropic SSPU, the spreading is weighted with the variables, the absolute values of the amplitude derivatives. The di erence in the calculation time in the respective methods is attributed to the above di erence in treatment.

5 Summary

The authors presented the modi ed SSPU, i.e., weighted SSPU, by utilizing the amplitude information. And we nd that more precise DEM is generated in the weighted SSPU, than in the conventional method or in the simple SSPU.

Acknowledgment

The authors would like to acknowledge Dr. M. Shimada of EROC/JAXA, Japan, for supplying the InSAR data and the height data for evaluation.

REFERENCES

1. Dennis C. Ghiglia and Mark D. Pritt, "Two-Dimensional Phase Unwrapping : Theory, Algorithms, and Software," JOHN WILERY & SONS, INC., 1998
2. A. B. Suksmono and A. Hirose, "Adaptive noise reduction of InSAR images based on a complex-valued MRF model and its application to phase unwrapping problem," IEEE Transactions on Geoscience and Remote Sensing, Vol.40, No.3, pp.699-709, March 2002
3. Mario Constantini, "A Novel Phase Unwrapping Method Based on Network Programming," IEEE Transactions on Geoscience and Remote Sensing, VOL.36, NO.3, pp.813-821, MAY 1998
4. A. Hirose and R. Yamaki, "Phase Unwrapping with Phase-Singularity Spreading," International Geoscience And Remote Sensing Symposium (IGARSS) 2006 Denver, to be presented
5. A.Hirose K.Sugiyama, "A radar system with phase-sensitive millimetric wave circuitry and complex-amplitude neural processing," Int'l Conf. on Art. Neural Networks (ICANN)'98 Proc.2, 707-712 (Sept. 2-4, 1998, Skovde), Springer-Verlag

Advances in Mathematical Methods for Electromagnetics: Nonlinear Problems and Nonselfadjoint Operator Theory (A Review)

Yury Shestopalov
Karlstad University, SE-65188 Karlstad, Sweden

Abstract–A review of the state-of-the-art and development of advanced mathematical methods of electromagnetics based on the spectral theory of nonselfadjoint operators is given. Several directions are identified for which fundamental results are obtained, including wave propagation and oscillations in metal–dielectric resonators and waveguides, vector screen problems and development of the spectral theory of pseudodifferential operators, interaction phenomena and perturbation theory, wave propagation and diffraction in nonlinear media, and inverse problems.

1. Introduction

Recent advances in mathematical methods for electromagnetics are connected with the development of specific branches of the theory of nonselfadjoint operator-valued functions (OVFs). In fact, nonselfadjoint boundary-value problems (BVPs) for the Maxwell and Helmholtz equations that arise in the mathematical theory of wave propagation and diffraction occupy a specific place because the spectral parameter enters the boundary conditions in a nonlinear manner and the problems are formulated in unbounded domains with noncompact boundaries containing irregularities (edges). Spectral theory of OFVs envelops different solution techniques for BVPs and operator eigenvalue problems with nonlinear dependence on the spectral parameter. The theory provides general methods for the solution of linear and nonlinear partial differential equations (PDEs), integral equations (IE)s, and BVPs, and often when traditional methods fail, e.g. when nonselfadjoint BVPs are considered in unbounded domains and the spectral parameter enters the conditions at infinity in a nonlinear manner.

In this respect, the spectral theory of OVFs clearly demonstrated advantages and served as a basis for *the spectral theory of open structures* [1, 2] constructed and developed during the last three decades. This theory is a collection of specific problem settings arising in the mathematical theory of wave propagation and diffraction and offers universal solution techniques for these problems.

The first studies which served as a basis of the spectral theory of open structures date back to the works of Hilbert [3] and Giraud [4]. They considered in particular integral operators (and infinite determinants) with kernels depending on a complex parameter. Many important results were obtained by Keldysh [5] and other mathematicians in the 1950s who studied abstract operator pencils. A breakthrough was made by Gohberg [6] in the 1950s; he introduced main definitions and constructed foundations of the modern spectral theory of OFVs and proved on this basis the so-called analytical Fredholm theorem. It was shown [7] that many statements of the theory of functions of one complex variable remain valid in the 'operator' case, in particular, the Rouchet's theorem [8]. Another significant contribution was made by Vainikko and coauthors in the 1970s [9] who performed a fine analysis of the spectrum of operator eigenvalue problems. The main achievements obtained within the frames of the spectral theory of open structures can be divided into five main groups.

2. Spectral theory: general

Boundary eigenvalue (spectral) problems of mathematical physics and, in particular, those arising

in electromagnetics can be reduced [1, 2, 10] to operator eigenvalue problems with nonlinear dependence on the spectral parameter $K(z,\vec{a})\varphi = 0$, (sometimes referred to as nonstandard eigenvalue problems [11]) called generalized dispersion equation (GDE), in which the operator $K(z,\vec{a}) : X \to Y$ nonlinear with respect to a spectral parameter z is an OVF acting on the pair of Banach spaces X, Y and $\vec{a}$ is a vector of nonspectral parameters describing the geometry of the domain, coefficients of the differential operator, etc. The methods based on the analysis of OVFs and associated GDEs was first applied to the solution of relevant electromagnetic problems in [12].

The reduction to an operator GDE has become a major tool of applications of the spectral theory of nonselfadjoint operators. In the majority of problems, it is necessary to determine families of functions $z = z(\vec{a})$ determined implicitly by GDE rather than separate eigenvalues. If K is a Fredholm operator, then its characteristic numbers (CNs) form a countable set σ_K of (complex) points. On the other hand, since the resolvent set ρ_K of OVF K is the complement to σ_K, the knowledge of σ_K enables one to prove the unique solvability of the corresponding inhomogeneous Fredholm operator equation $K(z,\vec{a})\varphi = f$ associated with various excitation problems [1, 2]. For a Fredholm operator, the spectral data $z(\vec{a}) = \{z_\nu(\vec{a})\}_{\nu=1,2,\ldots}$ can be obtained in the form of numbered families. Often, one parameter is varied (a_0) which may be chosen simultaneously as a small parameter (e.g., the diameter of an irregular perturbation of the boundary—a slot) and spectral data can be obtained [1, 2, 13] as asymptotic series with respect to a_0. Special methods have been proposed [1, 2] that enable one to prove the existence and verify basic properties of the spectrum in terms of the GDE. In the electromagnetic field theory, knowledge of the spectrum makes it possible to determine scattering frequencies and describe various resonance phenomena.

In many cases, K is a finite-meromorphic OVF of a definite structure characteristic to some problems; namely, $K = K(z) = P_n(z) + U_n(z) = T(z) + A_n(z)(z-\zeta_n)^{-1} + U_n(z)$, where $A_n(z)$ is finite-dimensional, $T(z)$ is an invertible, and $U_n(z)$ is completely continuous. In this case, CNs are located in the vicinities of poles ζ_n [1, 2]. Another typical example is K in the form of a scalar or matrix integral OVF $K(z,a_0)\varphi \equiv \int\limits_S K(t_0,t;z)\varphi(t)dt$ considered in [1, 2, 13], where there is only one nonspectral parameter, $a_0 = \operatorname{diam} S$. One more well-studied and typical situation is when K is defined by an infinite matrix $\|k_{mn}(z,\vec{a})\|_{m,n=1}^{\infty}$ and considered in the Hilbert space (l_p) of infinite complex sequences.

Development of the IE method [2, 13–16], theory of singular integral operators [16] and the spectral theory of integral OFVs with nonlinear dependence on the spectral parameter are aimed at the analysis of nonselfadjoint BVPs for the Helmholtz and Maxwell equations. An objective is often to solve nonselfadjoint eigenvalue problems in unbounded domains. A typical example of such BVPs arises [2] in the models of wave propagation in open metal–dielectric waveguides: $(-\Delta+\bar{\epsilon}(\mathbf{x}))\mathbf{u} = \lambda\mathbf{u}$, $\mathbf{x} \in \mathrm{R}^2\backslash(\Gamma_e \cup \Gamma_m)$, $\mathcal{L}(\lambda)\mathbf{u}|_{\Gamma_e} = 0$, $\mathcal{M}\mathbf{u}|_{\Gamma_m} = 0$, $\mathcal{E}(\lambda)\mathbf{u} = 0$, where the operators $\mathcal{L}(\lambda)$, $\mathcal{M}$, and $\mathcal{E}(\lambda)$ specifying, respectively, the transmission conditions on the break lines of $\bar{\epsilon}(\mathbf{x})$ (interface), surfaces of perfect conductors, and at infinity are functions of spectral parameter λ. It is shown that analysis of the existence and distribution of eigenvalues (scattering frequencies) in the complex plane can be performed on the basis of the OVF spectral theory using explicit semi-inversion of integral operator pencils defined on several intervals of integration [13]. Using a generalisation of this technique similar problems were solved [14] for two-dimensional dielectric scattereres.

Among a great number of results and applications summarized in [2] note the proof of (1) discreteness of the spectra of eigenwaves of strip and slot transmission lines including comprehensive analysis of waves in slotted circular waveguides [15]; (2) double completeness of eigenwaves propagating in arbitrary metal–dielectric waveguides obtained in terms of the analysis of eigenvectors and associated vectors of corresponding operator pencils (see [2], Ch. 3) which generalizes fundamental results concerning the wave propagation in empty waveguides; and (3) description of various resonance phenomena in irregular waveguides [2].

3. Pseudodifferential operators and vector screen problems

This research direction focuses on application of the methods of the spectral theory of OVFs and the theory of pseudodifferential operators (PDOs) [17–19] for the analysis and development of the solution methods for three-dimensional BVPs for the Maxwell equations. Three-dimensional vector problems of the mathematical theory of diffraction in unbounded spatial domains are considered which cannot be reduced to a scalar setting; namely, the wave diffraction (a) by bounded and perfectly conducting screens of arbitrary shape in free space [16, 17], (b) inclusions in a wedge [18], and (c) in infinite and semi-infinite waveguides (cylinders) and layers coupled by apertures [17, 19]. The problems are reduced to an integrodifferential equation over a screen Ω of the type $L\mathbf{u} = \nabla A(\nabla \cdot \mathbf{u}) + k^2 A\mathbf{u} = \mathbf{f}$, $A\mathbf{u} = \int_\Omega \exp(ik|\mathbf{x}-\mathbf{y}|)/|\mathbf{x}-\mathbf{y}|\mathbf{u}(\mathbf{y})d\mathbf{y}$. It is shown that, generally, L is a PDO with the degenerate principal matrix symbol which does allow one to apply the theory of elliptic PDOs and forces thus the PDO splitting on appropriate subspaces and replacing $L\mathbf{y} = \mathbf{f}$ by a system of pseudodifferential equations. The Fredholm property, unique solvability, smoothness, edge singularities, and the limiting absorption are established based on the analysis of associated OVFs performed in terms of vector PDOs [17, 19].

4. Perturbation theory and interaction phenomena

Analysis of the dependence of eigenvalues of operators on parameters is a specific part of the perturbation theory [20]. This dependence can be described [21] by functions and OVFs of several complex variables that have critical points (CPs) of various nature. Degeneration of eigenvalues as well as e.g. resonance scattering are shown [2, 11] to be connected with such points. Another important physical phenomena which can be explained using the analysis of CPs is interaction of oscillations and waves. Intertype interaction of oscillations in resonators occurs when small variation of a geometric parameter leads to sharp changes in the dependence of eigenfrequencies on parameters, sharp increase or decrease of diffraction losses, development of hybrid field configurations, etc. Rigorous analysis of interaction is reduced [2] to the study of the spectrum of canonical Fredholm OVFs of the second kind $I - A(z,\omega)$, where I is the identity operator and $A(z,\omega)$ is a compact OVF of the spectral (frequency) parameter ω and a nonspectral parameter z. The associated GDE often can be reduced to the form $F(z,\omega) = det[I - A(z,\omega)] = 0$, that is, to the determination of zeros of a function $F(z,\omega)$ (denoting an infinite determinant) of several complex variables. Define the analytical surface (the spectral set of F) $\sigma_0 = \{(z,\omega) : F(z,\omega) = 0\}$. To study interaction analytically means to analyze variation of the set $\sigma_0 = \sigma_0(z)$ of eigenfrequencies with respect to parameter z. It can be shown that if (z_0,ω_0) is an isolated Morse CP of $F(z,\omega)$ situated close to σ_0, then the local structure of σ_0 which may correspond to various physical effects including the interaction is specified by its position and type.

The determination and analysis of CPs for different OVFs arising in typical electromagnetic problems and the associated interaction phenomena are reviewed in [2, 11].

5. Wave propagation and diffraction in nonlinear media

Application of the GDE-based solution techniques enabled [22] a complete description of waves propagating in Kerr-type nonlinear three-layer medium. Later it was shown that mathematical modeling of the wave propagation and diffraction in nonlinear media generally gives rise to different statements of singular linear and semilinear BVPs for Helmholtz and Schrödinger equations with complex-valued coefficients nonlinear both with respect to the solution and the spectral parameter [23, 24]. The methods elaborated initially for the analysis of wave propagation in layered media were extended [25] to the case of dielectric waveguides (fibers); singular BVPs are reduced to nonlinear Volterra and Fredholm IEs and their unique solvability is proved and CNs are determined using

contraction [23–25].

The eigenvalue problems are formulated in unbounded domains, in particular, on the infinite and semi-infinite intervals, and with transmission-type conditions and conditions at infinity that contain the spectral parameter [24, 25]; for example, when the coefficient in the equation multiplying the nonlinear term differs from zero inside a finite interval $(0, a)$ and the conditions are stated at the point a (continuity), at the origin (e.g. boundedness), and at infinity (rate of decay). An example considered in [25] is $L(\lambda)u + B(u;\lambda) = 0$, where L is a linear differential operator and $B(u;\lambda)$ is a nonlinear operator, e.g. $B(u) = u^3$ when the wave propagation in a Kerr-type nonlinear medium is considered. The method of solution employs reduction to nonlinear IEs constructed using Green's function of the linear differential operator L; the eigenvalue problems are then replaced by the determination of characteristic numbers of integral OVFs that are nonlinear both with respect to the solution and the spectral parameter. The latter problems are reduced to the functional dispersion equations, and their roots give the sought-for eigenvalues. The existence and distribution of roots on the complex plane are verified. Eigenvalues and soliton-type solutions are obtained also as functions of the problem parameters and the techniques are developed to wider classes of nonlinearities B and operators L.

6. Inverse problems

Methods of solution to inverse problems are elaborated, in particular, for a class of domains with noncompact boundaries, that arise in mathematical models of the wave scattering by planar screens with arbitrary finite inhomogeneities [26]. The uniqueness of reconstructing the permittivity and the shape of the scatterer from the scattering data are proved.

Direct and inverse diffraction problems for cylindrical scatterers are considered whose (two-dimensional) cross sections are formed by domains with infinite noncompact boundaries under the restriction that the geometry of the parts of boundary contours that stretch to infinity is fixed (they are rectilinear). The problems in question arise in mathematical models of the wave scattering by planar screens with arbitrary finite inhomogeneities. Analysis of boundary value problems is reduced to the study of the corresponding OVFs of the complex frequency spectral parameter. The uniqueness of the direct scattering problems is proved by applying analytical properties (in particular, a generalization of the uniqueness theorem for analytical functions) of these operator-valued functions which are the same both for the direct and inverse problems. The inverse problems are formulated and uniqueness of reconstructing the permittivity and the shape of the scatterer from the scattering data is proved.

The knowledge of CPs often enables one to solve inverse problems [27] because it gives a specific alternative description of the object (a characterization of the domain where the eigenvalue problem is considered and the equation parameters). A particular family of cavity-backed slotted structures is considered in [27, 28] for which the proposed method of solution to the inverse problem of reconstructing the shape of the rectangular cavity based on the use of spectral data is applied.

References

1. A. Il'inski, Y. Shestopalov, *Applications of the Methods of Spectral Theory in the Problems of Wave Propagation*, Moscow Univ. Press, Moscow (1989).
2. V. Shestopalov, Y. Shestopalov, *Spectral Theory and Excitation of Open Structures,* Peter Peregrinus Ltd., London (1996).
3. D. Hilbert, *Grundzüge einer allgemeinen Theorie der linearen Integralgleichungen,* Leipzig (1924).
4. G. Giraud, Equations a integrales principales, *Ann. Sci. Ec. Norm. Sup.,* **51**, 251–272 (1934).
5. M. Keldysh, On the Characteristic Values and Characteristic Functions of Certain Classes of

Nonelfadjoint Equations, *Doklady Akad. Nauk SSSR Maths.,* **77**, 11–14 (1951).
6. I. Gohberg, On Linear Operators Depending Analytically on a Parameter, *Doklady Akad. Nauk SSSR Maths.,* **78**, 629–632 (1951).
7. I. Gohberg, M. Krein, Fundamental Aspects of Defect Numbers, Root Numbers and Indexes of Linear Operators, *Uspehi Mat. Nauk,* **12**, 43–118 (1957).
8. I. Gohberg, E. Sigal, Operator Generalization of the Logarithmic Residue Theorem and Rouchet's Theorem, *Mat. Sbornik,* **84**, 607–629 (1971).
9. G. Vainikko, O. Karma, Rate of Convergence of Approximation Methods for an Eigenvalue Problem in which the Parameter Occurs Nonlinearly, *Zh.Vych.Mat.Mat.Fiz.,* **14**, 1393–1408 (1974).
10. E. Sanchez-Palencia, *Nonhomogeneous Media and Vibration Theory*, Springer, New York, Berlin, Heidelberg (1980).
11. G. Hanson and A. Yakovlev, *Operator Theory for Electromagnetics. An Introduction*, Springer, New York, Berlin, Heidelberg (2001).
12. Y. Shestopalov, Properties of the Spectrum of a Class of Nonselfadjoint Boundary Value Problems for the Systems of Helmholtz Equations, *Dokl. Akad. Nauk SSSR,* **252**, 1108–1111 (1980).
13. Y. Shestopalov, Y. Okuno, N. Kotik, Oscillations in Slotted Resonators with Several Slots: Application of Approximate Semi-Inversion, *Progress Electromagnetics Research,* **39**, 193–247 (2003).
14. Y. Shestopalov, Resonance Scattering by a Dielectric Cylinder, *J. Comm. Tech. Elec.,* **50**, 172–179 (2005).
15. E. Chernokozhin, Normal Waves of Cylindrical Slot Lines, *Electromagnetic Waves Electron Syst.,* **6**, 3-81 (2001).
16. Y. Shestopalov, Y. Smirnov, E. Chernokozhin, *Logarithmic Integral Equations in Electromagnetics*, VSP Int. Science Publishers, Utrecht, Boston, Köln, Tokyo (2000).
17. A. Il'inski, Y. Smirnov, *Electromagnetic Wave Diffraction by Conducting Screens*, Y. Shestopalov, Ed., VSP Int. Science Publishers, Utrecht, Boston, Köln, Tokyo (1998).
18. Y. Podlipenko, Y. Shestopalov, On the Electromagnetic Scattering Problem for an Infinite Dielectric Cylinder of an Arbitrary Cross Section Located in the Wedge, *J. Math. Phys.*, **40**, 4888–4902 (1999).
19. Y. Shestopalov, Y. Smirnov, The Diffraction in a Class of Unbounded Domains Connected through a Hole, *Math. Methods in the Applied Sciences*, **26,** pp. 1363-1389 (2003).
20. T. Kato, *Perturbation Theory for Linear Operators,* Springer, New York, Berlin, Heidelberg (1966).
21. V. Arnold, S. Gusein-Zade, A. Varchenko, *Singularities of Differentiable Maps,* Birkhäuser, Boston (1988).
22. H.W. Schürmann, V. Serov, Y. Shestopalov, TE-polarized Waves Guided by a Lossless Nonlinear Three-layer Structure, *Phys. Rev. E,* **58**, 1040–1050 (1998).
23. H.W. Schürmann, V. Serov, Y. Shestopalov, Reflection and Transmission of a TE-plane Wave at a Lossless Nonlinear Dielectric Film, *Physica D*, **158**, 197-215 (2001).
24. H.W. Schürmann, V. Serov, Y. Shestopalov, Solutions to the Helmholtz Equation for TE-guided Waves in a Three-layer Structure with Kerr-type Nonlinearity, *J. Phys. A: Math. Gen.*, **35**, 10789-10801 (2002).
25. Y. Smirnov, H.W. Schürmann, Y. Shestopalov, Propagation of TE-Waves in Cylinrical Nonlinear Dielectric Waveguides, *Phys. Rev. E,* **71**, 0166141–10 (2005).
26. Y. Shestopalov, V. Lozhechko, Direct and Inverse Problems of the Wave Diffraction by Screens with Arbitrary Finite Inhomogeneities, *J. Inverse Ill-Posed Problems*, **11**, 643-653 (2003).
27. Y. Shestopalov, O. Kotik, Interaction of Oscillations in Slotted Resonators and its Applications to Microwave Imaging, *J. Electromagn. Waves Appl.*, **17**, 291-311 (2003).
28. Y. Shestopalov, E. Chernokozhin, Resonant and Nonresonant Diffraction by Open Image-type Slotted Structures, *IEEE Trans. Antennas Propag.*, **49**, 793–801 (2001).

An Analysis of Characteristic Impedance of LPDA Feeder

ZHANG Feng DU Xiao-yan ZHOU Dong-fang NIU Zhong-xia

Information Engineering University Zhengzhou 450002

Abstract — The formula of log-periodic dipole antenna(LPDA) input impedance given by Robert Carrel[1] is discussed and corrected in the paper. The new formula explains LPDA's feeder should be unparallel .The influence of angle variety on unparallel feeder lines is studied. According to the computed and measured results, it proves that the resistance of LPDA using unparallel transmission lines as the feeder performs better than that using parallel lines.

Index Terms — impedance, LPDA,VSWR,,dipole,moment

I. INTRODUCTION

The log-periodic dipole antenna is one of the most useful of the frequency independent antennas.The characteristic impedance of transmission feeder makes great affection on LPDA performance[2].In practice, the performance such as the voltage standing wave ratio(VSWR) can't satisfy the request specially in low frequency when using the formula given by Carrel which required the feeder lines parallel to design LPDA. The way to improve performance for VSWR includes setting a short circuit or a matching load on the back of the feeder lines. They make structure complex. We find that the VSWR using unparallel feeder lines performances better than that using parallel lines. However, the formula given by Carrel requires feeder parallel so that the antenna's impedance can be matched to the feed-in resistance. In this paper, the formula is discussed and corrected. It explains LPDA's feeder should be unparallel. The computed and measured results are shown to be in good agreement with the conclusion from the new formula.

II.LPDA MAIN DEFINITIONS

The LPDA is a coplanar linear array of unequal and unequally spaced parallel linear dipoles fed by the transmission lines, as shown schematically in Fig.1.

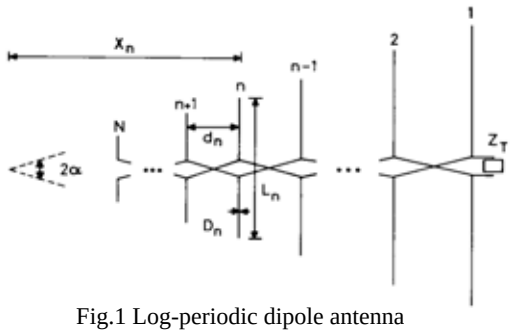

Fig.1 Log-periodic dipole antenna

The usual definitions are used. The scale factor τ is given by

$$\tau = \frac{L_{n+1}}{L_n} = \frac{d_{n+1}}{d_n} = \frac{D_{n+1}}{D_n} = \frac{X_{n+1}}{X_n} \tag{1}$$

the space factor σ is given by

$$\sigma = \frac{d_n}{2L_n} = \frac{1-\tau}{4}\cot\alpha \tag{2}$$

and dn is given by

$$d_n = R_n - R_{n+1} = 2\sigma L_n \tag{3}$$

III.FORMULA'S CORRECTIONS

The input impedance formula given by Carrel is:

$$R_0 = Z_0 / \sqrt{1+\frac{Z_0}{4\sigma' Z_a}} \tag{4}$$

where

$$\sigma' = \frac{\sigma}{\sqrt{\tau}} \tag{5}$$

is a mean spacing factor and

$$Z_a = 120(\ln\frac{h}{a} - 2.25) \tag{6}$$

is an average characteristic impedance of a short dipole as a function of h/a , h is the half length of the element ,and Z_0 is the characteristic impedance of the feeder.

We consider that R_0 is actually the characteristic impedance of a transmission line made up of the feeder and the small elements.If considering the capactive loading of the small elements,we note that the capacity is proportional to the length of the elements and the spacing d_n of the element n is proportional to the length of element n.As an approximation,the capacity per unit length is constant.Thus we add to the nominal capacity per unit length of unloaded feeder a term which represents the capacitive loading of the small elements.

Consider the approximate formula for the input impedance of a dipole antenna,

$$Z = -jZ_a Cot\beta h \tag{7}$$

where h is the half length of the element, β is the free space propagation constant.

Carrel considered $h/\lambda \ll 1$,hence

$$Z = -jZ_a Cot\beta h \approx -jZ_a \bullet \beta h = \frac{Z_a V}{jw} \bullet \frac{1}{h} \tag{8}$$

where V is the velocity of light in vacuo. In fact,these elements far from the resonance elements can be considered $h/\lambda \ll 1$,but some near and within the resonance elements don't accord with the condition $h/\lambda \ll 1$.So we expand $Cot\beta h$ to:

$$Cot\beta h = \frac{1}{\beta h} - \frac{1}{3}\beta h - \frac{1}{45}(\beta h)^3 \cdots \tag{9}$$

Replacing the cotangent function by its small argument approximation,we choose : $Cot\beta h = \frac{1}{\beta h} - \frac{1}{3}\beta h$, hence

$$Z = \frac{Z_a V}{jw}(\frac{1}{h} - \frac{1}{3}\beta^2 h) \tag{10}$$

the capacity of the n-th dipole is given by

$$Cn = \frac{1}{Z_a V(\frac{1}{h_n} - \frac{1}{3}\beta^2 h_n)} \tag{11}$$

If we use the mean spacing at dipole n,

$$\overline{d}_n = \sqrt{d_n d_{n-1}} = \frac{d_n}{\sqrt{\tau}} \tag{12}$$

the average capacity per unit length is given by

$$\Delta C_n = \frac{Cn}{\overline{d}_n} \tag{13}$$

and d_n/h_n is related to the spacing factor σ by

$$\sigma = \frac{1}{4}\frac{d_n}{h_n} \tag{14}$$

hence

$$\Delta C_n = \frac{1}{4Z_a V\sigma'(1-\frac{1}{3}\beta^2 h_n^2)} \tag{15}$$

Since

$$V = \frac{1}{Z_0 C_0} \tag{16}$$

the n-th element's practical characteristic impedance is:

$$R_n = \sqrt{\frac{L_0}{C_0 + \Delta C_n}} = Z_0 \frac{1}{\sqrt{1+m}} \tag{17}$$

where

$$m = \frac{\Delta C_n}{C_0} = \frac{1}{4C_0 Z_a V \sigma'(1 - \frac{1}{3}\beta^2 h_n^2)} = \frac{Z_0}{4\sigma' Z_a (1 - p)} \tag{18}$$

Compared (17) with (4),there is a parameter p which is related to the position of elements and frequence,

$$p = \frac{1}{3}\beta^2 h_n^2 \tag{19}$$

Inverting the formula to find the feeder impedance Z_0 in terms of R_n,we find

$$Z_0 = R_n \left\{ \frac{1}{8\sigma' \frac{Z_a}{R_n}(1 - p)} + \sqrt{\left[\frac{1}{8\sigma' \frac{Z_a}{R_n}(1 - p)} \right]^2 + 1} \right\} \tag{20}$$

According to the formula(20),we find that in order to make R_n constant, feeder impedance Z_0 should be unequal.The nearer to the feed-in point,the lower is the characteristic impedance.

The transmission line's characteristic impedance is given by

$$Z_0 = 120 \ln \left[\frac{D}{d} + \sqrt{(\frac{D}{d})^2 - 1} \right] \tag{21}$$

where d is the diameter and D is the distance between feeder lines.If parameter d is invariable,D should minish towards to the feed-in point in order to make R_n equal.Hence,the feeder should be unparallel.

IV. Results And Conclusions

A computer program has been written to analyze the theory given here.A moment method[3] was used to obtain the antenna impedance matrix.The piecewise sinusoidal basis functions,Galerkin method,and the gap source model[4] were used.,Change of Z_0 with the angle variety between feeder lines was considered in the program.The results correspond to a LPDA with τ =0.92, σ =0.165,N=18, h/a =250,fmin=450MHz and fmax=500MHz.Because radiation pattern's variety with angle is small, we only give the input impedance patterns shown in Fig. 2. The measured results of VSWR is shown in Fig. 3.

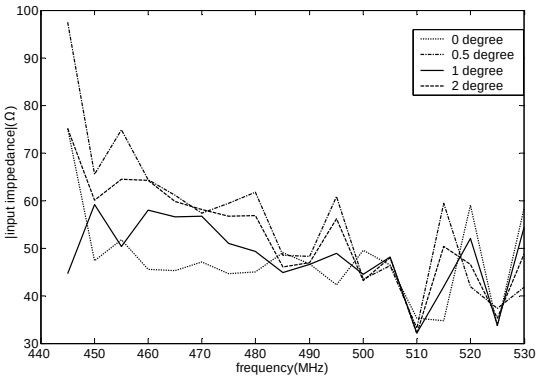

Fig.2 impedance variety pattern(computed)

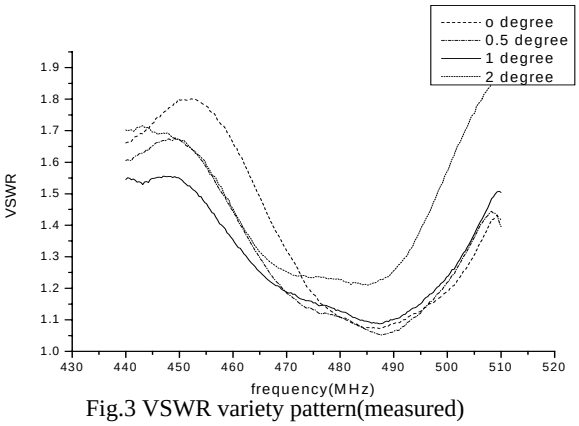

Fig.3 VSWR variety pattern(measured)

Fig.2 and Fig.3 show that the input impedance of LPDA using unparallel transmission lines as the feeder performs better than that using parallel lines.The angle variety affection in low frequency is obvious than that in high frequency.We also find that there is a optimal angle between feeder lines.We can change the angle to modulate the impedance of LPDA.

In the paper, the formula for impedance of LPDA is discussed and corrected. It explains LPDA's feeder should be unparallel. The computed and measured results are shown to be in good agreement with the conclusion from the new formula.

References

[1] Robert Carrel, "The Design of Log-Periodic Dipole Antennas" ,IRE International Covention Record.pp. 61-75, 1961.
[2] Crarles J.Drane, "An Analysis and Design optimization of the log-periodic Dipole Antenna" ,AD A028061
[3] Harrington, "Fiele computation by moment methods" ,The Macmillan Co.,1968
[4] Stutzman,w.L.,and Thiele,G.A, "Antenna theory and design" ,John Wiley&Sons.,1981

Resonant Scattering by Layered Dielectric Structure with Weakly Kerr-Like Nonlinearity

V. V. Yatsyk
IRE Nat. Acad. of Sci. of Ukraine.

Abstract – Numerical analysis of the diffraction by a transversely non-homogeneous, isotropic, nonmagnetic, linearly polarized, weakly nonlinear layer and layered dielectric structures (with Kerr-like nonlinearity) is performed in the resonant frequency range when the parameter of cubic susceptibility takes positive and negative values. It is shown that as the excitation field intensity increases the diffraction characteristics acquire essentially different properties for positive and negative values of susceptibility. For a layered structure consisting of layers with positive and negative susceptibility of the enveloping medium the effects inherent to environments with positive and negative value of susceptibility are observed in certain areas of variation of the excitation field intensity.

1. The Nonlinear Problem

Let the time dependence be $\exp(-i\omega t)$, $\vec{E}(\vec{r})$ and $\vec{H}(\vec{r})$ complex amplitudes of an electromagnetic field. We consider a nonmagnetic, isotropic, transverse non-homogeneous, non-conducting, linearly polarized $\vec{E} = (E_x, 0, 0)$ and $\vec{H} = (0, H_y, H_z)$, with vector of polarization $\vec{P}^{(NL)} = \left(P_x^{(NL)}, 0, 0\right)$, and Kerr-like weakly nonlinearity $\varepsilon^{(NL)} << \varepsilon^{(L)}$ layered dielectric structure, see Fig. 1 and [1], [2]. Where $P_x^{(NL)} = \frac{3}{4}\chi^{(3)}_{xxxx}|E_x|^2 E_x$ component of a vector polarization, $\varepsilon = \varepsilon^{(L)} + \varepsilon^{(NL)}$ at $|z| \le 2\pi\delta$ is dielectric permeability of nonlinear structure, $\varepsilon^{(L)} = 1 + 4\pi\chi^{(1)}_{xx}(z)$, $\varepsilon^{(NL)} = 3\pi\chi^{(3)}_{xxxx}(z)|E_x|^2 = \alpha(z)|E_x|^2$, $\alpha(z) = 3\pi\chi^{(3)}_{xxxx}(z)$, $\chi^{(1)}_{xx}(z)$ and $\chi^{(3)}_{xxxx}(z)$ is the components of susceptibility tensor.

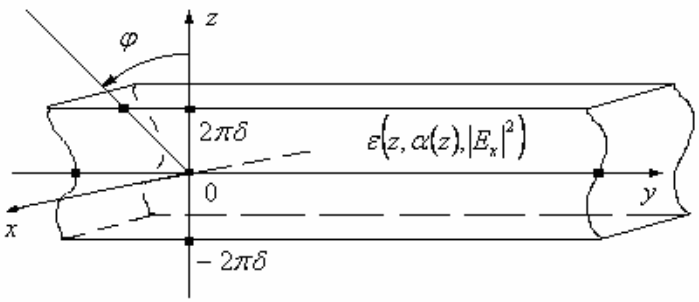

Figure 1: Weakly nonlinear dielectric layered structure.

The complete diffraction field $E_x(y,z) = E_x^{inc}(y,z) + E_x^{scat}(y,z)$ of a plane wave $E_x^{inc}(y,z) = a^{inc}\, exp[i(\phi y - \Gamma\cdot(z - 2\pi\delta))]$, $z > 2\pi\delta$ on the nonlinear dielectric layer (Fig. 1) satisfies such conditions of the problem:

$$\Delta\cdot\vec{E} + \frac{\omega^2}{c^2}\cdot\varepsilon^{(L)}(z)\cdot\vec{E} + \frac{4\pi\omega^2}{c^2}\cdot\vec{P}^{(NL)} \equiv \left(\Delta + \kappa^2\cdot\varepsilon\left(z,\alpha(z),|E_x|^2\right)\right)\cdot E_x(y,z) = 0, \qquad (1)$$

the generalized boundary conditions:

E_{tg} and H_{tg} are continuous at discontinuities $\varepsilon\left(z,\alpha(z)\cdot|E_x|^2\right)$;

$E_x(y,z)=U(z)\cdot exp(i\phi y)$, the condition of spatial quasihomogeneity along y; (2)

the condition of the radiation for scattered field:

$$E_x^{scat}(y,z)=\left\{\begin{matrix}a^{scat}\\ b^{scat}\end{matrix}\right\}\cdot e^{i(\phi y\pm\Gamma\cdot(z\mp 2\pi\delta))},\ z\begin{matrix}>\\<\end{matrix}\pm 2\pi\delta \tag{3}$$

Here: $\varepsilon\left(z,\alpha(z),|E_x|^2\right)=\begin{cases}1, & |z|>2\pi\delta\\ \varepsilon^{(L)}(z)+\alpha(z)\cdot|E_x|^2, & |z|\le 2\pi\delta\end{cases}$; $\Delta=\frac{\partial^2}{\partial y^2}+\frac{\partial^2}{\partial z^2}$; $\alpha(z)=3\pi\chi^{(3)}_{xxxx}(z)$;

$\Gamma=\left(\kappa^2-\phi^2\right)^{1/2}$; $\phi\equiv\kappa\cdot sin(\varphi)$; $|\varphi|<\pi/2$ (see Fig. 1); $\kappa=\omega/c\equiv 2\pi/\lambda$; $c=\left(\varepsilon_0\mu_0\right)^{-1/2}$, ε_0, μ_0 and λ length of the wave is the parameters of environment.

In this case the required of the solution of problem (1)-(3) are of kind:

$$E_x(y,z)=U(z)\cdot e^{i\phi y}=\begin{cases}a^{inc}\cdot e^{i(\phi y-\Gamma\cdot(z-2\pi\delta))} + a^{scat}\cdot e^{i(\phi y+\Gamma\cdot(z-2\pi\delta))}, & z>2\pi\delta,\\ U(z)\cdot e^{i\phi y}, & |z|\le 2\pi\delta,\\ b^{scat}\cdot e^{i(\phi y-\Gamma\cdot(z+2\pi\delta))}, & z<-2\pi\delta.\end{cases} \tag{4}$$

The nonlinear problem (1)-(3) is reduced to finding the solutions $U(z)\in L_2\left([-2\pi\delta,2\pi\delta]\right)$ (see (4)) of the non-homogeneous nonlinear integrated equation of the second kind [3]:

$$U(z)+\frac{i\kappa^2}{2\Gamma}\int_{-2\pi\delta}^{2\pi\delta}\exp\left(i\Gamma\cdot|z-z_0|\right)\left[1-\left(\varepsilon^{(L)}(z_0)+\alpha(z_0)|U(z_0)|^2\right)\right]U(z_0)dz_0=U^{inc}(z),\qquad |z|\le 2\pi\delta, \tag{5}$$

where $U^{inc}(z)=a^{inc}\,exp\left[-i\Gamma\cdot(z-2\pi\delta)\right]$ and $U(-2\pi\delta)=b^{scat}$, $U(2\pi\delta)=a^{inc}+a^{scat}$.

2. The Solution of the nonlinear integrated equation

The integrated equation (5) with application of the quadrature method is reduced to system of the nonlinear equations of the second kind [4].

$$\left(E-B\left(|U|^2\right)\right)\cdot U=U^{inc} \tag{6}$$

Here: $z_1=-2\pi\delta<z_2<...<z_n<...<z_N=2\pi\delta$; $U=\left\{U(z_n)\right\}_{n=1}^N$, $B\left(|U|^2\right)=\left\{A_m\cdot K_{nm}\left(|U|^2\right)\right\}_{n,m=1}^N$;

$K_{nm}\left(|U|^2\right)=\left(i\kappa^2/(2\Gamma)\right)\exp\left(i\cdot\Gamma|z_n-z_m|\right)\left[1-\left(\varepsilon^{(L)}(z_m)+\alpha(z_m)|U_m|^2\right)\right]$; $U^{inc}=\left\{a^{inc}\cdot e^{-i\cdot\Gamma\cdot(z_n-2\pi\delta)}\right\}_{n=1}^N$;

$E=\left\{\delta_n^m\right\}_{n,m=1}^N$; A_m are the numerical coefficients dictated by chosen quadrature form; δ_m^n is the Kronecker delta.

Solutions of the system (6) are carried out by the method of iterations:

$$\left\{\left(E-B\left(\left|\overset{(s-1)}{U}\right|^2\right)\right)\cdot\overset{(s)}{U}=U^{inc}\right\}_{s=1}^{S:\ \left\|\overset{(s)}{U}-\overset{(s-1)}{U}\right\|/\left\|\overset{(s)}{U}\right\|<\xi}. \tag{7}$$

3. Susceptibility and Effects Resonant Scattering of the Intensive Fields

Considering results of calculations, we shall use following designations for the factors describing a share of the reflected $R=\left|a^{scat}\right|^2/\left|a^{inc}\right|^2$ and last $T=\left|b^{scat}\right|^2/\left|a^{inc}\right|^2$ wave, that is factors of reflection and passage on intensity of a field of excitation, accordingly. And, at absence of losses in the environment, coefficients of reflection and transient on intensity of a field of excitation are connected by the equality $R+T=1$ representing the law of conservation of energy.

3.1 Intensity and Resonant Frequency

The effect of non-uniform shift of resonant frequency of the diffraction characteristics of nonlinear dielectric layer is found out at increase of intensity of inciting field [4] (see Fig. 2, at positive value of the susceptibility $\alpha = 0{,}01$, and also Fig. 3, at negative value of the susceptibility $\alpha = -0{,}01$).

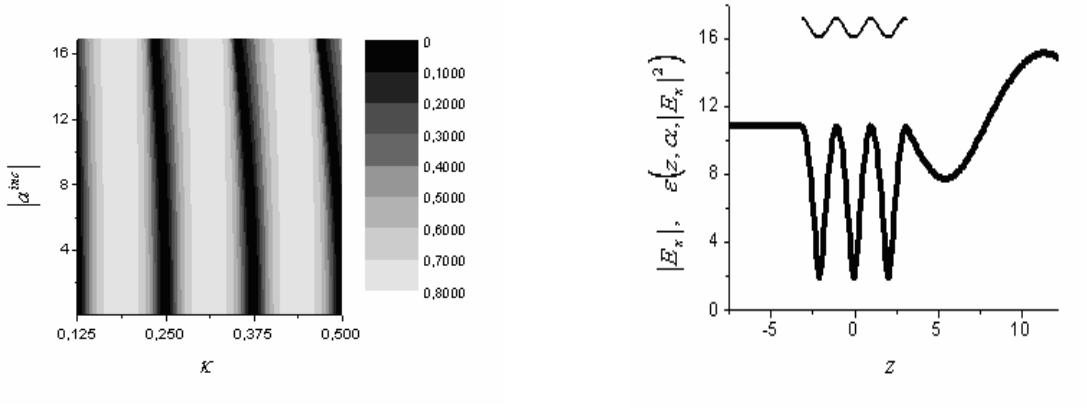

(a) (b)

Figure 2: Parameters of structure: $\delta = 0.5$; $\varphi = 45^0$; $\kappa = 0.375$; $\varepsilon^{(L)} = 16$, $\alpha = 0.01$; (a) The diagram of the reflection $R\left(\kappa, \left|a^{inc}\right|\right)$; (b) ——— $|E_x|$ and ——— $\varepsilon\left(z,\alpha,|E_x|^2\right)$ at $\left|a^{inc}\right| = 11.4$.

Growth of amplitude of the inciting field $\left|a^{inc}\right|$ results in change of the share of the reflected wave $R\left(\kappa, \left|a^{inc}\right|\right)$: reduction of value of resonant frequency with increase and reduction of a steepness of the diffraction characteristics before and after resonant frequency (Fig. 2, at $\alpha > 0$); increase of value of resonant frequency with reduction and increase of a steepness of the diffraction characteristics before and after resonant frequency (Fig. 3, at $\alpha < 0$).

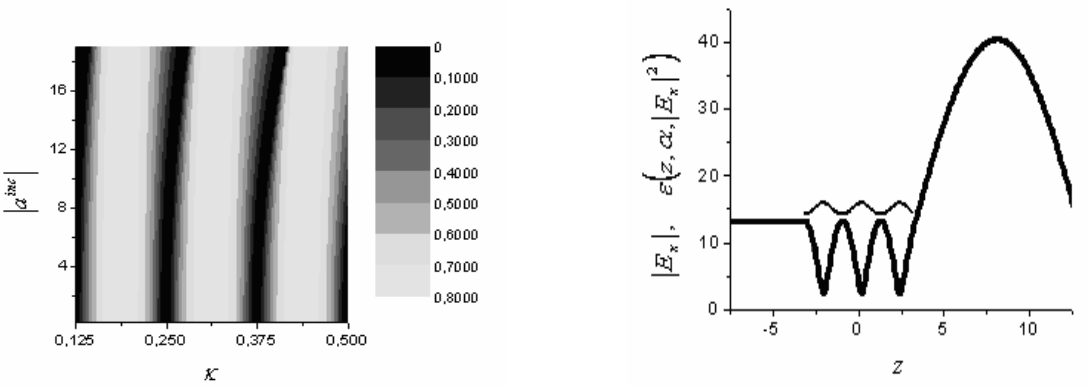

(a) (b)

Figure 3: Parameters of structure: $\delta = 0.5$; $\varphi = 45^0$; $\kappa = 0.375$; $\varepsilon^{(L)} = 16$, $\alpha = -0.01$; (a) The diagram of the reflection $R\left(\kappa, \left|a^{inc}\right|\right)$; (b) ——— $|E_x|$ and——— $\varepsilon\left(z,\alpha,|E_x|^2\right)$ at $\left|a^{inc}\right| = 22.4$.

3.2 Intensity and Angle

The effects: itself the channelling of a field – increase of the angle of the transparency of the nonlinear layer ($\alpha \neq 0$) when growth of intensity of the field (Fig. 4 (a), at positive value of the susceptibility, $\alpha > 0$); dechannelling of a field (Fig. 4 (b), at negative value of the susceptibility, $\alpha < 0$) are found out, [4].

The increase of the angle of a transparency with growth of intensity at positive value of the susceptibility $\alpha = 0{,}01$ is easy for tracking on Fig. 4 (a): $\left|a^{inc}\right| = 8$, $\varphi \approx 46^0$ and $\left|a^{inc}\right| = 11{,}4$, $\varphi \approx 85^0$.

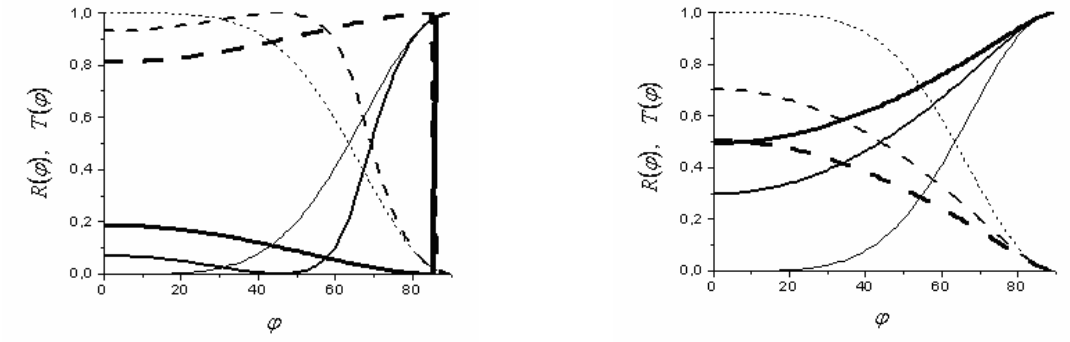

(a) (b)

Figure 4: Parameters: $\delta = 0.5$; $\kappa = 0.375$; $\varepsilon^{(L)} = 16$; (a) for $\alpha = 0.01$: —— $R(\varphi)$, ------ $T(\varphi)$ at $\left|a^{inc}\right| = 0.1$; —— $R(\varphi)$, - - - $T(\varphi)$ at $\left|a^{inc}\right| = 8$; ▬ $R(\varphi)$, ▬ ▬ $T(\varphi)$ at $\left|a^{inc}\right| = 11.4$; (b) for $\alpha = -0.01$: —— $R(\varphi)$, ------ $T(\varphi)$ at $\left|a^{inc}\right| = 0.1$; —— $R(\varphi)$, - - - $T(\varphi)$ at $\left|a^{inc}\right| = 8$; ▬ $R(\varphi)$, ▬ ▬ $T(\varphi)$ at $\left|a^{inc}\right| = 11.4$.

Let's consider diffraction characteristics of weakly nonlinear dielectric layered structure $\varepsilon\left(z, \alpha(z), |E_x|^2\right) = \left\{1, \text{ at } |z| > 2\pi\delta; \text{ and } \varepsilon^{(L)}(z) + \alpha(z) \cdot |E_x|^2, \text{ at } |z| \le 2\pi\delta\right\}$, with parameters

$$\left\{\varepsilon^{(L)}(z), \alpha(z)\right\} = \begin{cases} \left\{\varepsilon^{[1]} = 16,\ \alpha^{[1]} = \alpha_1\right\}, & z \in \left[-2\pi\delta, z_1 = -2\pi\delta \cdot \tau_1\right) \\ \left\{\varepsilon^{[2]} = a \cdot z + b,\ \alpha^{[2]} = \alpha_2\right\}, & z \in \left[z_1 = -2\pi\delta \cdot \tau_1,\ z_2 = 2\pi\delta \cdot \tau_2\right] \\ \left\{\varepsilon^{[3]} = 64,\ \alpha^{[2]} = \alpha_3\right\}, & z \in \left(z_2 = 2\pi\delta \cdot \tau_2,\ 2\pi\delta\right] \end{cases}; \quad \begin{array}{l} a = \dfrac{\varepsilon^{[3]} - \varepsilon^{[1]}}{z_2 - z_1}; \\ b = \varepsilon^{[1]} - a \cdot z_1; \\ \tau_1 = \tau_2 = 0. \end{array}$$

Growth of intensity of the inciting field results in change $R(\varphi)$ and $T(\varphi)$, see Fig. 5.

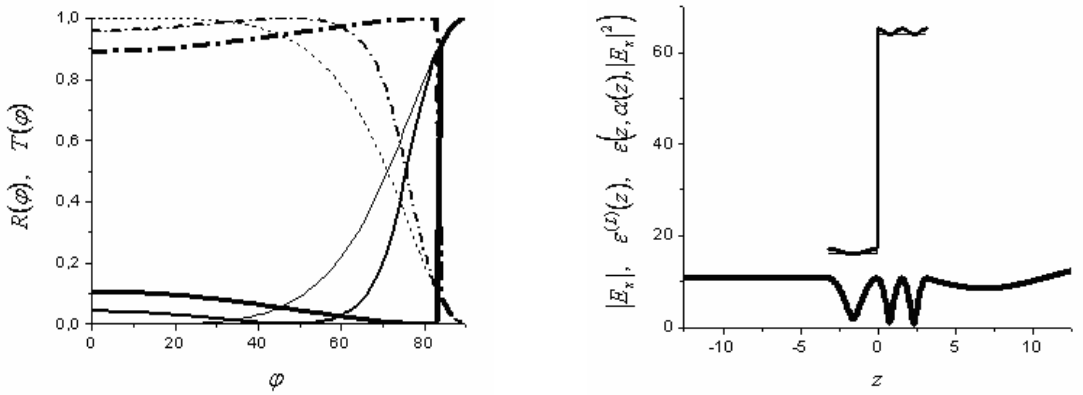

(a) (b)

Figure 5: Parameters of structure: $\delta = 0.5$; $\kappa = 0.25$; $\alpha_1 = \alpha_2 = \alpha_3 = 0.01$ and $\tau_1 = \tau_2 = 0$; (a) —— $R(\varphi)$, ------ $T(\varphi)$ at $\left|a^{inc}\right| = 0.1$; —— $R(\varphi)$, - - - $T(\varphi)$ at $\left|a^{inc}\right| = 8$; ▬ $R(\varphi)$, ▬ ▬ $T(\varphi)$ at $\left|a^{inc}\right| = 11$; (b) —— $\varepsilon^{(L)}(z)$, ▬ $|E_x|$ —— $\varepsilon\left(z, \alpha(z), |E_x|^2\right)$ at $\left|a^{inc}\right| = 11$, $\varphi = 45^0$.

The effect itself the channeling of a field (i.e. existence of angles $\varphi_{|a^{inc}|\geq 0} = \{\varphi \in [0, 90^0): R(\varphi) = 0\} \neq \{0\}$, the increase of angle of the transparency of the nonlinear layer when growth of intensity of the field, at positive values of the susceptibility, see Fig. 5 (a)), and also effect itself the channeling ($\varphi_{0\leq|a^{inc}|\leq 20} \neq \{0\}$) and de-channeling ($\varphi_{|a^{inc}|>20} = \{0\}$) of a field (at positive and negative values of the susceptibility of the dielectric layered structure, see Fig. 6 (a)) are found out. Here the symbol $\{0\}$ is empty set.

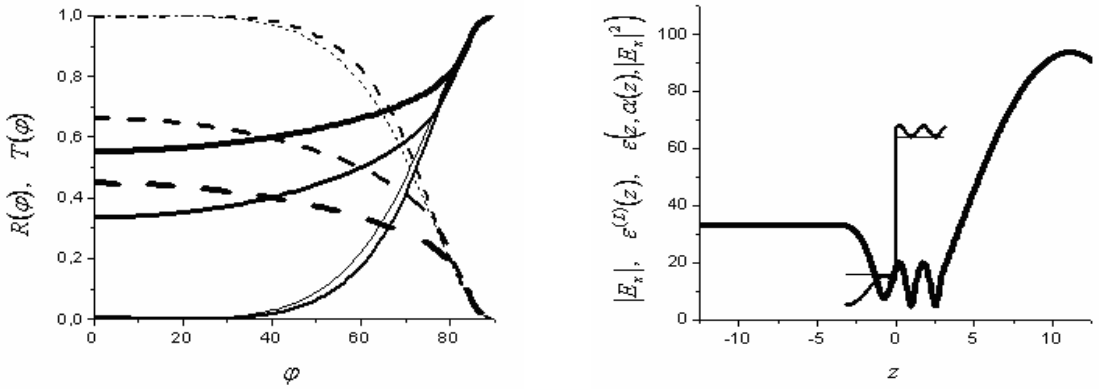

(a) (b)

Figure 6: Parameters of structure: $\delta = 0.5$; $\kappa = 0.25$; $\alpha_1 = -0.01$, $\alpha_2 = \alpha_3 = 0.01$ and $\tau_1 = \tau_2 = 0$;

(a) —— $R(\varphi)$, ----- $T(\varphi)$ at $|a^{inc}| = 0.1$; ——$R(\varphi)$, – – –$T(\varphi)$ at $|a^{inc}| = 20$; ——— $R(\varphi)$, – – $T(\varphi)$ at $|a^{inc}| = 40$; ——— $R(\varphi)$,– – $T(\varphi)$ at $|a^{inc}| = 52.5$.

(b) —— $\varepsilon^{(L)}(z)$, ——— $|E_x|$ —— $\varepsilon\left(z,\alpha(z),|E_x|^2\right)$ at $|a^{inc}| = 11$, $\varphi = 45^0$.

These effects (see Fig. 2 - Fig. 6) are connected to resonant properties of a nonlinear dielectric layer and caused by increase at positive value of the susceptibility or reduction at negative value of the susceptibility of a variation of dielectric permeability of a layer (its nonlinear components) when increase of intensity of a field of excitation of researched nonlinear object, see Fig. 2 (b), 3 (b), 5 (b), 6 (b).

4. Conclusion

The results of the numerical analysis are applied: at investigation of processes of wave self-influence; at the analysis of amplitude-phase dispersion of eigen oscillation-wave fields in the nonlinear objects; development of the approach of the description of evolutionary processes near to critical points of the amplitude-phase dispersion of nonlinear structure; at designing new selecting energy; transmitting, remembering devices; etc.

REFERENCES

1. Akhmediev N. N., Ankiewicz A., "Solitons," Moscow, Fizmatlit, 2003.
2. Schürmann H. W., Serov V. S., Shestopalov Yu. V., "TE-polarized waves guided by a lossless nonlinear three-layer structure", Physical Review E, vol. 58, no. 1, 1998, pp. 1040-1050.
3. Shestopalov V. P., Sirenko Yu. K., "Dynamic Theory of Gratings," Kiev, Naukova Dumka, 1989.
4. Yatsyk V. V., "The Numerical Simulations and Resonant Scattering of Intensive Electromagnetic Fields of Waves by Dielectric Layer with Kerr-Like Nonlinearity", E-print: Computational Physics, http://arxiv.org/pdf/physics/0412109, no. 12, 2004, pp. 1-11.

High-Jc Processing for YBCO Thick Films by TFA-MOD Method

R.Teranishi[a], N.Mori[a], K.Yamada[a], M.Mukaida[a], Y.Shingai[a], J.Matsuda[b], K.Nakaoka[b], T.Izumi[b], Y.Shiohara[b]

a) Kyushu University, 744 Motooka, Nishi-ku, Fukuoka, 819-0395 Japan

b) Superconductivity Research Laboratory-ISTEC, 1-10-13 Shinonome, Koto-ku, Tokyo, 135-0062 Japan

Abstract

The large-area and thick superconducting films with high crystallinity are required for most superconductivity applications. MOD process using trifluoroacetate precursors was applied to form thick YBCO films. The water vapor pressure during crystallization is a factor to control the supersaturation for the YBCO crystallization in this process. Then, the crystallization conditions such as P_{H2O} and heating rate were optimized to thicken the YBCO film maintaining high Jc performance. As a result, Jc depended strongly on both the water vapor pressure and the heating rate during the crystallization. Finally, a YBCO film with a high Ic value of 508A at 77K in self-field was fabricated with the YBCO film thickness of 2.7 μm under the optimized crystallization conditions.

1. Introduction

Development of coated conductors with $REBa_2Cu_3O_{7-\delta}$ (REBCO: RE is a rare earth element) have been proceeded since the REBCO superconductors have a high Jc potential at liquid nitrogen temperature. The large-area and thick superconducting films with high crystallinity are required for most superconductivity application. Metal organic deposition (MOD) method is an attractive process for the large-area deposition resulting in higher production rate for coated conductors, since this process can be utilized for the substrate with a large size under a non-vacuum low cost condition. Especially, it has been reported that the MOD process using metal trifluoroacetate (TFA) precursors can provide high-Jc YBCO films.

In this study, the TFA-MOD process was applied to form YBCO films. In this process, it was known that the $Y_2Cu_2O_5$, BaF_2 and CuO are converted into YBCO by the release of HF with supplying H_2O at the reaction interface. The water vapor pressure (P_{H2O}) during crystallization is a factor to control the supersaturation for the YBCO conversion reaction. Then, the crystallization conditions were optimized to thicken the YBCO film maintaining high Jc value.

2. Experimental

The precursor solution for fabrication of the YBCO film was prepared by dissolving the TFA salts for Y and Ba elements and a fluorine-free naphthenic salt for Cu with the 1:2:3 cation ratio into an appropriate solvent. The solution was controlled to have a total metal ion concentration of 1.2 mol/l, and was coated on the $LaAlO_3$ and $CeO_2/Gd_2Zr_2O_7$/Hastelloy substrates by the spin-coating method. Then, a two-step heat treatment was applied to the coated films. In the first step, the coated film was calcined to form a homogeneous amorphous precursor by increasing the temperature to 400°C in a humid oxygen atmosphere. In the case of multi-coating for the thickening, coatings and calcinations were repeated several times under the same condition of the first calcination. In the second step, the precursor films were heated to 760°C and held for an appropriate time in a mixed gas atmosphere of humid argon and oxygen with the low oxygen partial pressure of 0.1vol%. The total gas flow rate was fixed to be 1000 cm^3/min. and was humidified by bubbling in a heated water reservoir. In this study, P_{H2O} of the inlet gas

was varied in the range from 0.5 to 25% by controlling the temperature of the water reservoir in order to study the influence of the P_{H2O} on the microstructure and J_c in thicker YBCO films.

3. Results and discussion

The Jc values dependence of P_{H2O} is shown in figure 1. Jc depended strongly on the P_{H2O} condition during the crystallization in this process. Jc value increased with increasing P_{H2O} from 0.8 to 13.5%. Films crystallized at 13.5% of P_{H2O} showed a maximum J_c value of 2.1 MA/cm^2, Jc decreased as P_{H2O} increased over the values larger than 20%. TEM observation was performed to investigate the Jc values dependence of P_{H2O}. The pore size was smaller in the high Jc films crystallized under the medium P_{H2O} condition and became larger in the low-Jc films under both lower and higher P_{H2O} for the YBCO films with a constant thickness. These pores cause not only a reduced cross section of the electric current paths, but also a concentration of the electric fields. Both phenomena limit the critical currents in the film. Furthermore, crack generation was observed in the films crystallized at the higher P_{H2O} condition than 20%. Consequently, both pore and crack formations limited the Jc properties. Then, the dependence of the heating rate on the crack generation in the crystallization process was investigated. As a result, it was confirmed that the lower heating rate is effective in suppressing cracks. This suggests that higher Jc values may be expected even in thicker YBCO films using lower heating rates.

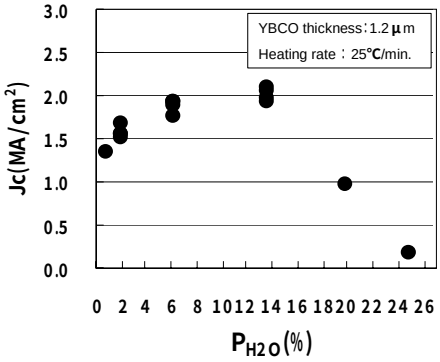

Figure 1. Jc values dependence of P_{H2O} condition in the crystallization step for films of 1.2 μm in thickness.

Finally, a YBCO film with a high Ic value of 508A at 77K in self-field was achieved with the YBCO film thickness of 2.7 μm under the optimized conditions of P_{H2O} and heating rate in the crystallization step.

4. Conclusion

In this study, the TFA-MOD process was applied to form YBCO films. The influence of processing parameters such as water vapor pressure, P_{H2O}, and heating rate on Jc have been investigated for thicker YBCO films. It was found that the Jc value strongly depended on the P_{H2O} during the crystallization. The pore size in the film becomes smaller in the high Jc films and becomes larger in the low-Jc films. Pore and crack formation affected the Jc properties in higher P_{H2O} conditions. Then, a low heating rate in the crystallization of thicker YBCO could suppress the crack formation. Finally, a high-Jc YBCO film with 2.7 μm in thickness was obtained under the optimized conditions of P_{H2O} and heating rate in the crystallization step.

5. Acknowledgement

This work was supported by the New Energy and Industrial Technology Development Organization (NEDO) through International Superconductivity Technology Center (ISTEC) as the collaborative research and development of fundamental technologies for superconductivity applications.

Effect of 0-D artificial pinning centers on surface resistance of Er123 films

M. Mukaida[a,h*], A. Saito[b], R. Kita[c,h], T. Horide[d,h], K. Matsumoto[d,h], A. Ichinose[e,h], Y. Yoshida[f,h], S. Horii[g,h], R. Teranishi[a,h], K. Yamada[a], N. Mori[a]

[a]Kyushu University, [b]Yamagata University, [c]Shizuoka University, [d]Kyoto University, [e]CRIEPI, [f]Nagoya University, [g]University of Tokyo, [h]CREST-JST

Abstract - Surface resistances are evaluated for dilute Zn substituted high quality $ErBa_2Cu_3O_{7-\delta}$ilms. Dilute Zn substituted high quality $ErBa_2Cu_3O_{7-\delta}$ films are grown on $SrTiO_3$ substrates by a pulsed laser deposition technique. Targets used in the experiments are un-substituted, 0.3at.%, 0.5at.%, 1.0at.% and 10at.% Zn substituted $ErBa_2Cu_3O_{7-\delta}$ ceramics. Crystal structures and surface resistance are evaluated.

Zn substitution into $YBa_2Cu_3O_{7-\delta}$ has been studied for understanding the origin of oxide superconductivity with substituting level of several ten %. In this study, dilute Zn below 1.0at.% is mainly adopted. Further substitution reduces its critical temperature.

We intended to introduce zero-dimensional superconductivity killer atoms into CuO_2 plane as artificial pinning centers. The obtained Zn substituted $ErBa_2Cu_3O_{7-\delta}$ films are *c*-axis oriented without peaks from other phases. The sharp drop temperature of surface resistance decreases as the Zn substitution. However, the surface resistance at low temperature around 20K is almost the same among the $ErBa_2Cu_3O_{7-\delta}$ films with different Zn substituting.

1 Introduction

One of the main applications of high-T_C superconductors is in superconducting microwave devices, because these have quite low insertion losses, sharp out-band rejection characteristics, low frequency-dispersions and flat group delay characteristics. Therefore these superconductors enable the production of passive microwave devices with excellent characteristics and small size in the frequency region lower than 100GHz.[1)] Cryogenic recieving front ends (CRFE) is already comarcially abairable now. However there are no cryogenic **emitting** and recieving front ends. In order to develop superconducting microwave emitting devices, low surface resistance films are strictly required.

It is controversial whether the surface resistance is dependent on the critical current density (J_C) of the films.[2)–5)] Critical current densities are increased by introduction of artificial pinnning centers. Nano-particle inclusions are receiving a lot of attention for enhancing the critical current density.[6)–10)] We have proposed using $BaSnO_3$ and $BaZrO_3$ buffer layers and $BaSnO_3$-$YBa_2Cu_3O_{7-\delta}$ and $BaZrO_3$-$YBa_2Cu_3O_{7-\delta}$ multilayers to reduce the surface resistance.[11)–13)] Furthermore, $ErBa_2Cu_3O_{7-\delta}$ films have higher crystalline quality than $YBa_2Cu_3O_{7-\delta}$ films.[14),15)] Then we focus on the films with artificial pinning centers.

In this paper, we discuss the effects of artificial pinning centers into $ErBa_2Cu_3O_x$ films on their surface resistance.

2 Experiments

Zn substituted and non-doped $ErBa_2Cu_3O_{7-\delta}$ films were grown by pulsed ArF excimer laser (Lambda Physik) deposition. The background pressure of the growth chamber (ULVAC) was 4 $\times 10^{-8}$ Pa. The targets used in this experiment were sintered $ErBa_2Cu_3O_{7-\delta}$ and Zn substituted $ErBa_2Cu_{3(1-x)}Zn_{3x}O_{7-\delta}$ceramics. The incident laser beam was focused on the target surface at 45 ° through an MgF_2 window. The focusing lens was also made of MgF_2 to avoid laser power absorption. The laser irradiated area was about 2 mm^2. The laser power was between 200∼300 mJ/pulse. The energy density measured on the target was about 6∼9 J/cm^2 through the window and the lens. The pulse frequency was fixed at 1 Hz. $SrTiO_3$ (100) substrates were used in this experiment. The substrate was attached by silver paste to a rotating metal substrate holder, which was irradiated by a lamp heater. The substrate temperature was controlled by input power monitored by a thermocouple and calibrated by an optical pyrometer. The substrate temperature was determined using an op-

*E-mail: mukaida@zaiko.kyushu-u.ac.jp

tical pyrometer. In this experiment, the substrate temperature was fixed near 750 ° C.

During deposition, the oxygen pressure was fixed at 53.3 Pa with an oxygen flow rate of 200 cc/min. After deposition, the substrate was cooled to a room temperature without any annealing processes. It is reported that additional annealing processes increase the J_C of $ErBa_2Cu_3O_{7-\delta}$ films.[15] However, in order to clarify the J_C enhancement by the introduction of pinning centers, we do not anneal the films.

The preferred orientations of $ErBa_2Cu_3O_{7-\delta}$ films with artificial pinning centers were determined by measuring the $\theta/2\theta$ scan of the films by x-ray diffraction (XRD) with Cu-K_α radiation. The in-plane orientations of the $ErBa_2Cu_3O_{7-\delta}$ films were evaluated by x-ray ϕ scan (in-plane rotation) using the (102) plane of $ErBa_2Cu_3O_{7-\delta}$. The film crystallinity was estimated by full width at the half maximum (FWHM) of the rocking curve using 005 peak of the $ErBa_2Cu_3O_{7-\delta}$ film.

The film thickness is measured by a scanning electron microscope (JSM-6500F) and a mechanical stylus. The lattice images of the films were observed by a transmission electron microscope (TEM).

The R_S which is the most important figure of merit for microwave applications was measured at 38GHz using a dielectric sapphire resonator in TE_{013} mode. It is noteworthy that the higher the measuring frequency, the more accurate the surface resistance.[16] The sapphire [Al_2O_3 (001) (Kyocera)] rod was sandwiched by two 10mm × 10mm high T_C films and placed on a cold stage of a cryocooler (Aishin). In the measurements, the loss tangent of Al_2O_3 (001) rods, which was less than 10^{-7}, was neglected.

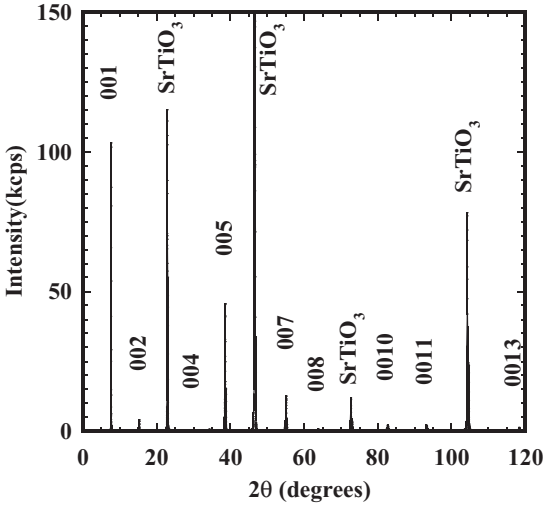

Figure 1: A typical x-ray diffraction pattern for $ErBa_2Cu_3O_{7-\delta}$ films with Zn addition on $SrTiO_3$ substrates.

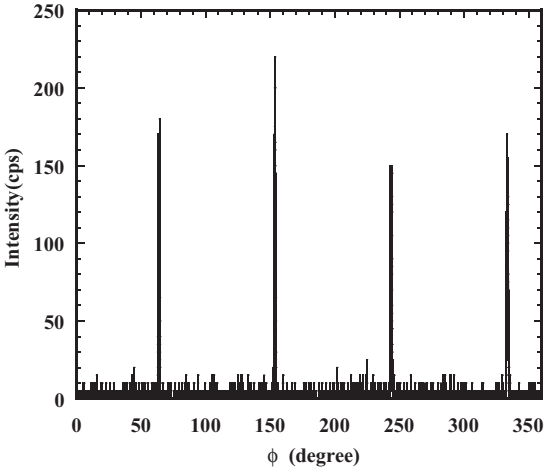

Figure 2: A typical x-ray ϕ-scan pattern for $ErBa_2Cu_3O_{7-\delta}$ films with Zn addition on $SrTiO_3$ substrates.

3 Results

3.1 Crystal structure

Figure 1 shows a typical x-ray $\theta/2\theta$ diffraction pattern of Zn doped $ErBa_2Cu_3O_{7-\delta}$ films grown on $SrTiO_3$ substrates. The same diffraction pattern is also obtained from $ErBa_2Cu_3O_{7-\delta}$ films. The $00l$ reflections of $ErBa_2Cu_3O_{7-\delta}$ are observed from the film. Thus, the $ErBa_2Cu_3O_{7-\delta}$ film is concluded to be c-axis oriented. The c-axis lattice constant calculated using the N-R function is 1.167nm. The short c-axis length indicates that the film is well oxidized. Figure 2 shows a typical x-ray ϕ-scan diffraction pattern of Zn doped $ErBa_2Cu_3O_{7-\delta}$ films. 4 strong peaks appear showing the epitaxial growth on the $SrTiO_3$ substrates.

In order to enhance the pinning force, $REBa_2Cu_3O_{7-\delta}$ films must be high quality. Therefore, we investigated the crystalline quality of the film by the rocking curves. A typical rocking curve for the $ErBa_2Cu_3O_{7-\delta}$ films with Zn doping is 0.27 degrees. Despite the addition of Zn, the crystalline quality of the $ErBa_2Cu_3O_{7-\delta}$ film is as high as those on non-doped $ErBa_2Cu_3O_{7-\delta}$ film(0.28 degrees).[14] This is one reason why $ErBa_2Cu_3O_{7-\delta}$ films were selected instead of $YBa_2Cu_3O_{7-\delta}$ films.

3.2 Surface resistance

Next we measureed the R_S of Zn doped $ErBa_2Cu_3O_{7-\delta}$ films. R_S of the $ErBa_2Cu_3O_{7-\delta}$, $ErBa_2(Cu_{0.9}Zn_{0.1})_3O_{7-\delta}$, $ErBa_2(Cu_{0.997}Zn_{0.003})_3O_{7-\delta}$, $ErBa_2(Cu_{0.99}Zn_{0.01})_3O_{7-\delta}$, and $ErBa_2(Cu_{0.995}Zn_{0.005})_3O_{7-\delta}$ films were shown

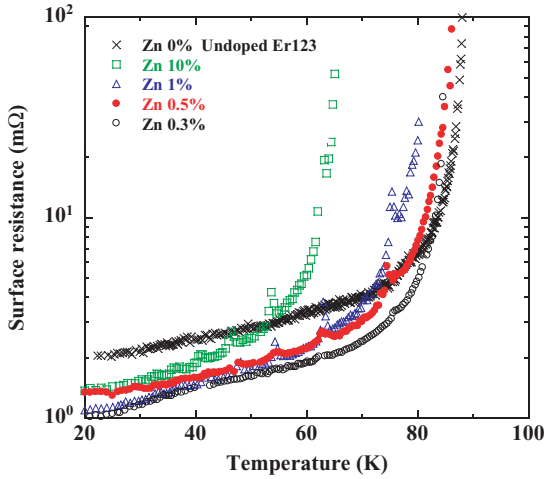

Figure 3: Surface resistance of Zn doped $ErBa_2Cu_3O_{7-\delta}$ films. In the figure Zn is substituted for Cu in a formula of $ErBa_2(Cu_{1-x}Zn_x)_3O_{7-\delta}$.

in Fig.3 as a function of a temperature. The $ErBa_2(Cu_{0.9}Zn_{0.1})_3O_{7-\delta}$ has the very low superconducting transition temperature (T_C) below 70K. Decrease of the T_C agrees well with the results of Zn over doping into $YBa_2Cu_3O_{7-\delta}$ bulk samples. The R_S value of the $ErBa_2(Cu_{0.997}Zn_{0.003})_3O_{7-\delta}$ and that of the $ErBa_2(Cu_{0.995}Zn_{0.005})_3O_{7-\delta}$ is lower than that of the non Zn-doped $ErBa_2Cu_3O_{7-\delta}$ films in the wide temperature region below 90K.

However, the R_Ss are seemed to be saturated. It is very interesting that the lowest R_Ss are almost the same for the various amount of Zn doped $ErBa_2Cu_3O_{7-\delta}$ films.

3.3 Critical current density

Finally we measured the field angular dependence of critical current density (J_C) of Zn doped $ErBa_2Cu_3O_{7-\delta}$ films grown on $SrTiO_3$ substrates as shown in Fig. 4. These J_Cs are measured in magnetic field between 1 to 6 T. By reducing magntic field, J_C in a magnetic field parallel to the c-axis is enhanced. In the measurement of surface resitance, magnetic field is the self field, then, the J_C is much higher than that shown in the Fig. 4. It is very interesting that 0-dimensional APC of Zn doping enhace J_C in a magnetic field parallel to around the a-axis in high magnetic fields as shown in the figure.

4 Conclusion

Effects of artificial pinning centers (APCs) into $ErBa_2Cu_3O_{7-\delta}$ films were discussed. The APC used in this paper was Zn which was mixed into an $ErBa_2Cu_3O_{7-\delta}$ ceramic target with various contents of APCs. The high crystalline quality $ErBa_2Cu_3O_{7-\delta}$ films were grown with Zn as APCs by pulsed laser deposition.

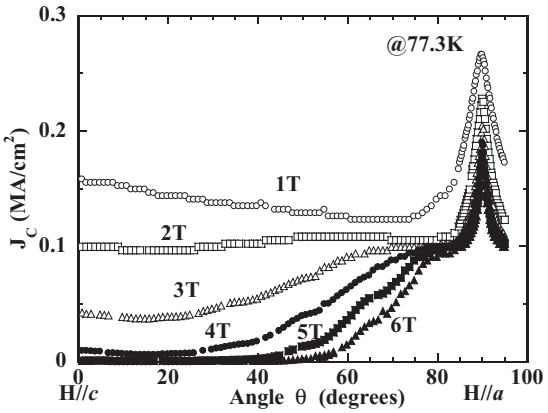

Figure 4: Field angular dependence of critical current density of Zn doped $ErBa_2Cu_3O_{7-\delta}$ films in 1 to 6 T magnetic field.

The introduction of APCs decreased surface resistance of $ErBa_2Cu_3O_{7-\delta}$ films and increased critical current density (J_C) of the films. Surface resistance (R_S) measurements revealed that the $ErBa_2Cu_3O_{7-\delta}$ films with APCs showed a lower R_S than that of the $ErBa_2Cu_3O_{7-\delta}$ films. The most important to note is the surface resistance of Zn doped $ErBa_2Cu_3O_{7-\delta}$ films coincide with other $ErBa_2Cu_3O_{7-\delta}$ films with APCs.

References

[1] H. Chaloupka: *Frequenz*, **443** (1990) 141.

[2] Yu N. Drozdov, S. V. Gaponov, S. A. Gusev, E. B. Kluenkov, Yu N. Nozdrin, V. V. Talanov, B. A. Volodin, and A. K. Vorobyev: *Supercond. Sci. Technol.*, **9** (1996) A166-A169.

[3] G. P. Srivastava, Mohan V. Jacob, M. Jayakumar, P. K. Bhatnagar, and N. D. Kataria: *J. Appl. Phys.*, **81** (1997) 6272-6276.

[4] T. C. Shields, J. B. Langhorn, S. C. Watcham, J. S. Abell, and T. W. Button: *IEEE Trans. Appl. Supercond.*, **7** (1997) 1478-1481.

[5] S. Ohshima, S. Oikawa, T. Noguchi, M. Inadomaru, M. Kusunoki, M. Mukaida, H. Yamasaki, and Y. Nakagawa: *Physica C*, **372** (2002) 671-674.

[6] T. Oka, Y. Itoh, Y. Yanagi, H. Tanaka, S. Takashima, and U. Mizutani: *Advances in Superconductivity*, **4** (1992) 651-654.

[7] T. Sakai, K. Nishio, N. Ogawa, and I. Hirabayashi: *Advances in Superconductivity*, **3** (1991) 761-764.

[8] Y. Y. Luo, Y. C. Wu, X. M. Xiong, Q. Y. Li, W. Gawalek, and Z. H. He: *J. Supercond.*, **13** (2000) 575-581.

[9] R. Weinstein, R.-P. Sawh, D. Parks, M. Murakami, T. Mochida, N. Chikumoto, G. Krabbes, and W. Bieger: *Physica C*, **383** (2002) 214-222.

[10] J. L. Macmanus-Driscoll, S. R. Foltyn, Q. X. Jia, H.Wang, A. Serquis, B. Maiorov L. Civale, M. E. Hawley, M. P. Maley, and D. E. Peterson: *Nature Materials*, **3** (2004) 439-443.

[11] M. Mukaida, Y. Takano, K. Chiba, T. Moriya, M. Kusunoki, and S. Ohshima: *Jpn. J. Appl. Phys. pt. 2*, **38** (1999) L926-L928.

[12] M. Mukaida, Y. Yamazaki, Y. Shingai, S. Makino, M. Kusunoki, A. Saito, and S. Ohshima: *Supercond. Sci. Technol.*, **17** (2003) 337- 341.

[13] M. Mukaida, S. Makino, K. Chiba, M. Kusunoki, and S. Ohshima: *AIP (Proceedings of Physics in Local Lattice Distortions)* (2001) 512.

[14] T. Ohazama, M. Mukaida, A. Ichinose, K. Matsumoto, Y. Yoshida, S. Horii, A. Saito, and S. Ohshima: *Physica C*, **412-414** (2004) 1301-1305.

[15] S. Horii, A. Ichinose, M. Mukaida, K. Matsumoto, T. Ohazama, Y. Yoshida, J. Shimoyama, and K. Kishio: *Jpn. J. Appl. Phys. PartII*, **43** (2004) L1223-L1225.

[16] M. Kusunoki, M. Mukaida, and S. Ohshima: *Abstract of JSAP 2001 spring meetings*, **I** (2001) 286.

Microwave Absorption in c-Oriented YBCO Thin Film Superconductors

Hong Zhu[1], Atsuya Akiba[1], Atsushi Kamiya[1], and Tamio Endo[1,2]
1 Graduate School of Engineering, Mie University, *Tsu, Mie 514-8507, Japan*

Hirofumi Yamasaki[2], Kazuhiro Endo[2]
2 National Institute of Advanced Industrial Science and Technology, *Umezono, Tsukuba, Ibaraki 305-8568, Japan*

Abstract — Magnetically modulated microwave absorption (MA) was studied in c-oriented $YBa_2Cu_3O_x$ films. Line shapes of MA signals are analyzed using weak link model. Curve fitting results indicate that Fraunhofer diffraction reduction of junction currents in the weak links dominates MA around zero field in the samples. By subtracting modulation-current-induced component, derivative curves of MA are separated from the measured MA signals. Different mechanisms in other superconducting samples are discussed also for comparison.

1. Introduction

Microwave absorption (MA) in high temperature superconductors (HTSs) is one of the most fascinating phenomena in both aspects of practical applications and fundamental science [1-3]. Although the mechanisms of magnetic field-dependent MA in HTSs have not yet fully been recognized to date, a few simple phenomenological models developed recently have helped to shed some light on them. The most popular mechanism is a viscous motion of the Abrikosov vortices [4], as well known in conventional type-II superconductors, which dominates MA in the mixed state. In HTSs, however, processes in the weak links complicate dissipation processes much around zero field. As originally suggested by Deutscher and Muller [5], point defects, oxygen vacancies, and even intrinsic insulating layers between superconducting planes can act like the weak links due to very short coherence length characterizing HTS materials. In fact, such weak links have been considered simply as Josephson junctions, and some groups have proposed that the low field MA can be attributed to alternating maximum supercurrent or decoupling of the junctions in the magnetic field [6-8]. Supercurrents can flow through the weak links via the Josephson junctions at zero external dc magnetic field. When the dc magnetic field is increased, the maximum supercurrent through a Josephson junction is reduced, which in turn results in the increase of absolute MA until the junctions are decoupled. The junction sizes are ranged from 10^1 nm to 10^3 nm, and there are varieties of Josephson current loops depending on sample quality. When the junction size d is larger than the London penetration depth L_λ, however, fluxons are nucleated within the weak links and their viscous motion dominates MA behavior. In such situation, the vortex motion model was proposed to explain the low-field MA in HTSs by Portis *et al* [9].

A magnetic field modulation and lock-in technique, in which the modulation field is superimposed on the dc magnetic field, have widely been employed to obtain highly sensitive MA in the measurements of field-dependent nonresonant MA signals. Usually, such experimental results show a strong derivative-like signal near zero field, which corresponds rationally to the absolute absorption minimum at zero field. Sometimes, however, a back-and–forth field sweep distorts the signals seriously due to boundary currents, which are induced by opposite directions of screening and shielding currents due to flux trapping, resulting in opposite phases of the signals for forward and reverse magnetic field sweeps. It is totally different from the derivative of dc-sweep absolute absorption. To obtain a clear idea for the derivative-type absorption signals in the dc magnetic field, therefore, it is necessary to analyze such distorted hysteretic signals in detail. In this work, we investigated the magnetically modulated MA in c-orientated $YBa_2Cu_3O_x$ (YBCO) thin films. The experimental signals with respect to magnetic filed were fitted by calculated curves in a framework of the weak link model. By subtracting a modulation-current-induced component, we obtained the derivative-like signals. Different mechanisms of MA in various superconducting samples are also discussed.

2. Experimental

The film of c-axis oriented YBCO was grown by pulsed laser deposition method on MgO (100) substrate at a substrate temperature T_S=710°C. Thickness of the film was measured to be 650 nm. X-ray diffraction results showed it is the c-oriented film with high epitaxy. The film exhibits critical temperature around 87 K which was obtained by ac susceptibility measurement. For comparison, we

also measured MA on superconducting $Bi_2Sr_2CaCu_2O_y$ (Bi2212) single crystals with T_C=86.5 K, which were grown by self-flux method.

The nonresonant MA experiments were performed using a Varian EPR spectrometer with 100 kHz field modulation and lock-in detection. The modulation field (H_m=10 G) was superimposed in the direction parallel to the dc field H_a, which was perpendicular to a plane of the film (i.e. H_a//c-axis). In the measurements, a rectangular cavity resonating at ~9.3 GHz in TE_{102} mode was employed. Throughout the measurement, the microwave power was held at 0.1 mW. Sample temperature was fixed at 77.3 K, by directly immersing a sample tube in liquid nitrogen. The dc magnetic field H_a was mostly swept between –50 and +50 G, in order to eliminate sweep-range-dependent phase reversal and hysteresis.

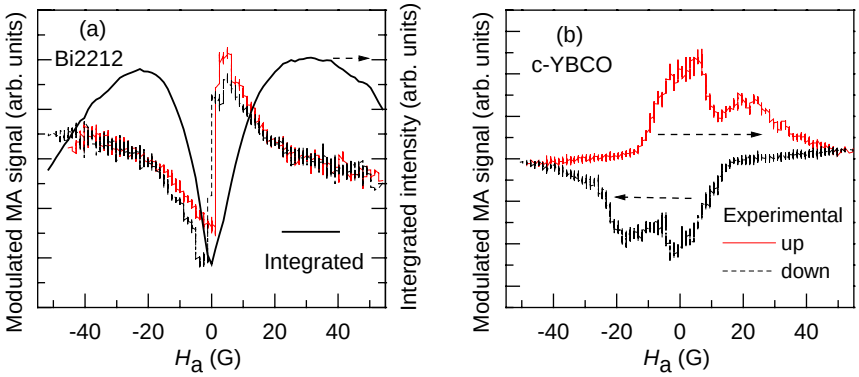

Figure 1: Experimental modulated MA signals for (a) Bi2212 single crystal and (b) c-YBCO film at 77.3 K. The integrated curve corresponding to the downward sweep is also shown in (a) by a thick solid curve.

3. Results

First, we show in Figure 1 (a) the results of MA on Bi2212 single crystal at 77.3 K. The experimental derivative-like signals for the upward and downward sweeps present strong intensities near zero magnetic field. By integrating the downward sweep signal, we obtained a corresponding curve as shown by a thick solid curve in Figure 1 (a). It is clear that there is a minimum in the integrated curve at zero field. With increasing H_a up to ~25 G, the curve shows a sharp increase, and with further increasing H_a up to ~50 G, it shows a gradual decrease. Usually, such derivative-like signals can be understood by one of models of the viscous flux motion. Then the negligible hystersis for the upward and downward sweeps is in agreement with rather weak flux pinning in Bi2212 superconductors. Negative MA signal in the higher field for the upward sweep is related to votex dynamics in liguid state of reentrant phase diagram, which is typical for strong two-dimensional systems like Bi2212 as we published before [10,11].

The experimental MA signals of the c-YBCO film, which are totally different from that of Bi2212, are shown in Figure 1 (b). For the upward sweep from negative to positive field, a main signal peak appears near zero field, then a subsidiary peak at ~20 G. It is obvious that one cannot consider such a signal as the mathematical derivative of the absolute MA; accordingly it is impossible to obtain the dc field dependence of microwave absorption by integrating MA signal directly. The other difference is that, for the downward sweep, the signal shows the opposite phase relative to that for the upward sweep, even the signal shapes are the same for the upward and downward sweeps. It means that MA signals are sweep-direction dependent in the c-YBCO film. In order to obtain the real dc component of microwave absorption, it is necessary to analyze the absorption mechanism and the measuring technique in more detail.

4. Discussion

4.1 Curve fitting

In the magnetically modulated MA measurement, the strong hysteretic signals with a main peak near zero field, hereafter we denote it A-type signal, have been reported by many groups. We show one of theoretical models in this paper. Considering a HTS sample as an effective weak superconductive medium, Dulcic *et al* [6] explained the A-type signals using a model, which assumes that the

microwave absorption occurs in weak link (Josephson) junctions. Josephson junction is a couple of superconductors isolated by a narrow normal gap, where supercurrent I_S can tunnel across the gap $I_S = I_C \sin(\Delta\phi)$, with I_C the critical current of junction and $\Delta\phi$ the phase difference of the electron-pair wave on the two sides. As well known, a voltage is developed across a superconductor, if the supercurrent in the superconductor is varying with time. The same is true for a Josephson tunneling junction. Then normal electrons participate in the transport process and energy dissipation occurs.

In an external magnetic field (H), the maximum supercurrent I_{max} of a junction is changed from I_C. Regarding the field dependence of I_{max}, the most elementary approximation is the familiar Fraunhofer diffraction pattern of a Josephon junction

$$I_{max} = I_C \frac{\sin(\pi H / H_0)}{(\pi H / H_0)} \qquad (1)$$

where H_0 corresponding to Φ_0 is the field for which the first flux quantum penetrates into the junction, which depends on the size of the junction. Considering some distribution in the junction size and nature, the effective field dependence of I_{max} in this paper is taken as an envelope of eq. (1).

For a weak-linked junction characterized by the maximum supercurrent I_{max} and the normal state resistance R under dc magnetic field, the microwave absorption P takes a form [12]

$$P = P_n \frac{1}{1+\eta} \qquad (2)$$

where $P_n = \frac{1}{2} I_{mw}^2 R$, I_{mw} is the microwave current of frequency ω_{mw} flowing through the junction. In this equation (2), $\eta = (2eRI_{max}\cos\varphi_0 / \hbar\omega_{mw})^2$, where φ_0 is the phase difference defined by $I_0 = I_{max}\sin\varphi_0$, I_0 is the screening current (we define it as boundary current in this study) induced by the magnetic-field sweep. In our calculation, for simplicity, I_0 is assumed to be a constant for the given field-sweep direction and to change its sign after the sweep reversal due to strong flux trapping. With sweeping the magnetic field (H), the maximum supercurrent I_{max} is changed, which in turn results in the changes of the parameter η and then the microwave absorption P.

Concerning the measuring technique, linear law detectors as a standard device are employed generally in EPR spectrometers, then the signal intensity is proportional to square root of the absorbed power, *i.e.* $S' \propto \sqrt{P}$. In the lock-in technique, S' is modulated by the modulation field $H_m \cos\omega_m t$ and can be expressed as

$$S'(H + H_m\cos\omega_m t) \approx S'(H) + \frac{dS'}{dH} H_m \cos\omega_m t + \frac{1}{2}\frac{d^2S'}{dH^2}(H_m\cos\omega_m t)^2 \qquad (3)$$

The first harmonic signal S is proportional to the amplitude of the second term in eq. (3). Then by a straightforward calculation, one yields

$$S \propto \frac{\sqrt{P_n}}{(1+\eta)^{3/2}} \frac{1}{(\hbar\omega_{mw}/(2eR))^2} (-I_{max}\frac{dI_{max}}{dH} H_m + I_0 I_m) \qquad (4)$$

where I_m is the modulation amplitude of the boundary current corresponding to the modulation field. Exactly speaking, I_m has very complicated background, but here we simply take it as a constant. The first term including the pre-factor of eq. (4) represents a sweep direction independent (reversible) signal

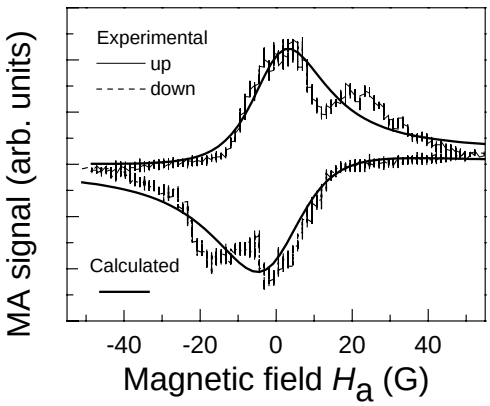

Figure 2: Fitting results of MA signals for the c-YBCO film using the weak link model. ($H \equiv H_a$).

component, whereas the second term is a sweep direction dependent component, which changes sign as the boundary current I_0 changes the direction with reversing the field sweep. Obviously, the total signal intensity and behavior as a function of H depends on the relative proportion of the two components.

Using I_{mw}, R, I_C, H_0, I_0, and I_m as fitting parameters, we fitted a calculated curve of S to the experimental MA signal taking $H \equiv H_a$, as shown in Figure 2. The fitted curves are mainly in coincidence with the measured MA signals, indicating that the diffraction reduction of junction currents in the weak links dominates the low-field microwave absorption in the c-YBCO film. It can be seen in Figure 2, however, the fit around 20 G is rather poor. It might indicate that the viscous vortex motion begins to participate in the microwave absorption at fields higher than 20 G. Remaining the other parameters unchanged, the reverse signal can be fitted as well just by changing the boundary current I_0 to $-I_0$, as shown in Figure 2. Because the signal is in arbitrary units, we cannot obtain the absolute values for the currents, such as I_{mw}, I_C, I_0, and I_m. The characteristic field H_0, however, is determined as 100 G through the fitting calculation. According to $\Phi_0 = \mu H_0 A$ where Φ_0 is the flux quantum and A is the effective area of the junction exposed to the external magnetic field, one can estimate the junction size in order of 10^3 nm, which is in agreement with a dimension of twin boundaries in YBCO films.

4.2 Two Components

To analyze the absorption mechanism in more detail, we plot the two components of fitted curve for the upward sweep in Figure 3. It can be seen that the second component, which is due to the modulation current I_m and boundary current I_0, is much larger than the first component, which is derivative-like and reversible depending on I_{max}. This second term results in the opposite sign of hysteresis of the experimental signal for the upward and downward sweeps depending on I_0 direction. According to Eq. (4), the first component is proportional to the amplitude of modulation field H_m. Another point we like to mention here is that such A-type MA signals are not observed in Bi2212 crystals and high quality YBCO crystals, instead the derivative-like signals are generally observed. We consider that the common origin for the derivative-like MA signals is the viscous vortex motion, but the details are different. In Bi2212 single crystals, the main process for MA is due to the characteristic weak flux pinning. Whereas in the good YBCO crystals, the vortex can be nucleated within the weak links, because the junction size d is larger than the London penetration depth L_λ, which in turn results in viscous vortex motion in the low magnetic fields.

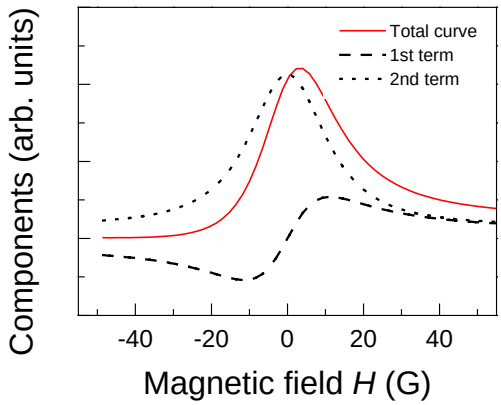

Figure 3: The two components of the fitted curve; the first (derivative-like) term and second (modulation current induced) term. The total curve is also shown.

4.3 DC absorption

Using the fitting parameters, the dc microwave absorption curve S_{dc} can be simulated by Eqs. (1) and (2), as shown in Figure 4. It shows a rational field dependence of the microwave absorption, having a minimum at zero field, increasing sharply around 20 G and then becoming saturation beyond 40 G. The main feature of the corresponding derivative curve, shown in Figure 4, is in almost agreement with that of the first component in Figure 3. It indicates that, by subtracting the modulation current induced effect, the first term of Eq. (4) mainly reflects the absolute absorption process in the c-YBCO film. It is noticeable that there are some small differences, such as the curvature around 20 G, between the first-term curve in Figure 3 and derivative curve in Figure 4. We argue that the Fraunhofer diffraction reduction of maximum supercurrents in the weak links is one of the possible origins for the microwave

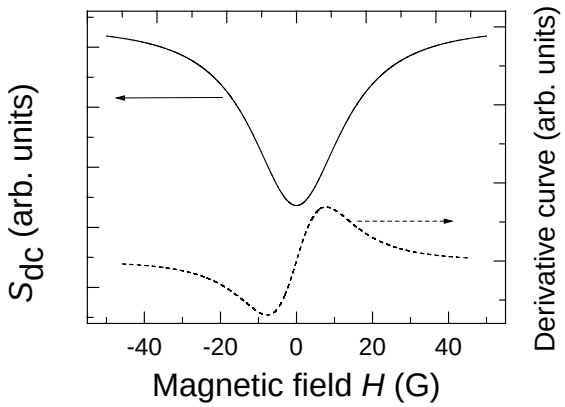

Figure 4: Calculated dc microwave absorption S_{dc} *vs.* magnetic field H and corresponding derivative curve.

absorption around zero field, whereas at the fields higher than 20 G other mechanisms have to be taken into account. More work is needed to understand the microwave absorption more quantitatively even under the low magnetic field.

5. Conclusions

In summary, we presented the experimental results on the magnetically modulated microwave absorptions in the c-YBCO film, which show the reinforced hysteresis and a main peak of MA around zero field. The numerical fitting results indicate one of the possible mechanisms for the microwave absorption. That is, the alteration of maximum supercurrent of the weak links dominates the microwave absorption process around zero field in the sample. The modulation current-induced component affects the modulated MA signals seriously. This model is effective in the c-YBCO thin films with the junction sizes in order of 10^3 nm, whereas in Bi2212 single crystals, the viscous vortex motion might play a key role in MA process.

Acknowledgment

Two of the authors, H. Zhu and T. Endo, would like to thank Japan Society for the Promotion of Science (JSPS) for supporting this work.

REFERENCES

1. Zaitsev A.G., Schneider R., Linker G., Fatzel F., Smithey R., and Geerk J., *Phys. Rev. B*, vol. 68, 104502, 2003.
2. Machida M., *Phys. Rev. Lett*, vol., 90, 037001, 2003.
3. Velichko A. V., and Porch A., *Phys. Rev. B*, vol. 63, 094512, 2001.
4. Gittleman J. I. and Rosenblum B., *Phys. Rev. Lett.*, vol. 16, 734, 1966; Rosenblum B. and Cardona M., *ibid*., vol 12, 657, 1964.
5. Deutscher G. and Muller K. A., *Phys. Rev. Lett.*, vol. 59, 1745, 1987.
6. Dulcic A., Rakvin B., and Pozek M., *Eurpphy. Lett*., vol. 10, 593, 1989.
7. Puri M., Masiakowski J. T., Marrelli S., Bear J., and Kevan L., *J. Phys. Chem*., vol. 94, 6094,1990.
8. Owens F. J., *Physica C*, vol. 171, 25, 1990.
9. Portis A. M., Blazey K. W., Muller K. A., and Bednorz J. G., *Eurpphy. Lett*., vol. 5, 467, 1988.
10. Ahmad G., Hashizume A., Iwasaki S., Yoshii K., Reddy B. J., Shahabuddin M., Uthayakumar S., Jayavel R., and Endo T., *Physica C*, vol. 388-389, 687, 2003.
11. Hashizume A., Yamada J., Kohmoto H., Yamada Y., Endo T., and Shahabuddin M., *Physica C*, vol. 357-360, 481, 2001.
12. Wosik J., Xie L. M., Wolfe J. C., Ren Y. and Chu C. W., *Phys. Rev. B*, vol. 51, 16289, 1995.

Numerical and Experimental Investigations of a Tropical Outdoor UWB Channel Characteristics for Short Pulse Transmission

Joko Suryana AB Suksmono Sugihartono A Kurniawan Kenji Tanaka K Igarashi Mitsuyoshi Iida
STEI ITB, Indonesia NICT Japan ARIB Japan
e-mail: joko@ltrgm.ee.itb.ac.id

Abstract—We report the numerical analysis and experimental measurement of a tropical outdoor ultrawideband (UWB) characterizations for short pulse transmissions. Raindrops cause attenuation of radio waves by both absorption and scatter. Absorption involves dissipation of some of the energy of an electromagnetic wave as heat. Scatter involves diversion of some of the energy of the wave into directions other than the forward direction. The theoretical performance of short pulse transmission over rain areas are then compared with experimental data which was performed in the campus environment. The bandwidth of the signal used in this experiment is 7.5 GHz and the measurement setup consists of Vector Network Analyzer, an UWB antenna array , metal sheet as reference reflector and raingauge. Our preliminary study, both numerical and experimental results concluded that the rain-filled medium modify the spectrum of UWB signals . This spectrum degradation will impact on pulse spreading of the transmitted monocycles in time domain and cause bit errors.

1. Introduction

Ultrawideband (UWB) is one of the most promising communication and sensing technologies in recent times with the promise of high data rates, spectral reuse as well as their capability to penetrate through the materials. With recent release of a large spectral mask from 3.1 GHz to 10.6 GHz by the Federal Communications Commission, there emerges an increasing interest in studying UWB technologies for both commercial and military networks. One big challenge of UWB application for 3.1 – 10.6 GHz outdoor links in tropical area is signal degradation due to high intense rain. The presence of hydrometeor, particularly rain, can produce major impairments to radio links. Rain drops absorb and scatter radio wave energy or change the polarization sense of the transmitted signals.

This paper analyses the electromagnetic scattering by raindrops of UWB signal transmission on tropical areas. At frequencies above 5 GHz, rain cause various degrading effects on the performance of communication links. The attenuation of the transmitted signals is a well-known example of such effects. These have given rise to the need of acquiring more detailed knowledge of interaction between raindrops and waves than is necessary for the calculation of attenuation. To obtain such knowledge, we have to know the detailed dielectric and microphysical properties of raindrops, such as shape, size distribution or the motion while they are falling. These properties are reviewed first and single scattering properties of raindrops whose sizes are generally comparable to wavelength are then studied. With the information of these scattering properties, various propagation phenomena are discussed from a theoretical point of view. Specific subjects treated include rain scattering other than forward and backward which is necessary in the estimation of rain scatter interference, pulse shape and channel transfer characteristics. The aim of this analyses is to provide the theoritical performance of UWB signal transmission over rain areas.

On the other hand, we also had performed the ultrawideband signal propagation experiment during high intense rain in the campus environment to characterize the tropical outdoor UWB signal propagation channel. The bandwidth of the signal used in this experiment is 7.5 GHz and the measurement setup consists of Vector Network Analyzer, an UWB antenna array , metal sheet as reference reflector and raingauge.

The preliminary study both numerical and exprimental investigations indicate that rain-filled medium modify the spectrum of UWB signals . This spectrum degradation will impact on pulse spreading of the transmitted monocycles in time domain and cause bit errors. This study also indicate that the impulse response of outdoor UWB channel is depend on the rain intensity. More intense rain will degrade more the outdoor UWB channel.

2. Dielectric and Microphysical Properties of Raindrops

2.1 Dielectric Properties of Raindrop

In the calculation of the scattering properties of raindrops, the knowledge of their dielectric properties is fundamental. Dielectric properties are usually expressed by the complex refractive index $N\ (= N_r - jN_i)$. Their imaginary part is related to the loss in the material. These two quantities are simply related by :

$$N = \sqrt{\varepsilon} \qquad (1)$$

The dielectric property of raindrop for wavelengths longer than 1 mm is due to the polar nature of the water molecule, whereas for wavelenths shorter than 1 mm, the dielectric property is governed by various kinds of resonance absorptions in the molecule. The dielectric property depends not only frequency but also on temperature.

2.2 Shape and Fall Velocity of Raindrops

Raindrops range in size from very small to fairly large ones. The smallest drops may be equivalent to those found in clouds. The largest drops will not exceed 4 mm in radius, since the drops with radii > 4 mm are hydrodynamically unstable and break up. Terminal velocity of raindrops has been measured by many investigators. The fall velocity increases as drop size increases. However, the rate of increase in the terminal fall velocity gradually decreases as the drop radius exceeds about 1 mm and at radius approximately of 2.5 mm, the fall velocity reaches at maximum (~9m/s)[2].

Further increase of the drop size results in the slight decrease of the fall velocity, and, finally, the drop reaches the size at which the drop breakup occurs. The existence of the maximum in the terminal fall velocity is due to the deformation of raindrops; the fall velocity of spherical drops go beyond 9 m / s when drop radius exceeds 2.5 mm. The terminal fall velocity depends on atmospheric pressure, humidity and temperature.

2.3 Drop-Size Distribution

The quantity needed in propagation study, however, is the number of drops per unit volume in space with radius a in a range da. This distribution $n(a)da$ can be obtained from the volume distribution on the ground $m(a)da$ through fall velocity of raindrops $v(a)$:

$$n(a)da = \frac{10^3}{4.8p}\frac{Rm(a)da}{a^3 v(a)}(m^{-3}) \qquad (2)$$

where R is the rain rate in mm/h, $v(a)$ is in m/s and a is in mm.
Marshal and Palmer proposed a negative exponential relation :

$$n(a)da = N_0 e^{-\Lambda a} da \qquad (3)$$

where : N_0 = 1.6 x 10^4 (m^{-3}. mm^{-1})
Λ = 8.2 $R^{-0.21}$ (mm^{-1})
and a is raindrop radius in mm and R is the rain rate in mm / h.

3. Raindrops Scattering using Mie Model

3.1 Single Scattering Properties of Raindrops

A raindrop is placed at origin of the Cartesian coordinar system as ilustrated in figure below :

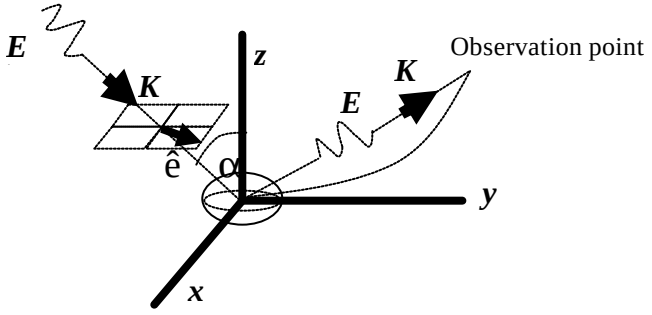

Figure 1. single scattering of raindrop model [1]

We consider just spherical raindrop shape. A plane wave incident on raindrop with an angle of incidence α induces a transmitted field in the interior of the drop and a scattered field. $\boldsymbol{E}^i$ denotes the electric field of incident wave, the polarization state of which is given by a unit vector ê, $\boldsymbol{K}_1$ is a unit vector directed toward the propagation direction of the incident wave, $\boldsymbol{E}^s$ denotes the electric field of the scattered wave, and $\boldsymbol{K}_2$ is a unit vector directed from the origin to the observation point. In the far-field region the electric field of the scattered wave may be written as:

$$\boldsymbol{E}^s = \boldsymbol{f}(\boldsymbol{K}_1, \boldsymbol{K}_2)\ r^{-1}\ exp(-jkr) \qquad (4)$$

where unit incident wave is assumed, k is the free propagation constant, r is the distance from the origin to the observation point, and $\boldsymbol{f}(\boldsymbol{K}_1, \boldsymbol{K}_2)$ is a vector function denoting scattering amplitude and the polarization state of the scattered wave.

An $exp(+jwt)$ time convention is assumed and is suppressed. The quantity of primary interest in scattering is this vector scattering amplitude $\boldsymbol{f}(\boldsymbol{K}_1,\boldsymbol{K}_2)$ and this function is obtained from the solution of the boundary value problem at the surface of raindrop. The scattering amplitude is not only a function of $\boldsymbol{K}_1$ and $\boldsymbol{K}_2$ but also a function of frequency, size, shape and material of raindrop, and the polarization state of the incident wave.

3.2 Mie Theory for Attenuation

Raindrops cause attenuation of radio waves by both absorption and scatter [2]. Absorption involves dissipation of some of the energy of an electromagnetic wave as heat. Scatter involves diversion of some of the energy of the wave into directions other than the forward direction. In the case of a beam of electromagnetic radiation, energy is scattered out of the beam. The term extinction is applied to the sum of absorption and scatter. Attenuation constants can be defined for extinction, absorption, and scatter such that :

$$a_{ext} = a_{abs} + a_{sca} \qquad (5)$$

where the a's are attenuation constants and can be identified by their subscripts.

Analysis of absorption and scatter by rain drops has often been based upon the assumption of spherical drop shape, but the recent tendency is to take account of the nonspherical form of drops [2]. For drops that are sufficiently small compared to wavelength, Rayleigh theory applies, but for drops that have sizes comparable to wavelength the more complicated Mie theory, or refinements of it, must be used. Drops with radii $\leq$170 μm are essentially spherical, whereas drops with radii betweem 170 and 500 μm are closely approximated by oblate spheroids. (An oblate spheroid is formed by rotating an ellipse about its shortest axis). Between 500 and 2000 μm, drops are deformed into asymmetric oblate spheroids with increasingly flat bases, and drops $\geq$ 2000 μm develop a concave depression in the base which is more renounced for the largest drop sizes . The ratio of the minor to major axes of oblate spheroid drops is equal to1- a, where a is the radius in cm of a spherical drop having the same volume. Figure 1 shows an example of the shape of a very large drop.

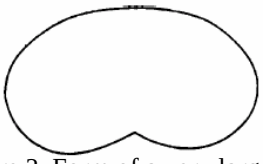

Figure 2. Form of a very large raindrop

The total or extinction power-density attenuation constant a for rain can be expressed as :

$$a_p = \int_a N(a).C_{ext}[n_c, a/l_o]da \qquad (6)$$

where a summation is indicated over all drop radii a, n_c is the complex index of refraction of water which is a function of temperature and frequency, and l_o is wavelength in air.

C_{ext} is an extinction coefficient and is shown as being expressed as a function of n_c and a/l_o. $N(a)\,da$ represents the number of drops per cubic meter in the size interval da and is determined by the drop size distribution which is a function of rain rate. $N(a)$ has units of m^{-4}, and $N(a)\,da$ has units of m^{-3} . Distributions of drop sizes have been determined empirically, the most widely used and tested distribution being the Laws and Parsons distribution.The determination of C_{ext} has been commonly based on the Mie theory for spherical drops .In this case C_{ext} has the form of:

$$C_{ext}[n_c, a/l_o] = (l_o^2/2).\mathrm{Re}\sum_{n=1}^{\infty}(2n+1)(a_n + b_n) \qquad (7)$$

where l_o is wavelength in air and a_n and b_n are coefficients involving spherical Bessel and Hankel functions of complex arguments. C_{ext} and S_o, which gives the amplitude of the forward scattered wave, are related by :

$$C_{ext}[n_c, a/l_o] = (4p/b_o^2)\,\mathrm{Re}\,S_o[n_c, a/l_o] \qquad (8)$$

where b_o is the phase constant $2\pi / l_o$.

3.3 Numerical Simulation of Short Pulse Transmission over Rain-filled Medium

The summary of the procedure to determine the transfer function of rain-filled medium [4] :

1. Determine the frequency range and calculate the complex permittivity as a function of frequency
2. Calculate the refractive index as a function of frequency and the scattering and absorbsion of random media as a function of frequency and rainfall rate.
3. Determine the raindrop size density used and calculate the effective refractive index of rain medium (as in illustrated in fig. 3)
4. Calculate the complex propagation constant and determine the transfer function of Outdoor tropical UWB channel (as in illustrated in fig.4)

Spesification of simulation parameters :

-Operating frequency : 3.1-10.6 GHz
-Complex permittivity derived from Liebe model [3]
-Raindrop size density : Palmer and Marshall
-Temperature of raindrop 290^o K

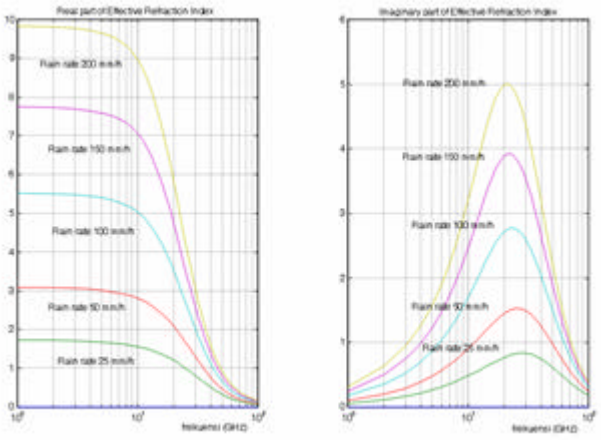

Figure 3. Results of complex refractive index of rain medium calculation

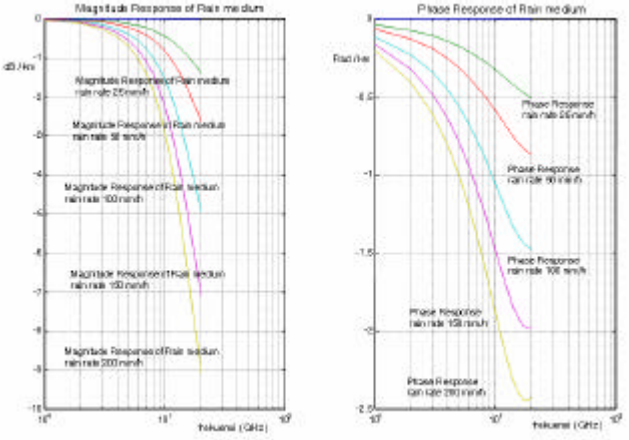

Figure 4. Results of Transfer function of rain medium calculation

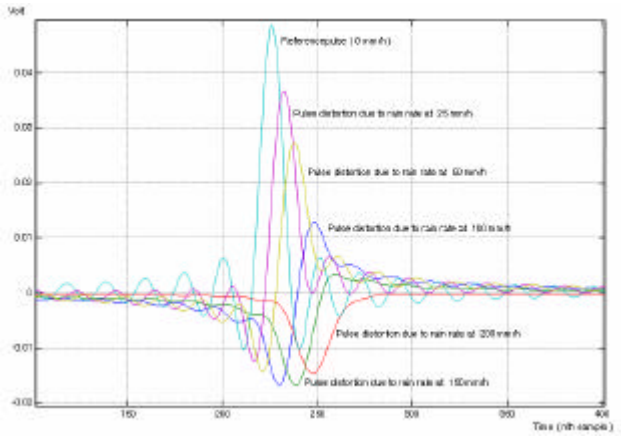

Figure 5. Impulses response of rain-filled medium for short pulse transmission

5. Experimental Setup of Tropical Outdoor UWB Propagation

5.1 Measurement System

The equipment used for the measurements is shown in Figure 6. The measurement setup consists of 13 GHz Vector Network Analyzer HP, an UWB antenna array , metal sheet as reference reflector and raingauge for measuring the rain intensity [5].

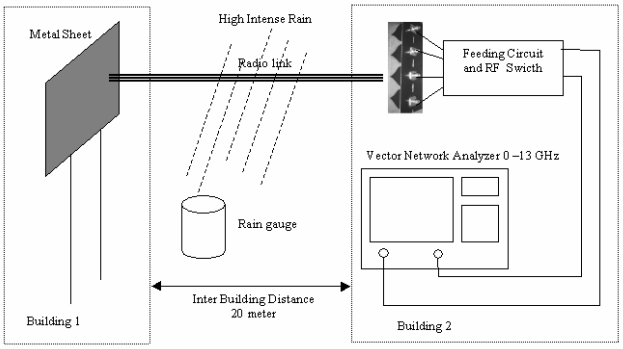

Figure 6. Measurement system of Tropical Outdoor UWB Propagation

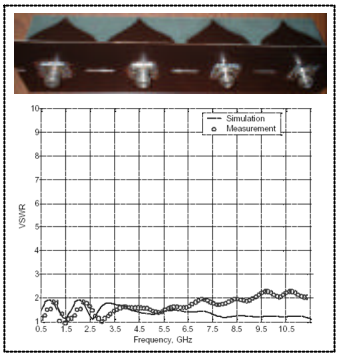

Figure 7 UWB Array using PICA elements their VSWR characteristics

The UWB antenna array is developed in our laboratory using Planar Inverted Cone Antenna (PICA) element which has bandwidth 0.5 – 11 GHz as shown in Figure 7. This UWB array has one transmitting antenna and three receiving antennas.

5.2 Measurement Environment

The test area is typical of the academics campus ITB Bandung, consisting of 4 – 6 Floors building, medium - high trees, and pedestrian roads. Bandung has $R_{0.01}$ 120 mm/h rain intensity and sometimes reach up to 200 mm/h as the highest rain intensity.

5.3 Experimental Procedure

Port 1 of VNA transmitting the sweep frequencies from 3.1 – 10.6 GHz to the Tx antenna, and then the metal sheet at other side building will reflect the VNA signal to three Rx antennas on Port2 of the VNA which will be recorded in three time series of received signals as complex numbers on PC. During rain event, the raingauge will record the rain intensity as a function of time and will be synchronized with propagation data.

5.4 Impulse Response of the Outdoor UWB channel

The frequency resolution of the VNA gave 2001 points of 3.1-10.6 GHz spectrum. The three complex numbers of propagation data then processed by Inverse Discrete Fourier Transform 2048 points for obtaining the impulse response of each Rx antenna after metal sheet and antenna deembedding. Example of impulse responses of the three Rx antenna during moderate rain intensity, 40 mm/h is depicted as figure 8 below :

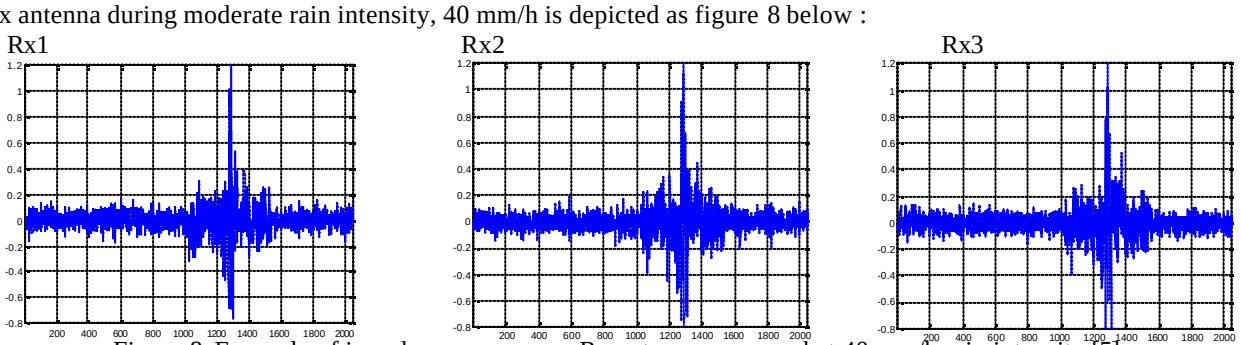

Figure 8. Example of impulse response per Rx antenna measured at 40 mm/h rain intensity [5]

The preliminary study indicates that the impulse response of outdoor UWB channel is depend on the rain intensity. More intense rain will degrade more the outdoor UWB channel. Figure 9 illustrates the variability of the impulse response on Rx2 antenna on different rain intensities :

Rx2, 20mm/h Rx2, 60 mm/h Rx2, 100 mm/h

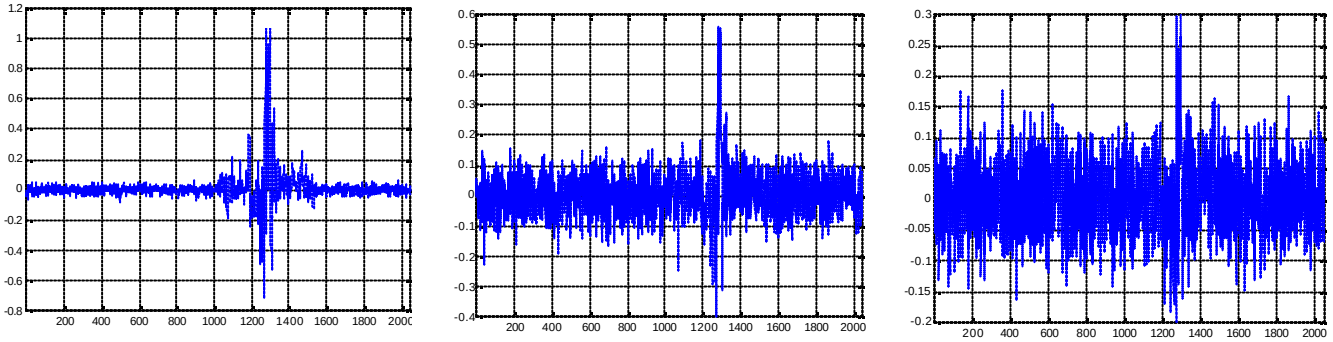

Figure 9. Example of impulse response of Rx2 antenna measured at several of rain intensities [5]

5.5 Pulse Transmission Performance on Tropical Outdoor UWB Channel

From figure 8 and 9, we can see that the rain will influence the outdoor UWB propagation. The higher rain intensity will degrade more the impulse response of the outdoor UWB channel due to frequency selective impacts on the spectrum. Therefore, during high intense rain, the raindrops modify the spectrum of UWB signals. This spectrum degradation will impact on pulse spreading of the transmitted monocycles in time domain and cause bit errors. Moreover, in the highest intense rain, the synchronization of UWB link will be lost due to high rain attenuation. Figure 7 below illustrate the performance degradation of pulse transmission over outdoor UWB channel during high intense rain (100 mm/h).

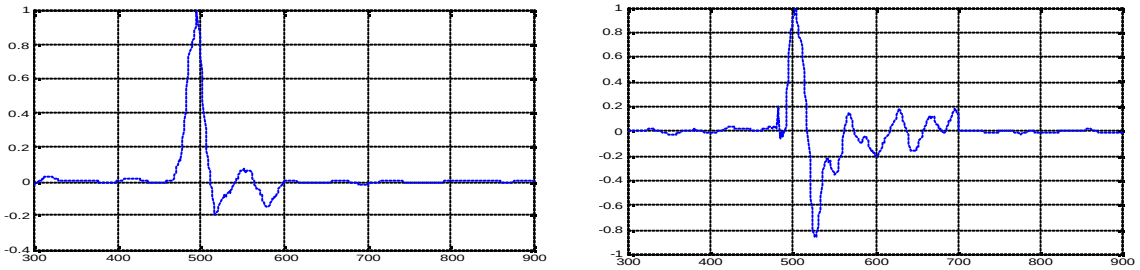

Figure 10. Pulse Transmission Performance during Rain event (left : no rain, right : high intense rainrate) [5]

6. Conclusions

We have reported the numerical analysis and experimental measurement of a tropical outdoor ultrawideband (UWB) characterizations for short pulse transmissions. Raindrops cause attenuation of radio waves by both absorption and scatter. Absorption involves dissipation of some of the energy of an electromagnetic wave as heat. Scatter involves diversion of some of the energy of the wave into directions other than the forward direction. These have given rise to the need of acquiring more detailed knowledge of interaction between raindrops and waves than is necessary for the calculation of attenuation by reviewing the detailed dielectric and microphysical properties of raindrops, such as shape, size distribution or the motion while they are falling. Our preliminary study, both numerical and experimental results concluded that the rain-fill medium modify the spectrum of UWB signals . This spectrum degradation will impact on pulse spreading of the transmitted monocycles in time domain and cause bit errors.

REFERENCES

[1]. T Oguchi, “Electromagnetic Wave Propagation and Scattering in Rain and Other Hydrometeors”,Proceeding of IEEE, September 1983

[2]. Warren L. Flock, “Propagation Effects on Satellite Systems as Frequencies Below 10 GHz”, NASA Reference Publication 1102(02) 1987

[3]. Christian Matzler, “Effect of Rain on Propagation, Absorption and Scattering of Microwave Radiation based on the Dielectric Model of Liebe”, Institute of Applied Physics, University of Bern, June 2002

[4]. Joko Suryana, “Simulation of Tropical Outdoor UWB Channel for Short Pulse Transmission”, Second years of PhD Progress report, STEI-ITB, 2006

[5]. Joko Suryana et.al, “Characterization of Outdoor UWB Channels for Inter Building Communication Links Application on High Intense Rain Area”, Proceeding of WPMC 2005, Aalborg, 2005

Frequency extrapolation in terrestrial microwave propagation simulations

M. Grabner and V. Kvicera
Department of Microwave Communications, TESTCOM, Czech Republic

Abstract—Electromagnetic wave propagation in clear air troposphere can be simulated by means of the parabolic equation method. This method gives only a single frequency response. Therefore, computationally expensive repeated simulations are needed for wideband propagation channel assessment. In order to speed the computation of the channel transfer function up, frequency extrapolation methods can be used. An application of the frequency extrapolation method suitable for terrestrial propagation simulations is presented in the paper. A complex received signal is modelled using the weighted sum of complex exponentials. The extrapolation method utilizes several single frequency responses calculated by the parabolic equation method in the examined frequency band. Complex exponential model parameters are extracted by means of the matrix pencil method. An extracted model is applied to calculate a wideband frequency transfer function of the microwave tropospheric channel that is impaired by an inhomogeneous refractivity distribution between the transmitter and receiver. Numerical examples of the application of the method are introduced. Results are compared with the channel transfer function obtained from repeated parabolic equation simulations. Computational cost of both methods is compared. Robustness of the extrapolation method as well as optimal selection of a model order and frequency points used for model extraction are discussed.

1. Introduction

Wideband terrestrial microwave communications are of growing importance today. Quality and availability of terrestrial microwave communication systems are affected by propagation characteristics of the tropospheric channel. Electromagnetic wave propagation in clear air troposphere (i.e. without influence of hydrometeors) can be simulated by means of the parabolic equation method (PEM) [3]. This full wave method gives only a single frequency solution. Repeated PEM simulations are needed in order to assess propagation channel characteristics in a wide frequency range [2]. In order to make the computation of a channel transfer function faster, a frequency extrapolation method can be used.

An application of the frequency extrapolation method suitable for terrestrial propagation simulations is presented in this paper. A complex received signal is modelled as the weighted sum of complex exponentials. This model is naturally related to physics of clear-air multipath propagation where several waves coming from different directions with different time delays [1] interfere at the receiver site. Complex exponential model parameters are extracted by means of the matrix pencil method (MPM) [4]. The method uses several single frequency responses calculated by the PEM method in the frequency band under study. An extracted model is then applied to calculate a wideband frequency transfer function of the microwave tropospheric channel that is impaired by an inhomogeneous refractivity distribution between the transmitter and receiver.

A channel model and implementation details of estimation of its parameters are outlined in Section 2. Numerical examples of the application of the method are introduced in Section 3. Results are compared with the channel transfer functions computed by repeated PEM simulations. Computational cost of both methods is compared. Robustness of the extrapolation method is discussed as well as selection of a model order and frequency points used for model extraction.

2. Channel Model and Estimation

2.1 Propagation Model and Matrix Pencil Method Overview

Propagation through the tropospheric channel may result in fading due to multipath. Frequency domain representation of the channel transfer function can be expressed as:

$$H(\mathrm{j}\omega) = \sum_{m=1}^{M} a_m \mathrm{e}^{-\mathrm{j}\omega\tau_m}, \tag{1}$$

where M is the number of multipath signals generated by the channel, a_m is the amplitude of the m-th component and τ_m is the corresponding time delay. If the transfer function is sampled in a frequency domain, the equation

(1) can be rewriten as:

$$H_k = H(\mathrm{j}2\pi k\Delta f) = \sum_{m=1}^{M} a_m z_m^k, \quad k = 0, \ldots, N-1, \tag{2}$$

where $z_m = \mathrm{e}^{-\mathrm{j}2\pi\Delta f \tau_m}$ and Δf denotes a sampling interval in a frequency domain. The channel transfer function (1) is to be found by estimating model parameters M, a_m, z_m.

The model parameters are extracted by the matrix pencil algorithm. Let us consider that the transfer function in the frequency range $f \in \langle f_{min}, f_{max}\rangle$ is to be described. N frequency points H_k (see eq. (2)) regularly spaced in the band with the sampling interval $\Delta f = \frac{f_{max}-f_{min}}{N-1}$ are input parameters of the algorithm. These values are obtained by means of the PEM simulation in our application. The following matrices are formed using these values:

$$\mathbf{X_1} = \begin{bmatrix} H_0 & \cdots & H_{L-1} \\ \vdots & \ddots & \vdots \\ H_{N-L-1} & \cdots & H_{N-2} \end{bmatrix}_{(N-L)\times L}, \qquad \mathbf{X_2} = \begin{bmatrix} H_1 & \cdots & H_L \\ \vdots & \ddots & \vdots \\ H_{N-L} & \cdots & H_{N-1} \end{bmatrix}_{(N-L)\times L}, \tag{3}$$

where L, for which $M \le L \le N - M$, is the MPM method parameter. It can be shown [4] that z_m are the eigenvalues of the generalized eigenvalue problem:

$$\det\left(\mathbf{X_2} - \lambda\mathbf{X_1}\right)) = 0. \tag{4}$$

Since $2M$ independent model parameters are to be found from N input values, it should be $M \le N/2$. The selection of N and consequently of M, which represents a number of multipath components, is related to propagation path geometry and requires some care as will be demostrated in the following section. Finally, after M and z_m are known, amplitudes a_m are solved from least square problem:

$$\begin{bmatrix} z_1^0 & \cdots & z_M^0 \\ \vdots & \ddots & \vdots \\ z_1^{N-1} & \cdots & z_M^{N-1} \end{bmatrix} \begin{bmatrix} a_1 \\ \vdots \\ a_M \end{bmatrix} = \begin{bmatrix} H_0 \\ \vdots \\ H_{N-1} \end{bmatrix}. \tag{5}$$

2.2 Implementation details

An important step in the described procedure is the estimation of parameters M and N. It relates to the way, how the extracted model is actually used. The MPM method is often understood as an *extrapolation* method. In our application, it means that an identified exponential model (2) is applied to get a transfer function outside the interval $\langle f_{min}, f_{max}\rangle$ so that the values H_k for the integers $k > N-1$ are calculated. This approach is usually presented in the papers on MPM. However numerical experiments show that an extrapolation error may rise rapidly outside the $\langle f_{min}, f_{max}\rangle$ band so that the results are not usable. An example of such a case is given in Figure 1. Real data obtained from the PEM simulation of a 50 km long link with multipath is used. A good fit is achieved in the first 1 GHz band, however the transfer function extrapolated to the frequency of 2 GHz diverges.

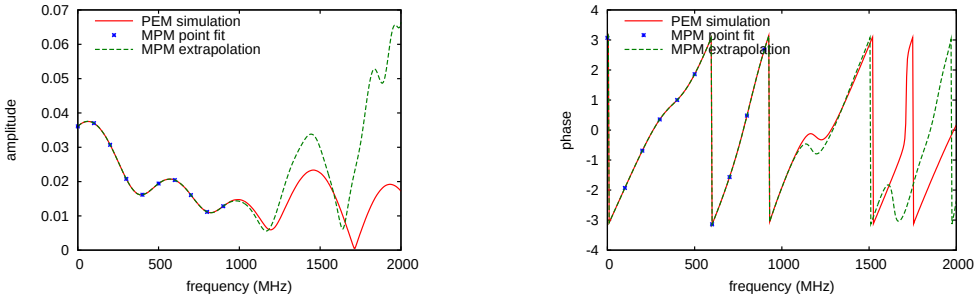

Figure 1: MPM frequency extrapolation example. ($N = 10, M = 5, \Delta f = 100\,\mathrm{MHz}$)

The interpolation of the transfer function between interpolated points is more robust approach than extrapolation as it is seen from the example above. However, in this case, a sampling interval should be chosen as

large as possible to obtain any significant computational advantage. In other words, the interval Δf should be maximized in order to have minimum interpolated points within the $\langle f_{min}, f_{max}\rangle$ band. Two criteria go against this requirement. First, $M(= N/2)$ should be a number of multipath components. Second, Δf have to fulfil the sampling theorem for the function (1). The first criterion is obvious, but the second one is not being mentioned in the context of MPM. Maybe it is because the second criterion is not necessary to get an exact fit in interpolated points, but it is necessary in order to obtain a right function in between these points. From equation (1) that is a sum of periodic functions, one can see that the higher value of the largest τ_m, which stands there as a "frequency" of the "fastest" component of the function $H(\mathrm{j}\omega)$, the lower Δf required and consequently higher N is needed. Written explicitly:

$$\Delta f \leq \min_m \left(\frac{1}{2\tau_m}\right). \tag{6}$$

The equation (6) is very restrictive if long range propagation is concerned with. For example, the time delay of a direct wave signal on a 50 km long path is about $\tau = \frac{50000}{c} = 0.17\,\mathrm{ms}$ which corresponds to $\Delta f = 3000\,\mathrm{Hz}$ only. However, the main time delay τ_0 due to a propagation range can be extracted from the transfer function as follows:

$$H(\mathrm{j}\omega) = \mathrm{e}^{-\mathrm{j}\omega\tau_0} K(\mathrm{j}\omega), \quad K(\mathrm{j}\omega) = \sum_{m=1}^{M} a_m \mathrm{e}^{-\mathrm{j}\omega\Delta\tau_m}, \quad \Delta\tau_m = \tau_m - \tau_0, \tag{7}$$

where the main delay τ_0 is calculated from the distance d of the transmitter and receiver and the light speed c as $\tau_0 = \frac{d}{c}$. The reduced transfer function $K(\mathrm{j}\omega)$ depends only on the differences $\Delta\tau_m$. It can be concluded that $\Delta\tau_m \ll \tau_0$ from the physical background of multipath propagation on terrestrial paths. It means that required Δf is much higher for model identification of $K(\mathrm{j}\omega)$. Finally, note that the order value of time delays $\Delta\tau_m$ can be estimated from the spherical earth reflection geometry which gives $\Delta\tau \approx \frac{2h_1h_2}{cd}$, where h_1, h_2 are heights of the trasmitter and receiver above the smooth earth surface, d is the distance between them and c denotes the light speed again. This information may be useful when the propagation above a well (or perfectly) reflecting terrain is investigated, however it typically gives a pessimistic estimate in practical propagation scenarios.

3. Examples

In this section, a numerical example of the algorithm application is presented. The PEM simulations for several frequencies are made and the MPM method is applied to extract the transfer function model. In Figure 2, the example of the coverage diagram calculated using PEM is shown. An elevated ducting layer above the transmitter causes multipath propagation towards the receiver which is located in the same altitude as the transmitter. A frequency band under study is from 3 to 5 GHz.

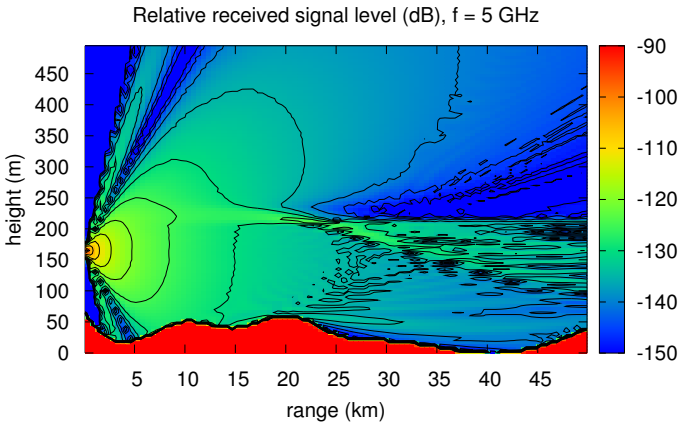

Figure 2: Microwave propagation on terrestrial path with elevated ducting layer located 40 meters above transmitter. (PEM simulation, 5 dB contour levels)

Based on the previous discussion about the selection of M and N, an iterative procedure was implemented. In the procedure, the sampling Δf is halved in every step until the fit within all the band is reached. It is sufficient to check the fit in two randomly selected subintervals, i.e. in the center between the interpolated

points from the last made step. An additional computational cost is reduced by this way, because only two redundant PEM simulations (two frequencies) are needed. Moreover, the method still stays robust. In Figure 3, two last steps of the procedure are shown. The most of calculation time is spent in the PEM simulations. One eigenvalue problem (4) and one least square problem (5) are solved in every step. In this particular example, iterations stop long before large and intractable matrix dimensions arise. It should be note, however, that algorithm efficiency also depends on the bandwidth $f_{max} - f_{min}$. In Figure 3, the PEM simulation is made with the sampling interval of 5 MHz, on the other hand the MPM procedure uses only values with the sampling interval of 100 MHz. It means the exact transfer function is calculated twenty times faster.

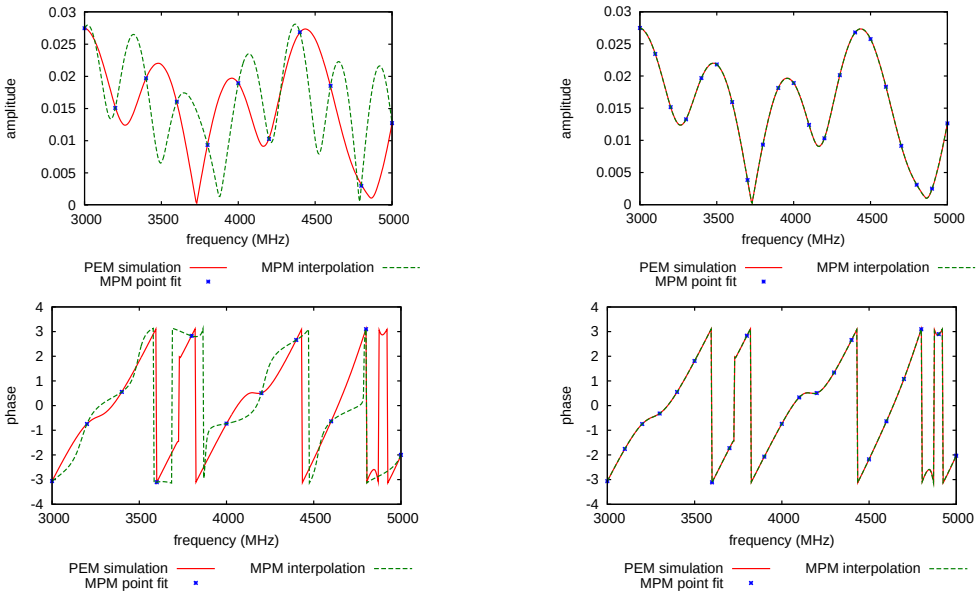

Figure 3: Estimation of channel transfer function. Second last (left, $M = 5, N = 11$) and last (right, $M = 10, N = 21$) step of iterative MPM procedure.

4. Conclusion

An application of the MPM method for the fast assessment of a wideband transfer function in terrestrial propagation simulations was presented. An iterative interpolation procedure was introduced which makes the transfer function computation more efficient on one hand and preserves robustness on the other hand. It was demostrated by the example that the method is applicable in practical propagation scenarios.

Acknowledgment

This work was supported by the Ministry of Informatics of the Czech Republic under the research project MI0 0000346806.

REFERENCES

1. Dharamdial, N., Adve, R., Farha, R., "Multipath delay estimations using matrix pencil," *IEEE Wireless Communications and Networking Conference*, New Orleans, 2003.
2. Gingras, D. F., Gerstoft, P., "The effect of propagation on wide band DS-CDMA systems in the suburban environment," *IEEE Signal Processing Workshop on Signal Processing Advances in Wireless Communications*, Paris, 1997.
3. Levi, M., *Parabolic Equation Methods for Electromagnetic Wave Propagation*, The Institution of Electrical Engineers, London, 2002.
4. Sarkar, T. K., Pereira, O., "Using the matrix pencil method to estimate the parameters of a sum of complex exponentials," *IEEE Antennas Propag*, Vol. 37, No. 1, 48–55, 1995.

Integrated Microstrip Feed Network for Phased Array Antennas

Sharif I Sheikh
EE department, K. F. University of Petroleum & Minerals (KFUPM),
Dhahran 31261, Saudi Arabia
E-mail: sheikhsi@kfupm.edu.sa

Abstract: Ferromagnetic material is widely used to realize the phase shift section of a phased array antenna. In this paper, the performance of a microstrip array feeder with integrated phase-shifter, designed on a transversely magnetized ferrite substrate, is described. Calculated differential phase shift and its tuning properties are presented and compared with the results obtained from a commercial CAD tool. The simulated reflection and transmission response of the integrated array feeder is corroborated by experimental data.

Introduction: Ferrite phase shifters are traditionally used to control the radiation properties of phased array antennas. Due to the recent availability of low loss and commercially viable microwave ferrites, there is an increasing interest in the performance of printed antennas on ferrite substrate. When immerged in an biasing magnetic field, ferrite substrates offer greater agility in controlling the beam steering and pattern shaping characteristics of the microstrip array antennas [1,2]. The high dielectric constant of the ferrite brings about a reduction in the antenna dimension [3] and the inherent anisotropy and non-reciprocal behavior of this media is often used to achieve frequency tuning and polarization diversity [4]. In this paper, a microstrip array feeder network with integrated phase shifter is realized on a transversely magnetized planar ferrite substrate. Tunable progressive phase shift is produced by varying the magnetic bias that changes the permeability of ferrite material, which in turn changes the phase velocity and, hence, the insertion phase of the propagating microwave signal. Analytical methods are used to calculate the tunable differential phase shift properties of the planar phase shifter. The four-way array feeder is implemented using Wilkinson type power splitter to improve the isolation and matching of the ports. A commercial CAD software is used to analyze the designed microstrip array feeder with integrated phase shifter. The simulated reflection and transmission responses are verified using experimental results.

Method of Analysis: Electromagnetic wave propagation in Parallel plate waveguide has long been used to study anisotropic microstrip structures [3]. Analytical method is used here to predict the phase shift properties of an externally magnetized ferrite filled parallel plate waveguide. In the presence of an external biasing magnetic field, the gyromagnetic behavior of ferrite material is described by its tensor permeability,

$$\left[\mu_r\right] = \begin{bmatrix} \mu & 0 & -j\kappa \\ 0 & 1 & 0 \\ j\kappa & 0 & \mu \end{bmatrix}$$

where,

$$\mu = 1 + \frac{\gamma^2 . H_0 . M}{\left(\gamma H_0\right)^2 - f^2}, \quad \kappa = \frac{\gamma . M . f}{\left(\gamma H_0\right)^2 - f^2}$$

and 'γ' is the gyromagnetic ratio, 'M' is the magnetization of the ferrite material, 'H_0' is externally applied bias field and 'f' is the frequency of the propagating microwave signal. Thus, for a lossless transversely (y-directed) magnetized ferrite filled parallel plate waveguide, substituting tensor permeability ($[\mu_r]$) into Maxwell's equation and imposing proper boundary conditions yields the following characteristic equation:

$$\frac{-\beta^2 + K_0^2 \varepsilon_r}{-\beta^2 + K_0^2 \mu \varepsilon_r} \left\{ -\beta^2 \mu + K_0^2 \mu \varepsilon_r . \mu_{eff} \right\} = \left\{ (2m+1) \frac{\pi}{d} \right\}^2 \qquad (1)$$

where, '$2d$' is the separation between plates, '$K_0 = \omega\sqrt{(\mu_0\varepsilon_0)}$', '$\mu_{eff}=(\mu^2-\kappa^2)/\mu$' and '$m$' determines the mode of operation. The solution of equation (1) is plotted in figure 1 in terms of phase-constant (β) and external biasing magnetic field (*in mT*). Note the sharp changes in the insertion phase near the resonance region, where β can be tuned significantly by slightly varying the biasing field. A simulated phase constant of the structure is also plotted in this figure to validate the CAD model. Figure 2 shows the ferrite based

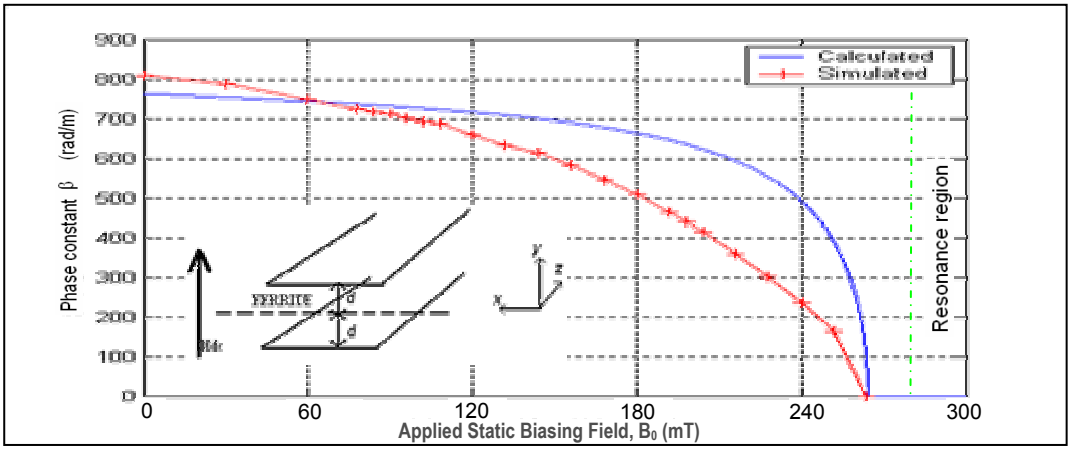

Fig 1. Phase constant (β) versus transversely applied magnetic field (B_0) plot for a planar transmission line with magnetized ferrite (YIG-G113) substrate at f=10GHz. (M_s=*140 KA/m,* ε_r=*14 , d=0.2mm*)

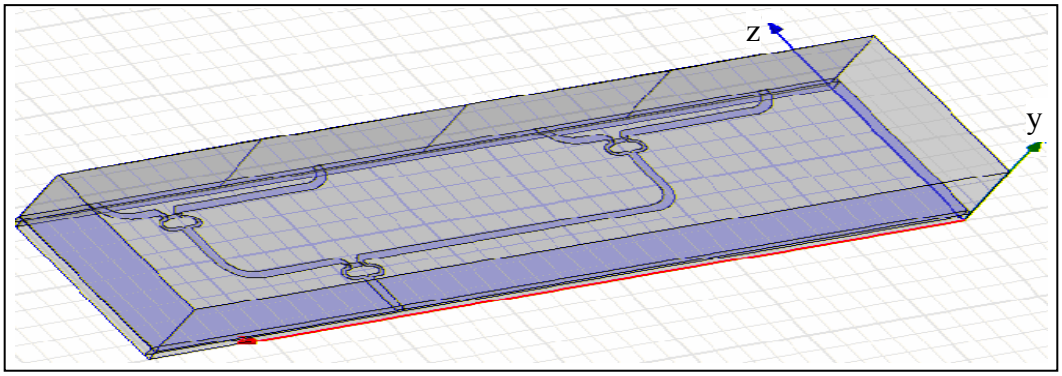

Fig 2. The designed ferrite based microstrip four-way array feeder (*Wilkinson type*) with integrated phase shifter

microstrip four-way power divider with integrated phase shifter. This structure is designed to provide a progressive phase shift of 360° for unbiased (H_0=0 mT) case. This phase shift value is selected to provide space (in the x-axis direction) for realizing radiating patches and the separation between patches. By varying the external biasing field (H_0), the progressive phase shift can be tuned in the same manner as shown in figure 1. The reflection and transmission responses of this structure, obtained by using a commercial CAD tool, are shown in figure 3. Note that the transmitted signals in different output ports have different magnitudes. This property of the ferrite substrate can be exploited to design the integrated feed network of a non-uniform phased array antenna. The simulated responses also exhibited that the remaining reflection (S_{22}, S_{33}, S_{44}) and isolation (S_{32}, S_{23}, S_{54}, S_{45}) responses of this structure remains well below -20dB. Figure 4 shows the superimposed plot of the simulated and experimentally observed reflection responses of the integrated array feeder. The fabricate device is also shown in this figure.

Conclusion: The tunable insertion phase property of a transversely magnetized planar ferrite phase shifter is investigated. Steep phase variation is observed near ferromagnetic resonance region, where small

change in the magnetic bias produces sharp changes in the differential phase shift. The response of the designed ferrite based microstrip array feeder with integrated phase shifter is observed. Acceptable power division and differential phase shift properties of the feed network are demonstrated.

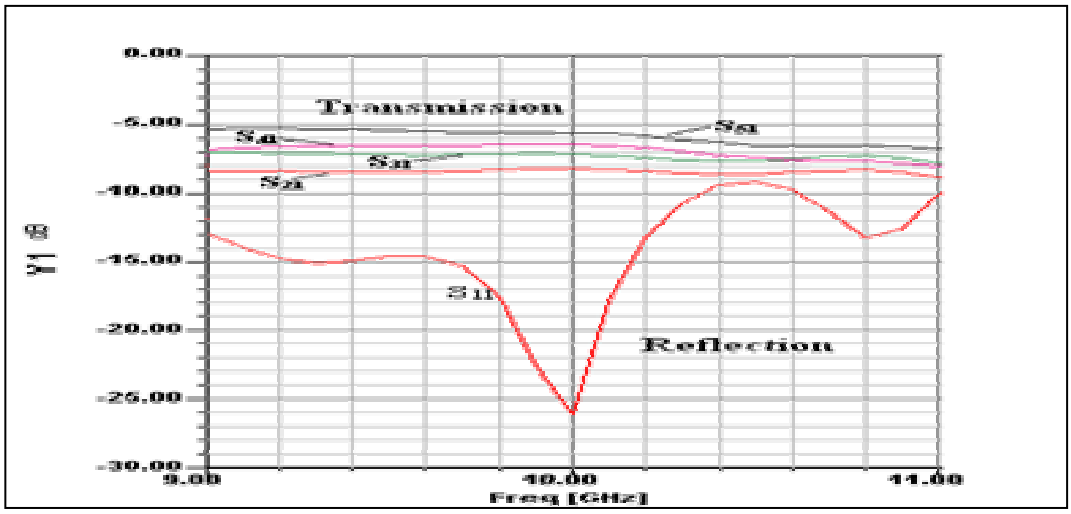

Fig 3. Transmission and reflection S-parameter curves for four-port power-divider with transversely magnetized ferrite (YIG-G113) substrate (M_s=140 KA/m, ε_r=14 , d=0.5mm)

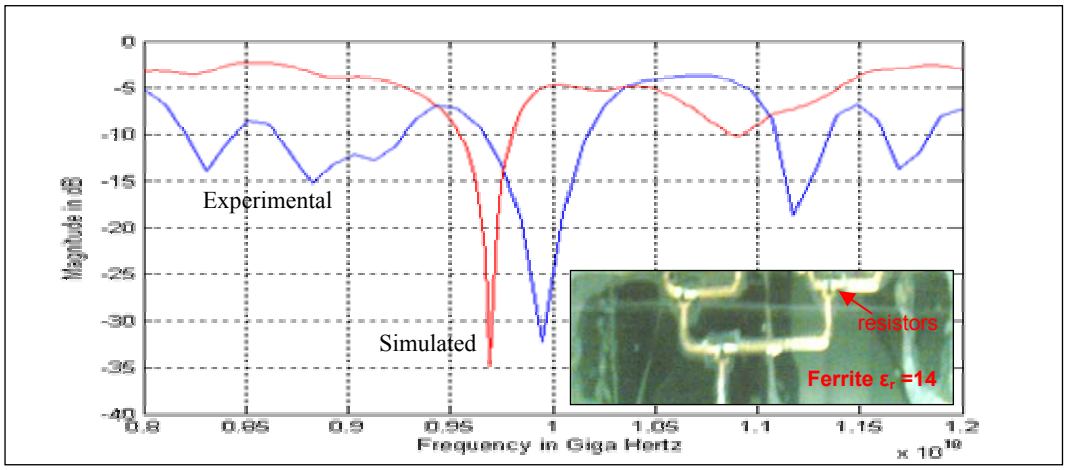

Fig 4. Comparison of simulated and experimental reflection responses (S_{11}) of a transversely magnetized ferrite based four-way power-divider with integrated phase-shifter. Fabricated device is also shown.

Acknoledgement: The author is grateful to King Fahd University of Petroleum & Minerals (KFUPM) and Mr, Mir Riyaz Ali for the support during the research work.

Reference:

[1] J.C. Batchelor, *et all*, "Scanned Microstrip Arrays Using Simple Integrated Ferrite Phase Shifters", IEE Proc. Microwave Antennas Propagation, Vol. 147, No.3, PP 237-241, June 2000

[2] A. Henderson and J.R. James, "Magnetized microstrip antenna with pattern control", Electronics Letter, Vol. 24, No.1, pp.45-47, 1988.

[3] D.M. Pozar, "Radiation and scattering characteristics of microstrip antennas on normally biased ferrite substrates", IEEE Trans. Antennas Propagation, Vol. AP-40, No. 9, pp. 1084-1092, 1992.

[4] P.J. Rainville and F.J.Harackiewiz, "Magnetic tuning of a microstrip patch antenna fabricated on a ferrite file", IEEE Microwave and Guided Wave Letters, Vol. 2, pp. 483-485, 1992.

CAVITY ANTENNA WITH PARTLY TRANSPARENT APERTURE FOR WIRELESS COMMUNICATIONS

N. I. Voytovich[(1)], A. V. Ershov[(1)], N. N. Repin[(2)], A. N. Sokolov[(3)]

[(1)]Design and Production of Radioequipment sub-faculty, Southern Ural State University, 76 Lenin Avenue, Chelyabinsk, 454080, Russia; E-mail: vni@chel.surnet.ru

[(2)]Nauchno-Issledovatelsky Institut po Izmeritelnoi Tekhnike, Open Corporation, 4 Vitebskaya Str., Chelyabinsk, 454080, Russia; E-mail: rnn17@mail.ru

[(3)]Radiophysics and electronics sub-faculty, Chelyabinsk State University, 129 Brat'ya Kashiriny Str., Chelyabinsk, 454021, Russia; E-mail: sokolov@csu.ru

ABSTRACT

The paper is devoted to the property analysis of a cavity antenna with a partially transparent wall. Cavity antenna with radiators in the form of rectangular openings on the cavity wide wall is excited by a stripline through the coupling opening bounded in perimeter by metal pin system shorting out the stripline screens. Cavity antenna has a so-called "short" structure (the distance between two wide walls of the cavity resonator is close to a half wave length) which allows to reach noticeable reduction of antenna dimensions. These advantages of cavity antennas with partly transparent aperture are attractive for external antennas designing for wireless communications.

INTRODUCTION

Cavity antennas with partly transparent aperture are known since the first part of the 20th century. Cavity antennas are more like three-dimensional cavity resonators. A basic electromagnetic mode H_{101} is excited inside the cavity. A multitude of small openings (slots or round holes) are made on one the metal cavity walls. Thus, the cavity antenna can also be considered as an antenna array. There is a critical review of the works on microwave cavity antennas in the [1]. It has been done since the 1950s for benefit of engineers and scientists in the fields of antennas and communication engineering. Known cavity antennas are excited by one a slot at the end of the waveguide. This paper presents cavity antennas with relatively big openings on one the metal cavity walls. Cavity antennas are excited by more than one of the slots. It is the author's opinion that cavity antenna is at an advantage. It has the selectivity, it has a good solidity, it has very simple excitation. These advantages of cavity antennas with partly transparent aperture are attractive for external antennas designing. Such antennas are good for high-speed wireless communication systems "point to point".

ANTENNA PHYSICAL ANALOGUE

Cavity antenna (fig.1,2) is a metal resonator 2 with dimensions a_2 x b_2 x H, the height H of which is close to half wavelength λ and cross sizes a_2 and b_2 are several λ. The resonator upper wide wall of thickness D arranged between the planes M_3 and M_4 has a system of K_0 radiating openings 5 with dimensions l_p x t_p ($p = 1,\ldots, K_0$) and separates the antenna from the half-space 3 by which an area external to the antenna is simulated. Through the coupling opening 4 with dimensions l_0 x t_0 in the low wall of thickness d arranged between the planes M_1 and M_2 the cavity antenna is excited by a stripline. Area 1 bounded by the stripline screens is considered as a transmission resonator with dimensions a_1 x b_1 x h, the height h of which is considerably less than λ. In middle of the region 1 ($z = h/2$) an infinitely thin strip of length L and width w is placed. Metal pins E_2 with radius ρ are arranged around the coupling opening 4 at points x_p, y_p ($p = 1,\ldots, K_2$, K_2 – pin number) and close the stripline screens (pins have not shown on fig.2). It is supposed that the strip width $w << \lambda$ and $\rho << \lambda$. An electromagnetic wave source is arranged on the transmission resonator side wall at the strip bottom. All cavity antenna and the stripline spaces are filled by a perfect dielectric and metal surfaces have infinite conductance.

STATEMENT AND SOLUTION OF ELECTRODYNAMIC PROBLEM

Within the scope of the antenna physical model a general electromagnetic problem is formed for a number of regions coupled electromagnetically through opening apertures. For the problem definition the method of equivalent currents is used which supposes that all regions are closed and structural components and opening apertures are taken into account

by the action of the corresponding equivalent currents. The equality to zero of tangential components of the electric field $\dot{\vec{E}}$ on the strip surface, the pins and the continuity of a tangential component of the magnetic field $\dot{\vec{H}}$ with transition from one region to another in the planes $M_1 - M_4$ (fig.1) are used.

As a result a system of integral equations is received relative to unknown distributions of electric currents on the strip $\dot{\vec{J}}^{E_1}$, the pins $\dot{\vec{J}}_q^{E_2}$ ($q = 1,\ldots, K_2$) and of magnetic currents on apertures of the coupling opening $\dot{\vec{J}}^{M_1}$, $\dot{\vec{J}}^{M_2}$ and radiating ones $\dot{\vec{J}}_q^{M_3}$, $\dot{\vec{J}}_q^{M_4}$ ($q = 1,\ldots, K_0$), in particular:

on the strip:
$$\dot{\vec{E}}_0^1\left\{\dot{\vec{J}}^{E_1}\right\}+\sum_{q=1}^{K_2}\dot{\vec{E}}_0^1\left\{\dot{\vec{J}}_q^{E_2}\right\}+\dot{\vec{E}}_0^1\left\{\dot{\vec{J}}^{M_1}\right\}=-\dot{\vec{E}}_0^s, \quad (1)$$

on the pins:
$$\dot{\vec{E}}_p^1\left\{\dot{\vec{J}}^{E_1}\right\}+\sum_{q=1}^{K_2}\dot{\vec{E}}_p^1\left\{\dot{\vec{J}}_q^{E_2}\right\}+\dot{\vec{E}}_p^1\left\{\dot{\vec{J}}^{M_1}\right\}=0,\ p=1,\ldots,K_2, \quad (2)$$

on the M_1:
$$\dot{\vec{H}}^1\left\{\dot{\vec{J}}^{E_1}\right\}+\sum_{q=1}^{K_2}\dot{\vec{H}}^1\left\{\dot{\vec{J}}_q^{E_2}\right\}+\dot{\vec{H}}^1\left\{\dot{\vec{J}}^{M_1}\right\}=\dot{\vec{H}}^4\left\{-\dot{\vec{J}}^{M_1}\right\}+\dot{\vec{H}}^4\left\{\dot{\vec{J}}^{M_2}\right\}, \quad (3)$$

on the M_2:
$$\dot{\vec{H}}^4\left\{-\dot{\vec{J}}^{M_1}\right\}+\dot{\vec{H}}^4\left\{\dot{\vec{J}}^{M_2}\right\}=\dot{\vec{H}}^2\left\{-\dot{\vec{J}}^{M_2}\right\}+\sum_{q=1}^{K_0}\dot{\vec{H}}^2\left\{\dot{\vec{J}}_q^{M_3}\right\}, \quad (4)$$

on the M_3:
$$\dot{\vec{H}}_p^2\left\{-\dot{\vec{J}}^{M_2}\right\}+\sum_{q=1}^{K_0}\dot{\vec{H}}_p^2\left\{\dot{\vec{J}}_q^{M_3}\right\}=\dot{\vec{H}}_p^{5p}\left\{-\dot{\vec{J}}_p^{M_3}\right\}+\dot{\vec{H}}_p^{5p}\left\{\dot{\vec{J}}_p^{M_4}\right\},\ p=1,\ldots,K_0, \quad (5)$$

on the M_4:
$$\dot{\vec{H}}_p^{5p}\left\{-\dot{\vec{J}}_p^{M_3}\right\}+\dot{\vec{H}}_p^{5p}\left\{\dot{\vec{J}}_p^{M_4}\right\}=\sum_{q=1}^{K_0}\dot{\vec{H}}_p^3\left\{-\dot{\vec{J}}_q^{M_4}\right\},\ p=1,\ldots,K_0, \quad (6)$$

$\dot{\vec{E}}_0^s$ – electric field intensity of outer source, the upper index of electric and magnetic field vectors indicating a region for which the corresponding characteristic is written; by "5*p*" *p*-th subregion of the fifth region is indicated.

Electric and magnetic fields are solved with Green tensor function usage. Galerkin method is used for the integral equation system solution. Fourier basis is used for definition of basic (test) functions on the strip and opening apertures. Then according to Galerkin method the procedure of integral equation system transformation into linear algebraic equation system is performed: $A \cdot I = V$, where I is a column of amplitude coefficients defining electric field on the strip, pins and magnetic field on opening apertures, V – a column of exciting voltage amplitudes (outer sources), A – a equivalent current interaction. As a result antenna numerical model is received. Standard approach to matrix equation solution is used.

NUMERICAL AND EXPERIMENTAL RESULTS

Numerical and experimental results have got for the antennas with one, two (fig. 3) and four (fig. 4) excited slots. The slots on fig. 3 have in-phase excitation. The antenna has got of linear polarization. The slots on fig. 4 have quadrature feed. The antenna has got of circular polarization. It is shown that the openings on the wide wall must be arranged so that the array spacing of the radiating openings placed in N number along each side of the resonator upper wide wall was equal to N-th part of this wall side length. In this case the directivity frequency response has maximum width. It is shown that for antenna excitation it is preferably to use two coupling openings arranged symmetrically at a distance of a quarter of the wide wall from the cavity center (fig.3). Antenna directivity graphs are given in fig. 5 in frequency range according to the resonator height H. Antenna ($a_2 = b_2$ =194 mm, a = 24.8 mm, K_0 = 8 x 8) is excited by two coupling openings. Directivity versus frequency relationship graphs (fig.5) is identical in the form to (tuned) circuit resonance curve. Maximum directivity is reached at the resonator height less than half wavelength. It is explained by the fact that the perforated wall has inductive character. With radiating openings dimension a_2, b_2 increase antenna resonance frequency decreases. With radiating openings dimension D increase directivity maximum shift to lower frequencies. That can be explained by the penetration of the field connected with the resonator into the region of radiating openings and outer space. There is a good matching of experimental patterns and calculated patterns obtained by presented approach (fig.6). Measured VSWR of the antenna with two excited slots is less than 1.34 for 8% frequency width (fig.7).

CONCLUSION

Physical, mathematical, numerical and calculated models of an antenna array are designed with elements in the form of radiating openings on the wide wall of a multimode metal resonator operating as a distributing device. As applied to cavity antenna-stripline system an electrodynamic problem is solved on excitation by electric and magnetic currents of a number of regions coupled by opening apertures.

The laws of cavity antenna patterns, directivity and polarization characteristic behavior are defined in frequency range depending on the dimensions of the cavity resonator and the perforated wall. There is a good matching of experimental and calculated patterns. Presented antennas are good as external antennas for high-speed wireless communication point to point systems.

REFERENCES

1. Kumar A. and Hristov H. D., *Microwave cavity antennas*, Artech House, Norwood, MA, 1989.

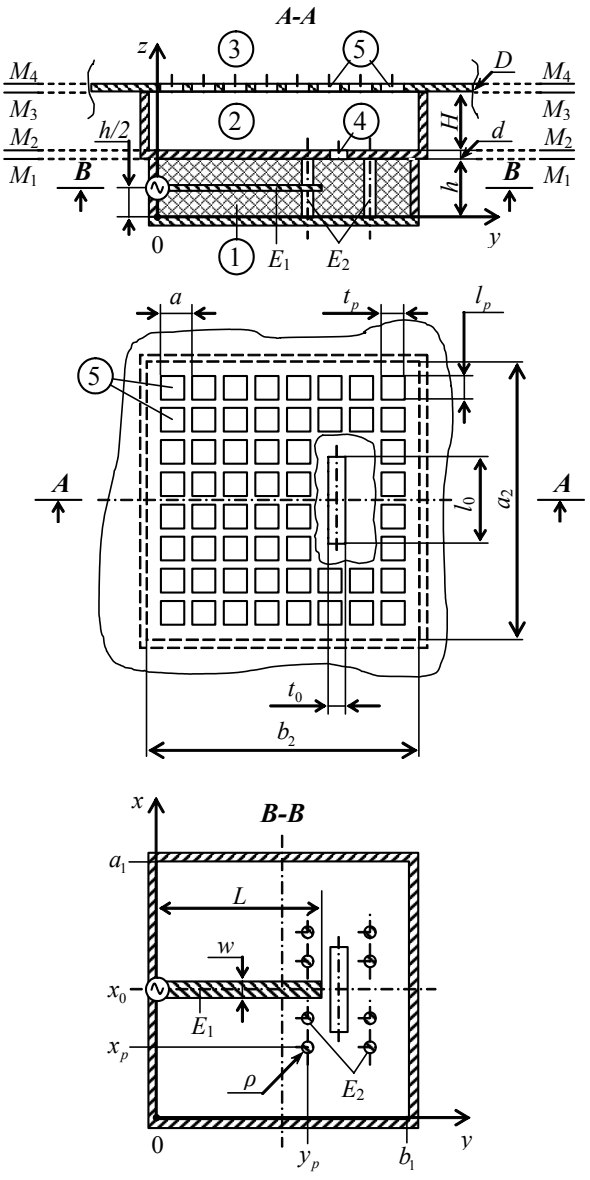

Figure1: Cavity antenna excited by a stripline.

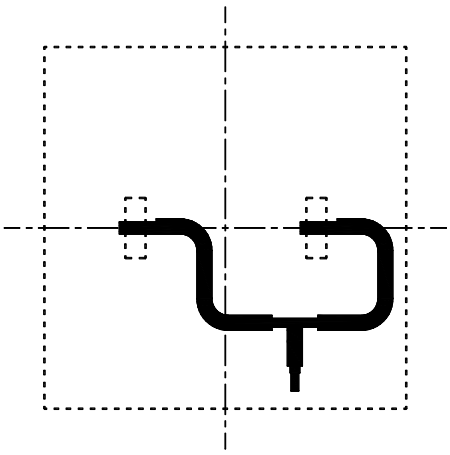

Figure 3: Power divider of the linear polarization antenna.

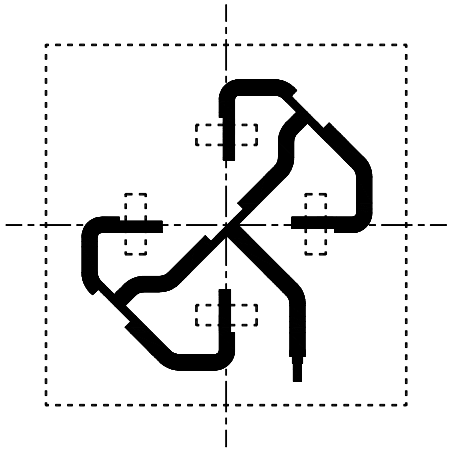

Figure 4: Power divider of the circular polarization antenna.

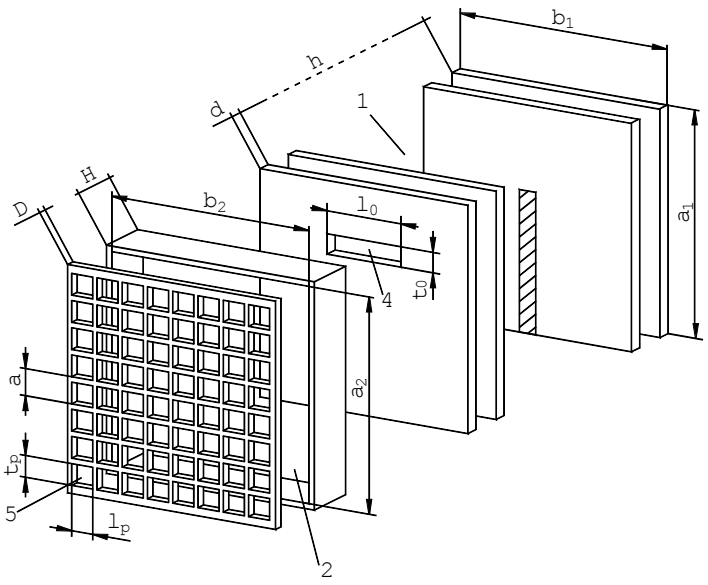

Figure 2: Cavity antenna with partly transparent aperture.

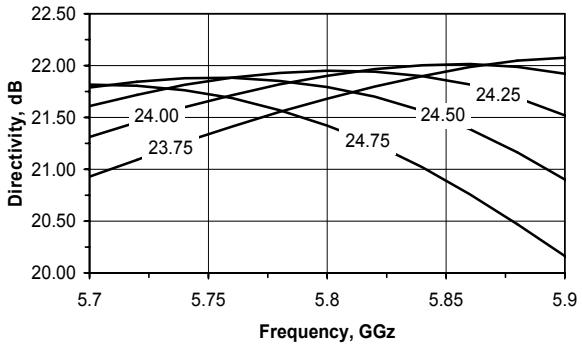

Figure 5: Cavity antenna directivity with different height of the resonator (mm).

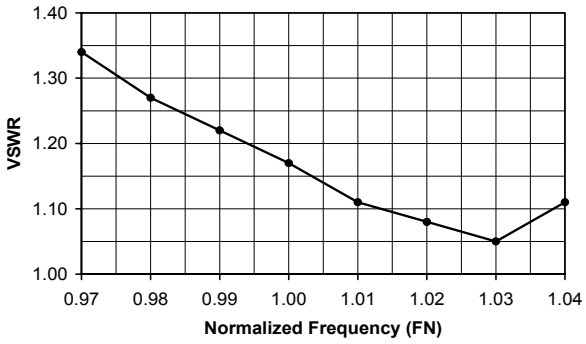

Figure 7: VSWR versus normalized frequency of antenna with one slot.

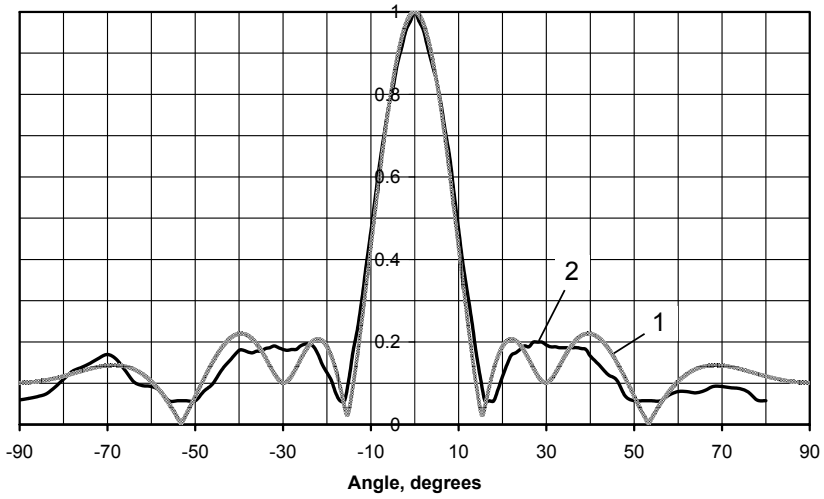

Figure 6: Calculated (1) and measured (2) patterns in *E*-plane.

Soil multi-scale roughness parameters and soil moisture retrieval from radar backscattering using a neural network technique

L Bennaceur Farah(1), I.R.Farah(2), R.Bennaceur(3), Z. Belhadj(1), and M. R.Boussema(1)
(1) Laboratoire de Télédétection et Systèmes d'Information à Référence Spatiale, ENIT, Tunisia
(2)Laboratoire de Recherche en Informatique Arabisée et Documentique Intégrée, ENSI, Tunisia
(3) Laboratoire de Physique de la Matière Condensée, FST, Tunisia

Abstract—The overall objective of this paper is to retrieve soil surfaces parameters namely, roughness and soil moisture related to the dielectric constant by inverting the radar backscattered signal from natural soil surfaces. Because the classical description of roughness using statistical parameters like the correlation length doesn't lead to satisfactory results to predict radar backscattering, we used a multi-scale roughness description using the wavelet transform and the Mallat algorithm. In this description, the surface is considered as a superposition of a finite number of one-dimensional Gaussian processes each one having a spatial scale. A second step in this study has consisted in adapting a direct model simulating radar backscattering namely the small perturbation model to this multi-scale surface description. We have investigated the impact of this description on radar backscattering through a sensitivity analysis of backscattering coefficient to the multi-scale roughness parameters. To perform the inversion of the small perturbation multi-scale scattering model (MLS SPM) we used a multi-layer neural network (NN) architecture trained by a backpropagation learning rule. The inversion leads to satisfactory results with a relative uncertainty of 8 percent.

1. Introduction

The retrieval of information related to physical surface parameters is a major objective of many studies in remote sensing investigations especially SAR applications. In that context, modeling radar backscattering through natural surfaces has become an important theme of research and active remote sensing has shown its utility for many applications in hydrology, geology and other fields[8][9][10].

Recent studies have shown that in natural conditions the agreement between experimental measurements and theoretical values is usually poor due to the large variability of the correlation function[3][4] and as a consequence tradtionnal backscattering models have often failed to predict correctly backscattering . In the context of S.A.R applications, Mattia and Al [1][2][4] have described one dimensional rough surfaces as band limited fractal random processes and studied the impact of this multi-scale description on radar backscattering. However, natural surface roughness changes from one direction to another and one-dimensional profiles are then insufficient. Thus, bi-dimensional profiles are required to describe more adequately natural surfaces. In this paper, we propose a theoretical modeling approach using the small perturbation model to describe radar backscattering on multi-scale bi-dimensional surfaces.

Extracting soil moisture and roughness parameters of natural surfaces from remotely sensed data is problematic for many reasons. In fact, many previous studies have dealt with model-based retrieval algorithm and have encountered many problems like the lack of information about the characteristics of natural surface roughness as well as the range of roughness parameters to use in one hand. In another hand, the uncertainties concerning the validity of the scattering models when applied to natural roughness conditions reduces the accuracy of the retrieval procedure. In addition, the relation-ship between the backscattering coefficient is non linear and the problem of retrieving parameters may be ill-posed and it may be not possible to separate the contributions from different mechanisms making the retrieval of several parameters simultaneously necessary.

We propose in this paper a neural network based inversion procedure using a multi-layer neural network (NN) architecture trained by a backpropagation learning rule.

2. Characteristics of natural surface roughness

The weakness of the classical description of natural surfaces is the large spatial variability which affects the correlation function and make classical roughness parameters very variable [1][2]. In that context, many

previous works have suggested that natural surfaces are better described as self affine random processes (1/f processes), multi-scale processes having an 1/f spectrum with a finite range of spatial scales going from a few millimeters b ($b \leqslant \frac{\lambda}{10}$) to several meters (resolution cell) [1][2].

Wornell has demonstrated that 1/f processes can be synthesized by exploiting a Karhunen-Loève expansion in terms of orthonormal wavelet functions [1][2][11]. One-dimensional natural surfaces description can be obtained by using an approximation of this expansion:

$$Z_p(x) = \sum_{m=-p1}^{p2} \sum_{p=-\infty}^{+\infty} Z_n^m \psi_n^m (x/L) \tag{1}$$

where Z_n^m is a collection of gaussian random independent variables with variance , x a normalized distance with respect to an arbitrary length L=2^bb and a collection of orthonormal wavelet. In this work, we have used 4^{th} order Daubechies wavelets.

Bi-dimensional profiles are required to describe more adequately natural surfaces that changes from one direction to another. Thus, wavelet theory has been extended from the one-dimensional to the two-dimensional case using the separable dyadic multi-resolution analysis introduced by Mallat [6] [7]. The bi-dimensional wavelet transform gives us respectively the vertical wavelet component (2), the horizontal wavelet (3) component and the diagonal wavelet component (4) of the height z considered as a 1/f process over a finite range of spatial scales going from an inner spatial scale b of a few millimeters to an outer spatial scale B of several meters [7] [13].

$$Z_p^V(x,y) = \sum_{m_x=0}^{p} \sum_{m_y=0}^{p} \sum_{n_x=0}^{+\infty} \sum_{n_y=0}^{+\infty} Z_{n_x}^{m_x} Z_{n_y}^{m_y} \psi\left(\frac{2^{m_x}}{B}x - n_x\right) \phi\left(\frac{2^{m_y}}{B}y - n_y\right) \tag{2}$$

$$Z_p^H(x,y) = \sum_{m_x=0}^{p} \sum_{m_y=0}^{p} \sum_{n_x=0}^{+\infty} \sum_{n_y=0}^{+\infty} Z_{n_x}^{m_x} Z_{n_y}^{m_y} \phi\left(\frac{2^{m_x}}{B}x - n_x\right) \psi\left(\frac{2^{m_y}}{B}y - n_y\right) \tag{3}$$

$$Z_p^D(x,y) = \sum_{m_x=0}^{p} \sum_{m_y=0}^{p} \sum_{n_x=0}^{+\infty} \sum_{n_y=0}^{+\infty} Z_{n_x}^{m_x} Z_{n_y}^{m_y} \psi\left(\frac{2^{m_x}}{B}x - n_x\right) \psi\left(\frac{2^{m_y}}{B}y - n_y\right) \tag{4}$$

where $Z_{n_x}^{m_x}$and $Z_{n_y}^{m_y}$ are a collection of uncorrelated zero mean Gaussian random variables.where i=V, H or D.

We have plotted the height of simulated multi-scale three-dimensional surfaces and studied the impact of the multi-scale surface parameters namely υ (Figure1 (a) and (b)) and P (Figure 2 (a) and (b)).It can be seen that for υ=1.1 the surface is rougher with a height maximum of 3.7 cm where as for υ=2.1, the surface is smoother with a height maximum of 2.3 cm.

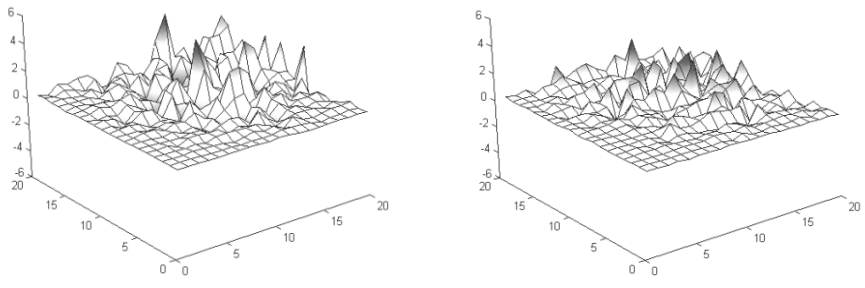

(a) (b)

Figure 1. 3D representation of the height for a multi-scale two-dimensional surface with : (a) υ_x=ν_y=1.1; γ_x=γ_l =0.2 cm ; γ_y=γ_2 =0.3 cm; Zmax = 3.7cm, (b) υ_x=ν_y=2.1; γ_x=γ_l =0.2 cm ; γ_y=γ_2 =O.3cm; Zmax = 2.3 cm

3. Multi-scale description of two-dimensional natural rough surfaces on radar backscattering using the SPM

The main purpose of the present study is to develop an inversion model for soil moisture and multi-scale roughness parameters retrieval over bare soil surfaces using remotely sensed data.

The retrieval of soil surfaces parameters from backscattered data can be carried out by using analytical models like the Integral Equation Model [8][9], the Physical Optics or the Small perturbation model, empirical models like the Oh model or semi-empirical [10]. The complexity of analytical models makes the inversion procedure difficult. The theoretical model used in this paper is the small perturbations model.

3.1. Validity of The Small Perturbations Model

The SPM model is used when the surface height standard deviation is much smaller than wavelength and the rms slope s is not high (ks<<0.3).

3.2. Radar Backscattering Coefficient Expression :

The backscattering coefficient according to the SPM leads to :

$$\sigma_{pq}^{0} = \left(8k^{4}\cos^{4}\theta\right)\left|\alpha_{pq}\right|^{2} W^{(1)}\left(-2k_{x}\right) \tag{5}$$

where $W^{(n)}$ is the Fourier transform of the nth power of the multi-scale ACF given by :

$$W^{(n)}\left(-2k_{x},0\right) = \frac{2}{\pi}\int_{0}^{\infty}\int_{0}^{\infty}\left(\frac{r_{C}^{i}\left(\xi,\eta\right)}{r_{C}^{i}\left(0,0\right)}\right)^{n}\cos\left(2k_{x}\xi\right)d\xi d\eta \ , \ \left\{\begin{bmatrix}\alpha_{hh} = \frac{\cos\theta-\sqrt{\varepsilon-\sin^{2}\theta}}{\cos\theta+\sqrt{\varepsilon-\sin^{2}\theta}} \\ \alpha_{hv} = \alpha_{vh} = 0 \\ \alpha_{vv} = \left(\varepsilon-1\right)\frac{\sin^{2}\theta-\varepsilon\left(1+\sin^{2}\theta\right)}{\left(\varepsilon\cos\theta+\sqrt{\varepsilon-\sin^{2}\theta}\right)^{2}}\end{bmatrix}\right.$$

, k_x is the x component of the incident wave number and is the respectively the horizontal, the vertical and the diagonal autocorrelation function for i =H,V and D.

To study the impact of the multi-scale roughness description, dielectric parameters and radar parameters on the backscattering coefficient we have varied each parameter of interest and analysed its impact on radar backscattering[7] [13].

4. Methodology of the retrieval procedure

In this section, an algorithm to retrieve multi-scale roughness parameters and soil moisture parameter is illustrated.

4.1.Inversion Procedure

The method consists of inverting the SPM direct model using a multi-layer perceptron architecture [9] and [12].Before applying the inversion procedure, the sensitivity of the backscattering coefficient to surface and radar parameters was established by using the SPM model [7] [13]. The inversion consists in retrieving roughness and soil moisture parameters ν_1, υ_2, γ_1, γ_2, ε_1 et ε_2 by using as input parameters the radar backscattering coefficients σ_{HH}, σ_{VV} and the incident angle θ varied from 20 to 80 degrees. The NN is trained by learning rules using the backpropagation method. Simulated data sets based on the SPM surface scattering model are used to train the neural network. The sensitivity analysis of the SPM model unable us to examine the dependence of the output of the scattering model to the inputs parameters. When the outputs of the scattering model became saturated or insensitive to a parameter, the parameter inversion range was narrowed.

4.2. Neural Network Training

The first step in the inversion procedure is the generation of a set of training patterns. In this study, a total of 300 training patterns were generated by using each of the signal models σ (Ξ) of the SPM backscattering coefficient. The parameters of interest Ξ used to generate the training patterns were randomly selected from within the range of parameters given by the sensitivity analysis.

Figure 3 represents the inversion process configuration. We have a total of 8 inputs corresponding to the backscattering coefficients σ_{HH}, σ_{VV} for 4 incident angles and 6 outputs. We have used 2 hidden layers containing 40 neurons after several tests.

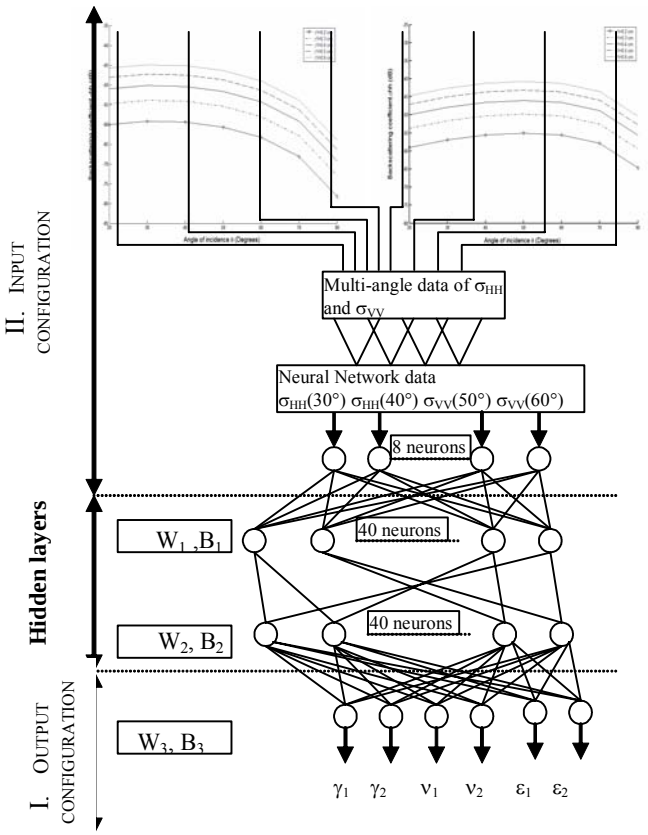

Figure 3. Inversion process configuration

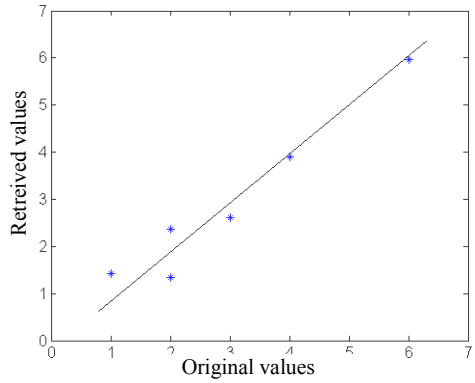

Figure 4. Retrieved values of ε_1 versus original values

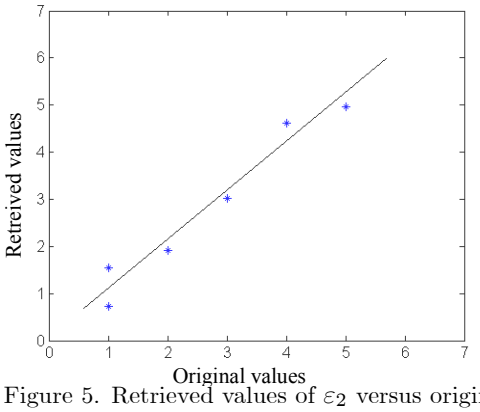

Figure 5. Retrieved values of ε_2 versus original values

4.3. Inversion algorithm results

We applied these inversion techniques to SPM simulated data. Before using the NN for the inversion we had to calculate the mean rms error of the network. We found that it converges well to a value smaller than 0.05 after 6000 iterations so that the NN is ready for the inversion procedure. We have plotted in figures 4-9 the retrieved values for each of the six parameters to retrieve.

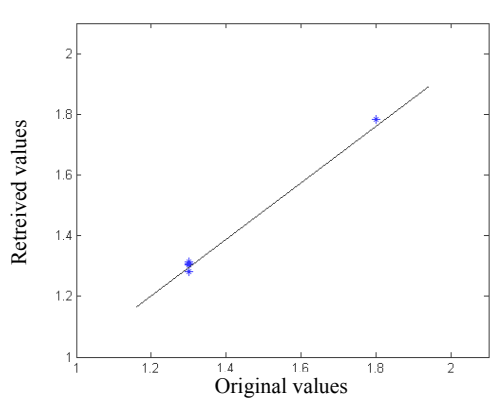

Figure 6. Retrieved values of ν_1 versus original values

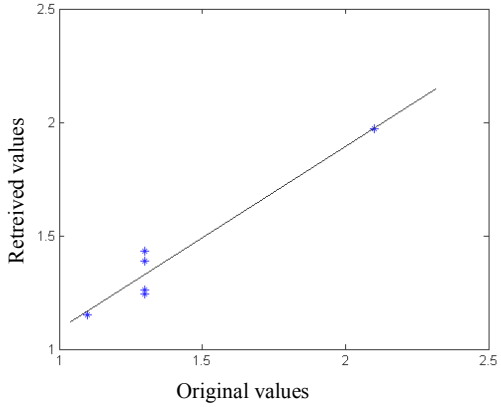

Figure 7. Retrieved values of υ_2 versus original values

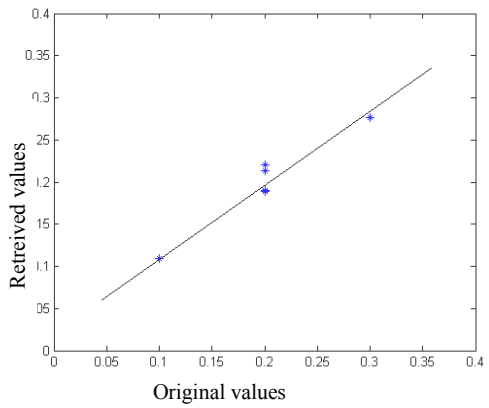

Figure 8. Retrieved values of γ_1 versus original values

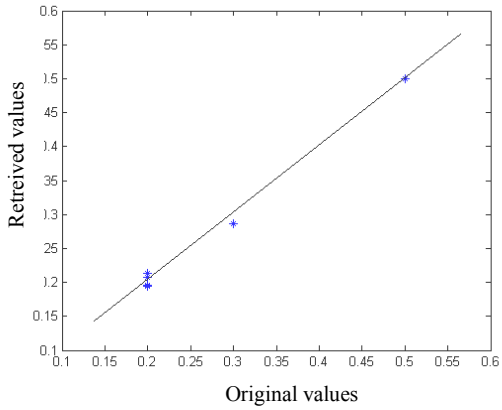

Figure 9. Retrieved values of $\gamma_2$versus original values

The straight diagonal line describes a perfect inversion algorithm where the estimated values match the original values. We notice that the deviations from this line are not very important and that the NN inversion algorithm gives interesting results.

5. Conclusion

In this study, we have used a multi-scale roughness description using the wavelet transform and the Mallat algorithm to describe natural surface roughness and investigated the impact of this description on radar backscattering through a sensitivity analysis.This sensitivity study permit us to determine the range of parameters to use in the training of the network.To perform the inversion of the small perturbation multi-scale scattering model (MLS SPM) we used a multi-layer neural network trained by a backpropagation learning rule.The inversion procedure has given quite satisfactory results with a mean error of 8 %. Future work will be dedicated to the inversion of real data.

REFERENCES

1. F. Mattia, and T. Le Toan, " Backscattering properties of multi-scale rough surfaces". Journal of Electromagnetic Waves and Applications, 13 : 493-528, 1999.
2. F. Mattia, and T. Le Toan, " An analytical, numerical, and experimental study of backscattering from multi-scale soil surfaces." Radio Science, Volume 36, Number 1 : 119-135, 2001.
3. L.E. Church,. "Fractal surface finish." Applied Optics, vol.27, n.8, 1998.
4. M. Davidson, T. Le Toan, F. Mattia, G. Satalino, T. Manninen, and M. Borgeaud,. "On the characterisation of agricultural soil roughness for radar sensing studies." IEEE Trans. Geosc.Rem.Sens., 38 : 630-640, 2000.
5. I. Daubechies, Ten lectures on Wavelets. CBMS-NFS Lecture Notes, NR.61, SIAM, 1992.
6. S.G. Mallat, "Theory of multi-resolution signal decomposition : The Wavelet representation", IEEE Trans.Pattern analysis and machine intelligence, vol II., 7, 1989.
7. L. Bennaceur, Z. Belhadj, and M. R. Boussema. "A study of radar backscattering multi-scale bi dimensional surface", Proceedings IEEE IGARSS 2002, Toronto, Canada, June 2002.
8. A.K. Fung, Z. Li, and K.S. Chen, "Backscattering from a randomly rough dielectric surface". IEEE Trans.Geosc.Rem.Sensing, 30 : 356-363, 1992.
9. A.K. Fung, Microwave scattering and emission models and their applications Artech House, 1994.
10. R. M. Axline, and A.K. Fung, "Numerical computation from a perfectly conducting random surface", IEEE, Trans.Antennas Propagat., 26 : 488-582, 1978.
11. G.W.,Wornell, " Wavelet-based representation for the 1/f family of fractal process", Proc IEEE, vol. 81, October 1993.
12. M., Dawson, A.K Fung. "A robust statistical based estimator for soil moisutre retrieval from radar measurments."IEEE Trans.Geosc.Rem.Sensing,35 :57-67 1997.
13. L. Bennaceur, R. Bennaceur, Z. Belhadj, and M. R. Boussema, "A sensitivity analysis of radar backscattering coefficient to multi-scale roughness description and radar parameters using the small perturbation model" Proceedings of IEEE ICTTA 04, Damascus, Sirius, April 2004.

Radiation Characteristics of a Finite Periodic Slot Array in a Parallel Plate Waveguide Filled with a Transversely Magnetized Ferrite

Kazuo Nishimura
Department of Mechanical and System Engineering, Ryukoku Univesrsity,
1-5 Yokotani, Seta Oe-cho, Otsu, Shiga 520-2194 Japan Email: nisimura@rins.ryukoku.ac.jp

Abstract—This paper presents radiation characteristics of a finite periodic slot array in a parallel plate waveguide filled with a transversely magnetized ferrite. The characteristics are analyzed by using the moment method and estimated numerically under the condition that the fundamental TE_1 mode is only the propagating mode in the unperturbed parallel plate waveguide. It is theoretically explained how the chacteristics can be tunned and the radiation patterns can be controlled by varying the DC magnetic field applied to the ferrite.

1. Introduction

Recently, research on RF electronic controllable high frequency devices and circuits has been paid attention to [1]. Research on microwave ferrite devices is a kind of the research on the RF electronic high frequency devices. Until now, the vigorous development and research on the microwave devices such as isolators, circulators, phase shifter, delay lines, magnetically tunable resonators has been carried out by using anisotropy and frequency dependence of the permeability of ferrite that can easily be controlled by an external dc magnetic field [2]-[4]. On the other hand, research on antenna applications of ferrite materials has not been carried out extensively.

As research on antenna applications using ferrites, electronic scanning of the radiation pattern of an open-ended retangular waveguide filled with ferrite [5], elecronic scanning of an antenna loaded with circularly arrayed ferrite bars [6], electronic scan of a millimeter-wave leaky wave antenna with a periodic structure loaded with ferrite [7], [8], and microstrip antennas on a ferrite substrate [9] have been researched. Of these, the periodic ferrite structure can work not only as a leaky-wave antenna but also as a magnetically tunable Bragg reflection filter. So, reseach on propagation in the periodic ferrite structure is very interesting. The Bragg reflection characteristics and leaky-wave antenna characteristics have been characterized theoretically by means of the improved perturbation method, the singular perturbation method, and spectral domain [7], [8], [10], [11]. As long as the author knows, the analytical research on ferrite waveguides with a finite array structure has been carried out little. So, the author have theoretically explained the radiation characteristics of a slotted parallel plate waveguide filled with a transversely magnetized ferrite by means of the method of moments. Then, the author have discussed the magnetic tunability of the radiation bandwidth of the slotted parallel plate waveguide filled with ferrite and radiation pattern control by an applied dc magnetic field [12].

In this paper, radiation characteristics of a finite periodic slot array installed in a upper plate of a parallel plate waveguide filled with a transversely magnetized ferrite are analyzed by means of the method of the moments [12]-[15] in the case which only the TE_1 mode propagates in the unperturbed parallel plate waveguide. At millimeter-wave frequencies, the dependence of the characteristics of the periodically slotted parallel plate waveguide on the applied dc magnetic field is estimated numerically. It is theoretically explained how the chacteristics can be tunned and the radiation patterns can be controlled by varying the dc magnetic field applied to the ferrite from the viewpoint of a leaky wave antenna.

2. Theoretical Analysis

Let us consider a peodically slotted parallel plate waveguide shown in Fig. 1 consisting of a a finie periodic slot array formed in the upper plate of a parallel plate waveguide that is filled with ferrite magnetized in the z direction. In Fig. 1, b, D, L and $2a$ show the height, the periodicity, the number of the slots and the slot width of the periodically slotted parallel plate wave guide, respectively. In Fig. 1, it is assumed that the electromagnetic field is uniform in the z direction (so that $\frac{\partial}{\partial z} = 0$) and the time dependence is $e^{j\omega t}$. The relative permittivity of the ferrite is ε_r. It is assumed that there is no loss in the ferreite used in the periodically slotted parallel plate

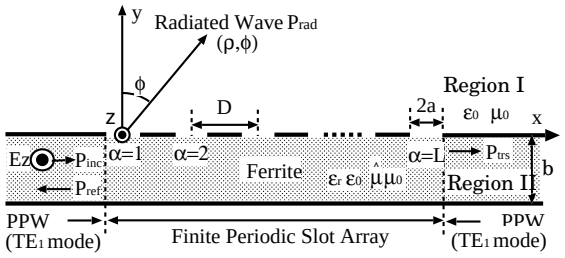

Figure 1: A finite periodic slot array in a parallel plate waveguide filled with a transversely magnetized ferrite.

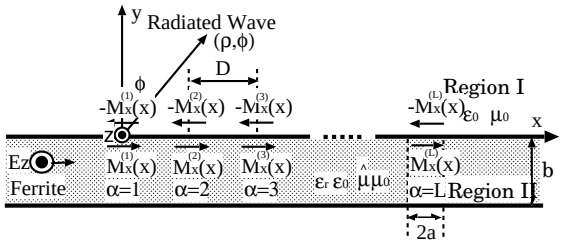

Figure 2: Equivalent analytical model.

waveguide. Then, the relative permeability tensor $\hat{\mu}$ is given by

$$\hat{\mu} = \begin{bmatrix} \mu & j\kappa & 0 \\ -j\kappa & \mu & 0 \\ 0 & 0 & 1 \end{bmatrix}, \quad \mu = 1 + \frac{\omega_h \omega_m}{\omega_h^2 - \omega^2}, \quad \kappa = \frac{\omega \omega_m}{\omega_h^2 - \omega^2}, \quad \omega_h = \gamma \mu_0 H_0, \quad \omega_m = \gamma \mu_0 M_s. \tag{1}$$

where μ_0 is the free space permeability, ω is the angular frequency, $\mu_0 H_0$ is the applied dc magnetic field, γ is the gyromagnetic ratio ($= 1.76 \times 10^{11} rad/T/sec$) and $\mu_0 Ms$ is the saturation magnetization of the ferrite. For the dielectric-filled slotted parallel plate waveguide in [13],[14], the cases in which both the permittivity and permeability are isotropic are analyzed. In the present paper, the case in which only the permeability is expressed with an anisotropic tensor is analyzed. In this paper, not only the magnetostatic mode obtained under the magnetstatic condition neglecting the electric field components, but also the electmagnetic modes containing the electric field components are rigorously analyzed as [12], [15].

Let us assume the case in which only the TE_1 mode propagates in the parallel plate waveguide filled with ferrite as shown in Fig. 1. The slot regions $S_\beta (\beta = 1, \cdots, L)$ are defined as $\{S_\beta : |x - (\beta - 1)D| \le a, y = 0\}$ in Fig. 1. The analysis is carried out with the equivalent analytical model in Fig. 2, in which each slots is replaced with equivalent magnetic current $M_x^{(\beta)}(x)$. In this case, the incident electromagnetic field($E_{z\mathrm{II}}^{inc}$, $H_{x\mathrm{II}}^{inc}$, $H_{y\mathrm{II}}^{inc}$), the scattered electromagneticfield in Region I(E_{zI}^s, H_{xI}^s, H_{yI}^s) , and the scattered electromagnetic field in RegionII ($E_{z\mathrm{II}}^s$,$H_{x\mathrm{II}}^s$,$H_{y\mathrm{II}}^s$) are given as follows:

$$\begin{aligned} E_{z\mathrm{II}}^{inc} &= \sin(\frac{\pi}{b}y)e^{-jk_{x1}x}, \\ H_{x\mathrm{II}}^{inc} &= -\frac{1}{j\omega\mu_0\mu_{eff}}\{\frac{\pi}{b}\cos(\frac{\pi}{b}y) + \frac{\kappa}{\mu}k_{x1}\sin(\frac{\pi}{b}y)\}e^{-jk_{x1}x}, \\ H_{y\mathrm{II}}^{inc} &= -\frac{1}{\omega\mu_0\mu_{eff}}\{k_{x1}\sin(\frac{\pi}{b}y) + \frac{\kappa}{\mu}\frac{\pi}{b}\cos(\frac{\pi}{b}y)\}e^{-jk_{x1}x}, \end{aligned} \tag{2}$$

$$\begin{aligned} E_{zI}^s &= \frac{j}{4}\sum_{\beta=1}^{L}\int_{S_\beta} M_x^{(\beta)}(x')\frac{\partial}{\partial y}\{H_0^{(2)}(k_0R^-) + H_0^{(2)}(k_0R^+)\}|_{y'=0+}dx' \\ H_{xI}^s &= \frac{1}{4k_0Z_0}\sum_{\beta=1}^{L}\int_{S_\beta} M_x^{(\beta)}(x')(k_0^2 + \frac{\partial^2}{\partial x^2})\{H_0^{(2)}(k_0R^-) + H_0^{(2)}(k_0R^+)\}|_{y'=0+}dx', \\ H_{yI}^s &= \frac{1}{4k_0Z_0}\sum_{\beta=1}^{L}\int_{S_\beta} M_x^{(\beta)}(x')\frac{\partial^2}{\partial x\partial y}\{H_0^{(2)}(k_0R^-) + H_0^{(2)}(k_0R^+)\}|_{y'=0+}dx', \end{aligned} \tag{3}$$

$$R^\pm = \sqrt{(x - x')^2 + (y \mp y')^2}.$$

$$\begin{aligned} E_{z\mathrm{II}}^s &= \sum_{\beta=1}^{L}\int_{S_\beta} M_x^{(\beta)}(x')G(x, y; x', y')|_{y'=0-}dx', \\ H_{x\mathrm{II}}^s &= -\frac{1}{j\omega\mu_{eff}\mu_0}\sum_{\beta=1}^{L}\int_{S_\beta} M_x^{(\beta)}(x')\{\frac{\partial G(x, y; x', y')}{\partial y} + j\frac{\kappa}{\mu}\frac{\partial G(x, y; x', y')}{\partial x}\}|_{y'=0-}dx', \\ H_{y\mathrm{II}}^s &= \frac{1}{j\omega\mu_{eff}\mu_0}\sum_{\beta=1}^{L}\int_{S_\beta} M_x^{(\beta)}(x')\{\frac{\partial G(x, y; x', y')}{\partial x} + j\frac{\kappa}{\mu}\frac{\partial G(x, y; x', y')}{\partial y}\}|_{y'=0-}dx', \end{aligned} \tag{4}$$

$$G(x,y;x',y') = \frac{j}{b}\sum_{q=1}^{\infty}\frac{1}{k_{xq}}\{q\frac{\pi}{b}\cos(q\pi\frac{y'}{b}) + \frac{(x-x')}{|x-x'|}k_{xq}\frac{\kappa}{\mu}\sin(q\pi\frac{y'}{b})\}\sin(q\pi\frac{y}{b})e^{-jk_{xq}|x-x'|}. \quad (5)$$

$$k_{xq} = \sqrt{\varepsilon_r\mu_{eff}k_0^2 - (\frac{q\pi}{b})^2}, \quad \mu_{eff} = \frac{\mu^2-\kappa^2}{\mu}, \quad k_0 = \omega\sqrt{\varepsilon_0\mu_0}, \quad Z_0 = \sqrt{\frac{\mu_0}{\varepsilon_0}}.$$

Here, ε_0 is the free space permittivity and $H_0^{(2)}(\cdot)$ is zeroth-order Hankel function of the second kind. From the condition that the tangential components of the magnetic field in Region I and Ⅱ are continuous over each slot region S_β, namely,

$$H_{xI}^s|_{y=0_+} = H_{x\text{Ⅱ}}^{inc}|_{y=0_-} + H_{x\text{Ⅱ}}^s|_{y=0_-}, \quad over S_\beta(\beta = 1,2,\cdots,L) \quad (6)$$

the integral equation on the equivalent surface magnetic current $M_x^{(\beta)}(x)$ over the βth slot can be obtained. All slot regions S_β are equally divided into N segments and each equivalent surface magnetic current $M_x^{(\beta)}(x)$ is expanded in terms of the piecewise sinusoidal function $\Phi_{n_\beta}^{(\beta)}(x)$ $(n_\beta = 1,\cdots,N-1)$ as

$$M_x^{(\beta)}(x) = \sum_{n_\beta=1}^{N-1} V_{n_\beta}^{(\beta)}\Phi_{n_\beta}^{(\beta)}(x) \quad V_{n_\beta}^{(\beta)} : \text{unknown coefficients.} \quad (7)$$

When both sides of Eq. (6) are multiplied by $\Psi_{m_\alpha}^{(\alpha)}(x) = \sin k_0 h\Phi_{m_\alpha}^{(\alpha)}(x)$ $(m_\alpha = 1,2,\cdots,N-1, h = \frac{2a}{N})$ and are integrated over S_α $(\alpha = 1,2,\cdots,L)$, then the above mentioned integral equation is reduced to the $L(N-1)\times L(N-1)$ matrix equation. From the undetermined coefficients $V_{n_\beta}^{(\beta)}$ obtained by solving the above mentioned matrix equation and Eqs. (7), (3) and (4), the equivalent surface magnetic currents and the scattered electromagnetic fields at each region can be determined.

The incident power per unit length in the z direction in this parallel plate waveguide P_{inc}, the Poynting power in the ρ direction $p_s(\rho,\theta)$, the radiated power P_{rad} and the radiation efficiency η_{rad} are given by

$$P_{inc} = -\frac{1}{2}Re\{\int_{-b}^{0} E_{z\text{Ⅱ}}^{inc}H_{y\text{Ⅱ}}^{*inc}dy\}, \quad (8)$$

$$p_s(\rho,\phi) = \frac{1}{2}Re\{E_{zI}(\rho,\phi)H_{\phi I}^*(\rho,\phi)\}, \quad (9)$$

$$P_{rad} = \int_{-\frac{\pi}{2}}^{\frac{\pi}{2}} p_s(\rho,\phi)\rho d\phi, \quad (10)$$

$$\eta_{rad} = \frac{P_{rad}}{P_{inc}}. \quad (11)$$

The radiation pattern is defined as

$$G_{rad}(\phi) = 10\log_{10}\{2\pi\rho\frac{p_s(\rho,\phi)}{P_{inc}}\}. \quad (12)$$

3. Numerical Results

In the numerical calculations, the relative permittivity ε_r and satuation magnetization $\mu_0 M_s$ of the ferrite and the numeber of the slots L, the slot width $2a$, the periodicity D and height b of the periodically slotted parallel plate waveguide filled with ferrite are

$$\varepsilon_r = 12.5 \quad \mu_0 M_s = 0.5T[16]-[17] \quad L = 60 \quad 2a = 1.0mm \quad D = 3.0mm \quad b = 1.5mm.$$

In the numerical calculation, ferrite is assumed to be lossless. The number of divisions N of the slot region $N$is fixed to $N = 40$ so that the width of the divided slot region h can be smaller than $\frac{1}{50}$ of the wavelength. The order of the trancated terms N_{tr} in the inifinite series in Eq. (5) is fixed to $N_{tr} = 200$. Also, it is confirmed that the numerical results satisfy the energy conservation law within an error of $10^{-3}\%$.

Fig. 3 shows the frequency dependence of the radiation efficiency η_{rad} at 40 to 50GHz for different values of the applied dc magnetic field. In the case of $\mu_0 H_0 = 0.05T$, the maximum radiation efficiency is about 0.9, and the frequency band for a radiation efficiency of less than 0.1 is caused by the Bragg reflection near 42GHz.

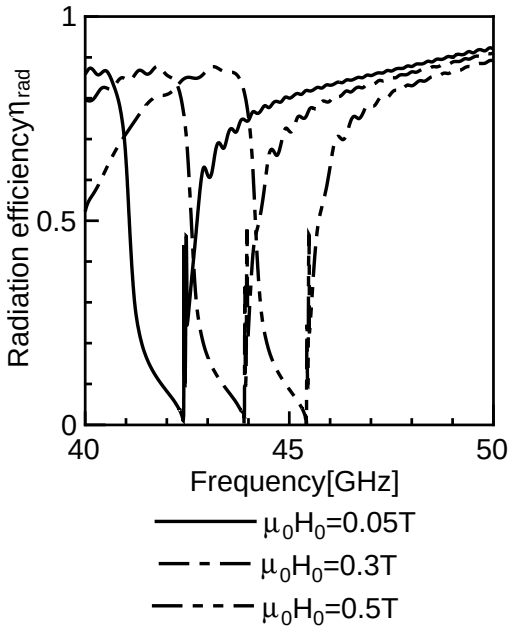

Figure 3: The Frequency dependent charactric of the radiation efficiency η_{rad} of the finite periodic slot array in the parallel plate waveguide filled with the transversely magnetized ferrite.

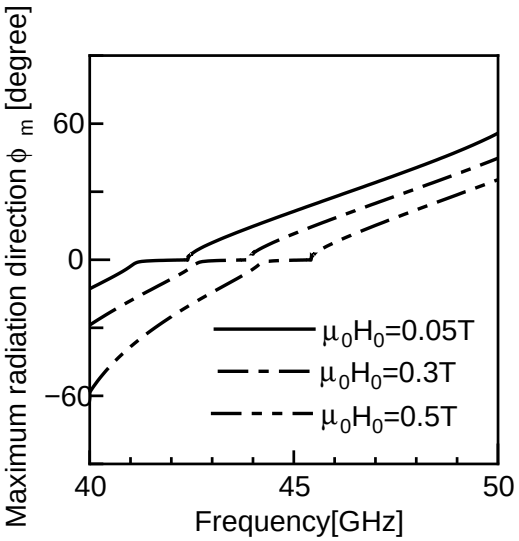

Figure 4: The Frequency dependent charactric of the maximum radiation direction ϕ_m of the finite periodic slot array in the parallel plate waveguide filled with the transversely magnetized ferrite.

If the applied dc magnetic field is changed from $\mu_0 H_0 = 0.05T$ to $\mu_0 H_0 = 0.5T$, it is found that the radiation range is tuned by about 3GHz, while the maximum radiation efficiency and the radiation bandwidth do not essentially change. From the above results, it is found that the operating fequency can be varied by simply changing the applied dc magnetic field without changing the physical dimensions. Therefore, there is possibility of constructing antenna suitable for various millimeter-wave systems.

Fig. 4 shows the frequency characteristics of the maximum beam direction ϕ_m of the radiated wave in the range of 40 to 50GHz, dependent on the applied dc magnetic field. From Fig. 4 it is found taht the maximum beam direction ϕ_m show the marked frequecncy beam-scanning characteristics. Specially, in the case of $\mu_0 H_0 = 0.05T$, the maximum beam direction ϕ_m changes from $-12..8°$ to $55.8°$ in the range of 40 to 50GHz and the Bragg reflection band with the bandwidth of about 1GHz is caused in the range of 41 to 43GHz. Also, if the applied dc magnetic field is varied from $\mu_0 H_0 = 0.05T$ to $\mu_0 H_0 = 0.5T$, the frequency dependence of the maxinum beam direction ϕ_m is tuned by about 3GHz.

Figs. 5 and 6 show the dependence of the radiation pattern $G_{rad}(\phi)$ on the applied DC magnetic field at 41GHz and the dependence of the the radiation pattern $G_{rad}(\phi)$ on the applied DC magnetic field at 47GHz. In the case of $\mu_0 H_0 = 0.05T$, The maxinum beam directions ϕ_m of Fig. 5 and Fig. 6 are $-2.92°$ and $34.1°$, respectively. From this, too, it is found that the maximum beam direction ϕ_m shows the marked frequecncy beam-scanning characteristic. Also, as the applied dc maganetic field $\mu_0 H_0$ is varied from 0.05T to 0.5T, the maximum beam direction ϕ_m is scanned from $-2.92°$ to $-38.3°$ in Fig. 5 and from $32.1°$ to $15.1°$ in Fig. 6. Further, it is found that the intensity of the radiated power is changed with the beam scan by the applied dc magnetic field, because the beam scan is caused with the tune of the radiation frequency band by the applied DC magnetic field.

4. Conclusions

Radiation characteristics of a finite periodic slot array in a upper plate of a parallel plate waveguide filled with a transversely magnetized ferrite is analyzed by the method of moments in the case which only the TE_1 mode propagates in the unperturbed parallel plate waveguide. Under the assumption that ferrite loss is noexistent, it is theoretically explained how the frequency dependence of the radiation efficiency and the frequency scanning

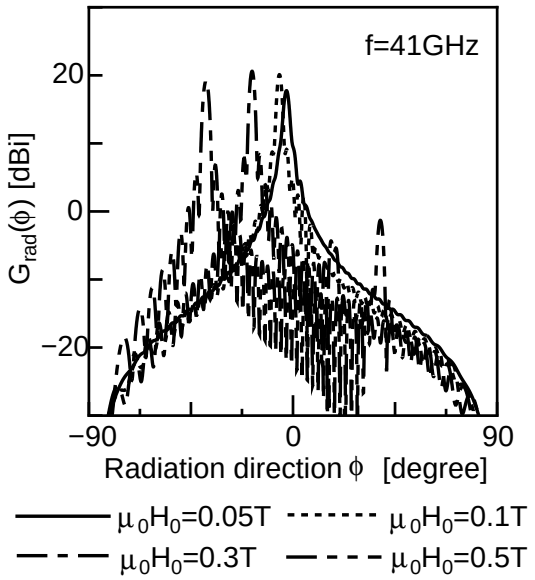

Figure 5: The radiation pattern $G_{rad}(\phi)$ of the finite periodic slot array in the parallel plate waveguide filled with the transversely magnetized ferrite at 41GHz.

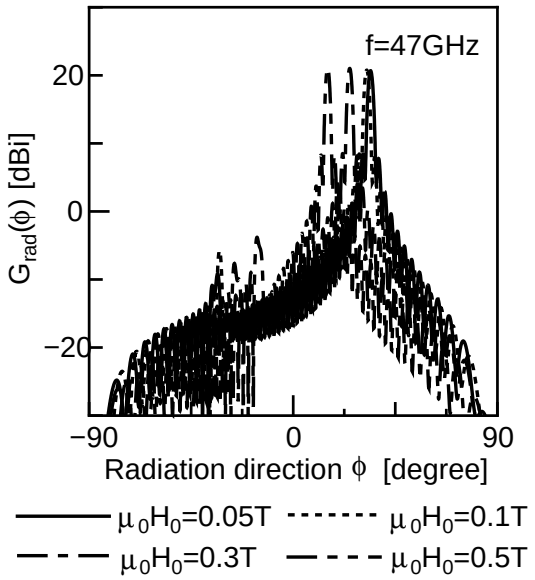

Figure 6: The radiation pattern $G_{rad}(\phi)$ of the finite periodic slot array in the parallel plate waveguide filled with the transversely magnetized ferrite at 47GHz.

characteristic of the radiated wave are controled by varying the applied DC magnetic field. From numerical results, it is found that the frequency dependences of the radiation efficiency η_{rad} and the frequency dependence of the maximum beam direction ϕ_m are tuned to higher frequency band without significantly changing the maximum radiation efficiency and the radiation frequency bandwidth by varying the applied DC magnetic field. Also, it is explained that the beam scanning of the radiation patterns are caused with the tuning of the frequency dependence of the maximum beam direction by changing the applied DC magnetic field.

REFERENCES

1. Special Session on Microwave Analog Smart Devices and Circuits, IEICE Trans. C, vol. J87-C, no. 1, Jan. 2004.
2. "SPECIAL SECTION ON MICROWAVE MAGNETICS," Proc. IEEE, vol. 76, no. 2, Feb. 1988.
3. Y. Konishi, Recent advances in microwave circuit techniques with ferrite. IEICE 1972.
4. T. Hashimoto, Microwave ferrite and its application. Sogo-Denshi Publication 1997.
5. G. Tyras and G. Held, IRE Trans. Microwave Theory & Tech., vol. MTT-6, pp. 268-277, July 1958.
6. N. Okamoto and S. Ikeda, IEEE Trans. Antenna Propagat., vol. AP-27, no. 3, May 1979.
7. K. Araki and T. Itoh, IEEE Trans. Microwave Theory & Tech., vol. MTT-29, no.9, Sept. 1981.
8. S. Erkin et al., IEEE Trans. Microwave Theory & Tech., vol. MTT-36, no.3, pp.568-575, March 1988.
9. D. Pozar, IEEE Trans. Antennas Propagat., vol. 40, no.9, pp.1048-1092, Sept. 1992.
10. C. Surawatpunya et al., IEEE Trans. Microwave Theory & Tech., vol. MTT-32, no. 7, pp. 689-695, July 1984.
11. M. Ozaki,M. Asai, J. Yamakita, S. Sawa, IEICE Trans. C, vol. J75-C, no. 11, , pp. 694-702, Nov. 1992.
12. K. Nishimura, IEICE Trans. C, vol. J84-C, no. 11, pp. 1061-1067, Nov. 2001.
13. C. W. Chuang, IEEE Trans. Antennas Propagat, vol. 36, no. 9, pp.1227-1230, Sept. 1988.
14. J-I. Lee, U-H. Cho and Y-K. Cho, IEEE Trans. Antennas Propagat, vol. 47, no. 4, pp. 701-706, Sept. 1988.
15. K. Nishimura, Tech. Rep. IEICE Japan, MW-04-06, June 2004.
16. M. Geshiro and T. Itoh, IEEE Trans. Microwave Theory & Tech, vol. MTT-35, no. 12, pp. 1377-1380, Dec. 1987.
17. T. Kitazawa, IEEE Trans. Microwave Theory & Tech, vol. MTT-39, no. 1, pp. 1377-1380, Jan. 1991.
18. Mini-Special Issue on Millimeter-Wave Technology and its Applications. IEICE Trans. vol. J77-C-I, no. 11, Nov. 1994.
19. T. Teshirogi and T. Yoneyama, Wave-Summit Series. New millimeter-wave technology. Ohm Press; 1999.

Experimental Evaluation of EM Wave Suppressions by Lattice Array of Conductive Wires

Akira Saito, Takeshi Saito, Kazuo Aizawa and Hiroshi Echigo

Tohoku Gakuin University, Japan

Abstract—In this paper, some results of the experimental evaluations for the real EM wave screens that were developed by authors recently. The results show that the suppression effectiveness by the constructed array was about 20dB in the band of 1GHz~3GHz electromagnetic waves.

The experimental evaluations of EM wave suppression behinds thin wires, especially for the near field area, have not reported. This paper gives some new evidences for the thin-wire scatterings.

Keywords- EM Scattering, Conductive Rod, Conductive Strip, EM Wave Rejection, EM Wave Suppression-Screen.

1. INTRODUCTION

Considering that the scattering of electromagnetic (EM) waves is one of the causes of the unwanted EM-environments, the authors have been studying on the scattering phenomena by conductive rods. In their analyses of the EM-wave scattering, the results gave the idea that a metal strip can form the shade of EM-wave or that it can reduce the EM-wave strength in the area behind the conductive rods or strips.

The authors had tried to estimate theoretically the reducing effectiveness (or rejection effectiveness) by the multiple layers of conductive strips, each of which was made of a few of conductive thin rods or wires. The calculation results gave the suppression effect of almost 20 dB for the appropriate frequency band.

2. SCATTERING BY A CONDUCTIVE CYLINDER[1][2][3]

Suppose that the longitudinal axis of the conductive cylinder is coincident with z-axis of Cartesian coordinate as shown in Figure 1. When the incident TM (transverse magnetic) wave propagating along the x-axis is given as,

$$E_z^i = E_0 e^{-jkx} \tag{1}$$

and this wave can be expressed by the Bessel series expansion form as,

$$E_z^i = E_0 \sum_{n=-\infty}^{\infty} (j)^{-n} J_n(kr)\, e^{-j n \cos^{-1}\left[\frac{x}{r}\right]} \tag{2}$$

The scattering wave from the cylinder is approximated by the Bessel series expansion form as Equation 3.

$$E_z^s = \sum_{n=-N}^{N} (j)^{-n} a_n H_n^{(2)}(kr)\, e^{-j n \cos^{-1}\left[\frac{x}{r}\right]} \tag{3}$$

On the surface of the cylinder,

$$E_z^i + E_z^s = 0 \tag{4}$$

This must be satisfied for each term of the series, the coefficients are determined by terms, so that the expansion series is given as,

$$E_z^s = -E_0 \sum_{n=-N}^{N} (j)^{-n} \frac{J_n(ka)\, H_n^{(2)}(kr)}{H_n^{(2)}(ka)}\, e^{-j n \cos^{-1}\left[\frac{x}{r}\right]} \tag{5}$$

where E_0 is the amplitude of the incident wave, k is the propagation constant, r is distance from the z-axis, J_n is the Bessel function of order n, a is the radius of the conductor and $H^{(2)}_n$ is the second kind Hankel function of order n. N is the number of terms to the approximation instead of infinity.

Especially for the thin conductive wire, the scattering wave is given as Equation 2 since it would be supposed that the current distribution on the surface of the cylinder is uniform and the total current ***Iz*** flows in the center of the cylinder,

$$E_z^s = -\frac{kZ_0}{4} I_z J_0(ka) H_0^{(2)}(kr) \qquad (6)$$

where Z_0 is the wave impedance and r is the distance between the conductor axis and the observation point.

Because the boundary condition on the surface of the cylinder forces $E^s_z + E^i_z = 0$, the equation relating the incident wave and the induced current is given as Equation 7.

$$E_z^i = \frac{kZ_0}{4} I_z J_0(ka) H_0^{(2)}(ka) \qquad (7)$$

From the condition of thin wire (that is a<<wave length), the term $J_0(ka)$ may be removed because its value nearly equals to unity.

$$E_z^i = \frac{kZ_0}{4} I_z H_0^{(2)}(ka) \qquad (7)'$$

This formula gives the way to estimate the current ***Iz*** on a thin conductive wire when illuminated by TM wave of ***Ez***

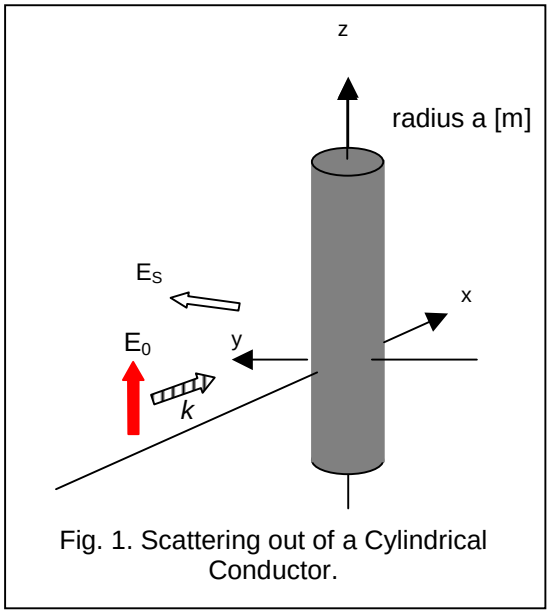

Fig. 1. Scattering out of a Cylindrical Conductor.

3. Scattering Waves From Conductive Cylinders Illuminated By Plane Waves[1][4]

Considering the scattering by multi-thin-conductor system of N wires with the same radius ***a*** [m] as shown in Fig. 2, the induced current on the n-th wire or the current of the n-th conductor; I_n causes the scattering as Equation 8 according to Eq. 6.

$$E_n^s = -\frac{kZ_0}{4} I_n J_0(ka) H_0^{(2)}(kr_n) \qquad (8)$$

where r_n is the distance from the n-th conductor to the observation point.

All N wires form the scattering EM wave E^s_z as Equation 8,

$$E_z^s = -\frac{kZ_0}{4} J_0(ka) \sum_{n=1}^{N} I_n H_0^{(2)}(kr_n) \qquad (9)$$

Since the electric field is zero on the surface of m-th conductor, the induced currents $\{I_n\}$ on the wires and incident electric field E_m at the position of m-th wire are related as Equation 10.

$$\frac{kZ_0}{4} J_0(ka) \sum_{n=1}^{N} I_n H_0^{(2)}(k\rho_{mn}) = E_m \qquad (10)$$

This relation gives the linear system as described by the following matrix expression of Equation 10.

$$\{E_m\} = [Z]\{I_n\} \qquad (11)$$

with

ρ_{mn} : distance between conductors m and n,

$$Z_{mn} \equiv \frac{kZ_0}{4} J_0(ka) H_0^{(2)}(k\rho_{mn}).$$

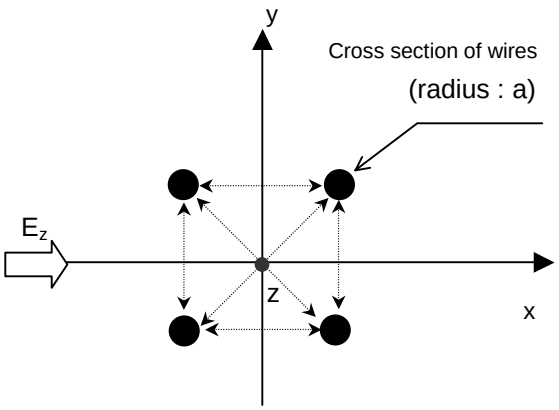

Fig. 2. Multi-conductor System.

When the electric fields at each wire position are given, the induced currents are determined using the inverse matrix [***Y***] of [***Z***]. As each current forms the scattering field, the scattering field is determined by summing up these fields. Then the total field is given as the superposition of the fields of the incident and the scattering waves.

4. SHADING BY LATTICE ARRAY OF CONDUCTIVE WIRES

For lattice arrays, the scattering and total electric fields were estimated by numerical calculations using the programming language ***Mathematica***. The structure is given in Fig.3. The parameters for this example are shown in the figure. The amplitude and frequency of the incident wave were supposed as 1[V/m] and 1GHz. The calculated result is given in Fig.4.

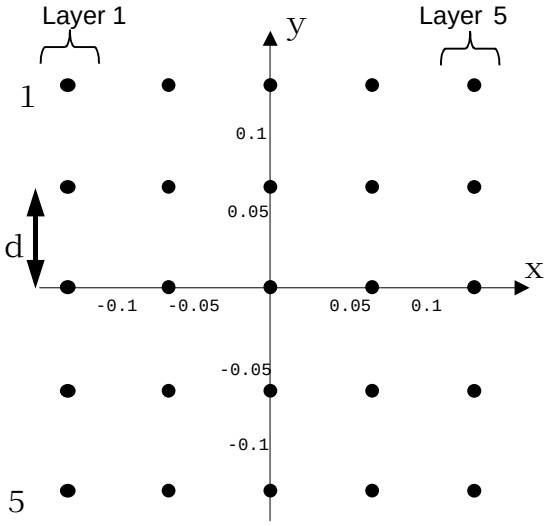

Fig.3 Lattice structure
(a/λ＝1/27, d＝13λ/20)

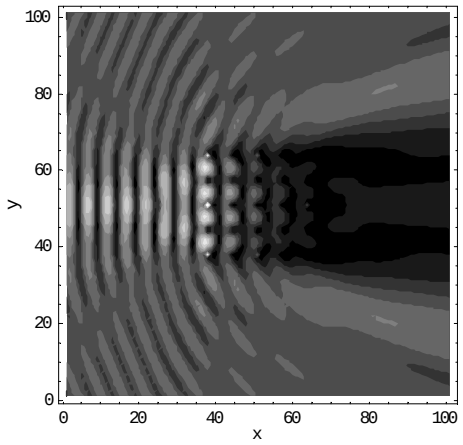

Fig.4 Electrical field distribution near the lattice.
(Area of 10 λx 10 λis shown)

The currents on the first lattice of thin wires cause reflection of the incident wave so that may form the standing wave superposing with the incident wave. As the scattering waves from the currents cancel the incident wave behind the lattice, the field amplitude is reduced to make shading. On the second lattice, the reduced field induces the less currents. The scattering waves of these currents also weaken the field behind the lattice. Other lattices make the same process so that the field behind of this lattice array can be suppressed to form the shade.

5. EM-WAVE SCREEN (EM-WAVE SUPPRESSION BY CONDUCTIVE STRIP ARRAYS)

Next, strip arrays shown in Fig.5 were analyzed to obtain the more shading-effectiveness. Each strip is made up with D conductive cylinders with separation d [m] between each other. The whole strip array is composed by 2N+1 or 2N strips piled up with the interval t [m] as shown in Fig.5.

One of the examples calculated for the incident wave of 100 micro-volts/m with the frequency of 2450MHz is shown in Fig.6 that is exhibiting the electric field strength distribution behind of the array whose parameters are d＝0.03 [m], t＝0.045 [m], D=10 and 2N+1=41.
In the picture, the electrical field distribution in the area of x:0.02～2.02[m], y:-2.0～+2.0[m] is given.

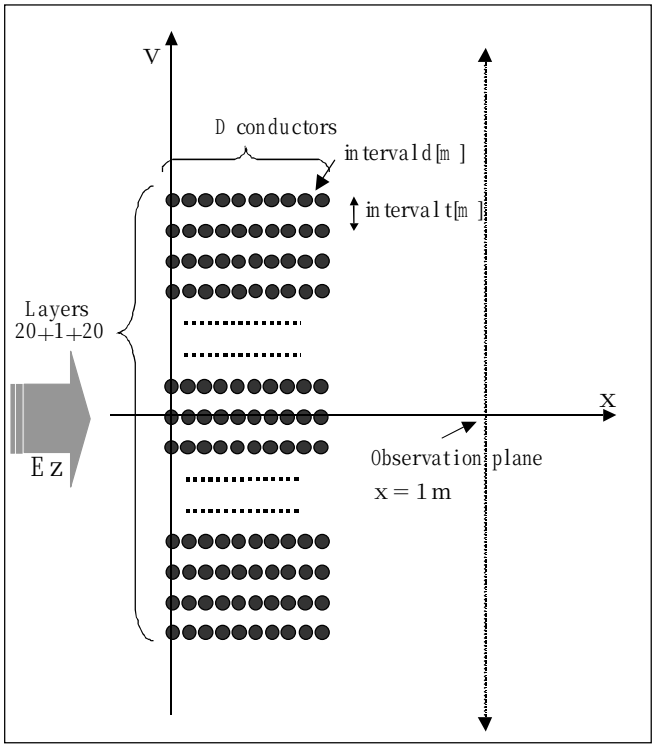

Fig.5 Structure of EM Screen

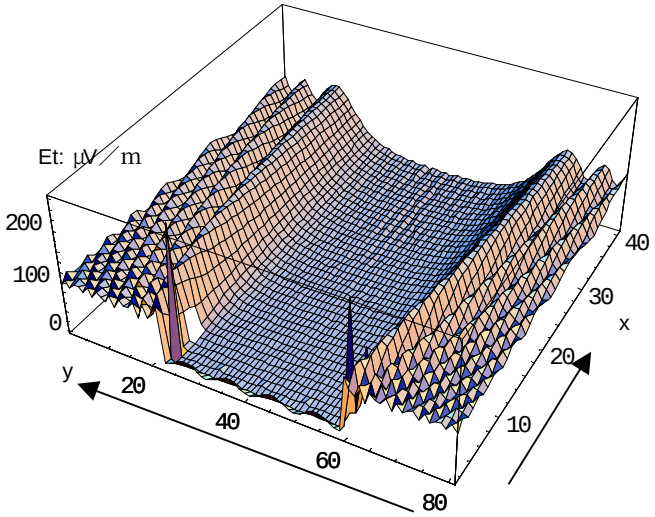

Fig.6 Electrical field distribution behind the EM screen

For the case of the array with D=10, d=t=0.03[m], calculations were achieved for the incident waves of several frequencies. The electric field strength on the line in parallel to y-axis and separating far from it by 1[m] were changed to the shading or suppression effect as given in Fig.7. The suppression effect for 2450MHz is more than 20dB.

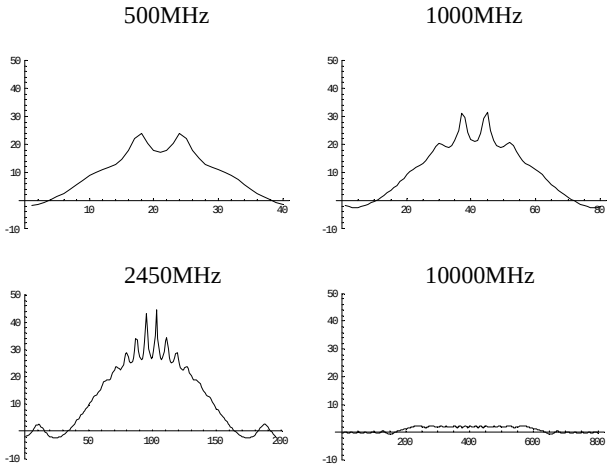

Fig.7 Field suppression effect of the EM screen (Vertical axes are in dB)

6. Experimental Evaluation Of Em-Wave Suppression

To confirm the effectiveness of the strip arrays to screen out the electromagnetic waves, several screens were constructed. The first model was composed by aluminum pipe of 1cm diameter. The second one was made of thin copper wires and the third one is formed with carbon fibers

The suppression effectiveness was estimated as follows. The screen was set between two DRG (double ridge guide horn) antennas using as a transmitting and receiving ones. The receiving antenna was moved up and down to record the receiving levels to draw the height patterns. The height patterns were recorded when the EM propagating path was interfered by the screen and when the screen was removed to make the free path. Those two patterns were compared and the averaged values of suppression effectiveness were estimated and used to make the graphs.

The shading or suppression effectiveness for these models is summarized in the following figures.

For the first model composed of aluminum pipes, shading effective ness is over 20dB for the frequency around 2.5GHz

The second model gave almost the same effectiveness but the suppression frequency range shifted to 1GHz or less. The carbon model gave the similar shading effectiveness in the same frequency range.

Fig.8 EM screen made of aluminum pipes with 1cm diameter and 2m lengths.

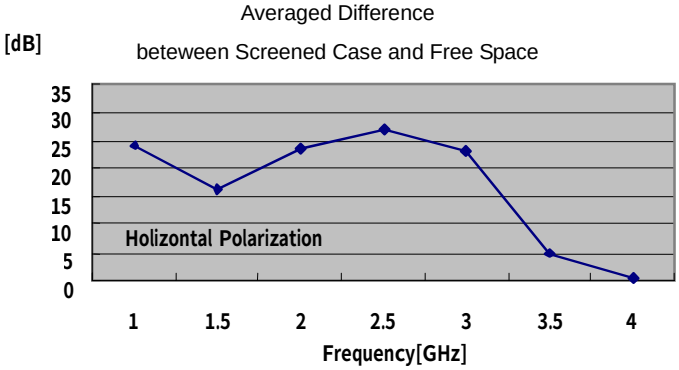

Fig.9 Suppression effectiveness of EM screen made of Al pipes of 10mm diameter.

7. Discussions

Electro-Magnetic (EM) Screens using the shade of multi-conductive rods (lattice), were tried to be developed since

the Electo-Magnetic environments in house or in rooms are becoming more complicated one and making the wireless communication equipments interfered each other. For examples, some one is using personal wireless LAN in his room and he uses daily the Microwave Oven to make his meal hot. To avoid the interferences, some screen should be used but it must not lose his sight and must not prevent air circulations in the room. To meet these requirements, conductive wire lattices were used to make the EM screen.

The experimental results show the enough effectiveness achieved using conductive pipe systems but it rather loses the sight. Thin wire lattices are good not to prevent the sights but it must be taken account that the frequency range of the suppression shifts to the lower band because the impedance (inductance) of the wires increase as the diameter ratio to the wave length reduces.

The experimental data are not exactly fit to the numerical analyses because the source of the incident waves are different; the analytical one is supposed to be plane waves and for the experiments, the point source was used.

And the height patterns changed their levels because the measurement room was not large enough. However, the inclinations of suppression effectiveness could be estimated well.

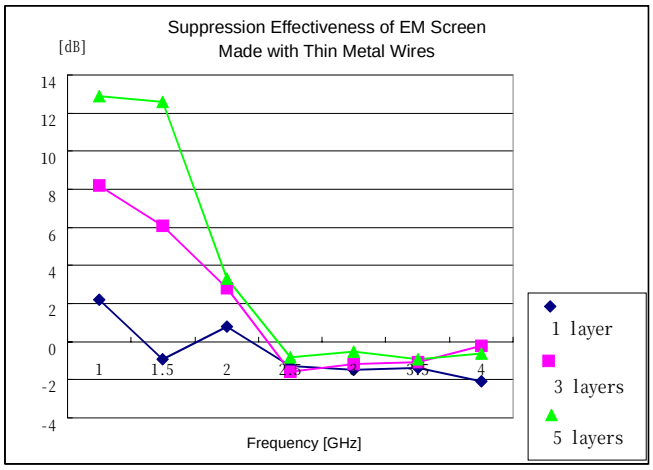

Fig.10 Suppression effectiveness of EM screen made of thin metal wires.

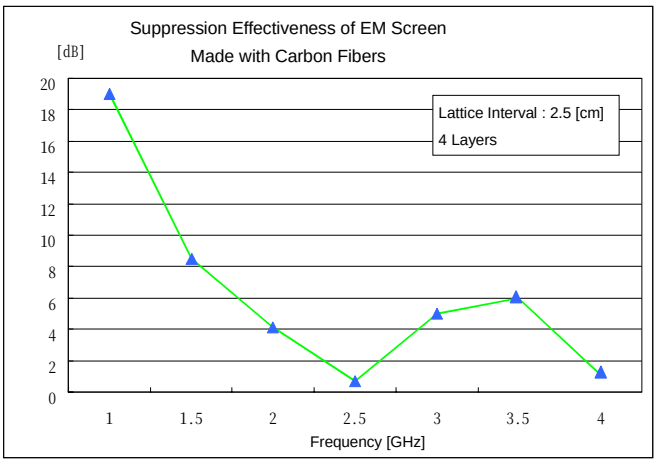

Fig.11 Suppression effectiveness of Carbon Fiber EM screen.

8. CONCLUSION

The scattering effect was analyzed numerically after the formulations were explained. The shading effects were tried to apply for the developments of EM-Screens, which can be used to suppress the interferences between wireless communications and the microwave apparatus in a room.

The experimental evaluations of EM-wave suppression behinds thin wires, especially for the near field area, have not been reported. This report gives some new evidences for thin wire scatterings. The results show the suppression effect of about 20dB in the band of 1GHz~3GHz for the constructed arrays of the thin wires.

REFERENCES

[1] T.Tsuchiya, H.Yamaguchi and Y.Kagawa,"Symbolic application to an electromagnetic wave problem--Scattering from wire array", Journal of the Japan Society for Simulation Technology, Vol.17, No.1,pp.59-68, (March 1998).

[2] Kouki Nakatsuka,"Scattering of Electromagnetic Waves", Springer-Verlag Tokyo (Nov. 1999).

[3] Harrington, "Time-Harmonic Electromagnetic Fields" MacGraw-Hill Book Company, Tronto, 1961.

[4] Kazuo Aizawa and Hiroshi Echigo,"EM Near Fields formed by Scattering of Multi-Wire Conductors under Illumination of TM Plane Wave", Proc. of IEEE Symposiumu on EMC/Boston, pp.307-312, (August 2003).

[5] A.Z.Elsherbeni, M.H.Al Sharkawy and S.F.Mahmoud, "Electromagnetic Scattering from a 2-D Chiral Strip simulated by circular Cylinders for uniform and nonuniform chirality distribution", IEEE Trans. on AP.,Vol.52, No.9, pp.2244-2252, (Sept. 2004).

[6] H.Echigo and K.Aizawa, "EM wave rejection effectiveness of multiple rod conductors" IEICE Tech. Rept. EMCJ2004-79, (Oct. 2004).

[7] A.Saito, T.Saito, K.Aizawa and H.Echigo "Experimental evaluation of EM wave supppressions by lattice arrays of metallic pipes" IEICE Tech. Rept. EMCJ2005-93, (Oct. 2005).

[8] A.Saito, T.Saito, K.Aizawa and H.Echigo "Experimental evaluation of EM wave supppressions by lattice arrays of conductive wires" IEICE Tech. Rept. EMCJ2005-148, (March 2006).

Dynamics of enhance-transmitted light beam through sub-wavelength slit

K. R. Chen, T. H. Tsai, J. Y. Lai, and J. S. Hong

Physics Department, Institute of Electro-optics, and Plasma and Space Science Center,

National Cheng Kung University, Taiwan, Republic of China

Abstract

The enhancement of light transmission through sub-wavelength slit is studied with our newly developed two dimensional simulation code of finite-difference time-domain method. The simulations verify the enhanced transmission that far exceeds the diffraction limit; the dynamics are helpful to understand in-depth the resultant beaming of light. Instead of one beam with a specific angle for a given wavelength [3-6], one additional beam with a different angle excited by the induced surface charge can be seen for the same wavelength from the electric field of different polarized direction. In additional to the interference of the scattered light with the transmitted light, the spatial de-coherence and coherence between the magnetic and electric fields is shown to be important for the transmitting process and the beaming mechanisms of the light. Thus, the dynamics will be illuminated in detail for deep understanding. The effect of different width of the exit groove on the enhanced transmission is also studied and explained as an application of above findings.

1. Introduction

Conventional diffraction theory predicts that the light can not pass a sub-wavelength hole because the amplitude of the transmitted light is scaled as the fourth power of the ratio of r/λ [1], where r is the radius of the hole and λ is the wavelength of the light. However, a recent experiment [2] shows an anomalous enhanced transmission of the light through the hole arrays of sub-wavelength scale. When the direction of the light is normal to the hole array, the intensity peak is measured; but, the light diffracts in all directions at each single hole. A more recent experiment [3] shows that the light can be confined as a divergent beam by patterning periodic grooves on the both sides of the surfaces. It is claimed that the beaming is at a specific angle for a given wavelength.

A theory [4] suggests that the formation of electromagnetic surface plasmon resonance causes the enhanced transmission. Another theory [5] indicates that the interference between the transmitted and the scattered (by the groove at the exit surface) lights is responsible for the beaming. In this paper, we study the dynamics of the transmission in order to understand the physics mechanisms and related electromagnetic phenomena with the emphasis on the electric and magnetic fields at and near the exit. An experiment of enhanced transmission of microwave radiation [6] shows good quantitative agreement with simulation result. Thus, we employ their case with a structure made of aluminum shown in Fig. 1, without loss of generality.

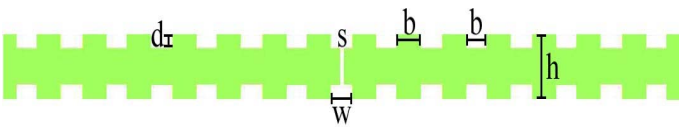

Figure 1. Periodic structure with a slit, where s=2mm, w=8mm, d=4mm, b=8mm, and h=16mm.

In the section 2, we will study the dynamics of the transmitted electric and magnetic fields. It is shown two beams with different angles can exist for a given wavelength. The de-coherence of the fields at the exit and their re-coherence near the exit will be studied in the following section. The exit groove width affects the electric and magnetic fields and thus on the transmission, and will be investigated in Sec. 4. Section 5 is the summary.

2. Dynamic of the light transmission and dual angles for a given wavelength

The experimental [3, 5, 6] and theoretical [4, 5, 6] results suggest that there is only one beaming angle of the enhanced transmission for a given wavelength. However, this is not what we have observed from our simulation.

In our finite difference time domain (FDTD) simulation, 1200x1200 cells are used with the cell size of 0.2mm. The incident plane light of constant amplitude normalized to be unity with the wavelength of 20.5 mm is sent from the top and propagating in the $-e_2$ direction. The electric (magnetic) field is polarized in e_1 (e_3, out of paper) direction to the right.

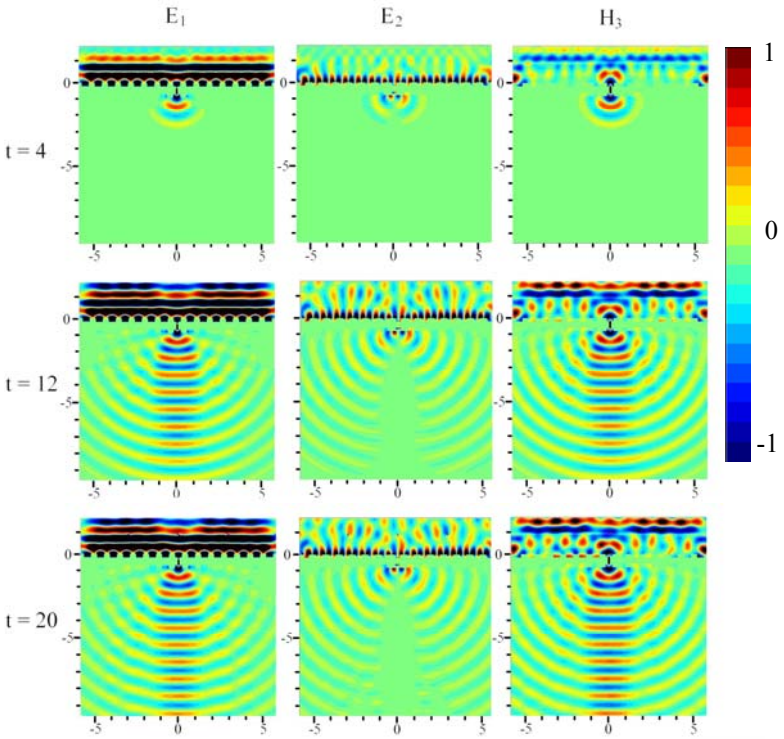

Figure 2. The E_1, E_2 and H_3 fields in (x,y) at time t= 4, 12, 20.

Figure 2 shows the contour plots of the electric E_1, E_2 and magnetic H_3 fields at different times. At time t=4, normalized to the period of the incident light, the light is just transmitted through the slit. The E_1 and H_3 fields are almost coherent, except near the exit surface, and peaks at the center (i.e., the line along x=0); that is, the direction of the beamed light is in the $-e_2$ direction so that the beaming angle is zero. However, there are E_2 fields extends from the metal groove at the exit surface. Later at t=12, the wave front of the light has reached the bottom boundary of the system. The contour plots of the E_1 and H_3 fields clearly demonstrate a beamed light is formed with a zero beaming angle. They reaches a state steady at t=20. However, from the contour plots of the E_2 field, we know that there is another wave propagating with the beaming angle of about 60 degree. This light is produced by the surface charge and current at the corrugated surface. Even, it is weaker here, but, it is notable. This also explains the fine structures of the E_1 and H_3 fields near 60 degree. Thus, there are two beamed lights produced for a given wavelength.

The corresponding E_1 and H_3 fields along the center at the different times are shown in Fig. 3. The wave fields are slowly built up from the front because the spatial curl of magnetic (electric) field is needed for the temporal changing of electric (magnetic) field, as indicated by the Maxwell equations. The wave amplitude reaches a constant and remains the same at the steady state. It is interesting to note that the electric and magnetic fields are not coherent within the slit and becomes coherent soon after the exit. Also, the

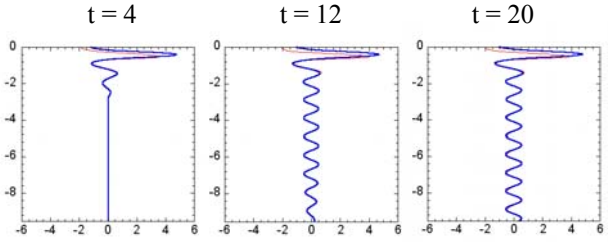

Figure 3. The electric E_1 (thin red) and magnetic H_3 (thick blue) along x=0 at the time of 4, 12, and 20.

amplitude of the electric field within the slit is higher than that of the magnetic field; both are much higher than unity (or that of the incident light) because of the induced surface charge and current.

3. De-coherence and re-coherence of the electric and magnetic fields near the exit

The dynamics of the wave fields near the exit surface is useful to understand the process of the de-coherence and the re-coherence of the electric and magnetic fields. Figure 4 shows the contour plots of the electric and magnetic fields near the exit surface in an area of 240x240 cells at the times of t = 2.2, 2.6 and 3.0, respectively, for the transmission of the first wavelength of the wave front. At t=2.2, the light has already transmitted through the slit. The E_1 and H_3 fields within the slit are coherent and uniform in x. Right at the slit exit and within the groove, the electric and magnetic begin to de-coherent because of the different boundary conditions required at the metal surface. The E_1 field diffracts and is perpendicular to the metal surface of the groove; that is, it is almost zero at the upper boundaries of the groove and strong at the side boundaries. The surface plasma (or charge) excited has produced the E_2 field extended from the upper metal surface. The H_3 field is strong near all the metal surfaces and is weak at the center. The E_1 field being positive indicates the left (right) hand side of the slit is with positive (negative) charge and the resultant current. Positive (negative) charge induces negative (positive) E_2 field. The currents resulted from the movement of the positive charge at the left hand side and the negative charge at the right hand side induce positive magnetic field H_3. At t=2.6, the fields have propagated out of the groove. The E_1 field has diffracted to have an oral shape while the H_3 field is in a shape of half circle; the difference in shaping is due to the boundary condition requirements of the metal surface at the groove exit. Again, the E_2 field is produced by the induced surface plasma. At t=3.0, both the E_1 and H_3 fields have propagated out of the groove metal surface. At the free space, they have managed to be in about the same shape; that is, they have re-established the coherence. It is interesting to note that the E_2 field can be detached from the metal surface. This creates the possibility for the radiation of the E_2 field later as observed in Fig. 2.

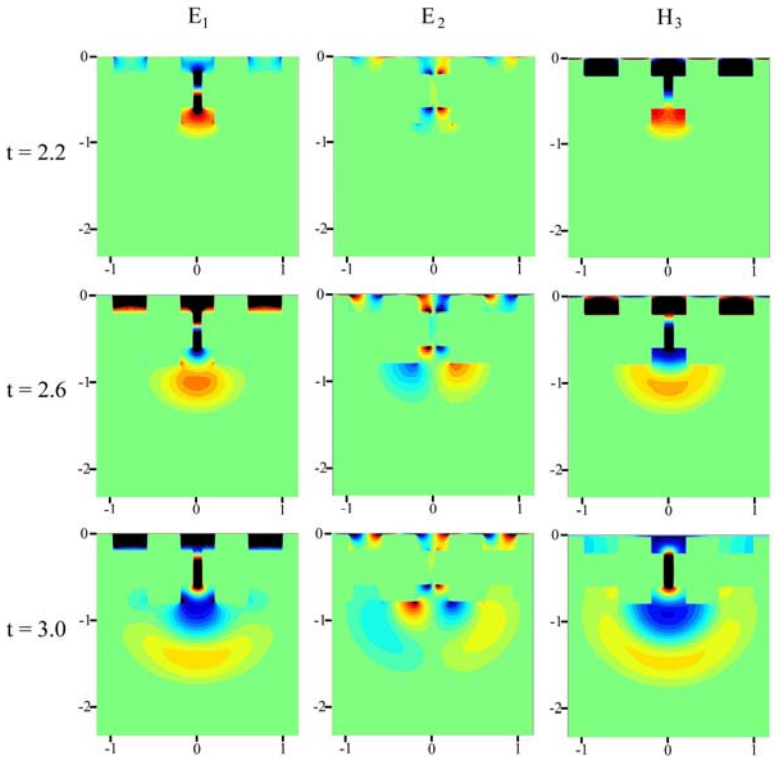

Figure 4. The E_1, E_2 and H_3 fields in (x, y) near the exit surface at time t = 2.2, 2.6, and 3.0.

4. Effect of the exit groove width on the enhanced transmission

The effects of the width of the slit and the groove at the exit on the enhanced light transmission are studied. The slit width does not have notable effect on the transmitted light, while the exit groove width does. The original groove width is 8mm. Only the exit groove

width is changed to 4mm and 16 mm, while all other groove widths remain the same. The increase of the exit groove width is at the expenses of the width of the corrugated exit surface. Figure 5 shows the contour plots of the electric and magnetic fields for the exit groove width being 4mm, 8mm and 16mm, respectively, at the end of the simulation at t=20. For smaller exit groove width, both E_1 and H_3 fields near the exit exhibit two peaks symmetrical about the center in one angle, and then they are merged to one peak with the angle decreased to zero at far field. The fields at the exit are flat for larger exit groove width.

When the exit groove width is smaller, the width of corrugated surface is larger. Small exit groove width would make the E_1 and H_3 fields exiting like a point source that will diffract at all directions. However, the magnetic field produced by the surface current at both sides of the corrugated surfaces forms a arc that is stronger near the corrugated surface. The combination of these fields generates the E_1 and H_3 fields with two peaks near the exit surface. The effect of the magnetic field produced by surface current is much weaker at far field so that the fields becomes one peak at the center (i.e., the beaming angle is zero.) For larger exit groove width, the width of the corrugated surface is smaller. Large exit groove width let the E_1 and H_3 fields exit somehow like a plant wave. Also, smaller corrugated surface has less surface current to produce magnetic field. Thus, the profile of the E_1 and H_3 fields is flat.

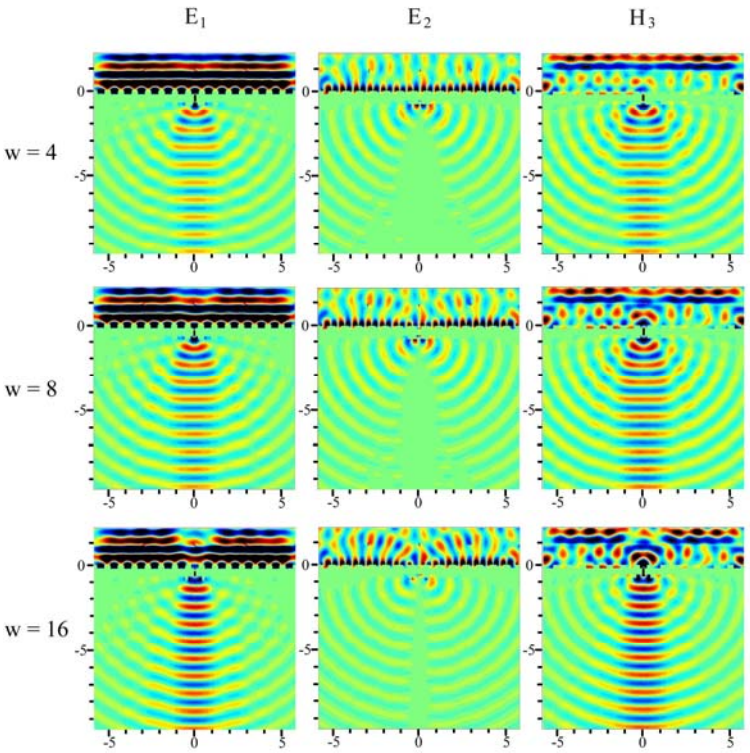

Figure 5. The E_1, E_2 and H_3 fields under different exit width w = 4 mm, 8 mm, 16 mm.

Regarding the E_2 field, smaller (larger) exit groove width produces stronger (weaker) field amplitude and smaller angle of the field cone. Since the E_2 field is produced by the surface charges on the corrugated surface, larger exit groove width makes the width of the corrugated surface smaller and thus less surface charges available and the field is weaker. Also, smaller corrugated surface width is more like point source so as to have larger diffraction angle (and the angle of the field cone.)

5. Summary

The dynamics of the enhanced transmitted light beam through sub-wavelength slit is studied with FDTD simulation. The physical process and mechanism are discussed in-depth. As in contrast to previous results, a light beam with its electric field polarized at different direction can be produced by the surface charge (and current), in additional to the transmitted light beam. The de-coherence and re-coherence of the electric and magnetic fields is due to the different requirements of the boundary conditions of metallic surface. The dynamics is

illuminated in details. As an application of these new findings, the effect of the exit groove width is investigated and explained.

Acknowledgement:

This work was supported by National Science Council of Taiwan under contract NSC# 94-2112-M-006-012 and by Ministry of Economic Affairs of Taiwan under contract MOEA# 94-EC-17-A-08-S1-0006.

REFERENCES:

1. H. A. Bethe, "Theory of diffraction by small holes", *Phys. Rev.* 66, 163 (1944).
2. T.W. Ebbesen *et.al.,* "Extraordinary optical transmission through sub-wavelength hole arrays", *Nature* 391, 667 (1998).
3. H. J. Lezec, *et. al*., "Beaming light from a subwavelength aperture" *Science* 297, 820 (2002).
4. L. Martin-Moreno, *et. al*., "Theory of Highly Directional Emission from a Single Subwavelength Aperture Surrounded by Surface Corrugations", *Phys. Rev. Lett.* 90, 167401 (2003).
5. Liang-Bin Yu, *et. al*., "Physical origin of directional beaming emitted from a subwavelength slit", *Phys. Rev. B* 71, 041405 (2005).
6. S. Sena Akarca-Biyikli, *et. al*., "Enhanced transmission of microwave radiation in one dimensional metallic gratings with subwavelength aperture", *Appl. Phys. Lett.* 85, 1098 (2004).

PIERS 2006, Aug. 2-5, in Tokyo, Japan

The quantum yield of a metallic nanostructure of dimer

Jiunn-Woei Liaw

Department of Mechanical Engineering, Chang Gung University,
259 Wen-Hwa 1st Rd., Kwei-Shan, Tao-Yuan, 333, Taiwan
email: markliaw@mail.cgu.edu.tw
TEL: 886-3-2118800 ext 5742 FAX: 886-3-2118050

Abstract

In this paper, a nanostructure of a metallic dimer is studied, which consists two nearby metallic nanoparticles, to find the possibility for the enhancement of a single molecule's fluorescence by this nanostructure. A simple model, an oscillating dipole within the gap of a metallic dimer, is used to simulate an excited molecule interacting with the dimer in the frequency range of UV to NIR. With the aid of a set of new surface integral equations, the electromagnetic fields in the proximity of the dimer are solved by the boundary-element method (BEM). The quantum yield, the ratio of the radiative power to the total power generated from the dipole, is used to evaluate the efficiency of the dipole's emission. The results of BEM show that the quantum yield of a metallic dimer is better than a single nanoparticle, even though the gap is very small. In addition, a metallic dimer behaves like a low-pass filter which allows most of the dipole's energy of the long-wavelength part radiate to the far field. In contrast, for the short-wavelength part, the nonradiative part is dominant; i.e. most of the dipole's energy is dissipated into Joule's heat inside the metallic dimer in high-frequency range. Two noble metals, Au and Ag, are used for the dimer, and both of them exhibit the same tendencies.

1. Introduction

Using a nanostructure (e.g. nanophotonics, or nanocavity) to enhance the fluorescence of a single molecule attracts considerable attention recently. In particular, several metallic nanostructures, e.g. metallic colloid [1], nanoprobe [2], dimer and nanoantenna [3], were proposed. The original idea is to utilize the surface plasmon resonance (SPR) effect of metallic nanostructures to induce a strong local electric field for the excitation of molecules in its vicinity, when the whole system is illuminated by a light. However some of the experimental results [4] show that the metallic nanostructure could cause a quenching, instead of an enhancement, on the

molecule's fluorescence. For example, a dye-molecule attached to a spherical gold nanoparticle was tested, and a severe suppression of the dye's fluorescence was observed [4]. The phenomena could be attributed to the poor quantum yield of the nanostructure on the fluorescence, even though the electric field in the proximity of the metallic nanoparticle is strong. Recently, a metallic dimer (a pair of nearby nanoparticles) and a nanoantenna (two aligned nanowires) [3] structures were studied, and could be useful for the purpose of the fluorescence enhancement. The common characteristics of the two structures are on the strong local field within the gap and on the symmetric structure for radiation. In order to realize the role of these two nanostructures play, we focus on the study of the metallic dimer to identify the mechanism for the enhancement or the quenching on molecule's fluorescence. Consider a molecule is placed in the gap of a dimer at the beginning, and is illuminated by an incident light, as shown in Fig. 1(a). Before being illuminated, the electrons of the molecule are at their ground states. When the molecule and the dimer are illuminated by the light, most of the light's energy will be focused on the proximity of the metallic nanostructure, and a portion of the light's energy could be absorbed by the molecule to pump the electrons to an excited state, and then the electrons return to their ground states to emit the fluorescence. At the initial stage, the local field factor K [5, 6], which is the ratio of the local electric field to the incident wave, can be used to evaluate the electric-field amplification in the proximity of the metallic nanostructure. Once the molecule is excited, it can be modeled simply by a dipole. At that stage, the interaction of the dipole with the dimer is concerned, as shown in Fig. 1(b). The quantum yield [5, 6] can be used to evaluate how much of the energy generated from the dipole can be delivered to the far field for detection. In order to calculate the near-field distribution, a set of new surface integral equations [7] are derived from the Stratton-Chu formulation for a 2D TM mode problem, and it is solve by boundary-element method (BEM) in the frequency range of UV to NIR.

2. Theory

Consider a dimer with a multi-connected boundary, $S_1 = S_{12} \cup S_{13}$, embedded in a domain Ω_1 (exterior), which is an infinite dielectric medium (host) with a boundary $S_1 \cup S_\infty$. From the Stratton-Chu formulation, a set of new surface integral equations [7] is derived for a 2D TM mode problem,

$$H_z(\mathbf{x}) = H_z^i(\mathbf{x}) - \sum_{j=2}^{3} [\int_{S_{1j}} H_z(\mathbf{x}')\mathbf{n}' \cdot \nabla'(G_1 - G_j)\, dl' + \mathrm{i}\omega \int_{S_{1j}} E_t(\mathbf{x}')(\varepsilon_1 G_1 - \varepsilon_j G_j)\, dl'], \ \mathbf{x} \in S_1$$

PIERS 2006, Aug. 2-5, in Tokyo, Japan

(1)

$$D_n(\mathbf{x}) = D_n^i(\mathbf{x}) - \sum_{j=2}^{3}[\mathrm{i}\omega\int_{S_{1j}}(\varepsilon_1\mu_1 G_1 - \varepsilon_j\mu_j G_j)H_z\mathbf{n}\cdot d\mathbf{l}' + \int_{S_{1j}} D_n\mathbf{n}\cdot\nabla'(G_1 - G_j)dl' - \int_{S_{1j}} E_t\mathbf{n}\cdot\mathbf{e}_z\times\nabla'(\varepsilon_1 G_1 - \varepsilon_j G_j)\,dl'], \quad \mathbf{x}\in S_1 \tag{2}$$

$$E_t(\mathbf{x}) = E_t^i(\mathbf{x}) - \sum_{j=2}^{3}[\mathrm{i}\omega\int_{S_{1j}}(\mu_1 G_1 - \mu_j G_j)H_z\mathbf{t}\cdot d\mathbf{l}' + \int_{S_{1j}} D_n\mathbf{t}\cdot\nabla'(\frac{G_1}{\varepsilon_1} - \frac{G_j}{\varepsilon_j})dl' - \int_{S_{1j}} E_t\mathbf{t}\cdot\mathbf{e}_z\times\nabla'(G_1 - G_j)\,dl'], \quad \mathbf{x}\in S_1 \tag{3}$$

where the Green functions G_j are the singular solutions of Helmholtz equations of medium j, j=1, 2, 3. The permittivity ε_j and the permeability μ_j of medium 2 and 3 are the same. These equations in terms of the surface components of the tangential magnetic field H_z, the normal displacement field D_n and the tangential electric field E_t can be solved systematically along the multi-connected interfaces of the two scatterers and the host by using the boundary-element method (BEM). Eqs. (1) to (3) belong to Fredholm equations of the second kind, so that their numerical stabilities are well.

3. Local field factor &quantum yield [5,6]

The definition of the local field factor is the ratio of the amplitude of the local electric field at the location of the molecule to the incident plane wave. The quantum yield η of the whole system is defined as the ratio of the radiative power to the total power generated from the dipole,

$$\eta = \frac{P^r}{P^r + P^a} \tag{4}$$

Since the metallic nanostructure is a dissipative system, the other energy will be absorbed by the metal and be converted into heat, which is the so-called nonradiative part. The local field factor, a function of frequency, can be regarded as the transfer function for the nanostructure to excite a molecule, while the quantum yield can be regarded as the transfer function of the nanostructure on the excited molecule's radiation. Both are the intrinsic properties of the nanostructure but independent of the molecule. However, to evaluate whether the nanostructure is for the enhancement of fluorescence or for the quenching, we need to consider both effects of the molecule's excitation and molecule's emission. The former is related to the combination of the

local field factor of the nanostructure and the absorption spectrum of the molecule. The latter is related to the combination of the quantum yield of the nanostructure and the emission spectrum of the molecule.

4. Numerical results & discussion

Consider a dimer composed of two nanoparticle of radius r=20nm (or 40nm) with a gap of d=5nm (or 10nm). A dipole is placed at the center of the two circular nanoparticles to interact with the dimer. Two noble metals, Au and Ag, are used for the dimer. Figure 2 shows the quantum yield versus the frequency for a dipole within an Au-dimer embedded in air. The quantum yield versus the frequency for a dipole within an Ag-dimer embedded in air is plotted in Figure 3. The results illustrate a metallic dimer behaves like a low-pass filter which allows the dipole's energy of the long-wavelength part radiate to the far field, but suppresses the short-wavelength part. This is to say the high-frequency photons will be dissipated into Joule's heat inside the metallic dimer. Normally, the quantum yields of Ag-dimer are better than Au-dimer, because the imaginary parts of permittivity of the Au are relatively larger than that of Ag. Furthermore, the cut-off frequency of Ag-dimer is higher than Au-dimer. These curves also indicate that the larger the gap, the higher the quantum yield is. However considering the local electric field enhancement, a small gap is preferred for the excitation of the molecule. Therefore it is a trade-off problem which has an optimal configuration for the nanostructure.

5. Conclusion

The results of BEM show that the quantum yield of a metallic (Au and Ag) dimer is like a low-pass filter which allows most of the dipole's energy of the long-wavelength part radiate to the far field. However, for the short-wavelength part, the nonradiative part is dominant; i.e. most of the dipole's energy is dissipated into Joule's heat inside the metallic dimer in high-frequency range. In comparison with a single nanoaprticle, a dimer structure is superior in both the electric field enhancement and the quantum yield for a dipole.

Acknowledgement

This research was supported by National Science Council, Taiwan, R.O.C. (Grant: NSC95-2221-E-182-002).

REFERENCES

PIERS 2006, Aug. 2-5, in Tokyo, Japan

1. R. Carminati, J.J. Greffet, C. Henkel, and J.M. Vigonreux, Optics Comm. (2006) (in press)
2. H. G. Frey, S. Witt, K. Felderer, R. Guckenberger, Phys. Rev. Lett. **93**, 200801 (2004).
3. P. Muhlschlegel, H.-J. Eisler, O.J.F. Martin, B. Hecht, and D.W. Pohl, Science **308**, 1607-1609 (2005).
4. E. Dulkeith, A.C. Morteani, T. Niedereichholz, T.A. Klar, J. Feldmann, S.A. Levi, F.C.J.M. van Veggel, D.N. Reinhoudt, M. Moller, D.I. Gittins, Phys. Rev. Lett. **89**, 203002 (2002).
5. J. Azoulay, A. Debarre, A. Richard and P. Tchenio, Europhys. Lett. **51**, 374-380 (2000).
6. M. Thomas, J.-J. Greffet, R. Carminati, and J.R. Arias-Gonzalez, Appl. Phys. Lett. **85**, 3863-3865 (2004).
7. J. W. Liaw, J. Opt. Soc. Am. A **23**(1), 108-116 (2006).

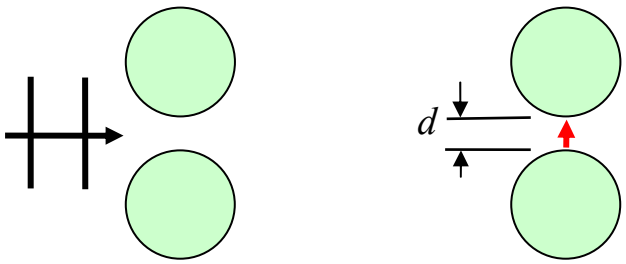

Figure 1. The configuration of a metallic dimer interacting with (a) an incident wave, and (b) a dipole.

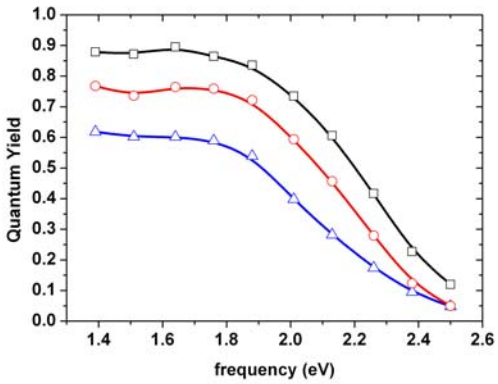

Figure 2. The quantum yield of a dipole within a gold dimer in air versus frequency; the square: r=40nm, d=10nm; the circle: r=40nm, d=5nm; the triangle: r=20nm, d=5nm.

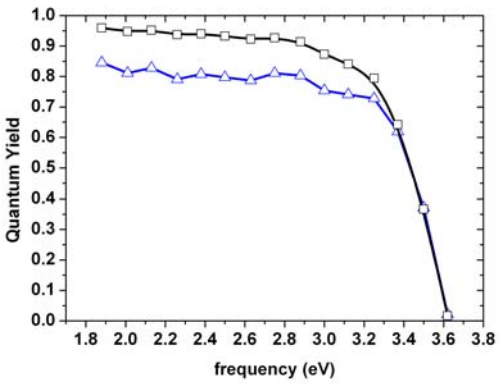

Figure 3. The quantum yield of a dipole within a silver dimer in air versus frequency; the square: r=40nm, d=10nm; the triangle: r=20nm, d=5nm.

Five-Band Microwave Radiometer System For Non-Invasive Measurement of Deep Brain Temperatures In Newborn Infants : First Phantom Measurement Study

T. Sugiura, S. Hoshino, Y. Sawayama, Y. Okita, H. Hirata, S. Mizushina*

Research Institute of Electronics, Shizuoka University, 3-5-1 Johoku, Hamamatsu 432-8011, Japan
*TAO Hamamatsu Lifeline Research Center, 621 Irino, Hamamatsu 432-8511, Japan
Phone: +81-53-478-1328, Fax: +81-53-478-1333, E-mail: sugiura@rie.shizuoka.ac.jp

Abstract — A five-band microwave radiometer system has been developed for non-invasive temperature measurement of deep brain tem- peratures in newborn infants. Center fre- quencies of five receivers are 1.2, 1.65, 2.3, 3.0 and 3.6 GHz with 0.4 GHz bandwidth each. The system with a waveguide antenna are calibrated using a water-bath, and temper- ature resolutions were 0.28 K (1.2 GHz), 0.32 K (1.65 GHz), 0.16 K (2.3 GHz), 0.11 K (3.0 GHz) and 0.12 K (3.6 GHz receiver). Using this system, we made the first temperature measurement experiments on a phantom which simulated the temperature profile of infant's brain. Results of the experiments showed that the experimental five-band radiometer system was capable of estimating the temperature distributions in the brain over a depth up to 5 cm with a confidence interval of ± 0.8 K. With this encouraging result, we now believe that it is possible to develop non-invasive thermometry based on the principles of multi-frequency microwave radiometry for monitoring deep brain temperatures with an accuracy of ± 0.5 K.

Keywords— microwave radiometry, brain temperature, hypothermia, non-invasive thermometry, baby

1. Introduction

It has been shown recently that cooling the brain of newborn baby can reduce neuro-developmental impairment after a hypoxic-ischaemic insult[1,2]. However, clinical trials are currently hindered by the difficulty in measuring brain temperature non-invasively as well as continuously. MRI and MR spectroscopy methods have been used to measure temperature changes in the brain [3, 4]. These require access to complex equipment and they are not suitable for routine measurements repeated over a prolonged period of time.

Possible alternative method for non-invasive temperature sensing and monitoring that is completely passive and inherently safe is microwave radiometry (MWR). Multi- frequency MWR has been investigated for non-invasive thermometry, and a number of methods have been reported including a model-fitting method combined with a Monte Carlo technique to retrieve a temperature profile together with the confidence intervals by Mizushina et al [5]. Feasibility studies of MWR for this purpose have been made recently especially on a temperature retrieval algorithm [6,7].

This paper describes the first temperature measurement experiments on a phantom which simulated the temperature profile inside baby's head. Estimated temperature at 5 cm from the surface was compared with that measured by a thermocouple probe. Confidence interval, which is the accuracy of estimation, is also described.

2. Microwave Radiometry

MWR measures the power in the microwave region of the natural thermal radiation from body tissues to obtain the brightness temperature $T_{B,i}$ of the tissue under observation. $T_{B,i}$ is

$$T_{B,i} = \frac{P_i}{k\Delta f_i} = \frac{(1-R_i)P_{tissue,i}}{k\Delta f_i} = (1-R_i)T_{B,tissue,i} \quad (1)$$

where $P_{tissue,i}$ is the thermal radiation power emitted by the tissue, P_i is the power received by a waveguide antenna in a bandwidth Δf_i around a center frequency of f_i, R_i is the reflection coefficient at the skin-antenna interface at f_i and k is Boltzmann's constant. Using the radiometric weighting functions $W_i(\boldsymbol{r})$, The measured brightness temperature is

$$T_{B,meas,i} = T_{B,tissue,i} = \frac{1}{1-R_i}\iiint_{afv} W_i(\boldsymbol{r})T(\boldsymbol{r})dv \quad (2)$$

and the integration is over the antenna's field of view (afv). $T(\boldsymbol{r})$ is the absolute temperature in an incremental volume of tissue dv located at the distance $\boldsymbol{r}$ from the surface. $W_i(\boldsymbol{r})$ is obtained by specific absorption rate (SAR) calculating electromagnetic field distribution. FDTD method was used to obtain SAR. A priori knowledge from thermal modeling ($T_{B,model,i}$) is used on the temperature profile in brain [8]. Estimated temperature profile is achieved by minimizing the error function,

$$Error = \sum_{i=1}^{n}\left(T_{B,\mathrm{model},i} - T_{B,meas,i}\right)^2. \quad (3)$$

3. Five-Band Radiometer System

Figure 1 schematically shows a five-band radiometer system. A single dual-polarized wavegudie antenna which is filled with high permittivity, low loss material is used to cover the entire frequency range (1.0 - 3.8 GHz). Dicke switches are used to compare the power from antenna with that of RNS, of which temperature is controlled by PC to equalize both powers. The whole system operates in a normal room and at normal room temperature.

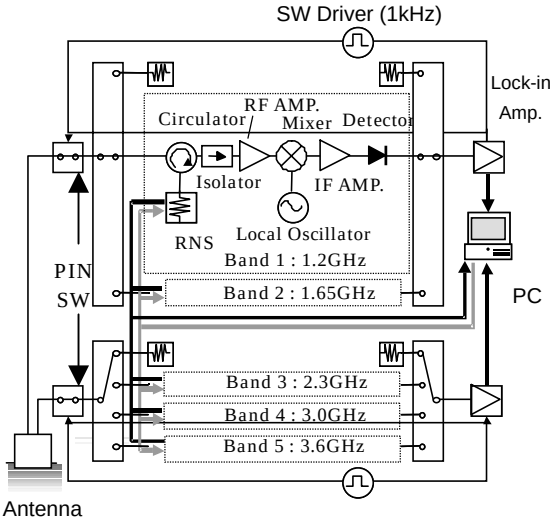

Fig.1 Five-band radiometer system [7].

The system consists of five Dicke receivers which have each reference noise source (RNS). A contact type waveguide antenna is used. PC balances the incoming power through the antenna and that of RNS adjusting the Peltier element attached to the RNS.

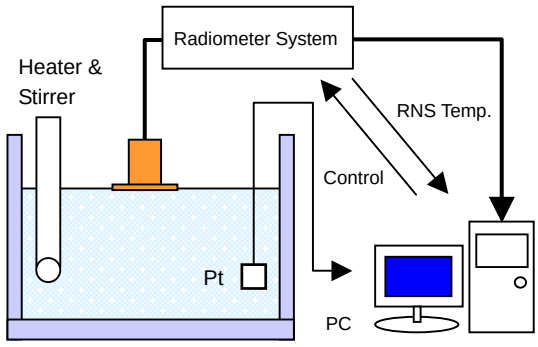

Fig.2 Setting of calibration experiment.

Water-bath temperature was increased very slowly, and both the brightness temperature and the water temperature were recorded in PC.

4. Temperature Measurement Experiments

System Calibration

The radiometer system was calibrated by measuring the brightness temperature of a water-bath which was stirred to maintain a uniform temperature. Figure 2 shows the setting of calibration experiment. and Typical result of the calibration is presented in Fig.3 (2.3 GHz receiver).

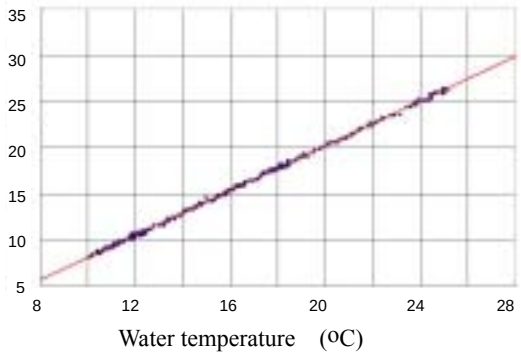

Fig.3 Typical result of system calibration.

Standard deviation at each temperature is defined as the temperature resolution.
Abscissa: water-bath temperature given in oC.
Ordinate: RNS temperature given in oC.

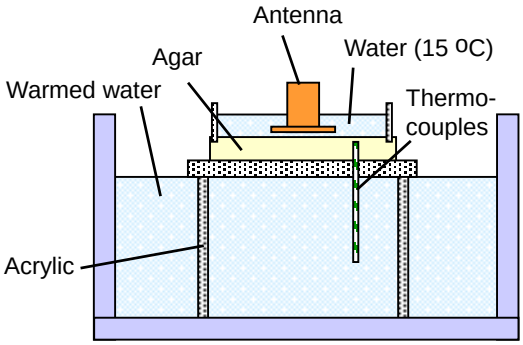

Fig.4 An arrangement for measurement experiment.

Temperature profile phantom consists of water, acrylic and agar. Agar surface was cooled by water (15 oC).

Temperature resolutions obtained from the calibration results for five receivers are listed in Table 1. Theoretical resolution is given by system noise temperature T_{sys}, brightness temperature $T_{B,obj,i}$, bandwidth Δf_i and integration time constant τ, and

$$\frac{2(T_{B,obj,i}+T_{sys,i})}{\sqrt{\Delta f_i \tau}}. \qquad (4)$$

Table 1 TEMPERATURE RESOLUTIONS

Receiver (GHz)	Resolution (K)	Theoretical (K)
1.2	0.28	0.02
1.65	0.32	0.02
2.3	0.16	0.36
3.0	0.11	0.04
3.6	0.12	0.04

Temperature Measurement Experiment

Using the five-band radiometer system and data analysis procedure described above, we made a temperature measurement experiment on phantom. An arrangement of brain temperature profile phantom is illustrated in Fig.4 (without antenna).

Temperature profile was measured by thermocouple probes. The water tempera- ture in the bath and the

thicknesses of agar and acrylic were adjusted so that the tem- perature profile was similar to that in infant's brain. Radiometric weighting functions were obtained by calculating SAR distribution in the phantom.

A waveguide antenna was placed on the cooling bolus (water) as shown in Fig.3, and the brightness temperature were meas- ured by the system. Once the measurement was initiated, the steps including the frequency selection, the feedback control to keep $T_{B,obj,i} = T_{RNS}$ and data acquisition are executed automatically.

Temperature profile in a phantom was retrieved using measured brightness tem- peratures and the data analysis procedure which we have proposed previously[6]. The result is shown in Fig.5. Blue solid line is an estimated temperature profile while red line is an interpolated profile obtained from thermocouple readings. Green dotted lines indicates confidence interval. Red dots are thermocouple readings.

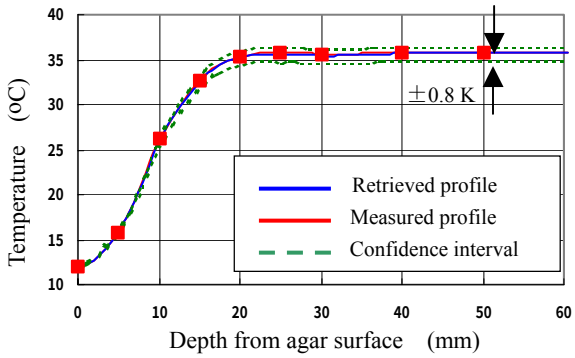

Fig.5 Retrieved temperature profile in phantom.
Accuracy at 5 cm depth (assumed to be the center of infant's brain) was ±0.8 K. Abscissa: depth from agar surface. Ordinate: estimated temperature given in ºC.

5. Conclusions

This study shows the first measurement result using a five-band microwave radio- meter system operating in a normal room (not in a shielded room) at room tempera- ture. The result shows that this system at the present stage is capable of estimating the temperature distributions in the brain over a depth up to 5 cm with a confidence interval of ±0.8 K. Since the realistic requirement from clinical work front for accuracy is ±0.5 K, we now believe that it is possible to realize non-invasive thermo- metry based on the principles of multi-frequency microwave radiometry for monitoring deep brain temperatures.

Future work will include further reduction of the system thermal noise and further thermal insulation of the system.

Acknowledgement

This work was supported in part by the Grant-in Aid for Scientific Research, No.13650460, the Ministry of Education, Culture, Sports, Science and Technology.

REFERENCES

[1] F.Colbourne et al, J Neurosci, vo.15, pp. 7250-7260, 1995.

[2] E.Sirimannc et al, "Pediatr Res, vol 39, pp.591-597, 1996.

[3] E.B. Cady et al., *Magn.Reson.Med*., vol.33, pp. 862-867, 1995.

[4] R.J. Corbett, et al., *J. Neurochem*., vol. 64, pp. 1224- 1230, 1995.

[5] S.Mizushina et al, J Electromagnetic Waves Appl, vol..7, pp.1515-1548, 1993.

[6] K.Maruyama, et.al., IEEE Transactions on Microwave Theory and Techniques, vol.48, pp.2141-2147, 2000.

[7] T.Sugiura et.al, Proceedings of 2004 Annual Conference of IEEE EMBS (San Francisco), pp.2292-2295, 2004.

Study of Appropriate Number of Receivers in Microwave Radiometry Based on Changes of Tissue Electric Constants

Y. Sawayama, S. Hoshino, H. Hirata, Y. Okita, M. Kimura, T. Sugiura

Research Institute of Electronics, Shizuoka University, 3-5-1 Johoku, Hamamatsu 432-8011, Japan

Phone: +81-53-478-1328, Fax: +81-53-478-1333, E-mail: sugiura@rie.shizuoka.ac.jp

Abstract: Multi-frequency microwave radio- metry (MWR) has been proposed as one of the promising methods for non-invasive moni- toring of deep brain temperatures. This paper investigates an appropriate number of radio- meter receivers to realize an accuracy of ± 0.5 °C at 5 cm depth from head surface consider- ing the changes or estimation error of tissue dielectric properties of brain. Results show that it is not a good choice to reduce the num- ber of receivers to three, but five receivers are desirable.

Keywords: microwave radiometer, tissue dielectric constant, non-invasive thermometry, brain temperature

1. Introduction

It has been reported that hypothermal neural rescue therapy is effective method for a treatment of newborn infants who have suffered hypoxia-ischaemia [1]. Although in this hypo- thermia therapy, the deep brain temperature must be monitored non-invasively and continuously, no technique is available in the world today. We have studied five-band microwave radiometry which receives thermal radiation from brain tissues and retrieves the temperature profile in brain, and have demonstrated its feasibility of non-invasive monitoring of brain temperature [2,3]. However, the appropriate number of radiometer receivers has not been examined.

This paper investigates the feasibility of reducing the number of receivers, for example from five to three, which means smaller system, in light of brain tissue variation or estimation error during hypothermic therapy.

2. Theory

Microwave radiometry is a method that receives thermal radiation from body tissues and obtains the brightness temperature, which has been widely used in radio astronomy [4]. Thermal radiation is the electromagnetic waves or noise that is radiated from molecules or atoms. Because the intensity of the noise is in proportion to the power of radiation over microwave region, measuring thermal radiation is equal to measuring the brightness temperature, $T_{B,i}$ of an object. As we assume a nearly one-dimensional temperature profile from head surface to the brain center [5], $T_{B,i}$ is given by the following equation,

$$T_{B,obj,i} = \iiint \frac{W_i(z)}{(1-R_i)} T(z) \cdots\cdots (1)$$

where $W_i(z)$ is the weighting function (WF) which links tissue temperature and antenna brightness temperature, R_i is the reflection coefficient between antenna and object, dz is an incremental distance along z-axis, $T(z)$ is the absolute temperature of tissues, and i is the number of the receiver. In our five-band radio- meter system: i = 1 (1.2 GHz), 2 (1.65 GHz), 3 (2.3 GHz), 4 (3.0 GHz) and 5 (3.6 GHZ receiver).

The tissue temperature profile T(z) is retrieved using the five brightness temperatures from these five radiometer receivers and the corresponding five WFs. The temperature retriev- al method is described in detail elsewhere [2].

$W_i(z)$ can be written as

$$W_i(z) = \frac{\frac{1}{2}\sigma_{tissue}\left|E(z)\right|^2 dz}{\iiint \frac{1}{2}\sigma_{tissue}\left|E(z)\right|^2 dz} \cdots\cdots (2)$$

where σ_{tissue} is tissue conductivity, and E(z) is electric field at z. The estimated temperature profile might therefore be influenced by head dielectric properties such as conductivity and permittivity.

3. Numerical Simulation Method

For the temperature profile simulation and the simplicity of arguments, it is assumed that the profile predicted by the thermal analysis in [5] is exact in this study. The profile is shown in Fig.1 and can be written as

$$T(z) = T_0 + \Delta T \cdot g(z) \quad with \ \left|g(z)\right|_{\max} = 1 \ \cdots\cdots (3)$$

where T_0 is the surface temperature, ΔT the magnitude of temperature elevation above T_0 and $g(z)$ the function describing shape of profile, and is called the shape function. Fitting of the profile to measurement was achieved by minimizing the error function,

$$Error = \sum_{i=1}^{n}\left(T_{B,\mathrm{model},i} - T_{B,meas,i}\right)^2$$

$$= \sum_{i=1}^{n}\left(\Delta T \int \frac{W_i(a,z)}{1-R_i} g(z)dz - T_{B,meas,i} - T_0\right)^2 \quad (4)$$

where $T_{B,model,i}$ is the radiometric data generated by the same procedure reported in [2], $T_{B,meas,i}$ the measured brightness temperature and a the conductivity.

We used a realistic shape model with simple structures with skin, fat, skull and brain. The model used for SAR calculation is shown in Fig.2.

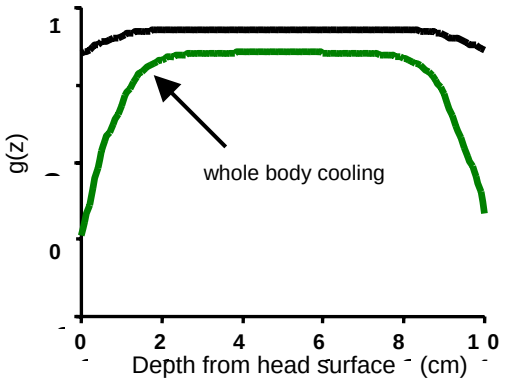

Fig.1 Temperature shape function. Anatomically realistic baby head model is used for thermal analysis to obtain the profile with (lower) and without (upper) cooling [4].

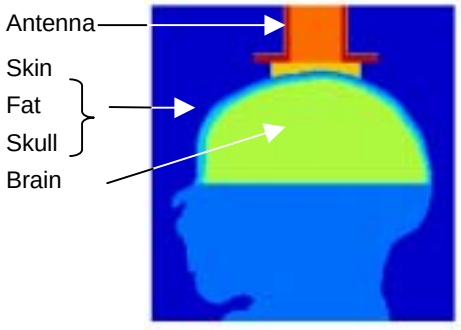

Fig.2 Cross section of a realistic baby head model used for SAR calculation.

Numerical values of the conductivity and permittivity were varied as standard ± 10 %, ± 20 % , and WFs at five frequencies were obtained. An example of radiometric WFs at 1.2 GHz for the conductivity variation is shown in Fig.3. When conductivity decreases, WF over shallower regions decreases while that over deeper regions increases, which means that more thermal noise from the deeper region can be detected at the antenna placed on the head surface. In this study, for simplicity, only conductivity and per- mittivity of brain, were separately changed.

Following two conditions were considered. (1) We inaccurately estimate dielectric properties. (2) Dielectric properties will be changed during therapy.

We simulated the brain profile with the five-band (i = 1 ~ 5) and three-band (i = 3 ~ 5) systems under above conditions. Standard dielectric nu- merical values used for newborn infants are listed in Tables 1 (conductivity) and 2 (permittivity) [3].

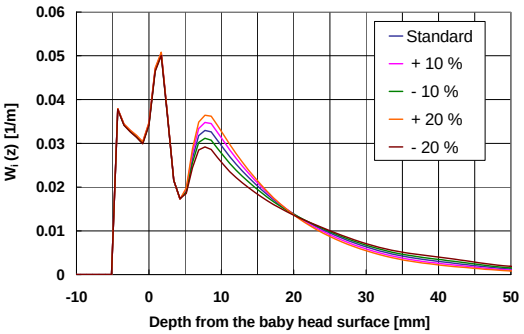

Fig.3 Weighting functions with various conductivty values. Center frequency: 1.2 GHz.

Table 1 Conductivity for newborn infants (S/m)

	Center frequency (GHz)				
	1.2	1.65	2.3	3.0	3.6
skin	0.97	1.13	1.40	1.74	2.09
fat	0.13	0.17	0.25	0.34	10.48
skull	0.12	0.14	0.18	0.22	0.26
brain	1.45	1.67	2.05	2.54	3.03
water	0.41	0.76	1.40	2.28	3.20

Table 2 Permittivity for newborn infants (ε_r)

	Center frequency (GHz)				
	1.2	1.65	2.3	3.0	3.6
skin	40.21	39.13	38.18	37.45	36.92
fat	11.22	11.07	10.87	1066	10.48
skull	16.23	15.71	15.10	14.51	14.04
brain	53.83	53.09	52.13	51.22	50.56
water	84.33	84.29	83.76	82.58	81.06

4. Numerical Simulation Results

Temperature retrieval simulations were made varying conductivity and permittivity as described in Section 3. Fig.4 shows an example of a retrieved profile and 2σ-confidence interval obtained by the same procedure reported in [2] using the standard values for the three-band system.

Confidence interval, which is an accuracy of the temperature estimation by this system, at 5 cm depth (brain center) is 0.94 ^{o}C with the three- band system. while that with five-band system is 0.42 ^{o}C. Since the practical clinical requirement for accuracy is about 1 ^{o}C, this result is satisfac- tory.

The estimated temperatures at the center of brain and its confidence intervals for the case (1) , in case of miss-estimation of tissue conductivity, are listed in Tables 3 and 4, respectively. Temper- ature estimation errors with the five-band system are 0.36 ^{o}C and 0.60 ^{o}C for the conductivity changes of –10 % and –20 % while those with three-band system are 0.40 ^{o}C and 0.88 ^{o}C, respectively. Temperature estimation accuracy with five-band system is 0.46 ^{o}C and 0.42 ^{o}C for –10 % and –20 % conductivity changes while those of three-band system are 0.94 ^{o}C and 1.06 ^{o}C, respectively. From these results, we can say that it is not desirable to reduce the number of receivers, for example three-band system, because the estimation accuracy might deteriorate and exceed 1 ^{o}C at the center of brain when we miss-estimate conductivity values in brain by 10 – 20 %. The estimation errors and the deterioration of accuracy for the case of (2) are also investigated, and nearly the same results are obtained.

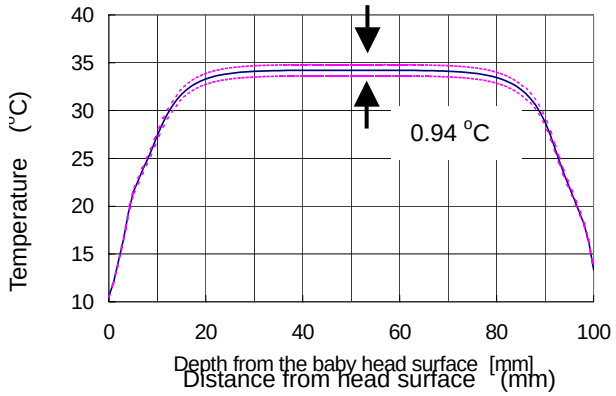

Fig.4 Retrieved temperature profile with standard conductivity and permittivity. Three-band system.

Table 3 Temperature estimation results (^{o}C)

Conductivity	Five-band	Three-band
+ 20 %	34.80	35.05
+ 10 %	34.52	34.61
Standard	34.22	34.22
– 10 %	33.86	33.82
– 20 %	33.62	33.34

Table 4 Accuracy of estimation (^{o}C)

Conductivity	Five-band	Three-band
+ 20 %	0.46	0.86
+ 10 %	0.44	1.06
Standard	0.42	0.94
– 10 %	0.46	0.94
– 20 %	0.42	1.06

5. Conclusion

The results of this feasibility study of reducing the number of the radiometer receivers in light of the variation of tissue dielectric properties show that the three-band system with higher frequencies (2.3, 3.0, 3.6 GHz) is not expected to provide an acceptable temperature accuracy at the center of brain. Confidence intervals are deteriorated by the estimation error of tissue dielectric properties and/or the changes of those properties during hypothermia therapy from the values estimated in advance

Future work will include to obtaine more accurate information on dielectric properties of infant's head tissue.

References

[1] E. Sirimanne, R.M. Blumberg, D. Bossano, M. Gunning, A.D. Edwards, P.D. Gluckman, and C.E. Williams, "The effect of prolonged modification of cerebral temperature on outcome following hypoxic-ischaemic brain injury in the infant rat," *Pediatr Res*., vol. 39(4), pp. 591-597, 1996

[2] Mizushina S., Maruyama K., Sugiura T., Van Leeuwen G.M.J., Hand J.W., Marrocco G., Bardati F., Edwards A.D., Azzopardi D., Land D., "Algorithm for retrieval of deep brain temp- erature in new-born infant from microwave ra- diometric data," 2000 IEEE MTT-S Digest, pp1033-1036, 2000

[3] Maruyama K., Mizushina S., Sugiura T., Van Leeuwen G.M.J., Hand J.W., Marrocco G., Bardati F., Edwards A.D., Azzopardi D., Land D., "Feasibility of noninvasive meas- urement of deep brain temperature in new- born infants by multifrequency microwave radiometry," IEEE Trans. MTT, vol.48(11), pp2141-2147, 2000

[4] Kraus JD., Radio Astronomy, MacGraw- Hill, New York, 1966.

[5] Van Leeuwen G.M.J., Hand J.W., Lagendijk J.J.W., Azzopardi D.V., Edwards A.D., "Numerical modeling of temperature distributions within the neonatal head," Pediatr Res., vol.48 (3), pp351-356, 2000

"EFFECT OF POROSITY ON MAGNETIC AND ELECTRIC PROPERTIES OF Mg-Zn NANO-FERRITES "

B. K. Bammannavar*, L. R. Naik* and R. B. Pujar[$]

***Karnatak University, Dharwad - 580 003, India.**

[$]S. S. Arts College and T. P. Science Institute, Sankeshwar – 591 313, India

Abstract: The use of magnetic materials with specific properties has stressed the need to invoke the role of microstructure on these properties. There are many ferrites that have replaced the conventional magnetic materials in the field of electronic technology. Among them soft poly crystalline nano-ferrites find vide applications from low frequency to radio frequency. Over the last few decades, a number of processing methods have been developed to improve the performance of existing materials by reducing their grain size. Hence, an attempt has been made to develop and characterize the nano-crystalline ferrites through chemical route.

The microstructure of ferrites plays a dominant role in determining high power ability as well as low power loss in microwave devices. In the recent years, much progress has been made in the control of ferrite material properties through chemical composition and preparation techniques. A variety of nano-sized ferrites with the general chemical formula Mg_{1-x} Zn_x Fe_2O_4 where x = 0.1, 0.2, 0.3, 0.4 and 0.5 have been prepared from a simple polymer matrix based precursor solution. The solution was composed of metal nitrates with polymer PVA and Sucrose. Thermolysis of the precursor mass at about 500°c resulted in the oxide phase. X-ray diffraction studies confirmed the formation of single-phase ferrites while IR studies give the information about absorption bands. SEM studies throw a light on the microstructure of ferrites. While the porosity helps to explain its effect on magnetic and electric properties. The variation of resistivity with temperature shows the break at Curie temp. This indicates the transition from ferrimagnetism to paramagnetism, where as hysteresis studies confirm the presence of MD particles in the samples.

Key words: Nano, feerites, Sucrose, PVA, SEM and MD.

1. Introduction

Ferrites are double oxides of iron. Because of their high resistivity, high permeability and low cost they have vast applications from microwave to radio frequencies. In this paper we introduce a new method of preparation of nano ferrites by chemical route to study how porosity

could influence the electric and magnetic properties. Though the intrinsic properties like saturation magnetization and anisotropy depend on chemical composition, electronic structure of magnetic ions and crystal symmetry about the lattice, the properties like permeability, coercivity etc are strongly depend on grain size, porosity and microstructure, which is in turn is governed by the method of preparation and sintering process. Thus, the intrinsic parameters decide the particular application of ferrites [1].

2. Experimental

Ferrites with general chemical formula $Mg_{1-x}Zn_xFe_2O_4$ with x = 0.1 to 0.5 were prepared by chemical route using metal nitrates, in molar proportion according to their chemical composition, sucrose and PVA. The samples were presintered at 800° C for 8 hours in air medium. The powders in the pellet form were subjected to final sintering at 1000°C for 10 hours and furnace cooled in air medium.

X-ray diffraction, IR studies and VSM (fig.3) analysis were carried out at Indian Institute of Science, Bangalore. Where as d. c. conductivity was measured by two probe method from room temperature to 500°C **(**Fig 2). SEM micrographs were obtained from Shivaji University Kolhapur to calculate the average grain diameter and are shown in the Fig 1.

Average grain diameter was calculated from SEM micrographs using Goel model.
Resistivity was calculated by using the relation

$$\rho = \rho_o e^{\Delta E/kT} \quad (1)$$

where ρ_o = constant depending on temperature.

ΔE = activation energy.

T = absolute temperature.

K = Boltzmann constant.

While activation energy was calculated by the relation

$$\Delta E = 1.982 \times 10^{-4} \times m \quad (2)$$

where m = slope from the graph of $\log\rho$ Vs $1/T$

Magnetic moment was calculated by using the relation

$$\mu_B = \left(\frac{M}{5585}\right) M_s \quad (3)$$

where M = molecular weight, Ms = Saturation Magnetization.

3. Figures and Tables

3.1 Figures

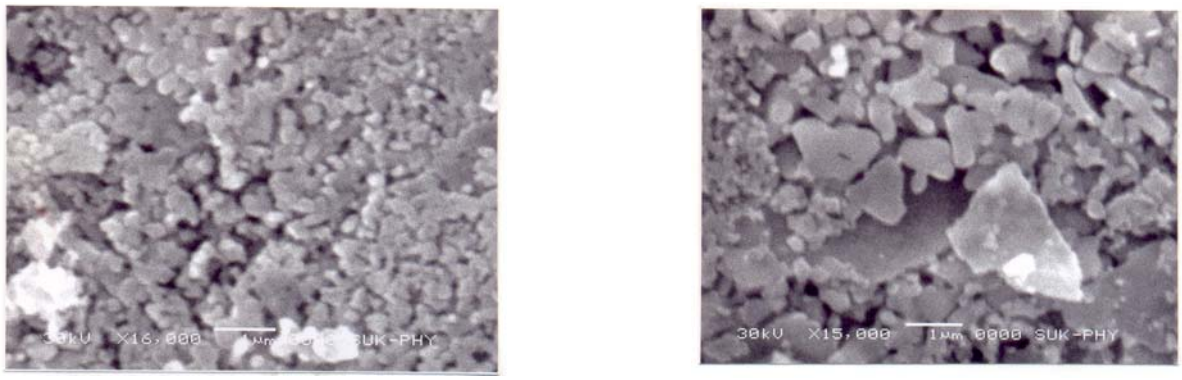

Fig 1. Micrographs of Mg_{1-x} Zn_x Fe_2O_4 Ferrites

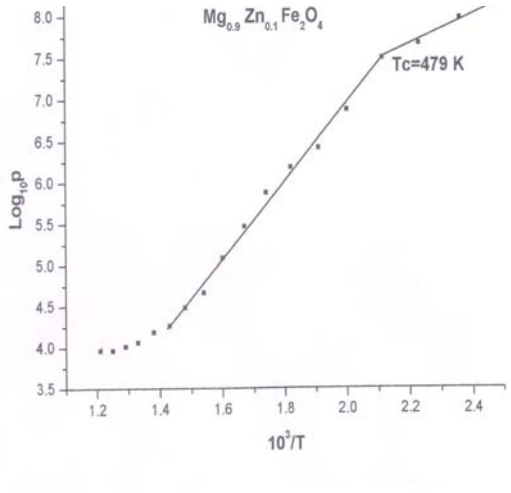

Fig 2. D.C. Conductivity

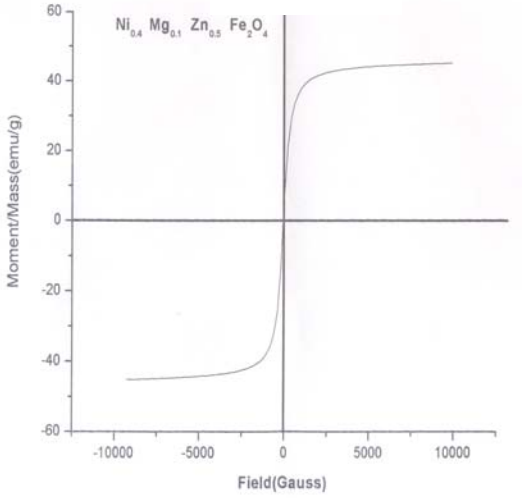

Fig 3. V. S. M. Analysis

3.2 Tables

Table 1. Data on average grain diameter

Composition	Average grain diameter(μm)
$Mg_{0.9}$ $Zn_{0.1}$ Fe_2O_4	0.32
$Mg_{0.8}$ $Zn_{0.2}$ Fe_2O_4	0.25
Mg_{07} $Zn_{0.3}$ Fe_2O_4	0.44
$Mg_{0.6}$ $Zn_{0.4}$ Fe_2O_4	0.25
$Mg_{0.5}$ $Zn_{0.5}$ Fe_2O_4	0.55

Table 2. Data on Activation Energy and Curie temperature

Content (x)	Activation Energy		Curie temperature T_c°K
	Para region ΔE_1 (e_v)	Ferri region ΔE_2 (e_v)	
0.1	0.86	0.37	479
0.2	0.96	0.62	498
0.3	0.92	0.35	473
0.4	0.70	0.21	465
0.5	0.91	0.33	498

Table 3. Data on Saturation magnetization, Magnetic moment, M_r/M_s and H_c

Content (x)	M_S (emu/gr)	μ_B	$\frac{M_r}{M_S}$	H_c (Gauss)
0.1	45.3	1.66	0.20	104.0
0.2	44.5	1.66	0.08	70.0
0.3	43.9	1.67	0.09	42.0
0.4	3.04 (emu)	0.12	0.20	69.0
0.5	35.7	1.41	0.081	69.0

4. Results and Discussion

X-Ray diffraction studies confirm the formation of single phase cubical ferrites [2]. IR studies indicate the existence of two prominent absorption bands near 600 cm^{-1} and 400 cm^{-1}, which are attributed to octahedral and tetrahedral origin.

The activation energy for all the samples is greater than 0.2ev. Hence conduction in the present samples are due to hopping of polarons between Fe^{3+} and Fe^{2+} ions on the octahedral site[3]. Break at Curie temperature is due to change in conduction mechanism. The increase in Curie temp with Zn content is due to increase in the strength of A - B interaction [4](Table 2).

Porosity is found to change from sample to sample (Table1). The presence of pores between the grains results in the formation of inhomogeneous structure[5]. This affects the conduction mechanism in ferrites to a large extent. Therefore conductivity in ferrites increases with increase in average grain size and decrease in porosity.

Both Mg and Zn being nonmagnetic, the addition of Zn decreases the amount of Mg and increases the amount of Fe^{3+} on B site. Hence saturation magnetization is found to increases with Zn up to $x = 0.3$, obeying Neel's model. The decrease in magnetization for $x > 0.3$ suggests the existence of Y-K angles with increase in Zn content. Hence it can be concluded that magnetization obeys Y-K model for $x > 0.3$. The small values of M_r/M_s and H_c suggest the existence of MD particles[6] in all the samples (Table 3).

The presence of pores breaks the magnetic circuits among the grains, resulting in the decrease of magnetic moment with increase in pore concentration. At higher sintering temperature porosity is reduced due to formation of large grains. Hence magnetization increases with increase in sintering temperature.

REFERENCES

1. Broese Van Groenou A., Bongers, P.F and Stuijts A.L., "Material Science Eng" 3, 317,1968.
2. Cullity.B. D., "Elements of X-ray Diffraction Wesley Publishing Company, INC, England, 1959.
3. Pujar.R.B., "Studies on Zerconium doped-magnesium-Zinc ferrites" Ph.D, Thesis Shivaji University, Kolhapur, India, 1995.
4. Patil. B. L., "Ph.D, Thesis" Shivaji University, Kolhapur, India, 1993.
5. Longkla W and Shouwu Chang Chung Wei., "Journal of Physics. D (G B)" 13/2, 1980, D.259.
6. Goel. N. C., Ph.D, "Thesis Delhi University Dehli", 1977, India

An exploration about possibly levitating magnets using nonvertical configurations

Joe Nhut Ho & Wei-Chih Wang
Mechanical Engineering Department
University Of Washington, Seattle WA 98195, USA

Abstract

Previous papers about diamagnetic levitation describe using vertical magnet configurations. At least one paper has mentioned a horizontal configuration using two permanent or electromagnets. However, none gives any quantitative analysis for the horizontal configuration. In addition none seems to have considered levitating a magnet at other angles, cases between these two configurations. The existence of these two extremes suggests that one possibly could levitate a magnet at other angles between 0 (vertical) to $\pi/2$ radians (horizontal). This paper explores one a configuration of two permanent suspending magnets for levitating a magnet using a horizontal configuration as well as another configuration using a permanent and electromagnet combo (allows variable field strength) for levitating magnets at angles not equal to $\pi/2$. This was done numerically by evaluating the basic equations and looking for equilibrium points where net forces and moments on a levitating magnet are zero. For all cases considered here, the two axes of the two suspending magnets were always directly aligned with each other. For a range of angles near $\pi/2$ radians, one can stably levitate a magnet parallel to the suspending magnets by using a permanent and electromagnet combo.

Introduction

Most examples of diamagnetic levitation use a vertical configuration for levitation. The vertical levitating force is generated from the radial component of the suspending magnet's field [1, 2]. The vertical component is important for radial stability and centers a levitating magnet along the suspending magnet's center axis [2]. Radial displacements cause a net radial force to pull the levitating magnet back to the center position. This suggests that a magnet could be levitated by using the radial stabilizing force as the lifting force and using two suspending magnets to balance each other (see figure 1) which has been shown by Simon, Heflinger, and Geim[2]. However, no one seems to have mention levitating a magnet at angles other than 0 or $\pi/2$ radians [1-2]. But seems to be no reason to believe that other angles are forbidden. Any real system can't be perfectly aligned to either 0 or $\pi/2$ radians and qualitative experiments by the authors using a vertical configuration show small perturbations do not cause a levitating magnet to destabilize. Thus levitating magnets at other angles seems perfectly reasonable.

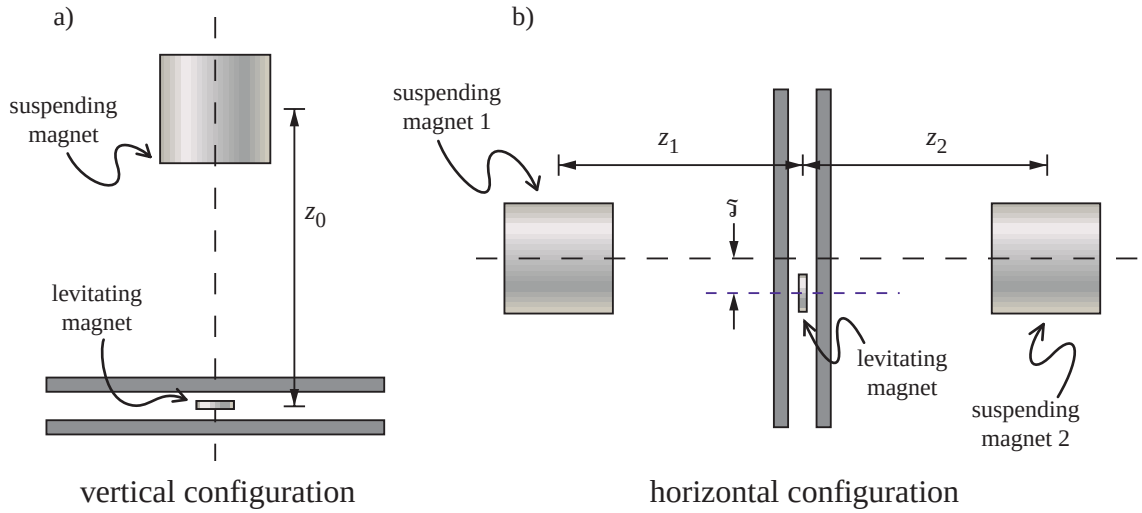

Figure 1: Vertical and horizontal configurations for levitating a magnet. The suspending magnets of both configurations are oriented so they attract the levitating magnet.

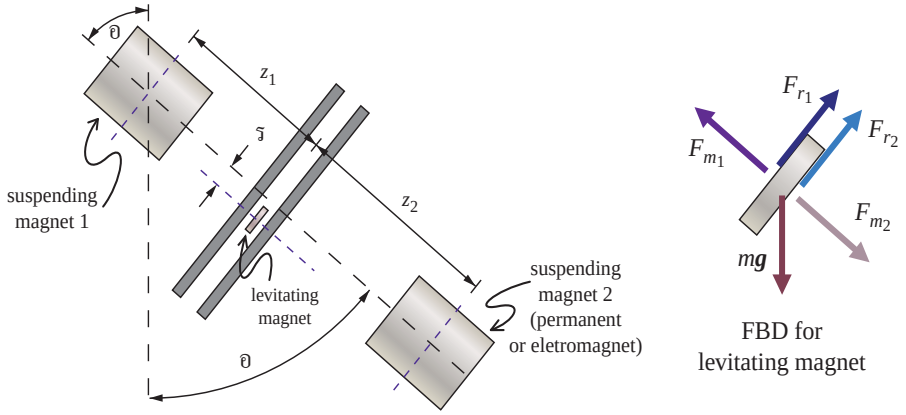

Figure 2: The simulated configuration for this paper. The first suspending magnet is a permanent magnet (constant field) and the second suspending magnet could be a permanent magnet or an electromagnet (variable field). Both suspending magnets' center axes were aligned and the levitating magnet's axis was kept parallel. Note that the simulations used only cylindrical magnets.

Analysis

In order to find the levitation (equilibrium) point horizontally and vertically, one needs to balance the forces from the suspending magnets and gravity on the levitation magnet (see figure 2, FBD). For the *z* direction:

$$F_{m_1} - F_{m_2} - W\cos\theta = 0 \tag{1}$$

where F_{m_1} and F_{m_2} are the forces from the suspending magnets acting on a levitating magnet with weight *W,* and a configuration oriented at angle θ from vertical. The Biot Savart Law can model the forces from the suspending magnets:

$$\iint \boldsymbol{M}_L da \times (\boldsymbol{B}_1 + \boldsymbol{B}_2) - mg\cos\theta = 0 \tag{2}$$

with $\boldsymbol{B}_1$ and $\boldsymbol{B}_2$ as the flux densities from the suspending magnets and *da* is a differential area along the levitating magnets surface (modeling it as a surface or ribbon current [6]).

All magnets are assumed to be cylindrical and the two suspending magnets have their central axes directly aligned with each other. The levitating magnet may shift away from this central axis (distance away from the central axis $\mathfrak{z}$) but is required to maintain its central axes parallel (though not collinear) with the suspending pair.

To approximate the effects of the two suspending magnets, a multipole expansion is used for $\boldsymbol{B}_1$ and $\boldsymbol{B}_2$ (using polar coordinates):

$$\boldsymbol{B} = \frac{3\mu_0 MHR^2 zr}{4(r^2+z^2)^{5/2}}\boldsymbol{e}_r + \frac{\mu_0 MHR^2(2z^2-r^2)}{4(r^2+z^2)^{5/2}}\boldsymbol{k} \tag{3}$$

where *H* is the height, *R* is the radius, *M* is the magnetization of a cylindrical magnet. Applying the cross product and substituting the multipole expansion gives:

$$-\frac{3}{4}\mu_0 M_1 H_1 R_1^2 M_L R_L \int_{z_{1_1}}^{z_{1_2}} \int_0^{2\pi} \frac{z_1(R_L + \mathfrak{z}\cos\theta)d\theta dz_1}{(R_L + 2R_L\mathfrak{z}\cos\theta + \mathfrak{z}^2 + z_1^2)^{5/2}} \tag{4}$$

$$-\frac{3}{4}\mu_0 M_2 H_2 R_2^2 M_L R_L \int_{z_{2_1}}^{z_{2_2}} \int_0^{2\pi} \frac{z_2(R_L + \mathfrak{z}\cos\theta)d\theta dz_2}{(R_L + 2R_L\mathfrak{z}\cos\theta + \mathfrak{z}^2 + z_2^2)} - W\cos\theta = 0$$

Now balancing forces for the radial direction:

$$F_{r_1} - F_{r_2} - W\sin\theta = 0 \tag{5}$$

After applying the same steps as above, the final expression is

$$6 \qquad \frac{1}{4}\mu_0 M_1 H_1 R_1^2 M_L R_L \int_{z_{1_1}}^{z_{1_2}} \int_0^{2\pi} \frac{\cos\theta(2z_1^2 - R_L^2 - 2\Im R_L \cos\theta - \Im^2)}{(R_L + 2R_L \Im\cos\theta + \Im^2 + z_1^2)^{5/2}} d\theta dz_1$$

$$+ \frac{1}{4}\mu_0 M_2 H_2 R_2^2 M_L R_L \int_{z_{2_1}}^{z_{2_2}} \int_0^{2\pi} \frac{\cos\theta(2z_2^2 - R_L^2 - 2\Im R_L \cos\theta - \Im^2)}{(R_L + 2R_L \Im\cos\theta + \Im^2 + z_2^2)^{5/2}} d\theta dz_2 - W\sin\Theta = 0$$

Where equations 4 and 6 are simultaneously become zero gives possible locations for equilibrium points for the levitating magnet.

In addition to zero net force on the levitating magnet, zero net moment is also necessary. For moments around the levitating magnet's center, a differential force from a suspending magnet is multiplied by its corresponding moment arm $\boldsymbol{r}$ (a vector to positions along the levitating magnet's outer surface) before integrating:

$$7 \qquad \mathcal{M} = \iint \boldsymbol{r} \times d\boldsymbol{F} = \iint \boldsymbol{r} \times (\boldsymbol{M}_L da \times \boldsymbol{B}_1) d\theta dz_1 + \iint \boldsymbol{r} \times (\boldsymbol{M}_L da \times \boldsymbol{B}_2) d\theta dz_2$$

where $\mathcal{M}$ is the net moment around the *y* axis (perpendicular to the plane containing the centers of all three magnets). After substituting multipole expansions for field density from the two suspending magnets, (using Cartesian coordinates this time) and applying the same steps as above results with:

$$8 \qquad \mathcal{M} = \frac{3}{4}\mu_0 M_1 H_1 R_1^2 R_L^2 M_L \int_{z_{2_1}}^{z_{2_2}} \int_0^{2\pi} \frac{(R_L \cos\theta + \Im) z_1 d\theta dz_1}{(R_L^2 + 2R_L \Im\cos\theta + \Im^2 + z_1^2)^{5/2}} + \frac{3}{4}\mu_0 M_2 H_2 R_2^2 R_L^2 M_L \int_{z_{2_1}}^{z_{2_2}} \int_0^{2\pi} \frac{(R_L \cos\theta + \Im) z_2 d\theta dz_2}{(R_L^2 + 2R_L \Im\cos\theta + \Im^2 + z_2^2)^{5/2}}$$

Because of the symmetry of the suspending magnets, only this moment needs consideration for equilibrium.

Finally, equilibrium does not guarantee stability. The stabilizing effect of diamagnetic plates is needed as well [1,2,3]. The complete theory for diamagnetic stabilization is rather complex and is covered in [5]. The stabilizing force is only needed for the *z* direction since for the radial direction, the levitating magnet is automatically stable (this is what allows the horizontal configuration to exist). The *z* direction stabilizing effect $\Re_z$ provided by diamagnetic plates only depends on the relative position of the levitating magnet with respect to the diamagnetic plates and plate spacing. The numerical calculations included this calculation as well.

A computer program was written to numerically integrate the above expressions to find the equilibrium points. The area integrals of 4, 6, and 8 were integrated numerically by applying Gaussian quadrature. The program was tested seeing if it could find the levitation point of the vertical configuration ($\Theta = 0$ radians) which should be at 134 mm [4]. The program found the equilibrium points by calculating the forces and moments on a levitating magnet placed along points on a finely spaced grid in the region between the suspending magnets and coloring each point according to the force strength producing a 24 bit color image (see figure 3) with lines marking the zero force lines (red for *z* direction force, green for radial force, and blue byte for moment). Areas were the diamagnetic stability requirement was below a set limit were shaded light (multiplied each color byte by 1.2 to highlighted those regions).

For these numerical simulations, the top suspending magnet was given these parameters: M_1 = 978 kA, R_1 = 19 mm, H_1 = 38 mm; the second suspending magnet has the same geometry as the first but with variable magnetiza-

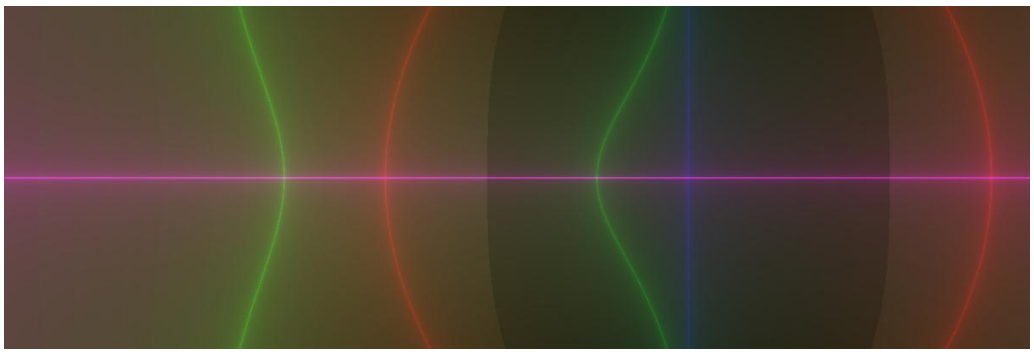

Figure 3: An example of a plot generated by the computer program to find equilibrium points. This plot is for two equal suspending magnets at $\pi/2$ and 120 mm from the symmetry plane.

tion M_2; and the levitating magnet M_L = 978 kA, R_L = 3.15 mm, H_L = 1.6 mm for common neodymium boron ferrite magnets (grade N38) readily available in the authors' lab [8]. In addition, the diamagnetic plates were assumed to be pyrolitic graphite with plate thickness of 3 mm and spaced 6 mm apart, which gives diamagnetic stabilization of $\mathfrak{R}_z$ = 0.114 N/m [5].

Results

If the two suspending magnets are identical to each other (same geometry and magnetization) and aligned as described above, the levitating magnet can't remain parallel the suspending magnets for any angles other than 0 and $\pi/2$ radians. This occurs because the weight vector is no longer aligned with the z or radial axes, so a levitating magnetic must move off these axes for magnetic attraction to balance its weight. However, the zero moment lines for two identical suspending magnets lies on the central axis and on a plane midway between the two magnets (symmetry plane). Thus, the levitating magnet will be forced to rotate to an angle not aligned with the suspending magnets.

For the horizontal configuration ($\theta = \pi/2$ radians), figure 4 shows possible equilibrium points along a line (parallel to gravity and intersects the central axis) in the symmetry plane (both suspending magnets are identical, so z forces and moments are always zero alone this line). If the magnets are too far apart (133.35 mm from symmetry plane for this simulation) there are no equilibrium points. This occurs because the radial field is no longer strong enough to balance the levitating magnet's weight. Moving the magnets closer than 133.5 mm produces two equilibrium points directly above each other with the lower one easier to stabilize. These locations represent where the forces from the radial field exactly balances the levitating magnet's weight, not too strong, not too weak (too strong between the points, too weak outside of them). This also suggests that a levitating magnet's position can be varied by shifting the suspending magnets. This is not possible with a vertical configuration using a single suspending magnet.

Replacing the second magnet with an electromagnet so the magnetic attraction can vary, one can levitate a magnet parallel to the suspending magnets for a wide range of angles as shown in figures 4a and 4b. After a certain limit, the levitating magnet gets too close to the lower electromagnet and becomes difficult to stabilize (diamagnetic requirement becomes large or can't balance all forces and moments at the same time), which also sets a lower limit on the orientation angle for this given suspending magnet configuration (which requiring the levitating magnet's axis to be parallel). This lower limit is around 0.325π to 0.350π radians for the cases studied here. Also, as the orientation angle decreases, the equilibrium points move further away from the symmetry plane (plane equal distant from both suspending magnets) and the necessary balancing electromagnet strength decreases (figure 4b). Increasing the suspending magnet separation distance spreads the equilibrium points (with equal) further apart in space.

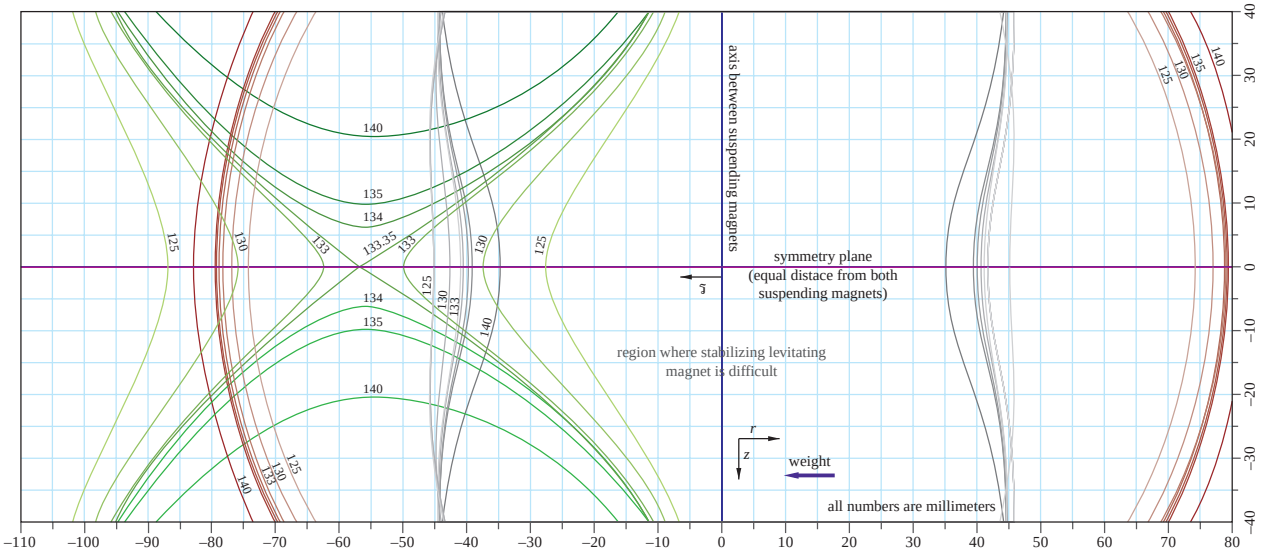

Figure 4: Stability region diagram for two suspending magnets levitating a small third magnet with magnets oriented at $\pi/2$ (90°) from vertical direction. The red curves show locations of zero net z direction forces, the green show zero net radial direction, the blue show location of zero net moments (at the purple symmetry line both has both zero force along z direction and zero moment), and the region between the grey lines shows the boundaries of the region were the diamagnetic stabilization requirement is larger than a specified limit. The numbers on the lines tell the distance of the suspending magnets from the symmetry plane that generates that particular line (mm).

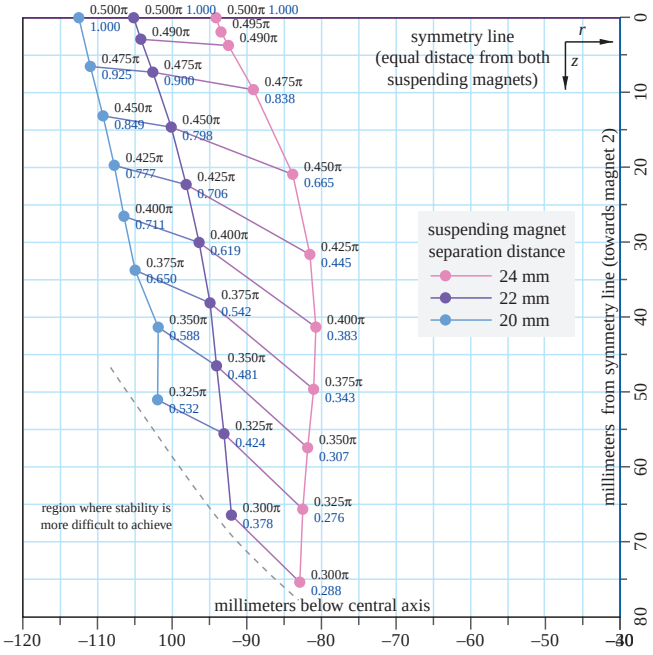

Figure 5a: A plot showing locations for equilibrium points at various angles and suspending magnet separations for magnets with the parameters given in the text (one permanent, on electromagnet). The black number next to each point is the orientation angle ϑ (radians) for that point and the blue number is the corresponding electromagnet strength to generate that equilibrium point (as a fraction of permanent magnet's magnetization).

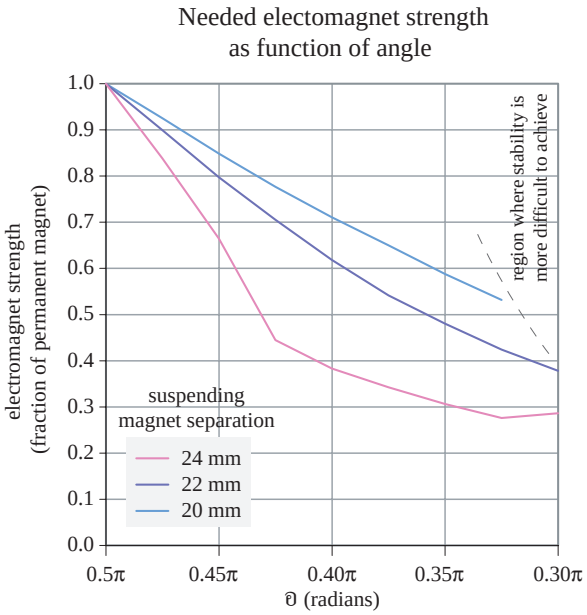

Figure 5b: Graphs of electromagnet strength (as a fraction of the permanent magnet's strength) for a permanent and electromagnet at three different separations distances. As the separation distance decreases and the angle increases, the electromagnet's current needs to decrease to maintain equilibrium.

Conclusions

For the horizontal configuration, the position of the equilibrium points depends on the separation distance of the suspending magnets. After a certain distance no equilibrium points exist but at closer distances, there are two equilibrium points. Only a certain range of angles around 0.5π±0.30π is allowed for a levitating magnet suspended with its axis parallel between two suspending magnets (central axes aligned with each other) and this requires an electromagnet with a field weaker than the permanent magnet. This can't be done with two equal permanent magnets.

Using other configurations of magnets such as two non aligned suspending magnets (both position or/and angle) could also allow a magnet to levitate at other angles not parallel to the suspending magnets. None of these cases was considered for this paper. In addition, one might possibly use a clever configuration of several magnets (both permanent or electromagnets of varying sizes and positions) to create multiple equilibrium points for a range of angles.

References

1. Berry, M.V., Geim, A.K., "Of Flying Frog & Levitrons", *European Journal Of Physics*, Vol. 18, 1997: 307-313.
2. Simon, M.D., Heflinger, L.O., Geim, A.K., "Diamagnetically Stabilized Magnet Levitation", *American Journal Of Physics*, Vol. 69, No. 6, June 2001: 702-713.
3. Lương Duyên Bình, Dư Trí Công, Nguyễn Hữu Hồ, *Vật Lý Đại Cương:* Tập 2, Nhà Xuất Bản Giáo Dục, Aug, 2001.
4. Hồ, J.N., Wang, W.C., "Diamagnetic Levitating Rotor", Proceedings Of PIERS Conference In Hangzhou, 2005.
5. Hồ, J.N., Wang, W.C., "Static Stability & Plate Spacing For Diamagnetic Levitating Magnets", Proceedings Of PIERS Conference In Tokyo, 2006.
6. Griffiths, D.J., *Introduction To Electrodynamics*, 3rd Ed., Prentice Hall, Upper Saddle River, 1999, ISBN 0-13-805326-X.
7. "Sintered NdFeB Magnets", MMC Enterprises Corporation, www.mmcmagnetics.com/ourproducts/pdf/SinteredNdFeB.pdf, 2003.

Mollifier and a Boundary Integral Equation on an Open Boundary

Yoshio Hayashi

Abstract- A solution of an integral equation on an open surface, which solves a scattering of wave by the surface, is not square-integrable because of its singularity in the vicinity of the periphery of it, hence a L_2-theory of solution which is the most powerful tool of analysis is not available. To resolve this trouble, we introduce functions called "mollifier", [1] which make their product with a solution belong to $L_2(S)$ hence is solvable by a $L_2(S)$-method. Then a solution of the original equation is given by dividing the L_2-solution thus obtained by the mollifier. Diverging modes are studied. The uniqueness of a solution is proved to hold in spite of the existence of infinitely many diverging modes. As the average of diverging modes, a representative of them is derived, which shows that the diverging order of it is $O(\rho^{-3/2})$ where ρ is the distance from the periphery of a surface. In a similar way, two dimensional problem where a boundary is a line segment of a finite length on a plane is also studied.

I. Introduction and Presentation of the Problem

An analysis of waves scattered by an open surface S is usually reduced to that of a boundary integral equation considered on S, which is a linear functional equation of the form $T(\tau) = g$, where g is a given element of a Hilbert space $L_2(S) = \{f | \int_S |f|^2 dS < \infty\}$ composed of functions square integrable on S. While, $\tau = \tau(P)$ is a unknown function which is looked for and is supposed to have a singularity of order $0(\rho^\beta)$ in the vicinity of the periphery ∂S of S, where ρ is the distance from ∂S and $-2 < \beta$. Therefore, it does not necessarily belong to $L_2(S)$ but may belong to $L_1(S) = \{f | \int_S |f| dS < \infty\}$ which is a Hilbert space composed of absolutely integrable functions on S. Hence a L_2-theory of solution which is the most powerful tool of an analysis is not available.

To avoid this trouble, we introduce in Section Ⅱ a function $J_\delta(\alpha; P)$ which we call a "mollifier", such that $J_\delta(\alpha; P) = 0$ when $P \in \partial S$, that $J_\delta(\alpha; P) = 1$ when P is an inner point of S apart from ∂S by a given distance, that it is piecewise infinitely many times differentiable everywhere in S, and that $J_\delta(\alpha; P) = O(\rho^\alpha)$ in the vicinity of ∂S. Furthermore, it is required that the product $J_\delta(\alpha; P)\tau(P)$ belongs to $L_2(S)$ and bounded in the vicinity of ∂S.

As is shown in Section Ⅲ, these requirements are equivalent to that the parameter α to satisfies the condition $1 < \alpha < 2$. Furthermore, since $J_\delta(\alpha; P)\tau(P) \in L_2(S)$, an equation $T(J_\delta(\alpha)\tau) = \hat{g}(\alpha)$ which is considered in a $L_2(S)$, can be solved by a $L_2(S)$-method, and a solution $J_\delta(\alpha; P)\tau(P)$ which depends on a parameter α is obtained, and a solution of the original equation $T(\tau) = g$ is then obtained by dividing $J_\delta(\alpha; P)\tau(P)$ by $J_\delta(\alpha; P)$.

A solution $\tau(P) = \tau_\delta(\alpha; P)$ thus obtained, which depends on a parameter α and diverges with the order of $O(\rho^{-\alpha})$ when $\rho \to 0$, is called a diverging mode of order $-\alpha$. There exist infinitely many diverging modes corresponding to $\alpha, 1 < \alpha < 2$.

[1] "Mollifier" is originally a terminology in a theory of function spaces [1].

Though a general explicit expression of $J_\delta(\alpha;P)$ is not known yet, only that of $J_\delta(3/2;P)$ is given explicitly by Theorem 1 in Section II. As a consequence, only the explicit expression of the corresponding solution $\tau_\delta(3/2;P)$ is available. Furthermore, $\tau_\delta(3/2;P)$ is shown to play the role of the representative of all solutions corresponding to $\alpha, 1<\alpha<2$.

In Section Ⅳ, the uniqueness of a solution is proved to hold in spite of the existence of infinitely many diverging modes.

In Section V, a two dimensional problem where a boundary is a line segment of a finite length on a plane is studied, in a way similar to that employed in the preceding sections.

Ⅱ. Mollifier

Assume that δ is a positive constant, that $S_{2\delta}=\{P|2\delta<\overline{PQ}, Q\in\partial S\}$, and that $S_\delta=\{P|\delta<\overline{PQ}, Q\in\partial S\}$. Let $\rho=min_{Q\in\partial S}\overline{PQ}$ be the distance of P from ∂S, and α be a positive real number. We define a function $J_\delta(\alpha;P)$ named a mollifier of order α as the one which satisfy the following requirements.

Definition

$$\begin{aligned} J_\delta(\alpha;P) &= 1, \qquad (P\in S_{2\delta}): \quad \in C^\infty, \quad (P\in S-S_{2\delta}) \\ &= O(\rho^\alpha)\to 0, \ (\rho\to 0): \quad =0, \quad (P\in\partial S) \end{aligned} \tag{1}$$

We set an aggregate of such functions as $\mathcal{J}(\delta)=\{J_\delta(\alpha;P)\}$. Then, it is shown that $\mathcal{J}(\delta)$ is not empty. In fact, the following function $J_\delta(\alpha;P)$ is proved to belong to $\mathcal{J}(\delta)$.

Theorem 1 The function $J_\delta(\alpha;P)$ defined below does belong to $\mathcal{J}(\delta)$.

$$\begin{aligned} J_\delta(\alpha;P) &= \delta^{-2}\gamma^{-1}\iint_{S_\delta\cap\{Q|R=\overline{PQ}<\delta\}} exp.\Big(-\delta^2/(\delta^2-R^2)\Big)dS_Q \\ \gamma &= 2\pi\int_0^1 exp.\Big(-1/(1-r^2)\Big)rdr \end{aligned} \tag{2}$$

Proof When $P\in\partial S$, a domain of integration $S_\delta\cap\{Q|R=\overline{PQ}<\delta\}$ is empty, hence the integral defining $J_\delta(\alpha;P)$ is zero, that is, $J_\delta(\alpha;P)=0$, $P\in\partial S$. While if $P\in S_{2\delta}$, $\{Q|R=\overline{PQ}<\delta\}\subset S_\delta$, hence $J_\delta(\alpha;P)=\delta^{-2}\gamma^{-1}\iint_{R<\delta} exp.\Big(-\delta^2/(\delta^2-R^2)\Big)dS_Q$=1.

[Note] The value of $J_\delta(\alpha;P)$ given by (2) is proportional to the area of a range of integration $S_\delta\cap\{Q|R=\overline{PQ}<\delta\}$, which is shown, by some elementary calculations, to be $(4/3)\sqrt{2\delta}\rho^{3/2}$ when ρ is small. Therefore, it may be $=J_\delta(3/2;P)$, which $=O(\rho^{3/2})$ when $\rho\to 0$.

Ⅲ. Solution of Equation and Diverging Modes

Now, we shall study how $(*): T(\tau)=g$ is solved. As a solution of $(*)$, τ must be integrable, that is, $\tau=O(\rho^\beta)\in L_1(S)$, and therefore, (i) $-\beta<2$. Assume that $J_\delta(\alpha;P)$ is such that $J_\delta(\alpha;P)\tau(P)=O(\rho^{\alpha+\beta})\in L_2(S)$, that is, (ⅱ) $\alpha+\beta+1>0$. Furthermore, let us assume that $J_\delta(\alpha;P)\tau(P)=O(\rho^{\alpha+\beta})=O(1)$, that is (ⅲ) $\alpha+\beta\geq 0$.

It is easy to see that if the set of conditions (i), (ii) and (iii) holds, then, we have

$$1 < \alpha < 2 \tag{3}$$

Conversely, if (3) holds, then the set of the three conditions (i), (ii), (iii) holds. That is, (3) and the set of the conditions (i), (ii), (iii) are equivalent to each other.

We redefine $\mathcal{J}(\delta)$ as $\mathcal{J}(\delta,\alpha) = \{J_\delta(\alpha;P)|1<\alpha<2\}$.

Before going to study the equation $(*)$, let us consider an equation $(**) : T(J_\delta(\alpha)\tau) = \hat{g}(\alpha)$, where T is the operator of the original euation $(*)$, and $\hat{g}(\alpha)$ is the image of $J_\delta(\alpha)\tau$ by T. As far as $J_\delta(\alpha) \in \mathcal{J}(\delta,\alpha)$, $J_\delta(\alpha;P)\tau(P) \in L_2(S)$ holds because of (ii). Therefore, the equation $(**)$ is in $L_2(S)$, and is solved by the authors method called MEC [2] that solves a linear functional equation in $L_2(S)$ generally and rigorously, yielding an approximate solution $J_\delta(\alpha;P)\tau(\alpha;P) = \Sigma_{n=1}^{N}\hat{c}_n(\alpha)\tau_n(P)$ which surely converges to the true solution when $N \to \infty$, while $\{\hat{c}_n(\alpha)\}$ is a set of coefficients of expansion $\hat{g}(\alpha;P) = \Sigma_{n=1}^{N}\hat{c}_n(\alpha)u_n(P)$, $u_n(P) \equiv T(\tau_n)$, where $\{\tau_n\}$ is a complete system in $L_2(S)$ such that the only function which is orthogonal to all functions τ_n is necessarily 0. Consequently, a solution $\tau(P)$ of an equation $(*)$ is obtained by $\tau(P) = \tau_\delta(\alpha;P) = \Big(1/J_\delta(\alpha;P)\Big)\Sigma_{n=1}^{N}\hat{c}_n(\alpha)\tau_n(P)$, namely

Theorem 2 A solution $\tau_\delta(\alpha;P)$ is given by

$$\begin{aligned}
&\tau_\delta(\alpha;P) = \Sigma_{n=1}^{N}\hat{c}_n(\alpha)\tau_n(P), \quad (P \in S_{2\delta}) \\
&\tau_\delta(\alpha;P) = \Big(\frac{1}{J_\delta(\alpha;P)}\Big)\Sigma_{n=1}^{N}\hat{c}_n(\alpha)\tau_n(P), \ (P \in S - S_{2\delta}); \ \to \infty, \ (\rho \to 0)
\end{aligned} \tag{4}$$

Such solution is called a diverging mode of order $O(\rho^{-\alpha})$, and the aggregate of $\tau_\delta(\alpha;P)$ is denoted as $\mathcal{T}(\delta,\alpha)$; $\mathcal{T}(\delta,\alpha) = \{\tau_\delta(\alpha;P)|1<\alpha<2\}$.

As was shown above, when a solution τ of $T(\tau) = g$ exists, it is necessarily accompanied by a set $\mathcal{T}(\delta,\alpha)$ of diverging mode $\tau_\delta(\alpha;P)$.

Obviously, there are infinitely many diverging solutions $\tau_\delta(\alpha;P)$ in $\mathcal{T}(\delta,\alpha)$ corresponding to α; $1 < \alpha < 2$, which is more than countable. (Such set is called a continuum.) In order to capture the characteristic of diverging modes as a whole, or of a set $\mathcal{T}(\delta,\alpha)$, the average of them may be helpful. The average is given by the mean value thorem $\int_a^b \tau_\delta(\alpha)d\alpha = (a+\theta(b-a))(b-a)$, where $a=1, b=2$ and $\theta = 1/2$, as

$$\tau_\delta(\alpha;P) = \tau_\delta(3/2;P) \tag{5}$$

(5) means that $\tau_\delta(3/2;P)$ corresponding to $J_\delta(3/2;P)$ given by (2), is not only a particular solution of order $O(\rho^{-3/2})$, but also is the representative of all diverging waves. Furthermore, it is noted that $\tau_\delta(3/2;P)$ is the only diverging mode whose explicit expression is available. [3]

[2] Because of the shortage of space, it is impossible to give a detail of MEC here. It is expected that the full paper on MEC will appear soon.

[3] As was mentioned before, it may be impossible to have a general and explicit expression of $J_\delta(\alpha;P)$ for $\alpha \neq 3/2$. Consequently, elements $\tau_\delta(\alpha;P)$ given by (4) for $\alpha \neq 3/2$ are formal and their explicit expression are also not known. Contrary to this, only $J_\delta(3/2;P)$ is given by (2), and $\tau_\delta(3/2;P)$ is the only element of $\mathcal{T}(\delta,\alpha)$ which is given explicitly. On the other hand, the mean value which represents the characteristics of $\mathcal{T}(\delta,\alpha)$ is also $\tau_\delta(3/2;P)$. This accidental coincide brought us a happy result (5).

Ⅳ. The Uniqueness of Solution and Diverging Modes

The existence of diverging modes $\mathcal{T}(\delta,\alpha)=\{\tau_\delta(\alpha;P);1<\alpha<2\}$ looks like to contradict to the uniqueness thorem of a solution of an equation $(*)$. However, this inconsistency is dissolved by making $\delta\to 0$.

Since $J_\delta(\alpha;P)=1$ when $P\in S_{2\delta}$, we have [4] $\hat{g}(\alpha;P)=\iint_S \Psi(P,Q)J_\delta(\alpha;Q)\tau(Q)dS_Q=\iint_S \Psi(P,Q)\tau(Q)dS_Q+\iint_{S-S_{2\delta}}\Psi(P,Q)\{J_\delta(\alpha;Q)\tau(Q)-\tau(Q)\}dS_Q$ at $P\in S_{2\delta}$, which turns out to be $g(P)$ when $\delta\to 0$, since the range of integration of the last integral is reduced to empty, and the integral itself, whose integrand being regular at $P\in S_{2\delta}$, tends to zero.

Let $\hat{c}_n(\alpha)$ and c_n be expansion coefficients of $\hat{g}(\alpha)$ and g, respectively, such that $\hat{g}(\alpha;P)=\Sigma_{n=1}^N\hat{c}_n(\alpha)T(\tau_n)(P)$ and $g=\Sigma_{n=1}^N c_nT(\tau_n)$. Then, since $c_n(\alpha)=c_n$ in $S_{2\delta}$, Theorem 2 is reduced to the uniqueness thorem

Theorem 3 When $\delta\to 0$, a solution in $S_{2\delta}$ is given uniquely and independently to α by

$$\tau(P)=\Sigma_{n=1}^N c_n\tau_n(P), \tag{6}$$

The second expression of (4), which keeps the diverging property, remains unchanged, though $S-S_{2\delta}$ tends to empty.

V. Boundary Line Integral Equation on an Open Line Segment

In this section, in a way similar to that for a three dimensional problem, a two dimensional scattering problem where a boundary is an open line segment L on a plane is studied, A boundary line integral equation $T(\tau)=g$ is solved, where g is in $L_2(L)$, while τ is supposed to have a singularity at the end points A, B of L, and $\tau\notin L_2(L)$. Therefore, we again introduce a "mollifier" $J_\delta(\alpha;P)$ which is defined so as to satisfy the conditions $(1)J_\delta(\alpha;P)=0$ when $P=A,B$, $(2)J_\delta(\alpha;P)=1$ when $P\in L_{2\delta}$, where $L_{2\delta}\subset L$ is a set of points which are more than 2δ away from A and B, and $(3)J_\delta(\alpha;P)$ is piecewise infinitely many times differentiable on L. Such a function does really exist. For example, $J_\delta(\alpha;P)=\delta^{-1}\gamma^{-1}\int_{L_\delta\cap\{Q|\overline{PQ}=R<\delta\}} exp.\Big((-\delta^2)/(\delta^2-R^2)\Big)dR_Q$, where $\gamma=\int_{r<1} exp.\Big((-1)/(1-r^2)\Big)dr$, and L_δ is a set of points which are more than δ away from A and B, is proved to satisfy all of the conditions (1), (2) and (3).

On the other hand, the following conditions are also required; $(4)J_\delta(\alpha;P)=O(\rho^\alpha)$ where ρ is the distance of P from A and B, (5) $\tau\in L_1(L)$ and (6) $J_\delta(\alpha;P)\tau(P)$ is finite in the vicinity of A and B. It is easy to see that the set of conditions (4), (5) and (6) is equivalent to $(1/2)<\alpha<1$.

Then, an equation $T(J_\delta\tau)=\hat{g}$ can be solved in $L_2(L)$ by MEC, and approximate solutions $J_\delta(\alpha;P)\tau(P)=\Sigma_{n=1}^N\hat{c}_n\tau_n$ are obtained, where $\{\hat{c}_n\}$ is a set of constants, while $\{\tau_n\}$ is a given set of functions which is complete in $L_2(L)$. Thus, similarly to the three dimensional case, we have a solution of $T(\tau)=g$ which are $\tau(P)=\tau_\delta(\alpha;P)=\frac{1}{J_\delta(\alpha;P)}\Sigma\hat{c}_n\tau_n(P)$ when $P\in L-L_{2\delta}$ and $\tau(P)=\Sigma\hat{c}_n\tau_n(P)$ when $P\in L_{2\delta}$. Since

[4] For a detailed discussion, we assume an operator $T(\tau)$ to be $T(\tau)=\iint_S\Psi(P,Q)\tau(Q)dS_Q$, where $\Psi(P,Q)=e^{-ikR}/4\pi R$, $R=\overline{PQ}$, and k is a wave number.

$\tau_\delta(\alpha;P) = O(\frac{1}{J_\delta(\alpha;P)}) = O(\rho^{-\alpha})$, $\tau_\delta(\alpha;P) \to \infty$ when $P \to A, B$. Such solution is called a "diverging mode of order α".

Though there are infinitely many modes, they converge to the unique solution of the equation $T(\tau) = g$ in the limit as $\delta \to 0$. The unique solution is $\tau(P) = \Sigma_{n=1}^{N} c_n \tau_n$ when P is in the inside of S excepting on ∂S, where $\{c_n\}$ are known constants given in terms of g.

Since $(1/2) < \alpha < 1$, the mean value of $J_\delta(\alpha;P)$ with respect to α is $J_\delta(3/4;P)$. Therefore, we may consider that diverging modes diverge with the order of $O(\rho^{-3/4})$ in the vicinity of ∂S.

[Note] If a line L is defined by $a < x < b$, then a function $J(P)$, say, $J(P) = \sqrt{(x-a)(b-x)}$, may make $J(P)\tau(P)$ belong to $L_2(L)$. However, such "mollifier" is insufficient in comparison with our mollifier. For example, a solution derived with the help of $J(P)$ does not converge to the true solution, since it does not depend on any parameter such as δ and no limiting operation is possible.

VI. Conclusion

In this paper, a solution of an integral equation $T(\tau) = g$ taken over an open surface S, which models problems of scattering of scalar and vector waves by S, was studied.

Since a solution is not square integrable because of a singularity on a periphery ∂S of S, a method of solution in a $L_2(S)$ is not available. To avoid this trouble, a mollifier $J_\delta(\alpha;P)$ was introduced so that the product $J_\delta(\alpha;P)\tau(P)$ is square integrable and is obtained by a method in $L_2(S)$, and that τ is derived by dividing $J_\delta(\alpha;P)\tau(P)$ by $J_\delta(\alpha;P)$.

Since $J_\delta(\alpha;P) = O(\rho^\alpha)$, where ρ is a distance from ∂S, the corresponding solution $\tau_\delta(\alpha;P) \to \infty$ with the factor $O(\rho^{-\alpha})$. Such solution is called a diverging mode α. Though there are infinitely many solutions $\tau_\delta(\alpha;P), 1 < \alpha < 2$, they are reduced to the unique solution $\tau(P)$ when $\delta \to 0$, showing that they do not contradict to the uniqueness theorem of a solution.

Among diverging modes $\tau_\delta(\alpha;P)$, $\tau_\delta(3/2;P)$ given by (3) in terms of $J_\delta(3/2;P)$, is the representative of them, and also is the only solution which is expressed explicitly, showing how the solution is actually obtained. This also implies that we may say a solution of $T(\tau) = g$ diverges with an order of $O(\rho^{-3/2})$.

A two dimensional problem where a boundary line integral equation whose solution has a singularity was solved with the help of a two dimensional mollifier, and obtained results similar to those of a three dimensional problem.

References

[1] A.Kufner, O.John & S.Fučik, "Function Spaces", Noordhoff, Leiden, 1977

[2] Y.Hayashi, "The Dirichlet problem for the two-dimensional Helmholtz equation for an open boundary", *Journal of Mathematical Analysis and Applications*, vol.44, no.2, pp.489-530, 1973

Detection of Aircraft Embedded in Ground Clutter

S.I.Hwang, S. Ishii, S.Sayama and M.Sekine
Department of Communications Engineering, National Defense Academy
Yokosuka, Japan

Abstract

It is reported that various radar clutter obey a Weibull distribution under certain conditions. To suppress such Weibull-distributed clutter and detect targets such as aircraft or ships embedded in clutter, various anti-clutter techniques have been utilized.

In this paper, we propose a LOG/CFAR with transformation from Weibull to Rayleigh distribution and apply this method to practical problems observed by an X-band radar at the Niigata airport in Japan. Finally an improvement value of target-to-clutter ratio 26.4dB was obtained for the detection of an aircraft embedded in ground clutter.

1. Introduction

Radar clutter is defined as the unwanted reflective waves from irrelevant targets. For example, there exist ground clutter, sea clutter, sea-ice clutter and weather clutter for ground, sea, sea-ice and rain clouds, respectively.

In order to improve target detectability in the presence of such clutter, various anti-clutter techniques have been utilized[(1)~(2)].

And it has been reported that ground, sea, sea-ice and weather clutter amplitude statistics obey the Weibull-distribution, which incorporate the Rayleigh-distribution as a special case in recent[(3)~(4)]. To suppress such Weibull-distributed clutter, a new method has been considered[(5)].

In this paper we considered LOG/CFAR with transformation from Weibull to Rayleigh distribution.

To this end, we made a computer simulation for this research. As a result, we could detect the aircraft (target) embedded in ground clutter by applying a LOG/CFAR circuit with transformation from Weibull to Rayleigh distribution.

2. LOG/CFAR circuit with transformation from Weibull to Rayleigh distribution

Now it is shown that if any clutter, distributed according to the Weibull distribution,

$$p_w(x) = \frac{c}{b}\left(\frac{x}{b}\right)^{c-1} \exp\left[-\left(\frac{x}{b}\right)^{c}\right]$$

is passed through a conventional LOG/CFAR circuit, then the variance of the receiver output depends on the shape parameter c and CFAR is not maintained.

The value of c and the scale parameter b are determined before and after the logarithmic amplifier, respectively. The circuit structure is shown in Figure 1.

Before passing through a logarithmic amplifier, the mean value and the mean-squared value of x are calculated as

$$\langle x \rangle = \int_0^\infty x p_w(x) dx = b\Gamma\left(\frac{1}{c}+1\right) \quad (1)$$

$$\left\langle x^2 \right\rangle = \int_0^\infty x^2 p_w(x)dx = b^2\Gamma\left(\frac{2}{c}+1\right) \tag{2}$$

where $\Gamma(x)$ is gamma function.

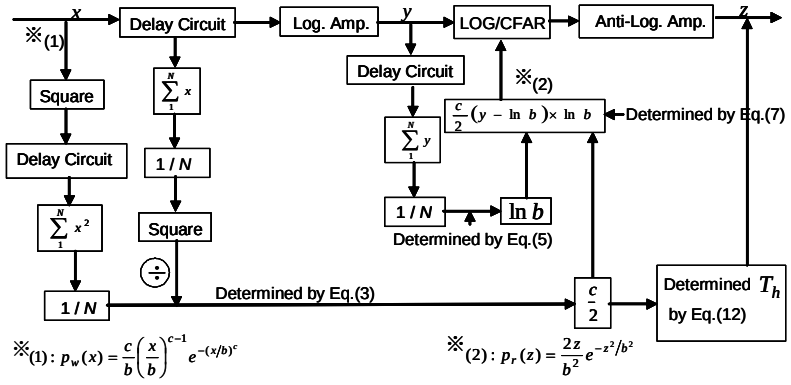

Figure 1: LOG/CFAR circuit with transformation from Weibull to Rayleigh distribution.

Now a ratio of Equation (1) and (2) is formed

$$\frac{\langle x \rangle^2}{\left\langle x^2 \right\rangle} = \frac{\Gamma^2\left(\frac{1}{c}+1\right)}{\Gamma\left(\frac{2}{c}+1\right)} \tag{3}$$

This ratio is independent of b and depends only on c. Thus the value of c can be determined by calculating $\langle x \rangle$ and $\left\langle x^2 \right\rangle$ from Equation (3) and parameter b are determined by Equation (5), as shown in Figure 1.

Then if the Weibull clutter amplitude x is passed through an idealized logarithmic amplifier, the output y is represented by

$$y = k\ln(lx) \tag{4}$$

where k and l are constants of the amplifier.

The mean value of y is given by

$$\langle y \rangle = \int_0^\infty k\ln(lx)p_w(x)dx = \ln(lb) - \frac{k}{c}\gamma \tag{5}$$

where $\gamma = 0.5772\cdots$ is Euler's constant.

We can transform from Weibull to Rayleigh distribution with parameters b and c determined by Equation (3) and Equation (5). The Rayleigh distribution is given by

$$p_r(z) = \frac{2z}{b^2}e^{-(z/b)^2} \tag{6}$$

Hence, the mean value of y can be written as

$$\langle y_r \rangle = \int_0^\infty k\ln(lz)p_r(z)dz = k\ln(l\sigma) - \frac{k}{2}\gamma \tag{7}$$

Here σ indicates a mean square of Rayleigh clutter amplitude x.

Subtracting the mean value $\langle y \rangle$ from y, we can obtain

$$v = y - \langle y \rangle \tag{8}$$

The output signal z of an anti-logarithmic amplifier is represented by

$$z = me^{nv} \qquad (m,n \text{ are constants of the amplifier}) \tag{9}$$

We can write the variance of z using Equation (9).

$$V(z) = \langle z^2 \rangle - \langle z \rangle^2 = m^2 e^{\gamma} \left\{ \Gamma(2) - \Gamma^2\left(\frac{3}{2}\right) \right\} \tag{10}$$

The false alarm probability p_{fa} is the probability that a clutter signal above the threshold T_h is misjudged as a target signal and it is given by

$$p_{fa} = \int_{T_h}^{\infty} p_r(z)dz = \exp\left[-\left(T_h / m e^{\gamma/c} \right)^c \right] \tag{11}$$

We now put the threshold level T_h as

$$T_h = k\sqrt{V(z)} \quad , \tag{12}$$

where k is a constant. From Equations (10), (11) and (12), finally we obtain

$$p_{fa} = \exp\left[-\left(k\sqrt{1 - \frac{\pi}{4}} \right)^2 \right] \tag{13}$$

The target to clutter ratio is defined as

$$T/C = 10\log\frac{t^2}{\langle x^2 \rangle} = 10\log\frac{t^2}{\sigma^2} \tag{14}$$

where t is the amplitude of the target.

The detection probability p_D is found to be

$$p_D = \int_{T_h}^{\infty} p_r(z)dz = \exp\left[-\left(\sqrt{-\ln p_{fa}} - 10^{(t/x)/20} \right)^2 \right] \tag{15}$$

3. Simulation for a Finite number of Samples N

Fluctuation of c caused by a finite number of samples was not taken into account in the above discussion and the results obtained correspond to the case of an infinite number of samples. A Weibull-distributed variable x was generated by

$$x = b(-\ln\xi)^{1/c} \tag{16}$$

where ξ is a uniformly distributed random number over the interval $(0,1)$. To maintain CFAR in Figure 2, a computer simulation was made for N = 32.

Figures 2 and 3 shows threshold level T_h and detection probability p_D versus T/C ratio respectively.

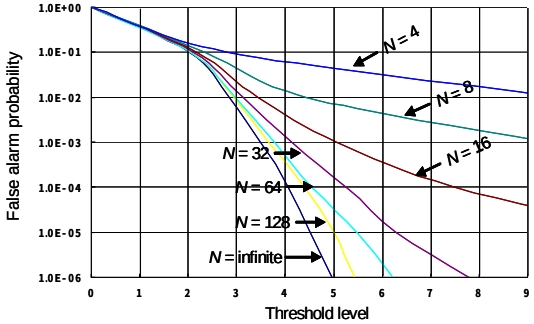

Figure 2: p_{fa} versus T_h.

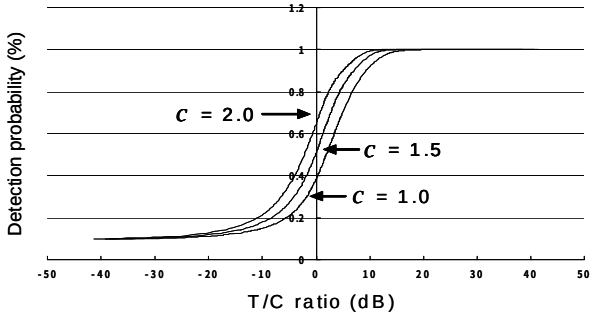

Figure 3: p_D versus T/C ratio.

4. Observations of Ground Clutter and Targets

Ground clutter was measured at the Niigata airport in Japan. Figures 4 and 5 show the amplitude against the azimuth and radial directions with and without an aircraft, respectively. Figure 6 illustrates an area MTI (Moving Target Indicator) by subtraction from map of Figure 4 to map of Figure 5. It is easily seen that an aircraft is detected. In the following, we will investigate the suppression of residue after an area MTI.

5. Amplitude Statistics of Residue of Ground Clutter after Area MTI

First, we shall investigate the statistical amplitude properties of the residue of ground clutter after the area MTI. The investigation of statistical amplitude properties is shown in Figure 7.

These results show that the residue amplitude after the area MTI obey a Weibull distribution with shape parameter of $c = 0.713$ and scale parameter of $b = 6.92$.

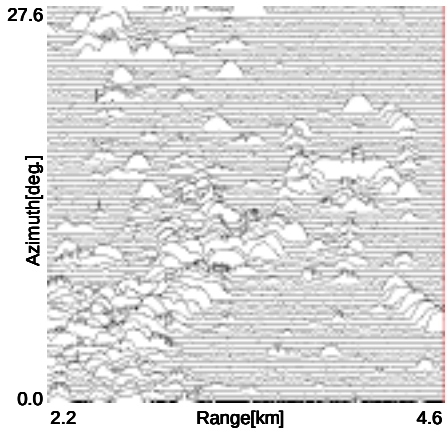

Figure 4: Result of observation.

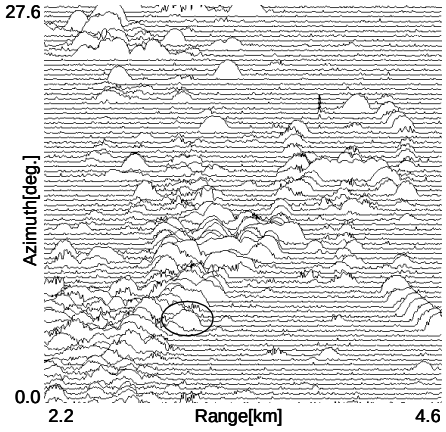

Figure 5: Result of observation. (Circle means target).

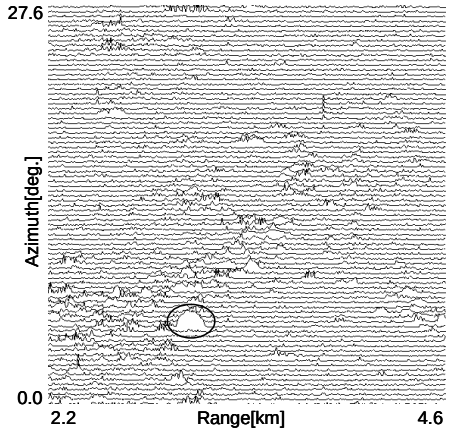

Figure 6: After area MTI processing.

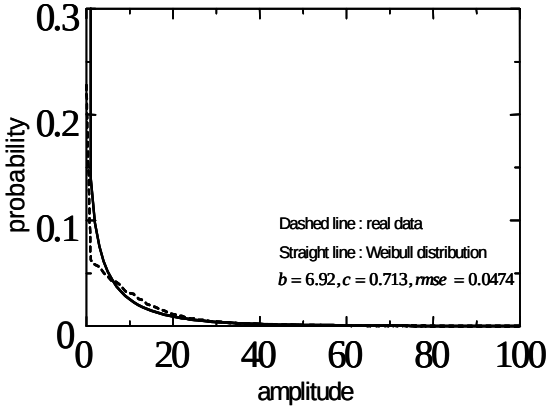

Figure 7: Statistical amplitude properties

6. Application to raw radar data

The LOG/CFAR with transformation from Weibull to Rayleigh distribution technique in Figure 1 has been applied to raw data in Figure 6 for a finite number of samples $N = 32$ and a false alarm rate $P_{fa} = 10^{-1}$. The result is shown in Figure 8

We obtained the target to clutter ratio T/C=47.7dB. Compared to the original radar image in Figure 7 with T/C=21.3dB, we obtained 26.4dB improvement.

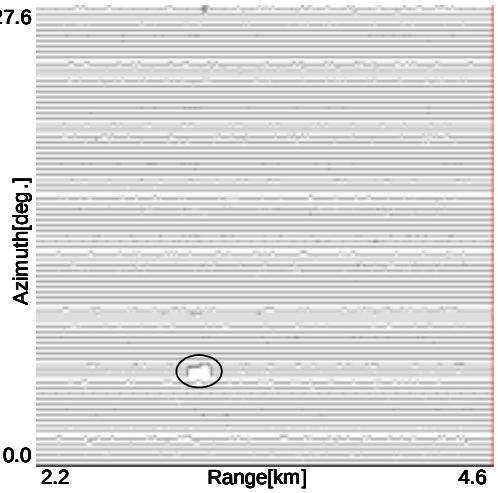

Figure 8: The result of LOG/CFAR with transformation from Weibull to Rayleigh distribution for $P_{fa} = 10^{-1}$.

7. Conclusion

In this paper we applied the LOG/CFAR with transformation from Weibull to Rayleigh distribution technique to practical problems observed by an X-band radar at the Niigata airport in Japan. Then, we can transform from Weibull to Rayleigh distribution with parameters and the processing is applied to raw radar data with cell-averaging LOG/CFAR.

Finally we obtained an improvement value of target-to-clutter ratio 26.4dB for the detection of an aircraft embedded in ground clutter.

REFERENCES

1. M, Sekine, "Radar Signal Processing Techniques," The Institute of Electronics, Information and Communication Engineers, Tokyo, Japan, 1991.
2. Skolnik, M. L. "Introduction to Radar System, "McGraw-Hill, New York, 1980.
3. M, Sekine and Y. Mao, "Weibull Radar Clutter," IEE Radar, Sonar, Navigation and Avionics Series 3, London, 1990.
4. S.Sayama and M, Sekine, "Weibull, log-Weibull and K-distribution ground clutter modeling analyzed by AIC," *IEEE Trans. Aerosp. & Electron. Sys.*, ASE.37, No.3, 1108-1113, 2001.
5. G.B. Goldstein, "False-alarm regulation in log-normal and Weibull clutter," *IEEE Trans. Aerosp. & Electron. Sys*, ASE.9, No.1, 84-92, 1973.

Amplitude Statistics of Sea Clutter Observed by an X-band Radar Analyzed by MDL Principle

S. Sayama, S. Ishii, and **M. Sekine**
National Defense Academy, Japan

Abstract We observed sea clutter using an X-band radar having a frequency 9,380 MHz, a beamwidth 0.6°, and a pulsewidth 0.25 μs. To determine the sea clutter amplitude, we use five probability distribution models, the log-normal, Weibull, log-Weibull, K-, and generalized gamma distributions and introduce the Minimum Description Length (MDL) principle, which is more rigorous fit of the distribution to the data than Akaike Information Criterion (AIC). As a result, it is discovered that the sea clutter amplitudes obey the generalized gamma distribution with shape parameter of 5.24 for entire data and the log-normal, log-Weibull, K-, and generalized gamma distributions with the shape parameters of 0.515, 1.94 to 2.49, 1.15 to 12.59, and 3.43 to 5.86, respectively, for data within the beam width of an antenna.

1. Introduction

In the design of radar systems, it is important to improve target detectability over various clutters, such as ground clutter, sea clutter, weather clutter, and angel echo which is apparently caused by birds, insects, and atmospheric density fluctuations. Various anticlutter techniques have been utilized. For examples, a moving target indicator (MTI) is used against ground clutter, a circular polarizer is used against weather clutter, and a dual beam antenna is used against short-range ground clutter, sea clutter, and angel echoes [1], [2]. By using these techniques, a significant improvement has been obtained with regard to the signal-to-clutter ratio. However, these types of clutter have a large dynamic range that can cause the receiver output to be saturated, rendering target detection impossible.

To overcome such difficulties, a constant false alarm rate (CFAR) techniques is employed, which keeps the receiver output level constant against these types of clutter and effectively suppresses the clutter to the receiver noise level [3].

The LOG/CFAR system makes use of the fact that the amplitudes of weather and sea clutters generally obey a Rayleigh distribution. The system reduces the clutter output to about the receiver noise level by means of a logarithmic amplitude and CFAR circuit. However, when the clutters are not distributed according to a Rayleigh distribution, the output clutter level is not kept constant and discrimination of the target from clutters is no longer easy. Therefore, some additional distributions, for example, the log-normal, Weibull, log-Weibull, and K-distributions should be considered [4].

In the following we observed sea clutter using an X-band radar having a frequency 9,380 MHz, a beamwidth 0.6°, and a pulsewidth 0.25 μs. To determine the sea clutter amplitude, we use five probability distribution models, the log-normal, Weibull, log-Weibull, K-, and generalized gamma distributions and introduce the Minimum Description Length (MDL) principle [5], which is more rigorous fit of the distribution to the data than Akaike Information Criterion (AIC) [6].

2. Observations of Sea Clutter

Sea clutter was observed using an X-band radar. The characteristics of the radar system are shown in Table 1. This radar is located on the top of Mt. Yahiko with the height of 630 m in Niigata prefecture. The data was recorded at November 1, 1990.

Radar echoes were observed from sea in a range interval of 2.0 km to 4.4 km, over an azimuth interval of 0° to 27.6°. The observed area of sea clutter formed waves of a relatively high sea state 7. The height of waves were 6 to 9 m. This is illustrated in Fig. 1. The grazing angles are calculated to be 3.1° at 4.4 km and 17.5° at 2.0 km. The observed wind velocity was 25 m/s and the direction of the upwind was towards the radar site.

Data was recorded digitally on a floppy disk as video signals after passing through an IF amplifier and a phase detector. The amplitude value was recorded on the floppy disk as an 8 bit signal, and hence the minimum and maximum integer values were 0 and 255, respectively.

Table 1 Radar characteristics.

Frequency	9,380 MHz
Transmitted power (peak)	53 kW
Pulsewidth	0.25 μ s
pulse-repetition frequency	1,000 Hz
antenna scan rate	18 r.p.m.
horizontal beamwidth	0.6°
vertical beamwidth	20.0°
receiver	logarithmic
intermitted frequency	60.0 MHz

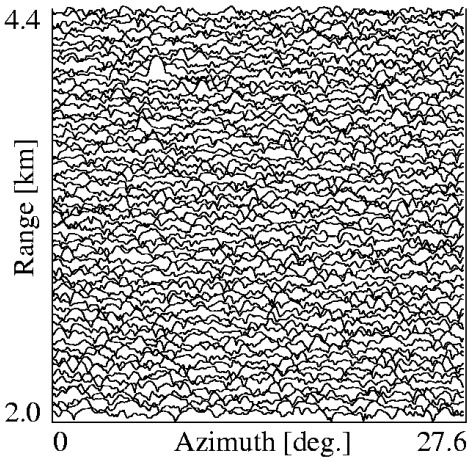

Fig. 1 Observed data.

3. Probability Distribution Models for Clutter and MDL Principle

To determine the sea clutter amplitude, we apply some models to observed data and compare "goodness" of models. In this paper, we use five probability distribution models, the log-normal, Weibull, log-Weibull, K-, and generalized gamma distributions and introduce the MDL principle [5]. We explain the probability density functions and the properties of these five models and summarize the MDL principle.

3.1 The Log-normal Distribution

The log-normal distribution is written as follows:

$$p_{LN}(x) = \frac{1}{\sqrt{2\pi}\sigma x} \exp\left[-\frac{(\ln x - \mu)^2}{2\sigma^2} \right]. \tag{1}$$

Here x is the amplitude of the return signals, μ is an average of $\ln x$ (a scale parameter) and σ is the standard deviation of $\ln x$ (a shape parameter). The character of the log-normal distribution is its long tail. Recently, to develop a high-resolution radar, return signals accompany many spikes. It has been observed that the clutter amplitude has a longer tail [4].

3.2 The Weibull Distribution

The Weibull distribution was proposed by Prof. Walodi Weibull at the Swedish Royal Institute of Technology [7]. This distribution is written as follows:

$$p_W(x) = \frac{c}{b}\left(\frac{x}{b}\right)^{c-1} \exp\left[-\left(\frac{x}{b}\right)^{c}\right]. \tag{2}$$

Here b is a scale parameter and c is a shape parameter. It is important that the Weibull distribution includes the exponential and Rayleigh distributions. That is, for $c = 1.0$ and 2.0 in Eq. (2), the Weibull distribution is identical to the exponential and Rayleigh distributions, respectively. The Weibull distribution is flexible in its shape and relatively easy in its calculation. Therefore, this is the very important distribution to investigate the properties of the radar signals [4].

3.3 The Log-Weibull Distribution

We proposed a new log-Weibull distribution as the probability distribution model for clutter [8], [9]. The log-Weibull distribution is written as follows:

$$p_{LW}(x) = \frac{c}{bx}\left(\frac{\ln x}{b}\right)^{c-1} \exp\left[-\left(\frac{\ln x}{b}\right)^{c}\right]. \tag{3}$$

Here b is a scale parameter and c is a shape parameter. The log-Weibull distribution has the advantage of both the log-normal and Weibull distributions. That is, the log-Weibull distribution has a long tail and is flexible in its shape.

3.4 The K-Distribution

The K-distribution was proposed by E. Jakeman and P.N. Pusey in 1976 [10]. This distribution is written as follows:

$$p_K(x) = \frac{4h^{\nu+1}}{\Gamma(\nu)} x^{\nu} K_{\nu-1}(2hx) \tag{4}$$

Here h is a scale parameter and ν is a shape parameter. $\Gamma(x)$ is the gamma function and $K_\nu(x)$ is the νth modified Bessel function. ν has been found to lie in the region $\nu = \infty$, indicating Rayleigh distributed clutter. The smaller the value of ν becomes, the longer the tail of the K-distribution becomes and the larger the gap between the Rayleigh and K-distributions becomes [10]–[13]. The K-distribution includes the modified Bessel function. Therefore, the K-distribution is more difficult than the other four distributions in its calculation.

3.5 The Generalized Gamma Distribution

The generalized gamma distribution was proposed by E.W. Stacy in 1962 [14]. The generalized gamma distribution is written as follows:

$$p_G(x) = \frac{\gamma \beta^{\frac{\alpha}{\gamma}}}{\Gamma\left(\frac{\alpha}{\gamma}\right)} x^{\alpha-1} \exp(-\beta x^{\gamma}) \tag{5}$$

Here β, γ are scale parameters and α is a shape parameter. The number of parameters of the generalized gamma distribution is three. It is different from that of the other four distributions. For $\alpha = \gamma = c$ and $\beta = b^{-c}$ in Eq. (5), the generalized gamma distribution is identical to the Weibull distribution.

3.6 The MDL Principle

We have investigated various clutter using the AIC [4]. But when there are many data points and the differences in the number of parameters included in the probability distribution models, it is doubtful whether the differences in the values of the AIC are significant. We explain such a problem in the AIC and summarize the MDL principle.

Now we assume that the M numbers of the independent values $\{x_1, x_2, \cdots, x_M\}$ are observed. We consider applying a model $p(x|\theta)$ to these observed data (θ are parameters of the probability density function of this model). The logarithmic likelihood $L(\theta)$ of this model is defined as

$$L(\theta) = \sum_{i=1}^{M} \ln\{p(x_i|\theta)\}. \tag{6}$$

We obtain θ_0 (the maximum likelihood estimation) which gives the largest $L(\theta)$. The AIC [6] is defined as

$$L_{AIC} = -2\{L(\theta_0) - k\}. \tag{7}$$

Here k is a number of parameters in a model [15].

When the AIC is derived, to minimize the expectation average logarithmic likelihood, two values of the unbiased estimation are substituted. That is, the unbiased estimation of the average maximum logarithmic likelihood is substituted for the entropy of the true probability distribution of the observed data. The unbiased estimation of the expectation average logarithmic likelihood is substituted for $L(\theta_0) - k$. But it is doubtful whether these substitutions are correct.

The number of parameters in the best model selected by the AIC does not make the probability of growing more than the number of parameters in the true probability distribution below a positive definite value. Therefore, the larger the gap between the number of parameters in the model and the number of parameters in the true probability distribution becomes by minimized the AIC, the smaller the logarithmic likelihood which must be maximized becomes. The AIC includes such a "self-contradiction". This is the problem which is caused by the substitution depending on only an unbiased character [16].

To solve such a problem, the MDL principle is invented [5]. The value of the MDL estimation of a model $p(x|\theta)$ is defined as

$$L_{MDL} = -L(\theta_0) + \frac{k}{2}\ln M + \ln N. \tag{8}$$

Here N is the number of models. Comparing Eq. (7) with Eq. (8), the characteristics of the MDL estimation consist in the second term on the right hand side in Eq. (8). In general, to decrease the first terms (the logarithmic likelihood), k (the number of parameters) must increase. But the second term increases along with increasing k. We can interpret that the second term prevents a model from excessively fitting the observed data. The prevention of excessive fit plays an important role of selecting the number and values of parameters which express the characteristics of the observed data for the best. The model which yields the smallest MDL estimation is regarded as the best one [17].

4. Sea Clutter Amplitude Analyzed by MDL Principle

We estimate the sea clutter amplitude using this MDL principle and five probability distribution models. We summarize the parameters and the MDL values for different range sweep

numbers in Table 2. The smallest MDL estimation is indicated by underline.

4.1 Distribution Estimation of Entire Data

We examine entire data for range sweep 0–255. The number of data points is 65,536. This is shown in Fig. 2. The MDL values are calculated to be 126,611.5 for a log-normal distribution, 128,247.0 for a Weibull distribution, 126,640.0 for a log-Weibull distribution, 126,957.5 for a K-distribution, and 126,012.3 for a generalized gamma distribution using Eq. (8). The best fit of the entire distribution is a generalized gamma distribution. The sea clutter amplitudes obey the generalized gamma distribution with shape parameter of 5.24 for entire data.

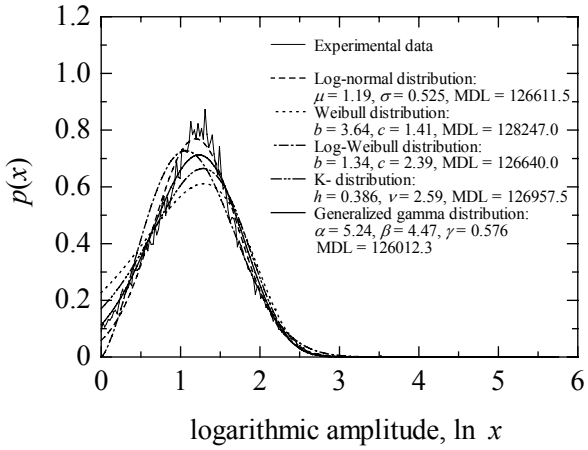

Fig. 2 Result of distribution estimation for entire data for range sweep 0–255.

4.2 Distribution Estimation of Data within the Beam Width of an Antenna

In general, return signals have strong correlation and the same properties within the beam width of an antenna. Thus we divide the observed data into data within the beam width of an antenna. The size of data is 256 range bins corresponding to a range interval of 2.4km and 6 range sweeps corresponding to an azimuth interval of 0.6°. The number of data points is 1,536. The observed data is divided into 42 data within the beam width of an antenna. In Table 2, the numbers of the smallest MDL of the log-normal, log-Weibull, K-, and generalized gamma distributions are 1, 6, 12, and 23, respectively, from 42 range sweep numbers.

The sea clutter amplitudes obey the log-normal, log-Weibull, K-, and generalized gamma distributions with the shape parameters of 0.515, 1.94 to 2.49, 1.15 to 12.59, and 3.43 to 5.86, respectively, for data within the beam width of an antenna. It is very interesting that the sea clutter amplitudes obey the generalized gamma distribution for entire data but the log-normal, log-Weibull, K-, and generalized gamma distribution for data within the beam width of an antenna. Three typical examples are illustrated in Figs. 3–5.

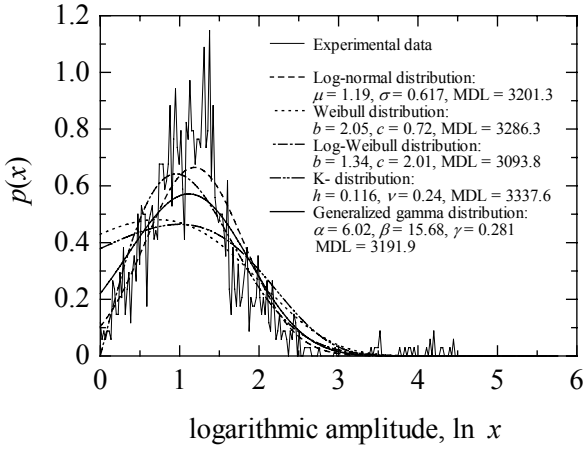

Fig. 3 Log-Weibull distribution is best fit to data for range sweep 60–65.

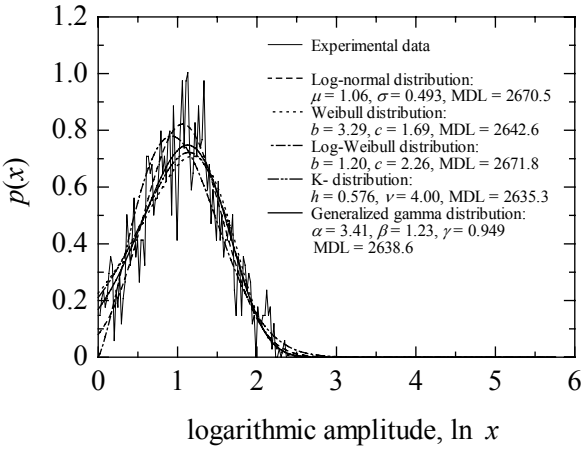

Fig. 4 K-distribution is best fit to data for range sweep 30–35.

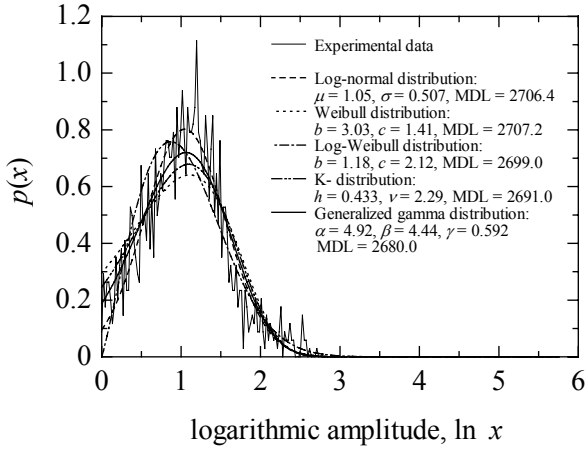

Fig. 5 Generalized gamma distribution is best fit to data for range sweep 48–53.

Table 2 Parameters and MDL values for different range sweep numbers.

Range sweep numbers	Log-normal		Weibull		Log-Weibull		K- distribution		G-distribution	
	σ	MDL	c	MDL	c	MDL	ν	MDL	α	MDL
0 – 255	0.525	126611.5	1.41	128247.0	2.39	126640.0	2.59	126957.5	5.24	126012.3
0 – 5	0.618	3287.8	1.25	3246.6	2.09	3261.1	1.15	3242.6	2.44	3244.3
6 – 11	0.578	3126.4	1.30	3117.2	2.17	3106.3	1.49	3106.4	3.84	3100.0
12 – 17	0.572	3166.7	1.24	3201.3	2.24	3129.7	1.38	3183.6	5.15	3157.8
18 – 23	0.543	3023.5	1.39	3040.9	2.28	3013.0	2.00	3020.8	4.80	3009.4
24 – 29	0.479	2700.9	1.73	2706.3	2.45	2691.2	5.30	2694.2	4.81	2685.6
30 – 35	0.493	2670.5	1.69	2642.6	2.26	2671.8	4.00	2635.3	3.41	2638.6
36 – 41	0.487	2717.7	1.65	2730.2	2.38	2721.9	4.00	2712.5	5.10	2703.4
42 – 47	0.498	2741.3	1.49	2774.3	2.34	2711.9	2.74	2753.6	5.92	2733.1
48 – 53	0.507	2706.4	1.41	2707.2	2.12	2699.0	2.29	2691.0	4.92	2680.0
54 – 59	0.496	2782.0	1.50	2817.7	2.34	2775.2	2.97	2793.5	5.86	2772.8
60 – 65	0.617	3201.3	0.72	3286.3	2.01	3093.8	0.24	3337.6	6.02	3191.9
66 – 71	0.593	2996.9	0.82	3030.4	1.94	2906.6	0.44	3048.5	5.55	2964.4
72 – 77	0.520	2860.7	1.40	2888.0	2.27	2841.3	2.21	2866.7	5.34	2848.3
78 – 83	0.467	2519.4	1.75	2508.1	2.30	2521.1	5.81	2499.6	4.39	2495.5
84 – 89	0.473	2527.6	1.70	2508.2	2.22	2533.9	4.99	2499.4	4.05	2497.8
90 – 95	0.496	2770.8	1.77	2743.4	2.39	2781.1	6.00	2738.9	3.15	2740.9
96 – 101	0.482	2688.8	1.86	2658.4	2.46	2688.5	9.72	2655.4	3.00	2657.3
102 – 107	0.491	2614.1	1.75	2568.0	2.24	2619.1	5.98	2567.3	2.27	2570.7
108 – 113	0.493	2680.0	1.70	2651.9	2.27	2697.8	4.97	2644.5	3.39	2646.3
114 – 119	0.491	2667.5	1.73	2637.8	2.29	2677.7	5.34	2633.0	3.20	2634.9
120 – 125	0.500	2806.6	1.76	2781.2	2.41	2812.7	5.82	2777.1	3.14	2778.6
126 – 131	0.499	2911.3	1.83	2896.0	2.60	2914.3	7.64	2892.0	3.43	2891.0
132 – 137	0.503	2940.3	1.80	2926.8	2.54	2982.9	6.58	2919.7	3.61	2918.3
138 – 143	0.521	3007.3	1.70	2992.5	2.48	3016.7	4.00	2983.8	3.46	2985.6
144 – 149	0.554	3174.6	1.58	3153.4	2.43	3177.1	2.89	3147.0	3.03	3148.8
150 – 155	0.490	2878.2	1.77	2889.1	2.59	2883.5	5.68	2878.1	4.67	2868.2
156 – 161	0.524	3011.5	1.57	3027.4	2.44	3015.6	3.04	3010.8	4.71	3000.8
162 – 167	0.501	3010.9	1.84	3005.1	2.70	3024.4	7.52	2998.3	3.84	2994.0
168 – 173	0.481	3083.2	2.05	3076.3	3.04	3103.3	29.56	3075.8	3.92	3065.5
174 – 179	0.490	3125.7	1.96	3133.6	2.99	3133.1	13.32	3130.4	4.33	3118.1
180 – 185	0.515	3238.6	1.75	3274.7	2.86	3252.3	4.68	3258.5	5.07	3239.9
186 – 191	0.512	3069.0	1.77	3067.8	2.63	3090.4	5.46	3058.3	3.96	3053.9
192 – 197	0.478	2929.2	1.95	2930.1	2.84	2950.7	11.87	2921.9	4.27	2911.0
198 – 203	0.531	3179.6	1.64	3196.2	2.65	3193.9	3.84	3178.1	4.30	3170.1
204 – 209	0.551	3263.3	1.21	3391.0	2.49	3259.7	1.60	3350.0	6.82	3282.3
210 – 215	0.497	3174.3	1.82	3214.9	2.96	3192.3	6.34	3196.5	5.25	3173.5
216 – 221	0.497	3000.4	1.80	3012.5	2.71	3009.6	6.00	2999.5	4.56	2989.7
222 – 227	0.520	3059.5	1.69	3058.7	2.53	3065.5	4.00	3047.5	3.93	3045.5
228 – 233	0.517	3065.9	1.79	3048.3	2.60	3088.5	6.00	3042.6	3.27	3043.2
234 – 239	0.486	2840.7	1.91	2816.0	2.62	2853.1	12.59	2812.8	3.16	2813.0
240 – 245	0.520	3081.8	1.72	3074.3	2.56	3114.9	4.89	3063.3	3.63	3061.7
246 – 251	0.548	3167.2	1.55	3163.7	2.43	3168.8	2.73	3152.2	3.73	3149.5

5. Conclusion

We observed sea clutter using an X-band radar having a frequency 9,380 MHz, a beamwidth 0.6°, and a pulsewidth 0.25 μs. To determine the sea clutter amplitude, we use five probability distribution models, the log-normal, Weibull, log-Weibull, K-, and generalized gamma distributions and introduce the MDL principle, which is more rigorous fit of the distribution to the data than the AIC. As a result, it is discovered that the sea clutter amplitudes obey the generalized gamma distribution with shape parameter of 5.24 for entire data and the log-normal, log-Weibull, K-, and generalized gamma distributions with the shape parameters of 0.515, 1.94 to 2.49, 1.15 to 12.59, and 3.43 to 5.86, respectively, for data within the beam width of an antenna. The design of a CFAR depends on a knowledge of various amplitude distribution of sea clutter. It is therefore concluded that suppression of sea clutter will require a unified CFAR which is independent of the distribution parameters of log-normal, Weibull, log-Weibull, K-, and generalized gamma distributions.

REFERENCES

1. F.E. Nathanson, *Radar Design Principles*, McGraw-Hill, New York, 1990.
2. M. Sugie, Y. Tomita, and T. Hagisawa, "Advanced air route surveillance radar with various unique clutter elimination capabilities," *NEC Res. Develop.*, No. 39, 71–83, Oct. 1975.
3. J. Croney, "Clutter on radar displays," *Wireless Eng.*, Vol. 33, 83–96, 1956.
4. M. Sekine, and Y. Mao, *Weibull Radar Clutter*, IEE, Peter Peregrinus Ltd., London, 1990.
5. J. Rissanen, "Modeling by shortest data description," *Automatica*, 465–471, 1978.
6. H. Akaike, "A new look at the statistical model identification," *IEEE Trans. on Autom. Control*, vol. AC-19, 716–723, 1974.
7. W. Weibull, "Statistical theory of strength of materials," *IVB-Handl.*, 1939.
8. M. Sekine, T. Musha, Y. Tomita, T. Hagisawa, T. Irabu, and E. Kiuchi, "Log-Weibull distributed sea clutter," *IEE Proc.*, vol. 127, Pt. F, no. 3, 225–228, 1980.
9. S. Sayama and M. Sekine, "Weibull, Log-Weibull and K-Distributed Ground Clutter," *IEEE Trans. on Aerosp. & Electron. Syst.*, Vol. AES-37, No. 3, 1108–1113, 2001.
10. E. Jakeman, and P.N. Pusey, "A model for non-Rayleigh sea echo," *IEEE Trans. Antennas. & Propag.*, Vol. AP-24, No. 6, 806–814, 1976.
11. J.K. Jao, "Amplitude distribution of composite terrain radar clutter and the K-distribution," *IEEE Trans. on Aerosp. & Electron. Syst.*, Vol. AP-32, No. 10, 1049–1062, 1984.
12. S. Watts, "Radar detection prediction in sea clutter using the compound K-distribution model," *IEE Proc.*, vol. 132, Pt. F, no. 7, 613–620, 1985.
13. S. Watts, "Radar detection prediction in K-distributed sea clutter and thermal noise," *IEEE Trans. on Aerosp. & Electron. Syst.*, Vol. AES-23, No. 1, 40–45, 1987.
14. E.W. Stacy, "A Generalization of the Gamma Distribution," *Annals of Mathematical Statistics*, Vol. 33, No. 3, 1187–1192, 1962.
15. Y. Sakamoto, M. Ishiguro, and G. Kitagawa, *Information Statistics*, Kyoritsu Shuppan Co., Ltd., Tokyo, Japan, 1983, (in Japanese).
16. T.S. Han, and K. Kobayashi, *Mathematics of Information and Coding*, Baifukan Co., Ltd, Tokyo, Japan, 1999, (in Japanese).
17. K. Yamanishi, and T.S. Han, "Introduction to MDL from Viewpoints of Information Theory," *Journal of Japanese Society for Artificial Intelligence*, 427–434, 1992, (in Japanese).

Bandwidth enhancement of a microstrip antenna with a loaded chip-resistor

Chih-Yu Huang, Pei-Yuan Chiu and Chun-Cheng Lin
Dept. of Electronic Engineering, National Kaohsiung Normal University,
Kaohsiung 824, Taiwan

Abstract - A resistive loading technique as a method for improving the bandwidth of planar antennas is presented. Appropriate arrangement of the loaded slit and resistance offer large improvements in antenna bandwidth. Measured impedance bandwidth in this study can be increased to 7.74% while conventional one has merely 1.9%. Details of the antenna design are described and typical experimental results are presented and discussed.

1. Introduction

Microstrip antennas are popular planar antennas due to their low cost, low profile, ease of design and manufacturing. Unfortunately, microstrip antennas exhibit low bandwidth and limit these antennas to narrowband applications. One technique for resistively loading microstrip patch antenna is to replace the short circuit normally found on one side of a quarter-wave patch with a low-valued resistor [1]. And, it has been proposed as an effective method of increasing the bandwidth of microstrip antennas by five to six times [1], [2]. By lowering the antenna quality factor, an improved bandwidth is achieved. But the antenna efficiency is unacceptably low [3]. Other technique chose lossy conductive paste as distributed resistor [4] to broaden the bandwidth for specific manufacture process.

In this paper, a chip-resistor loading of a half-wave patch antenna is implemented by introducing a slit to the non-radiating edge of the patch antenna and by loading the open end of the slit with a chip-resistor. Adjusting the slit length and resistance allows the amount of current flowing through the resistor and hence the bandwidth characteristic can be broadened. The resistance can be made to have less effect by mounting it at the centerline of patch where current density is less, improving efficiency while still providing the bandwidth-enhancing effects of resistive loading. Typical experimental results of different slit length and resistance are presented and analyzed.

2. Antenna Design and Experimental Results

The proposed microstrip antenna with resistive loading is shown in Fig. 1. A narrow slit of length ℓ and width w is inset at the boundary of the microstrip antenna. The square patch has a side length of A and is printed on a substrate of relative permittivity ε_r and thickness h. A probe feed at a position dp away from the patch center. A chip-resistor of resistance R is mounted on the open end of the slit. Then, a wider impedance bandwidth can easily be obtained by adjusting the slit length and resistance.

In this study, the square patch was printed on a FR4 substrate with relative permittivity of $\varepsilon_r = 4.4$ and a thickness of 1.6 mm. Several prototypes were constructed with patch side length 30 mm and slit width 1 mm. Fig. 2 shows the measured center frequency and bandwidth against resistance. The loaded resistance has little effect on center frequency. As expected, as the resistance approaches zero or infinity, the antenna bandwidth is minimized as the resistor has minimum effect on the surface current. Fig. 3 shows the measured center frequency and bandwidth against slit length. The longer slit length result in lower center frequency for its longer surface current length, and larger bandwidth for the current amount flow through the resistor is less. The corresponding measured data are also listed in Table 1, 2 for comparison. A maximun bandwidth was found to be 7.74% occured at ℓ = 9 mm, R = 47 Ω and dp = 14 mm. It would be hard to get impedance matching when slit length longer than 9 mm. The maximun bandwidth 7.74% is about 4.1 times that of a conventional patch (1.9%). Fig. 4 shows the simulated surface current distribution by using software IE3D^{TM}, the current flow lengthened by the inset slit and some flow bypass through loaded resistor. Fig. 5 shows the measured x-z, y-z planes radiaion patterns of the case with ℓ = 9 mm and R = 47 Ω. Good linear polarized radiation is observed and maximum antenna gain is measured to be –0.4 dBi while a regular quarter-wave patch antenna has antenna gain of 2.5 dBi and a quarter-wave patch antenna loaded with 1 Ω resistance [1] of bandwidth (9.3%) has antenna gain of –18.7 dBi.

3. Conclusions

Resistive loading has the potential to improve the bandwidth of microstrip patch antennas significantly, this paper has illustrated that appropriate arrangement of slit and loaded resistance can obtain better antenna gain. This simple design has the benefit of broadening the bandwidth where the antenna gain is not major concern.

REFERENCES

1. Wong, K.L. and Lin, Y.F.: 'Small broadband rectangular microstrip antenna with chip-resistor loading,' Electron. Lett., 33 (1997), 1593–1594.
2. Wong, K.L., Compact and Broadband Microstrip Antennas. New York: Wiley, 2002.
3. S.V. Hum, J.Z. Chu, R.H. Johnston, and M. Okoniewski, 'Efficiency of a resistively loaded microstrip patch antenna' IEEE Antennas and Wireless Propagation Letters, 2 (2003), 22-25.
4. C.Y. Huang, 'Microstrip antenna with lossy patch,' Microwave Optical Technol. Lett., 18 (1998), 228-230.

Tables

Table 1: Comparison between the proposed chip-resistor loaded microstrip antenna against various loaded-resistance at fixed slit length ℓ = 5 mm, w = 1 mm, h = 1.6 mm, ε_r = 4.4, A = 30 mm, ground-plane size = 75 mm × 75 mm.

R (Ω)	dp (mm)	Bandwidth range ($\lvert S_{11} \rvert$ < 10 dB)	Bandwidth (MHz, %)	fc = $\frac{f_L + f_H}{2}$ (MHz)
1	6	2311 ~ 2364	53, 2.27	2337.5
20	8.5	2297 ~ 2383	86, 3.68	2340.0
47	8.5	2277 ~ 2371	94, 4.04	2324.0
68	8.5	2268 ~ 2358	90, 3.89	2313.0
82	8.5	2264 ~ 2351	87, 3.77	2307.5
110	7.0	2263 ~ 2336	73, 3.17	2299.5
220	7.0	2262 ~ 2328	66, 2.88	2295.0

Table 2: Comparison between the proposed chip-resistor loaded microstrip antenna against various slit length at fixed loaded-resistance R = 47 Ω, w = 1 mm, h = 1.6 mm, ε_r = 4.4, A = 30 mm, ground-plane size = 75 mm × 75 mm.

slit length (mm)	*dp* (mm)	Bandwidth range ($\lvert S_{11} \rvert$ < 10 dB)	Bandwidth (MHz, %)	fc = $\frac{f_L + f_H}{2}$ (MHz)
1	5.5	2328 ~ 2378	50, 2.12	2353.0
3	6.5	2298 ~ 2363	65, 2.79	2330.5
5	8.5	2277 ~ 2371	94, 4.04	2324.0
7	12.0	2205 ~ 2344	139, 6.11	2274.5
9	14.0	2148 ~ 2321	173, 7.74	2234.5

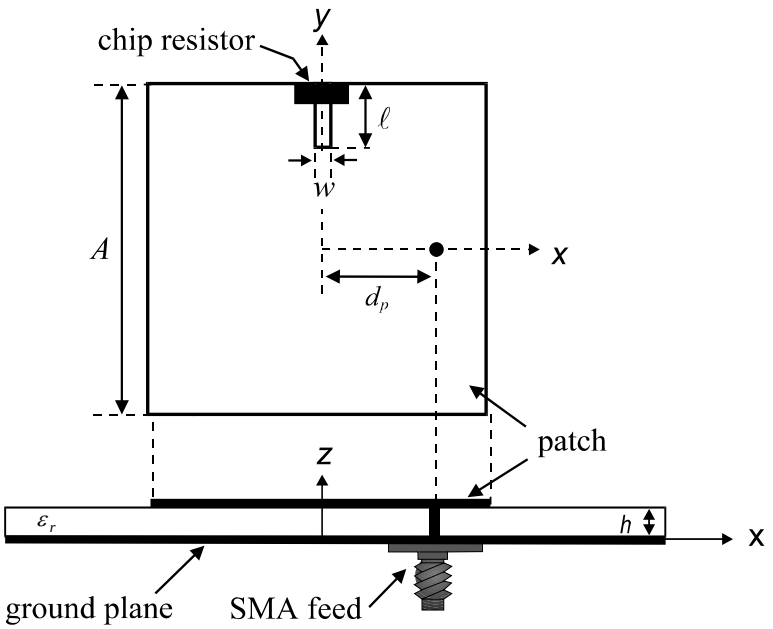

Figure 1. Geometry of a chip-resistor loaded microstrip antenna.

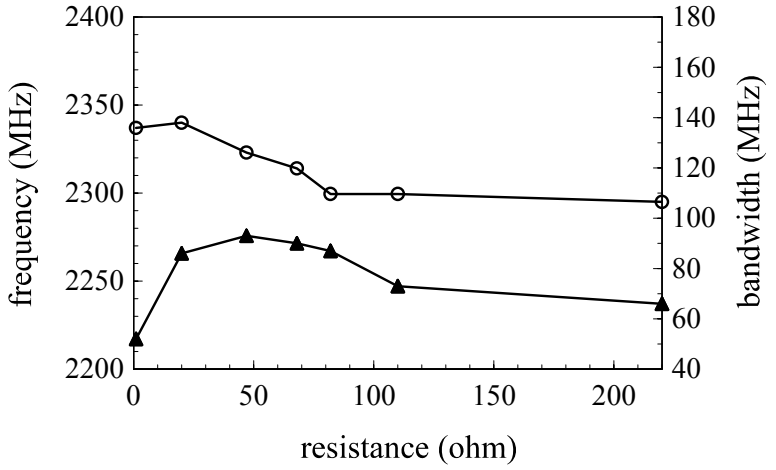

Figure 2. Measured center frequency and bandwidth against different loaded- resistance at fixed slit length ℓ = 5 mm, w = 1 mm, h = 1.6 mm, ε_r = 4.4, A = 30 mm, ground-plane size = 75 mm × 75 mm. frequency bandwidth

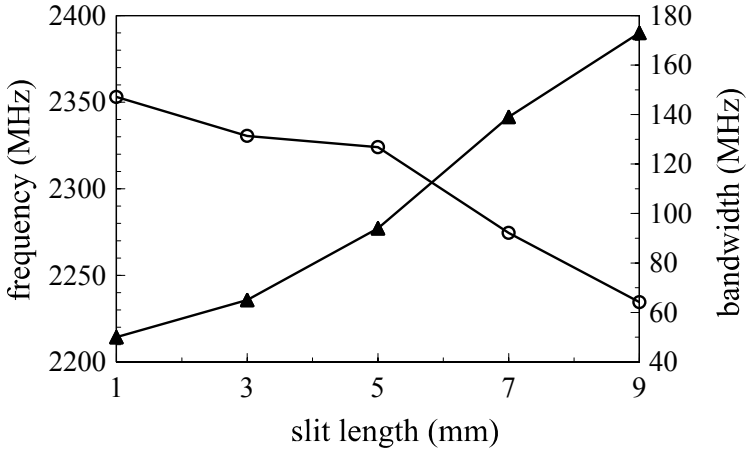

Figure 3. Measured center frequency and bandwidth against different slit length at fixed loaded-resistance R = 47 Ω; other antenna parameters are given in Fig. 2.

frequency bandwidth

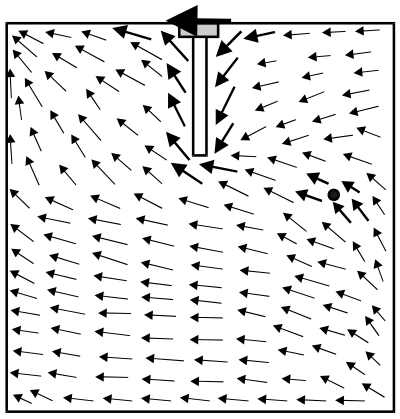

Figure 4. Simulated surface current distribution for the antenna ℓ = 9 mm, R = 47 Ω; other antenna parameters are given in Fig. 2.

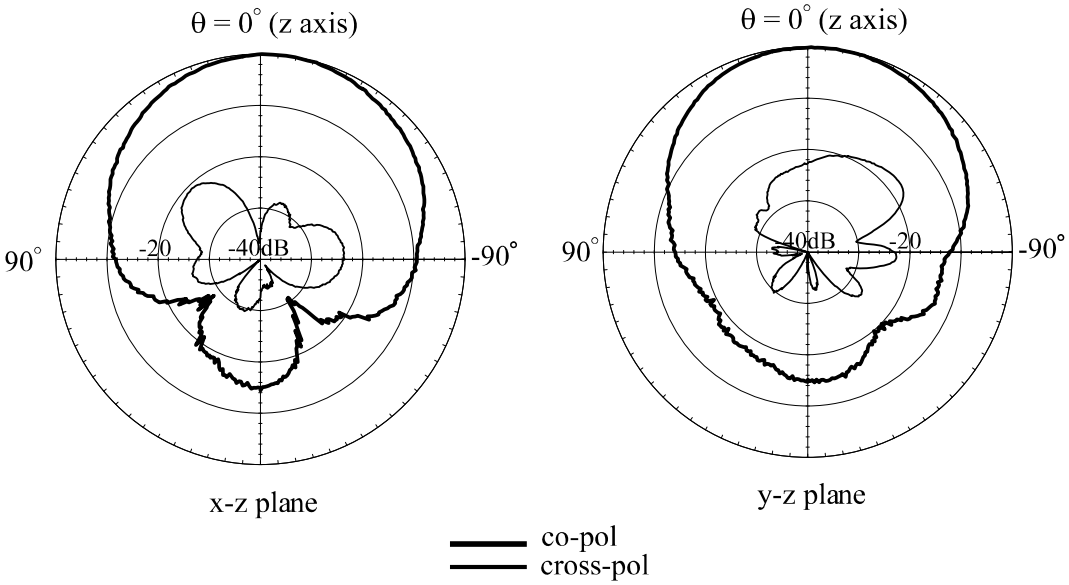

Figure5. Measured radiation patterns for the proposed design in two orthogonal *x*-*z*, *y*-*z* planes, f_c = 2234.5 MHz for the proposed design ℓ = 9 mm, R = 47 Ω; other antenna parameters are given in Fig. 2.

Design and Fabrication of a Novel V-band Tapered Slot Antenna

Chao-Tang Chuang and Nan-Wei Chen*
Department of Electrical Engineering, National Central University, Taiwan
No. 300, Jhongda Rd., Jhongli, Taoyuan 32001, Taiwan
TEL: +886-3-4227151 ext. 34520, FAX: +886-3-4258530
nwchen@ee.ncu.edu.tw

Abstract—A V-band (50-75 GHz) coplanar-waveguide (CPW) fed linear tapered slot antenna (LTSA) is demonstrated. The LTSA is fabricated on a rectangular-grooved silicon substrate to ensure good radiation characteristics. Compared to its ungrooved version, the V-band CPW-fed LTSA shows significantly improved endfire radiation patterns in the whole band. Also, moderately high gain (7.6-9.8 dBi), high front-to-back ratio (14.7 - 18.2 dB and 14.8 - 23.5 dB for E- and H-planes, respectively), and low side-lobe level (-16 - -18 dB and -12 - -18 dB for E- and H-planes, respectively) are achieved. The proposed CPW-fed LTSA is expected to find applications, such as the transceiver antenna in millimeter-wave wireless communication systems, owing to its easy integration with the uniplanar monolithic millimeter-wave integrated circuits.

I. Introduction

Enfire tapered slot antennas (TSAs) [1-2] have found wide applications from communication systems, automotive radars to imaging arrays for remote sensing due to their planar design, high bandwidth, symmetrical radiation pattern, and low side-lobe level (SLL). It appears that the low manufacturing cost, low sensitiveness to manufacturing error at millimeter (mm)-wave frequency, and high compatibility with integrated circuits make the TSAs well-suited for mm-wave applications, particularly for mm-wave communication systems. However, the radiation patterns of the TSAs are sensitive to the thickness as well as the dielectric constant of the supporting substrate. Specifically, the constraint for ensuring good radiation patterns of the TSA is $0.005\lambda_0 \le t_{eff} \le 0.03\lambda_0$, where t_{eff} represents the effective thickness and λ_0 is free space wavelength at the radiating frequency. Indeed, the upper bound of the constraint renders the substrate thickness impractical for mm-wave applications, especially for the high permittivity substrate like silicon, GaAs, or InP, since the TSA of such a thin thickness is fragile.

Here, the LTSA that can be fabricated on a traditional silicon wafer without pattern deterioration is proposed and developed. The developed LTSA is free of pattern deterioration. Furthermore, the moderately high gain, high front-to-back (F/B) ratio, and low SLL are achieved in the whole band. Below, the design, fabrication, and measurement of the CPW-fed LTSA are described.

II. Design

The top view, side view, and bottom view of the proposed CPW-fed LTSA are depicted in Fig.1 (a), (b), and (c), respectively. In Fig. 1(a), the LTSA is of dimension $L_a = 10.7$ mm and $W_a = 4$ mm. That is, the electrical length L_a and width W_a of the proposed TSA are 2.9 λ_0 and 1 λ_0 at the center frequency (62.5 GHz) of the band, respectively. The CPW-fed LTSA is realized via the slot-to-CPW transition structure detailed in Fig.1(a). The dimensions of the slot-to-CPW transition are $g = 0.041$ mm, $W_f = 0.117$ mm, $R = 0.251$ mm, $S_s = 0.065$ mm, $S_c = 0.065$ mm, and $W_c = 0.016$ mm. For impedance matching, a short slot-line stub is inserted between the transition and LTSA. The short stub is of dimension $L_s = 1.17$ mm and $W_s = 0.048$ mm. On the other hand, the two side edges of the CPW-fed LTSA are corrugated with rectangular gratings, which are of dimensions $L_c = 0.96$ mm, $L_w = 0.24$, and $L_p = 0.48$ mm, for improving the radiation patterns under a relatively narrow width design [3, 4]. The CPW-fed LTSA is supported by a silicon substrate ($\varepsilon_r = 11.9$) of thickness 100 μm. As shown in Fig. 1(b), the substrate is rectangular-grooved to form a bridge-like profile. The depth H_g and width W_g of the rectangular groove are 0.05 mm and 4.8 mm, respectively. This design is shown to drastically improve the radiation patterns of the LTSA when compared to its ungrooved version. Furthermore, two groups of periodic metal strip structures are imprinted on the bottom surface of the rectangular groove, as shown in Fig. 1(c). As proposed in [5], this design has shown for suppressing the substrate modes. The metal strip is of length 11.328 mm and width 0.1296 mm. The period of each periodic structure is 0.26 mm, and the spacing between the two groups, denoted as S_p in Fig. 1(c), is 1.32 mm. As a result, the whole CPW-fed LTSA is of length (L) 13.92 mm and width 6.72 mm. The CPW-fed LTSA is characterized using the commercial full-wave simulator HFSS. The simulated parameters of the CPW-fed LTSA are listed in Table I. The E- and H-plane radiation patterns at 52.5 GHz, 62.5 GHz, and 72.5 GHz are shown in Fig. 2 (a), (b), and (c), respectively.

III. Fabrication and Measurement

The main processes associated with the LTSA fabrication are described as follows. (i) Deposit Si_3N_4 membranes on both sides of a 300μm-thick silicon wafer via the PECVD. (ii) Etch the membrane on the region which is designed as a rectangular groove via HDP. (iii) Etch the exposed region using KOH to form a rectangular groove of depth 50μm. (iv) Evaporate gold onto the bottom surface of the rectangular groove via the E-Gun Evaporator to form periodically arranged metallic strips (v) Grind the ungrooved surface of the 300μm-thick wafer to 100μm and then polish the ground surface. (vi) Evaporate gold on the polished surface via the E-Gun Evaporator to form the CPW-fed LTSA. The photographs shown in Fig. 3(a) and (b) are for the top view and bottom view of the fabricated LTSA, respectively. The measured S_{11} of the LTSA is compared against the simulated one. As shown in Fig.4, the measurement and simulation results are in good agreement at frequencies between 50 GHz and 57GHz. The discrepancy at frequencies larger than 57 GHz is likely owing to the effect of the measurement probe. The results for including the probe modeling in the simulation will be presented at the conference.

V. Conclusion

In conclusion, the V-band LTSA that can be fabricated on a conventional silicon wafer without pattern deterioration is proposed and developed. The well-behaved and symmetric E- and H-plane radiation patterns are observed in the whole band. Additionally, the developed LTSA features moderately high gain, high F/B ratio, and low SLL. The proposed LTSA is expected to find applications, such as the transceiver antenna in mm-wave wireless communication systems, due to its easy integration with the uniplanar monolithic mm-wave integrated circuits.

Reference

[1] K. S. Yngvesson, D. H. Schaubert, T. L. Korzeniowski, E. L. Kolberg, T. Thungren, and J. F. Johansson, "Endfire Tapered Slot Antennas on Dielectric Substrate," *IEEE Trans. Antennas Prograt.*, Vol. AP-33, pp. 1392-1400, 1985.

[2] R. Janaswamy, and D. H. Schaubert, "Analysis of the Tapered Slot Antennas," *IEEE Trans. Antennas Propagat.*, Vol. AP-35, pp. 1058-1065, 1987.

[3] S. Sugawara, Y. Maita, K. Adachi, K. Mizuno, "A mm-wave tapered slot antenna with improved radiation pattern," *IEEE MTT-S IMS Dig.*, Vol. 2, pp. 959-962, 1997.

[4] S. Sugawara, Y. Maita, K. Adachi, K. Mizuno, "Characteristics of a mm-wave tapered slot antenna with corrugated edges," *IEEE MTT-S IMS Dig.*, Vol. 2, pp. 533-536, June 1998.

[5] T. G. Lim, H. N. Ang, I. D. Robertson and B. L. Weiss, "Tapered slot antenna using photonic bandgap structure to reduce substrate effects," *Electronics Letters.*, Vol. 41, pp. 393-394, March 2005.

Table I. Antenna parameters at different frequencies

Frequency[GHz]		52.5	62.5	72.5
F/B ratio[dB]	**E-plane**	15	19	20
	H-plane	18	22	22
SLL[dB]	**E-plane**	-16	-19	-18
	H-plane	-12	-18	-13
Gain[dBi]		10	11	11
Directivity[dB]		12	12	12

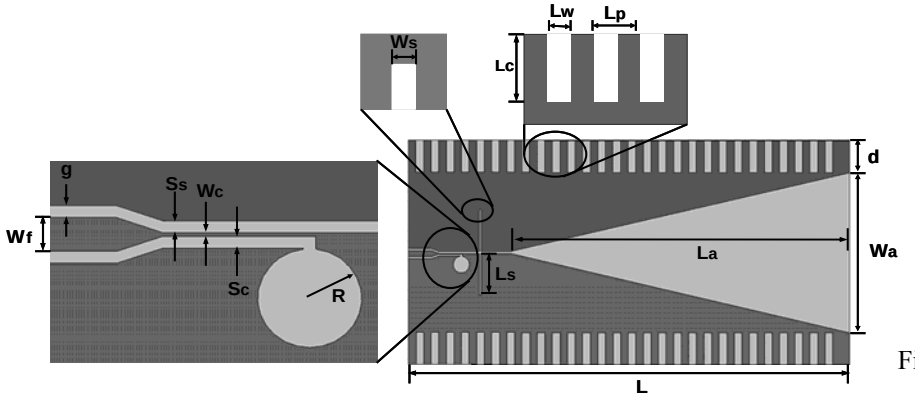

Fig. 1(a)

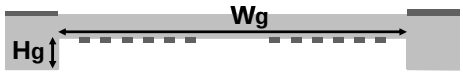

Fig. 1(b)

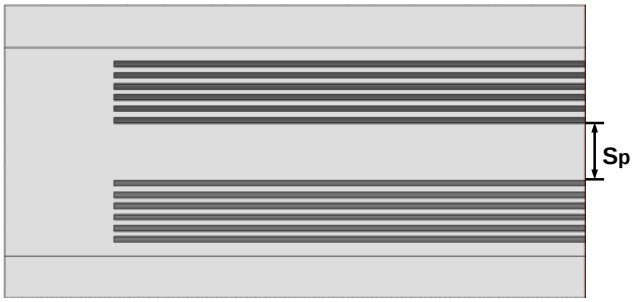

Fig. 1(c)

Fig. 1 (a) Top view of the LTSA (b) Side view of the LTSA (c) Bottom view of the LTSA.

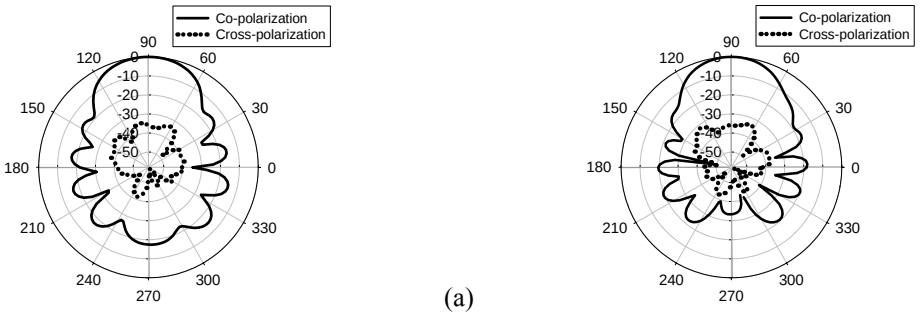

(a)

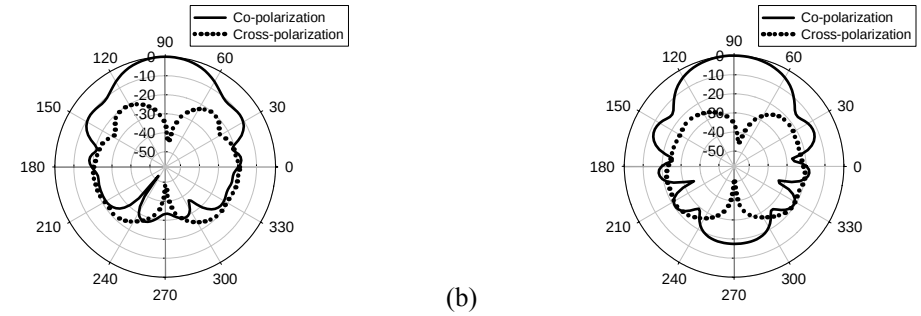

(b)

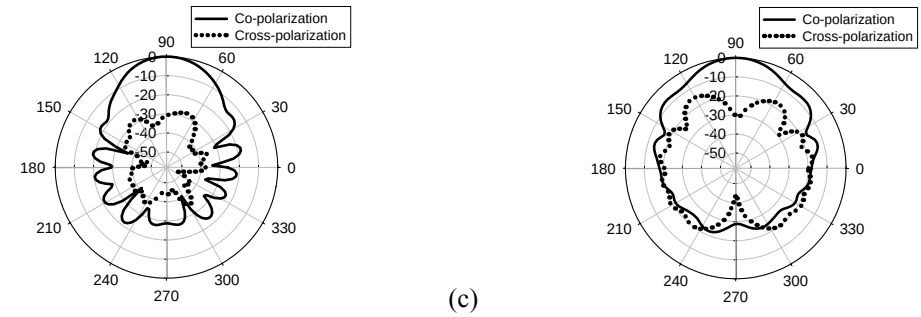

(c)

Fig. 2 E- and H-plane radiation patterns at (a) 52.5 GHz (b) 62.5 GHz, and (c) 72.5GHz.

(a) (b)

Fig. 3 (a) Top view of the fabricated LTSA. (b) Bottom view of the fabricated LTSA.

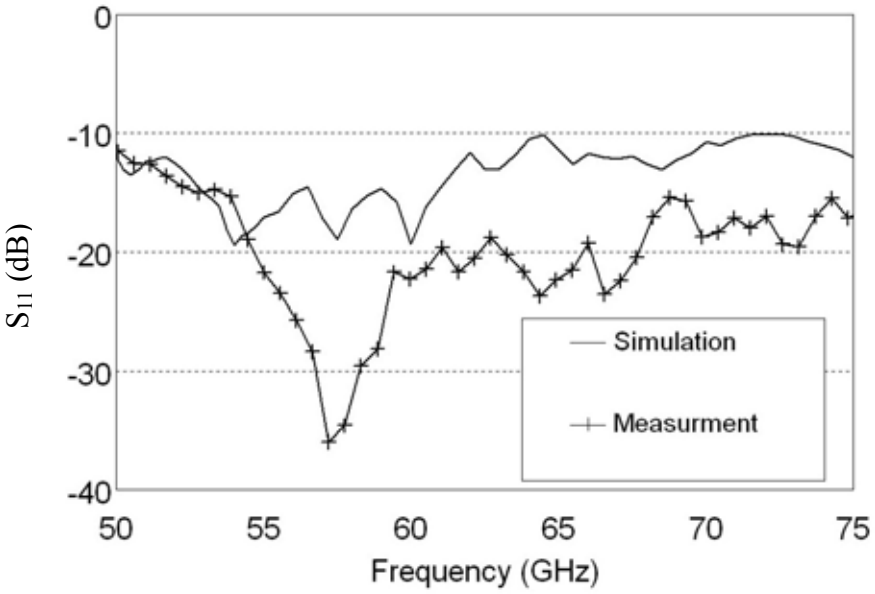

Fig. 4 The measured and simulated S_{11} of the LTSA.

Investigation of CPW-fed Triangular-ring Slot Antennas and Triangular-ring Slot Coupled Patch Antennas

Jin-Sen Chen and Wen-Fan Chang*

Department of Electronic Engineering, Cheng shiu University, Taiwan, R.O.C.

*Graduate student of the Department of Electronic Engineering, Cheng shiu University, Taiwan, R.O.C.

Abstract: Designs of coplanar waveguide (CPW)-fed equilateral triangular-ring slot antennas with tuning-stub and triangular-ring slot coupled patch antennas are proposed and experimentally investigated. The impedance matching of the resonant frequency can be obtained only by adjusting the tuning-stub length for the proposed triangular-ring slot antenna with tuning-stub. For the design of ring-slot coupled patch antenna, slightly changing the patch size causes the tunable frequency-ratio f_2/f_1 between the first two operating frequencies to fall in the range of about 1.1-1.42. Details of the proposed designs are investigated by experimental as well as theoretical studies.

1. Introduction

Ring slot antennas have been analyzed and designed for wireless communication systems. It is found that the perimeter of the slot ring is equivalent to about one and a half guided wavelengths of the first operating frequency of the conventional CPW-fed ring slot antennas [1], and about one guided wavelength for microstrip feedline at proper tuning-stub length [2]. In addition, the length of a conventional dipole slot antenna is about a half guided wavelength with a capacitive type feed, and about one guided wavelength for inductive type feed. In this study, a tuning-stub will be introduced to a conventional CPW-fed triangular-ring slot antenna for lowering the first operating frequency. The proposed and conventional slot-ring antennas are constructed by adding the same slot at two ends of the modified dipole slot antenna with capacitive and inductive type feed, respectively. Thus, it is expected that the resonant frequency of the proposed slot-ring antenna is lower than that of the conventional slot-ring antenna. A conventional CPW-fed triangular-ring slot antenna will be fabricated for comparison.

In [3], a slot-loop coupled rectangular patch antenna is designed for use in the 2.4GHz ISM band. The patch size is slightly smaller than the slot-loop size in the design. The design of annular-ring slot antenna [4] for obtaining dual-frequency operation is achieved by introducing a circular back-patch to perturb the slot's electric-field distribution. For the two cases in [3, 4], the two operating frequencies should be excited by slot-ring and patch. Also note that a part of the power provided by the slot-ring is radiated directly, and the other part of the power is exciting the patch [5]. In this article, a triangular back-patch is introduced to a conventional CPW-fed triangular-ring slot antenna. To obtain bi-directional radiation pattern, the triangular back-patch size in this study is made comparable to that of the triangular-ring slot. Owing to the back-patch disturbing the slot's electric-field distribution and the ring slot coupling the back-patch, dual-frequency operation is observed.

2. Triangular-Ring Slot Antenna with Tuning-Stub

Figure 1(a) shows a CPW-fed equilateral triangular-ring slot antenna with tuning-stub. The triangular-ring slot, having mean perimeter $3\times L$ and slot width S, is printed on FR4 microwave substrate of thickness 1.6mm and permittivity 4.4. The CPW feedline is designed to have 50-Ω characteristic impedance on the substrate in order to match the measurement system. The CPW's signal strip has a width of W_c, and the gap spacing between the signal strip and the coplanar ground plane is S_c. The CPW feedline has a tuning stub of length t, and is a distance g away from the conducting strip in the center of the triangular-ring slot. From IE3D^{TM} simulated results, the resonant frequency remains

almost unchanged when the distance *g* is in the range of 0.1mm to 1.0mm. For convenient fabrication, the distance g and the gap spacing S_c of the feedline have the same size (0.3mm) in this study.

2-1 Experimental Results and Discussion

For conventional ring slot antenna, adjusting the width of *S* can excite the first operating frequency of this antenna with good impedance matching. The experimental return loss for *S*=3mm, denoted as Reference antenna, is shown in Figure 2 and the calculated return loss has also been demonstrated for comparison.

Figure 1(a) shows the geometry of the CPW-fed triangular-ring slot antenna with tuning-stub. It is noted that good impedance matching of the proposed antenna can be achieved only by adjusting the tuning-stub length *t*. Three different slot widths, 1, 2 and 3mm, were fabricated and studied. Measured results of the return losses for these antennas are also shown in Figure 2, and the best impedance matching of antenna for *S*=1, 2, and 3mm are denoted as Antennas A, B, and C, respectively. From these results, it is found that the resonant frequencies of the proposed antenna without and with tuning-stub correspond approximately to the perimeter of the slot ring of about $1.47\lambda_g$ (Reference antenna) and $1.08\text{-}1.11\lambda_g$ (Antennas A-C). It is also noted that the wavelength in the slot, λ_g, is determined to be about 0.78 ($\sqrt{(1+\varepsilon_r)/2\varepsilon_r}$, ε_r=4.4) free-space wavelength from [6] by considering the presence of different dielectric substrate on the two sides of the slot. In addition, the effects of other substrates have also been investigated by simulation, which shows that the frequency ratio of Reference antenna and Antenna C is in the range of 1.44-1.53 (1.47 in this study) at various substrate of ε_r=3~10. Furthermore, the maximum gain within operating band is about the same, about 3dBi, for various slot widths of the proposed slot-ring antenna with tuning-stub. From the experimental studies, the ground plane size changes from 70mm×80mm to 100mm×100mm for Antenna C. The gain level increases from 3dBi to 5dBi, and the resonant frequency increases about 5%.

The excited slot electric-field distribution for the proposed antenna has been studied using IE3D^{TM} simulation software. It is shown that the electric-field distribution on the slot ring for the simulated resonant frequency is about 1.5 guided wavelengths (three maximum electric-field points at midpoint of each side) for Reference antenna and about one guided wavelength (two electric-field zero points at about midpoint of two bevel sides) for Antennas A-C. These results confirm that the first resonant frequency of the proposed antenna is lower than that of Reference antenna. The electric-field magnitude at the two bevel side slot of the proposed antenna is smaller than that of Reference, which results in less cross-polarization in the H-plane than in the Reference antenna. The radiation patterns of Antennas A-C and Reference antenna have been measured. The results reveal that these antennas have similar radiation patterns at the resonant frequency. Two measured orthogonal radiation plane cuts of Reference antenna and Antenna C are shown in Figure 3.

3. Triangular-Ring Slot Coupled Back-Patch

In a previous study, a triangular-ring slot antenna with or without tuning-stub has bi-directional radiation pattern only at its first operating frequency. In this section, we introduce a triangular back-patch to a conventional triangular-ring slot antenna; the first two resonant frequencies of the proposed antenna with bi-directional radiation patterns can be available. In this study, the size of the triangular back-patch and the triangular-ring slot is about the same. We slightly change the back-patch size of this antenna. It is shown that the different effects of this design on the first two resonant frequencies result in a tunable frequency-ratio f_2/f_1 between the two resonant frequencies.

3-1 Antenna Design

The geometry of a CPW-fed tunable frequency-ratio triangular-ring slot coupled patch antenna is shown in Figure 1(b). Many prototypes of the CPW-fed triangular-ring slot coupled patch antennas were demonstrated and studied. The mean perimeter of the slot is 3×43.5mm. To investigate the impedance characteristics with respect to back-patch size, the good impedance matching of the slot-ring coupled patch antenna with L_p=43.5mm should be designed first. By properly choosing the slot width, it is found that the best impedance matching can be obtained at S=3mm.

3-2 Experimental Results and Discussion

Figure 4 shows the measured effects on the antenna's frequency response by changing the distance d ($=d_2-d_1$ in Fig. 1(b)) and keeping triangular-ring slot circumference (3×43.5mm) and slot width (S=3mm) constant. Figure 5 shows the two measured resonant frequencies f_1 and f_2, and their frequency-ratio f_2/f_1. From these results, it is clearly seen that, with increasing distance d (slightly increasing the size of back-patch), the lower resonant frequency f_1 is significantly decreased. However, the higher resonant frequency f_2 is slightly varied, which provides a tunable frequency-ratio ranging from 1.1 to 1.42. Furthermore, when the distance, d, is greater than 2.5mm or less than -1.5mm in this design, the feed mechanism for exciting the two resonant frequencies with good matching conditions becomes difficult. This suggests that there exists a limit for the present dual-frequency design.

Some typical radiation characteristics of dual-frequency operation antennas have been studied. The radiation patterns of Antenna 3 with typical dual-frequency operation are shown in Figure 6. The measured maximum gains of Antennas 3 are 4.1dBi for the lower operating band and 4.9dBi for the higher operating band. The other antennas have also been measured and their radiation patterns are about the same as that of Antenna 3 except that the radiation pattern of Antenna 7 has relatively larger F/B ratio (~10dB) at the higher band.

4. Conclusions

Two designs of CPW-fed triangular-ring slot antenna with tuning-stub and back-patch have been demonstrated. The first resonant frequency of the triangular-ring slot antenna with tuning-stub occurs when the slot-ring perimeter is about one guided wavelength. This is different with conventional triangular-ring slot antenna which excites the first resonant frequency at about 1.5 guided wavelengths. To obtain bi-directional radiation patterns, the slot-ring size is made comparable to that of the back-patch in the design of slot-ring coupling back-patch. The dual-frequency operation provides a low, tunable frequency ratio of ranging about 1.1 to 1.42 by slightly adjusting the back-patch size.

4. References

1. Ming-Hau Yen, Powen Hsu, and Jean-Fu Kiang, "Analysis of a CPW-fed Slot Ring Antenna", Proc. of APMC2001 Int. Conf., pp. 1267-1270, 2001.
2. Hooman Tehrani and Kai Chang, "Multifrequency Operation of Microstrip-fed Slot-Ring Antennas on Thin Low-Dielectric Permittivity Substrates", IEEE Trans. Antennas Propagat., vol. AP-50., pp. 1299-1308, Sept. 2002.
3. S.W. Lu, T.F. Huang, and P. Hsu, "CPW-fed slot-loop coupled patch antenna on narrow substrate", Electronics Letters, vol. 35, No. 9, pp. 682-683, April, 1999.
4. Jin-Sen Chen and Horng-dean Chen, "Dual-band Characteristics of annular-ring Slot Antenna with Circular Back-patch", Electronics Letters, vol. 39, No. 6, pp. 487-488, March 20, 2003.
5. L. Giauffret, J.M. Laheurte, and A. Papiernik, "Study of Various Shapes of the Coupling Slot in CPW-Fed Microstrip Antennas", IEEE Trans. Antennas Propagat., vol. AP-45, no. 4, pp. 642-646, April 1997.
6. J.S. Rao and B.N. Das, "Impedance characteristics of transverse slots in the ground plane of a stripline", Proc. IEE 125 (1978), 29-31.

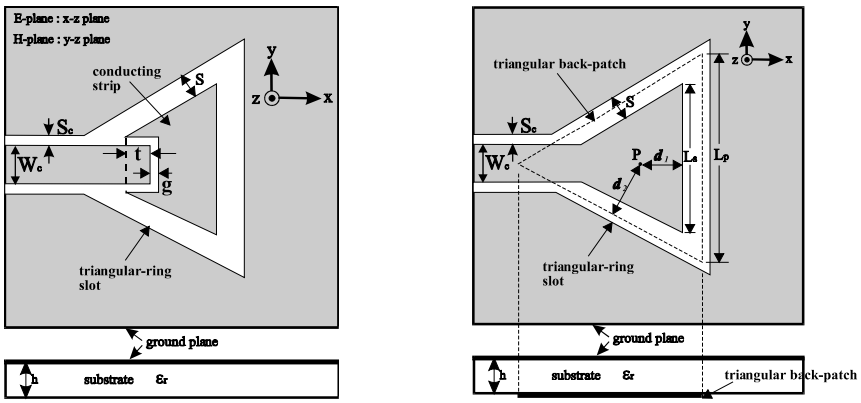

(a) **(b)**

Fig. 1 Geometry of a CPW-fed equilateral triangular-ring slot antenna: (a) with tuning-stub; (b) with back-patch.

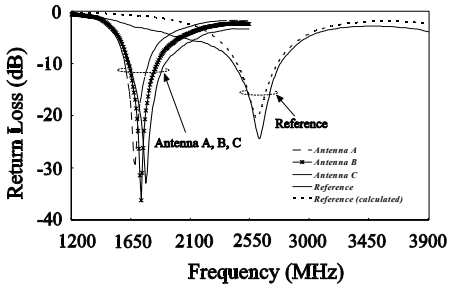

Fig. 2 Measured return loss for CPW-fed equilateral triangular-ring slot antennas with and without tuning-stub; $\varepsilon_r = 4.4$, $h = 1.6$ mm, ground-plane size($x \times y$) = 70 mm × 80 mm, mean slot perimeter = 3 × 43.5 mm, $S_c = 0.3$ mm, $W_c = 3$ mm.

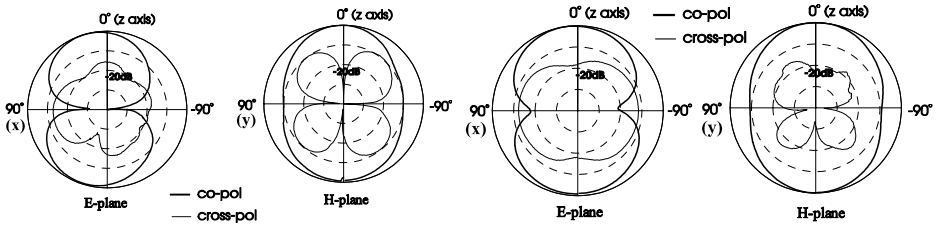

(a) **(b)**

Fig. 3 Measured E-plane (x-z plane) and H-plane (y-z plane) radiation patterns for the proposed antenna without and with tuning-stub: (a) Reference antenna; (b) Antenna C.

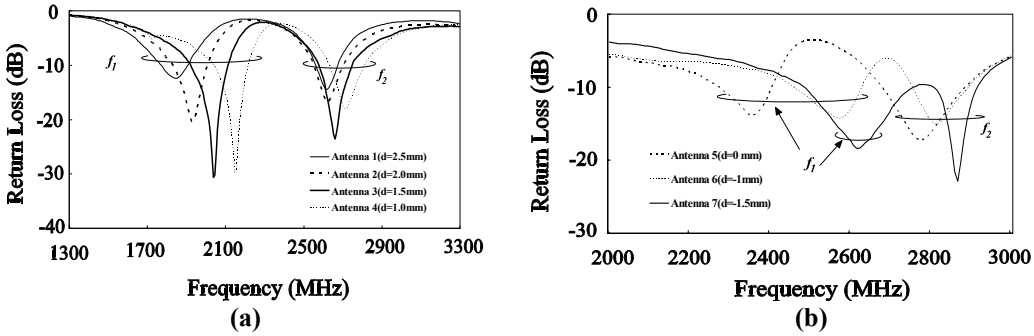

(a) **(b)**

Fig. 4 Measured return loss for the triangular-ring slot coupled patch antenna shown in Figure 5: (a) Antennas 1-4; (b) Antennas 5-7; $\varepsilon_r = 4.4$, $h = 1.6$ mm, ground-plane size($x \times y$) = 70 mm × 80 mm, mean slot perimeter = 3 × 43.5 mm, $S_c = 0.3$ mm, $W_c = 3$ mm.

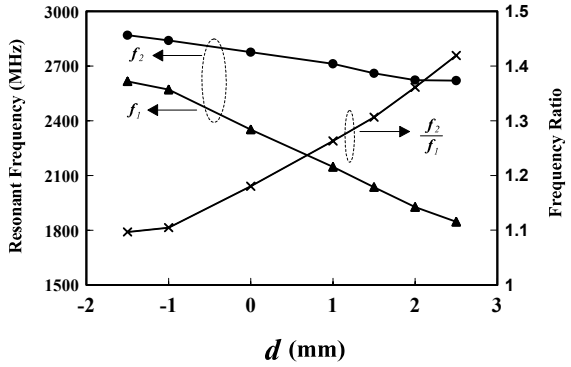

Fig. 5 Measured two resonant frequencies f_1 and f_2, and their frequency ratio f_2/f_1 for Antennas 1-7.

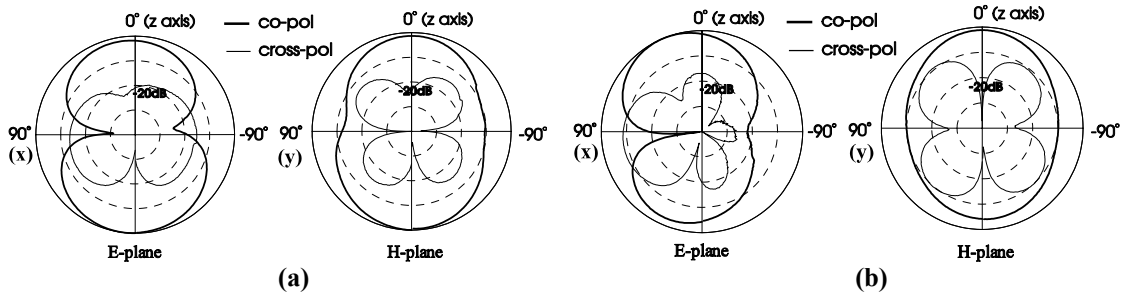

Fig. 6 Measured E-plane and H-plane radiation patterns for Antenna 3: (a) at lower resonant frequency; (b) at higher resonant frequency.

Compact Folded Monopole Antennas

Chih-Yu Huang, Hsiao-Cheng Lin and Jyun-Jie Wang

Dept. of Electronic Engineering, National Kaohsiung Normal University,

Kaohsiung 802, Taiwan

Abstract - An investigation of broadband folded monopole antennas with shorting pins is proposed. The proposed antennas are compact in size, and can provide sufficient bandwidths for DCS (1710-1880 MHz), PCS (1850-1990 MHz), 3G (1920-2170 MHz), and WLAN (2400-2484 MHz) bands. The method to realize the compact in size is introducing a folded monopole antenna. Folded monopole is difficult to be accomplished with planer substrate. Here, we introduce the shorting pin and find its optimal position to approaching as folded antenna. Details of the antenna design and experimental results are presented and discussed.

1. Introduction

Broadband planar monopole antennas with compact dimensions have potential applications for multi-band mobile phones [1-3]. By increasing the width of patch, it had larger bandwidth than before [3]. It is difficult to accomplish a folded patch with planer substrate. In this paper, we propose a design of broadband folded monopole antennas with shorting pins. The proposed folded monopole has compact dimensions of 6×40×0.8 mm^3, and shows a very wide bandwidth of 965MHz, from 1.66 to 2.62 GHz and the bandwidth covers the DCS (digital communication system, 1710-1880 MHz), PCS (personal communication system, 1850-1990 MHz), 3G (the 3rd generation wireless, 1920-2170 MHz), and WLAN (wireless local area network, 2400-2484 MHz) bands. Broadband and omnidirectional radiation patterns are given for the broadband folded monopole. Simulated surface current distribution of different positions are presented and discussed.

2. Antenna Design

Fig. 1 shows conventional broadband monopole antennas with simple rectangular patch and the proposed broadband folded monopole antennas with shorting pins. Different shorting pins A, B and C of equal spacing are located at the patch edges to connect the patches at opposite sides of the substrate to approach a folded antenna. The antennas were printed on a FR4 substrate with size $W_s \times L_s$ mm^2, thickness h = 0.8 mm and relative permittivity ε_r = 4.4. The size of the ground plane is chosen to be $W_s \times L_G$ mm^2. A gap d = 2 mm between the folded planner monopole and the ground plane. A tuning stripline section of width W_f and length L_f connects the antenna and graded to the 50-Ω stripline was found to be very effective in achieving good impedance matching.

3. Experimental Results and Disscussion

Fig. 2 shows the measured return loss for the case of simple rectangular patch with W_p = 12, 9 and 6 mm. It is clear that the bandwidth is decreased with patch width decreased. The corresponding measured data are also listed in Table 1 (denoted as Antenna 1, 2 and 3) for comparison. Fig. 3 shows the measured return loss for the

case of folded patch. Not only compact in patch width W_p = 6 mm but also compact in substrate width W_s = 10 mm. The folded patch with three shorting pins at positions A, B and C (denoted as Antenna 4) and one shorting pin at position A or B or C (denoted as Antenna 5, 6 and 7) are constructed. As the results shown, three shorting pins can be seen as a good folded monopole for it can achieve wide bandwidth that is the same with simple planar rectangular monopole antenna. With tuning stripline width W_f = 0.1 mm, we can get good return loss of bandwidth with a shorting pin (Antenna 7, BW = 45.0%) which is similar to the simple patch one (Antenna 1, BW = 46.6%), The corresponding measured data are also listed in Table 1 for comparison. It can be seen that a shoring pin at the corner position A or C has higher bandwidth than that at the middle position B. Simulated surface current using IE3D software shows that shorting at the corner make the current paths spread a wide wavelength range as in Fig. 4(a), 4(b) and 4(d) while shorting at position B has limited wavelength path range.

The radiation characteristics have also been measured. Fig. 5 shows measured radiation patterns at 1800, 1900 MHz, 2050 and 2450 MHz. The obtained patterns are in general close to the monopole-like patterns. However, in the azimuthal plane, relatively stronger radiation in left-hand half-plane (θ = 90°– 180°–270° half-plane, where the shorting pin exist) is seen. Figure 6 shows the measured antenna gain across the operating bandwidth. A peak antenna gain of about 2.76 dBi at about 2.0 GHz is seen, and the gain variations are less than about 0.5 dB for operating frequencies from about 1.7 to 2.5 GHz.

4. Conclusions

Design of compact broadband folded monopole antennas with shorting pins has been proposed. Prototypes of the proposed antennas are compact in size, and can provide sufficient bandwidth for DCS (1710-1880 MHz), PCS (1850-1990 MHz), 3G (1920-2170 MHz), and WLAN (2400-2484 MHz) bands have also been successfully implemented. The introduce of three shorting pins can be seen as good folded monopole, and a shorting pin at the corner can be seen as an effective folded monopole.

REFERENCES

1. W. Dou and W.Y.M. Chia, Small broadband stacked planar monopole, Microwave and Optical Technol. Lett., 27 (2000), 288-289.
2. M.J. Ammann and Z.N. Chen, An asymmetrical feed arrangement for improved impedance bandwidth of planar monopole antennas, Microwave and Optical Technol. Lett., 40 (2004), 156-158.
3. Y.F. Lin, H.M. Chen and K.L. Wong, Parametric study of dual-band operation in a microstrip-fed uniplanar monopole antenna, IEE Proc. - Microw. Antennas Propag., 150 (2003), 411-414.

Tables

Table 1: Performance of the proposed compact broadband folded monopole antennas with shorting pins shown in Fig. 1. L_S = 65 mm, L_P = 40 mm, L_G = 20 mm, d = 2 mm, S = 1.53 mm, ε_r = 4.4, h = 0.8 (a); simple patch with W_P = 12 mm, 9mm and 6 mm, W_S = 20 mm, W_f = 0.5 mm and (b) folded patch with W_P = 6 mm, W_S = 20 mm, W_f = 0.1 mm, shorting pin radius r_S = 0.45 mm.

	geometry	W_P (mm)	f_C (MHz)	Bandwidth $\lvert S_{11}\rvert$<10dB(MHz, %)	shorting pin position
Antenna 1	simple patch	12	2224.5	1037, 46.6%	___
Antenna 2	simple patch	9	2197	977, 44.5%	___
Antenna 3	simple patch	6	2045	682, 33.4%	___
Antenna 4	folded patch	6	2212	1031, 46.6%	A, B, C
Antenna 5	folded patch	6	2156	930, 43.1%	A
Antenna 6	folded patch	6	2294	785, 34.2%	B
Antenna 7	folded patch	6	2144	965, 45.0%	C

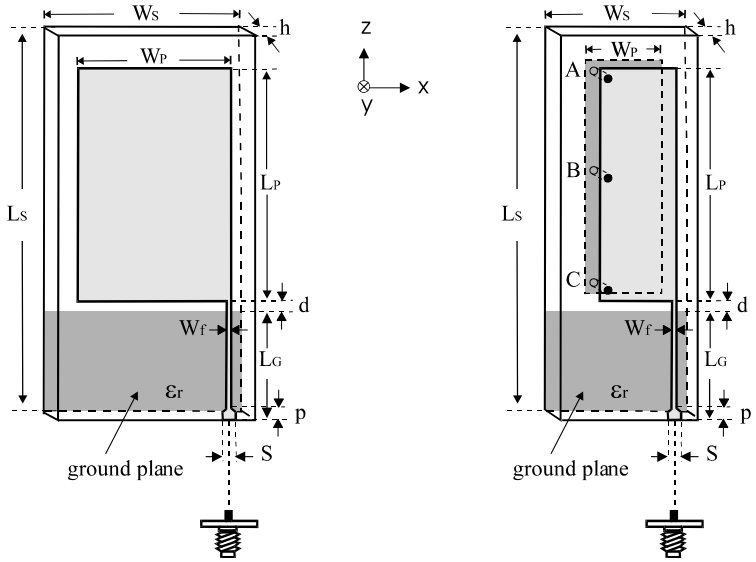

Figure 1. Geometry of the simple monopole antenna and the proposed folded monopole antenna with shorting pins.

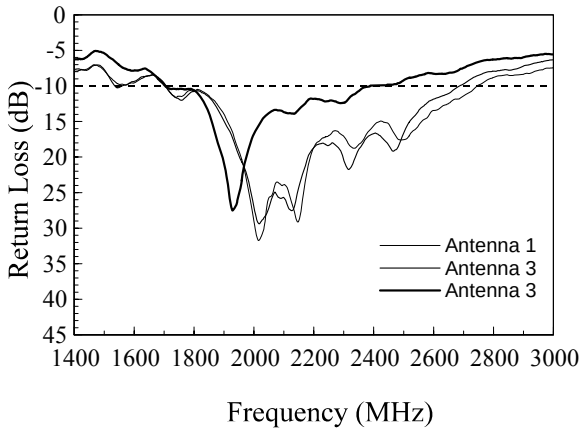

Figure 2. Measured return loss against frequency for simple patch with different patch width in the patch for W_P = 12, 9 and 6 mm (Antennas 1, 2 and 3); L_P = 40 mm, L_G = 20 mm, d = 2 mm, p = 3 mm, S = 1.53 mm, ε_r = 4.4, h = 0.8, W_S = 20 mm, W_f = 0.5 mm.

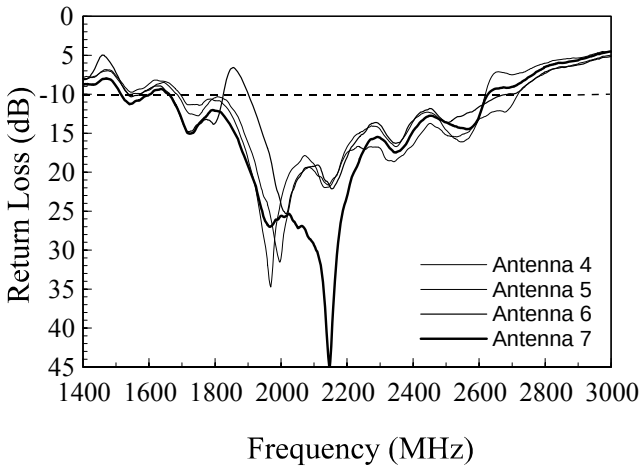

Figure 3. Measured return loss against frequency for different shorting pins position (Antenna 4, 5, 6, 7); L_P = 40 mm, L_G = 20 mm, W_P = 6 mm, d = 2 mm, p = 3 mm, S = 1.53 mm, ε_r = 4.4, h = 0.8, W_S = 10 mm, W_f = 0.1 mm, shorting pin radius r_S = 0.45 mm.

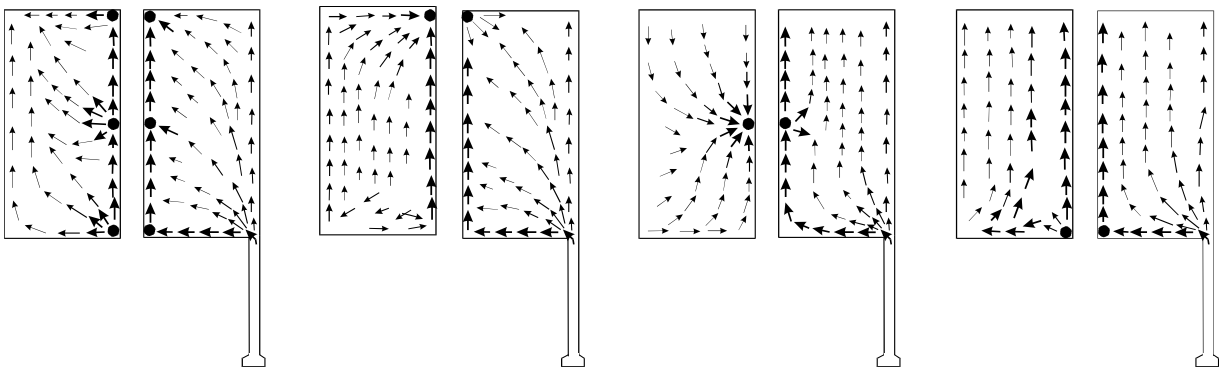

(a) (b) (c) (d)

Figure 4. Simulated surface current distribution of exploded folded-patch with different shorting position; (a) shorting at A, B, C (b) shorting at A (c) shorting at B (d) shorting at C.

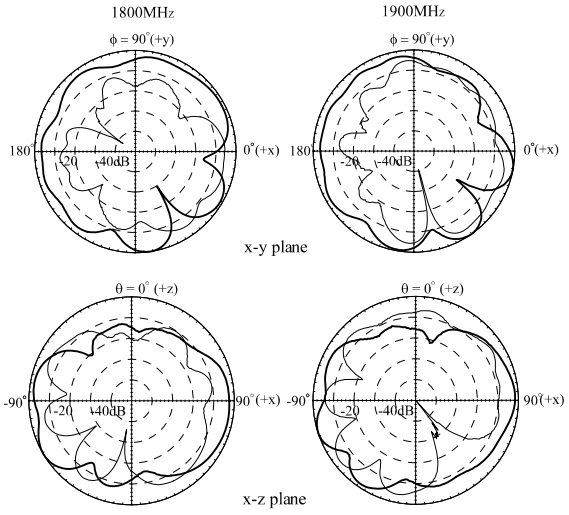

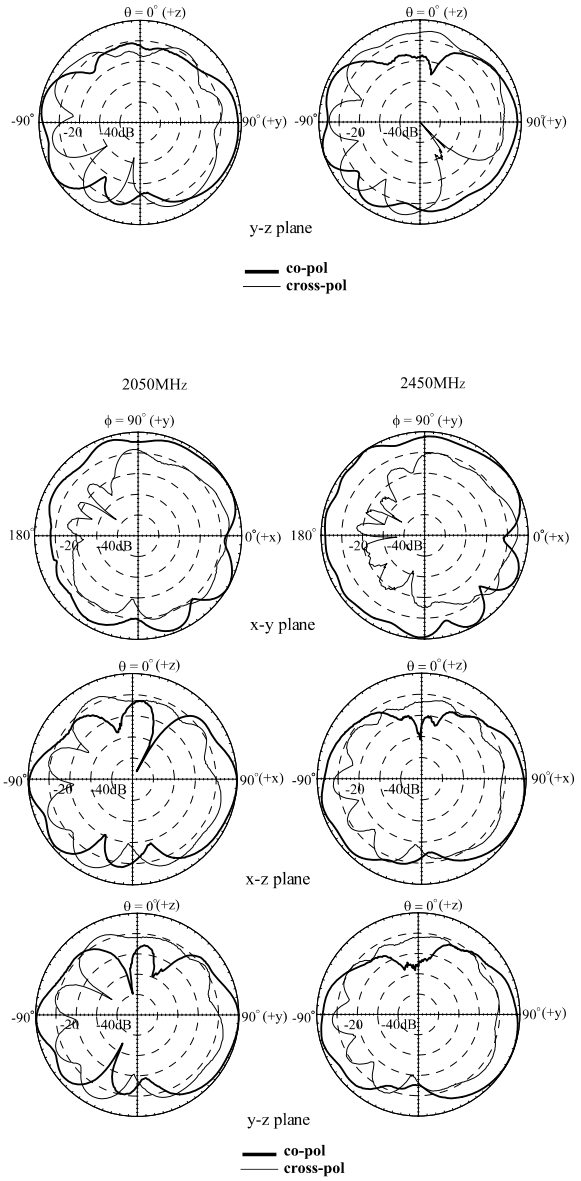

Figure 5. Measured radiation patterns for the proposed antenna at (a) 1800 and 1900 MHz (b) 2050 and 2450 MHz.

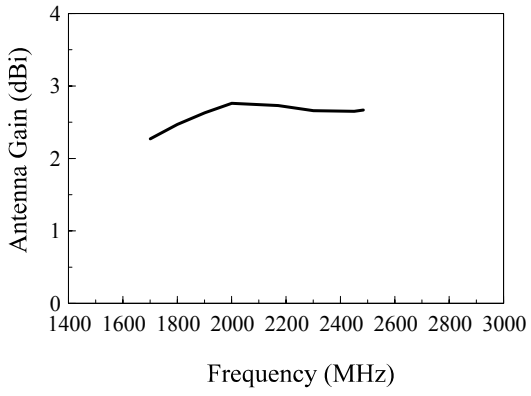

Figure6. Measured antenna gain for the proposed antenna.

A Miniaturized Microstrip Dual-Mode Filter For Spurious Suppression

Chien-Jen Wang, Shao-Yi Chen and Ze-Chang Ker*

Department of Electrical Engineering, Feng-Chia University, Taichung, Taiwan

Abstract -- A miniaturized microstrip dual-mode open-loop filter with defected ground structures has been presented in this paper. The proposed filter has the characteristics of wide stopband, size reduction, and high selectivity. The combination of dual-mode loops and defected ground structures successfully eliminates the nearest two spurious harmonics. The results show that the transmission coefficients are -30 and -25 dB at 2^{nd}- and 3^{rd}-harmonic frequencies.

Key Words: dual-mode; spurious suppression; defected ground structure (DGS)

1. Introduction

Compact and high performance bandpass filters are required in modern wireless communication systems. The conventional cross-coupled open-loop microstrip bandpass filter has two transmission zeros which result in sharp rejection on both side of the passband [1]. However, it suffers from large size and spurious response at 2^{nd}- and 3^{rd}-harmonic frequencies that could limit its application. Recently, several techniques for spurious suppression have been proposed such as lowpass filter into or out of the coupled ring [2], spur line [3] or wiggly-coupled form [4]. All above methods are exploited to eliminate only the second harmonic.

In this paper, miniaturized dual-mode bandpass filters with spurious suppression have been proposed. We fold the traditional open-loop resonator so that a size reduction of 26.3 % can be obtained. An edge-coupled feeding structure is utilized in order to reduce the second harmonic. Furthermore, the asymmetrical circuitous shaped DGS bandstop filters are designed to improve third harmonic so that the filter could have a wider rejection bandwidth. Details of the filter design are described.

2. Filter Design

The open-loop bandpass filters designed in this paper are fabricated on a substrate of FR-4 with relative dielectric constant ε_r = 4.4 and thickness of 0.8 mm. Fig. 1 depicts three configurations of the open-loop bandpass filter, including the conventional, modified and proposed filters. The total length of one loop of the conventional filter (see Fig.(a)) is close to be approximately equal to one guided wavelength at first resonant frequency. One arm of the open-loop resonator is folded to form a inner

close loop such that the filter size could be reduced. Meanwhile, the feed lines are replaced by a pair of edge-coupled transmission line as shown in Fig. 1(b). The purpose of changing feeding structure is to suppress the second harmonic due to the bandstop effect by utilizing a coupled line [5].

In order to mitigate the effect on the third harmonic, asymmetrical DGSs are etched on the ground plane as shown in Fig. 1(c). The proposed DGS with circuitous shape can provide bandstop performance for spurious suppression and wouldn't affect the structure and characteristics of open-loop resonators.

3. Simulated and Measured Results

Fig. 2 plots the performance of the conventional open-loop filter centered at 2.4 GHz. It offers two transmission zeros near the passband located at 1.86 GHz and 2.78 GHz with insertion loss of 48.9 dB and 20.6 dB, respectively. As shown in Fig. 3, the modified filter has a 10-dB bandwidth of 10.4 % operating at 2.4 GHz with low insertion loss 4.43 dB in the passband. The folded bandpass filter fed by the coupled line can achieve a size reduction of 27 % and the second harmonic is suppressed by more than 20 dB. Fig. 4 shows the frequency response of the proposed filter (see Fig. 1(c)) by incorporating DGSs. The difference between simulation and measurement may be attributed to fabrication tolerances. Comparison of transmission characteristics of the three filters is shown in Fig. 5. The band-rejection performance shows that the asymmetrical DGSs not only suppress the third harmonic by 37 dB but also reduce the second harmonic by 7 dB. The rejection of 34.5 and 31 dB at harmonic frequencies 5.36 and 8.15 GHz have been achieved.

4. Figures

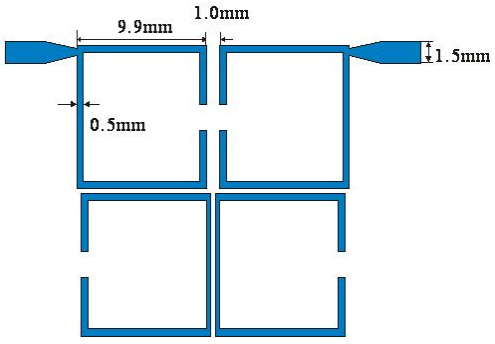

(a)

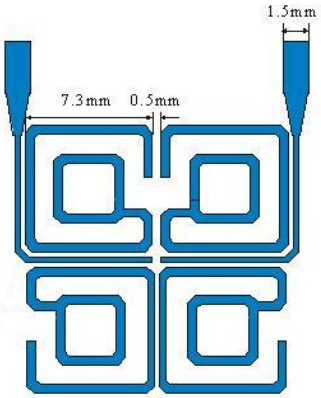

(b)

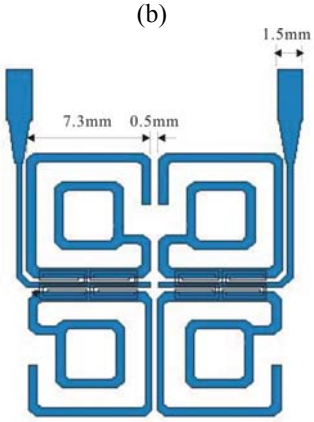

(c)

Fig. 1 Configuration of the open-loop bandpass filter (a)conventional (b)modified (c)proposed

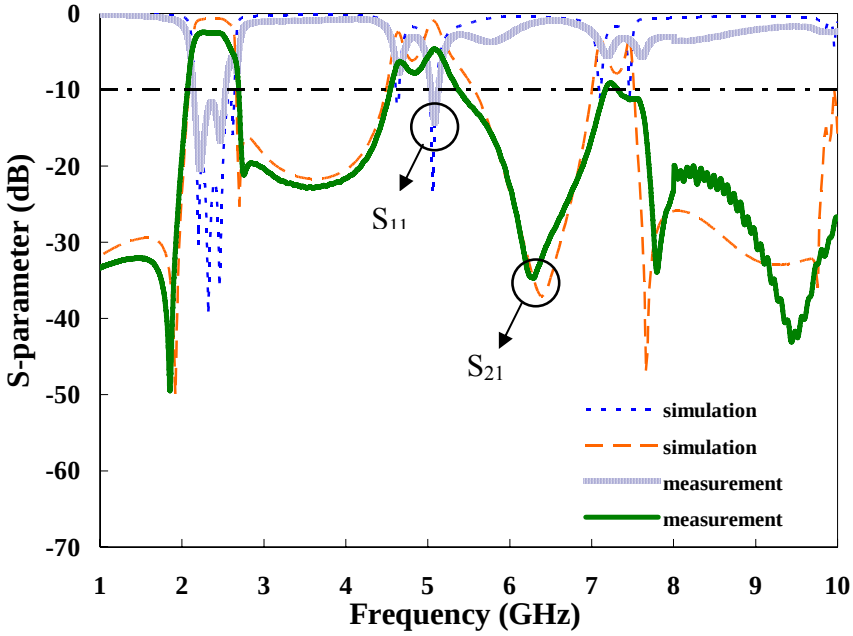

Fig. 2 Frequency response of the conventional open-loop bandpass filter

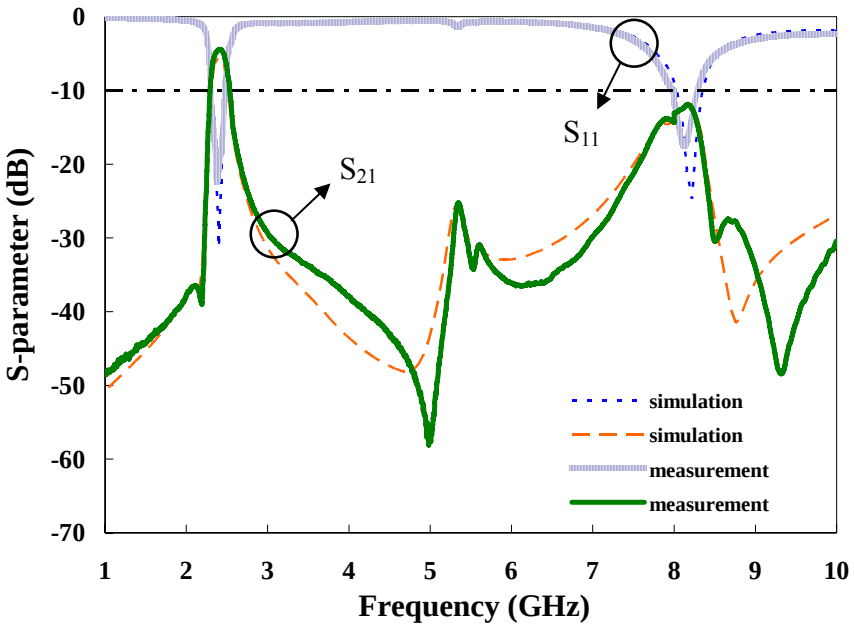

Fig. 3 Frequency response of the modified open-loop bandpass filter

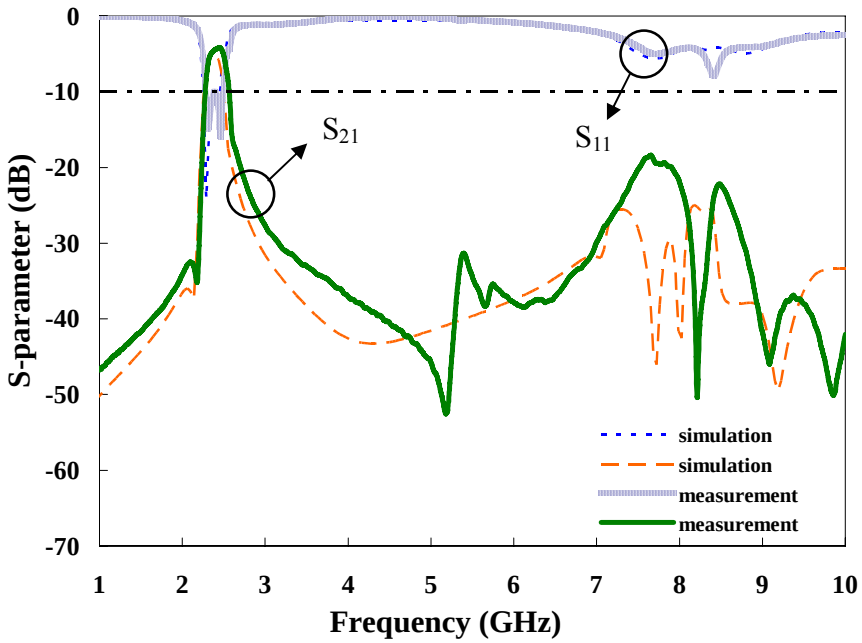

Fig. 4 Frequency response of the proposed open-loop bandpass filter

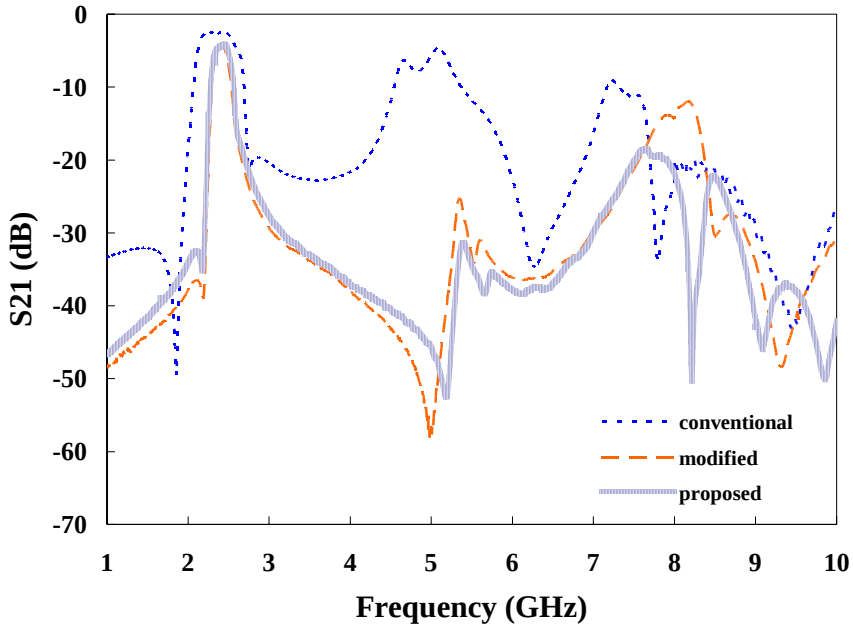

Fig. 5 Comparison of S_{21} of the three filters

5. Conclusion

A miniaturized microstrip dual-mode filter for spurious suppression has been presented. The techniques of reducing the filter size and improving the spurious response have been shown. The edge-coupled feeding structure and DGS filter are utilized to eliminate second and third harmonic suppressed. The experimental results demonstrated that spurious rejection better than 19.5 dB around the 2nd- and 3rd-harmonic frequencies. The good performance of the proposed bandpass filter with wide stopband and compact size of 15.5 mm× 16.3 mm is suitable for many wireless communication applications.

REFERENCES

1. J.-S. Hong and M. J. Lancaster, "Couplings of microstrip square open-loop resonators for cross-coupled planar microwave filters," *IEEE Trans. Microwave Theory and Tech.*, Vol. 44, No. 12, 2099-2109, 1996.
2. J. Marti and A. Griol, "Harmonic suppressed microstrip multistage coupled ring bandpass filters," *Electron. Lett.*, Vol. 34, No. 22, 2140-2142, 1998.
3. Y. Sung, C. S. Ahn, and Y.-S. Kim, "Parallel-coupled microstrip bandpass filters with a wide stopband using spur lines," *Microwave Optical Tech. Lett.*, Vol. 43, No. 1, 9-11, 2004.
4. S.-F. Chang, Y.-H. Jeng, and J.-L. Chen, "Tapped wiggly-coupled technique applied to microstrip bandpass filters for multi-octave spurious suppression," *Electron. Lett.*, Vol. 40, No. 1, 46-47, 2004.
5. M.-H. Weng, R.-Y. Yang, C.-Y. Hung, H.-W. Wu, W.-N. Chen, and M.-P. Houng, "A dual-mode bandpass filter with a wide stopband," *Microwave Optical Tech. Lett.*, Vol. 43, No, 2, 177-179, 2004.

Dual patch Butterfly Shape Stacked Structure Wide Band CP Microstrip Antenna

Huan-Cheng Lien *, Huei-Chiou Tsai
Wu Feng Institute of Technology, 117 Chian-Ku Rd., Sec.2, Ming-Hsiung (621), Chiayi, Taiwan, R.O.C.
lhcaa@mail.wfc.edu.tw

Abstract—This paper investigates the design, measurement and characteristics of a Dual Butterfly shape patch Antenna (DBA). Make use of a special impedance transformer, is less than quarter-wave length, to improve the impedance bandwidth of the antenna. Tune by a differences dielectric and spacing each other to achieve the desired of a larger impedance/ Axial Ratio (AR) bandwidth. The experimental results verify that the antenna has an impedance bandwidth (VSWR < 2) more than 30% and a 3-dB AR bandwidth of 400MHz. Simulation and measurements results on circular polarization (CP) gain and polar patterns are presented and compared.

1. Introduction

Microstrip antennas have many desirable features, such as low profile, lightweight, and are usually fabricated by a photolithographic etching process or a mechanical milling process of these kinds antenna, making the construction relatively easy and inexpensive. These features make microstrip antennas are one of the most widely used types of antennas in the microwave frequency range, and they are often useful for many applications in the satellite communication and mobile communication systems.

The majority of current Global Positioning Satellite (GPS) receivers operating typically use a CP antenna. In general, a microstrip antenna has a narrow 3-dB AR bandwidth, therefore, in the practical design of CP antennas, develop broadband techniques to enhance the bandwidths of the microstrip antennas is very important.

Various microstrip patch configurations such as annular-ring, disk, rectangular and triangular have been investigated, with rectangular and circular being the most common. However, the principal disadvantages of such antennas include the fact that it is usually narrowband, with bandwidths of a few percent being typical. The duty of designing an antenna that transmits or receives in CP over a wide range of angles is often complicated. Many bandwidth enhancement techniques have been suggested and implemented in recent years, and one of such techniques is stacking patches either horizontally or vertically [1-3].

The aim of this paper is to realize a low cost CP for GPS application using microstrip technique: The first introduction the fractal multilayer substrates structures of the microstrip antennas, which can be fabricated using known printed circuit board fabrication techniques and processes, is designed for Left-Hand Circular Polarized (LHCP) at a center frequency of 2.1GHz, when the dimension of DBA is adjusted to suitable values and the feed point is chosen correctly. Secondly describes the design and simulation results of the DBA, finally, the results of measurement will be discussed of the propose antenna.

2. Antenna Structure and Antenna Design

The proposed antenna configuration is shown in Fig. 1, First layer is ground plane, second layer is a 50 ohms rectangular feed line and the signal feed at its back with a coaxial probe, the third and the fourth layers are two radiate elements.

The present design of DBA is choice of a high permittivity substrate (FR4) with ε_r of 4.4, loss tangent 0.025 and thickness 1.6 mm was used to situate the bottom layer for the feed line and the ground. The choice of lower permittivity substrate for the driven layer would be more suitable. Hence, a lower permittivity substrate (RO) with ε_r of 3.8, loss tangent 0.0022 and thickness 0.508 mm on third and the fourth layers for the radiate elements, the radiating elements consists of dual butterfly patch with stacked vertically, while the dual butterfly patch was etched a equilateral triangle slot on inside, and separated a higher air-spacing each other by polymer ($\varepsilon_r = \varepsilon_0$) of a thickness h and placed in a centered way with stacked vertically.

In the present configuration of DBA a lossless foam material of the polymer is used to control the distance between the two patches and to provide a mechanically stable height separation. In practice, it was found that the height separation plays a significant role in achieving the optimum impedance bandwidth of the antenna.

Feeding mechanism plays an important role in the design of microstrip patch antennas. The input

impedance depends upon the feed position or the separate distance of the two radiating elements and the impedance transformer configuration. To overcome its inherent limitation of narrow impedance bandwidth due to feed networks with quarter-wave transformer or hybrid circuit, and meet the demand for miniaturization the antennas, in the present configuration of DBA, the impedance transformer is placed at the back of the butterfly shape radiate element, and consists of two elements of a rectangular microstrip feed line and a cylindrical conductor, they are connected erectly each other and the total length is less than λ /4 wavelengths as shown in Fig. 1, while the rectangular microstrip feed line was printed on the second layer substrate up side and the signal is fed at back side by a 50 ohms SMA connector.

3. Simulation and experimental results

The proposed antenna has been designed and simulated by using [4]. Fig. 2 shows the variation of simulated and measured RL with frequency, it can be seen that an optimum matching impedance bandwidth for in excess of 30% and the minimum RL reaches-30 dB at 2.1 GHz from the proposed antenna.

The measurements of the DBA were finished in anechoic chamber and the AR result obtained from simulation and experiment are shown together in Fig. 3 as a comparison. The AR value of experimental results less than 3 dB is in excess of 400MHz bandwidth was approximate simulation purpose, the measured AR patterns for CP in both principal E (x-z) and H (y-z) planes are shown in Fig. 4 a and b, the 3dB AR bandwidth is about 45 degree at the operating frequency 2.1GHz, Further, The CP gain is over 5 dBi across a frequency band between 1.6 to 2.6 GHz from simulation and measurement as shown together in Fig. 5.

4. Conclusion

The DBA has been made and measured, the structure is easily fabricated and a large antenna size can be reduced of the conventional CP antenna for operating at a fixed frequency by using the proposed Configuration. Measurement results almost correspond with simulation confirming the wide frequency behavior of the DBA. The results show that the propose antenna is not limited to the improvement on the impedance and AR bandwidths but also the radiation characteristics such as CP gain. Furthermore, due to its compactness and broad bandwidth more applications can be anticipated.

REFERENCES

1. Smith, H. K., and Mayes, P. E., “Stacking Resonators to Increase the Bandwidth of Low Profile Antennas,” IEEE Trans. Antennas and Propagation, 1987, Vol. AP-35, pp 1473-1476.
2. Al-Charchafchi, S. H., and Loukrezis, F., “Electromagnetically Coupled Stacked Patch Antenna,” Microwave J., June 1995, Vol. 38, No 6, pp 76-79.
3. Dahele, J. S., Tung, S. H., and Lee, K.F., “Normal and Inverted Configurations of The Broadband Electromagnetically Coupled Microstrip Antennas” IEEE AP-S Int. Symp. Digest, 1986, pp 841-844.
4. IE3D Software Release 8 developed by M/S Zeland Software, Inc.

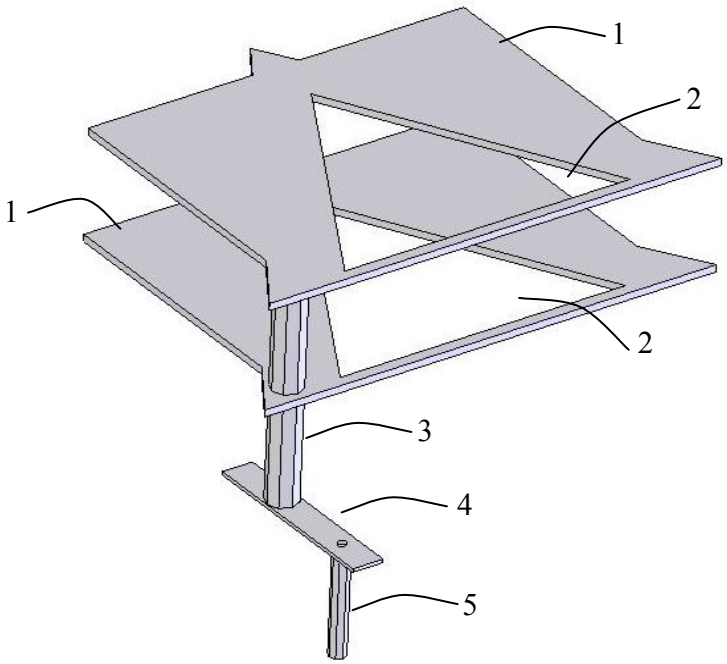

1	Butterfly Shape radiating element
2	Equilateral triangle slot
3	Cylindrical conductor
4	Rectangular feed line
5	SMA connector

Fig.1 Geometry of the proposed antenna

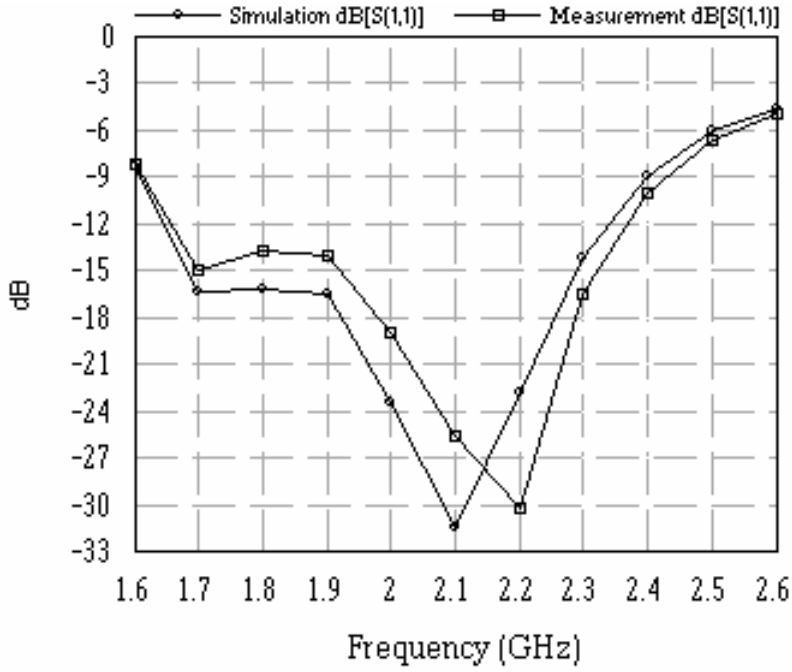

Fig. 2 The variation of simulated and measured RL with frequency.

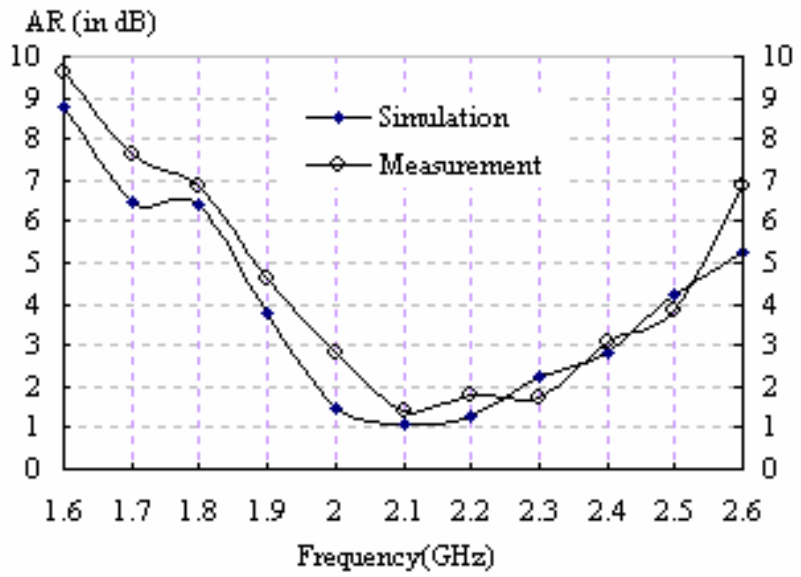

Fig. 3 The AR result obtained from simulation and experiment

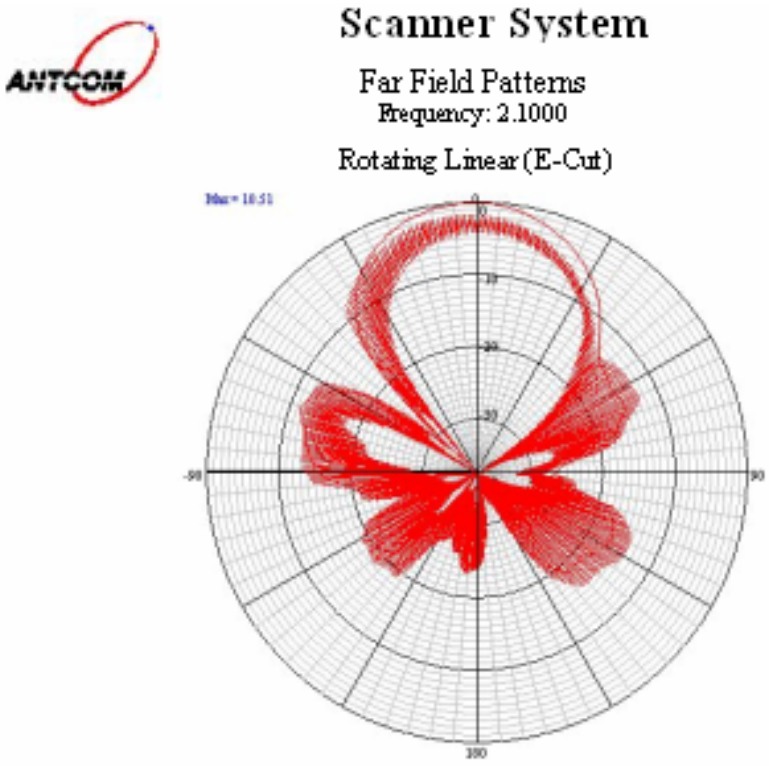

Fig. 4 a The AR results from experiment (E-Cut).

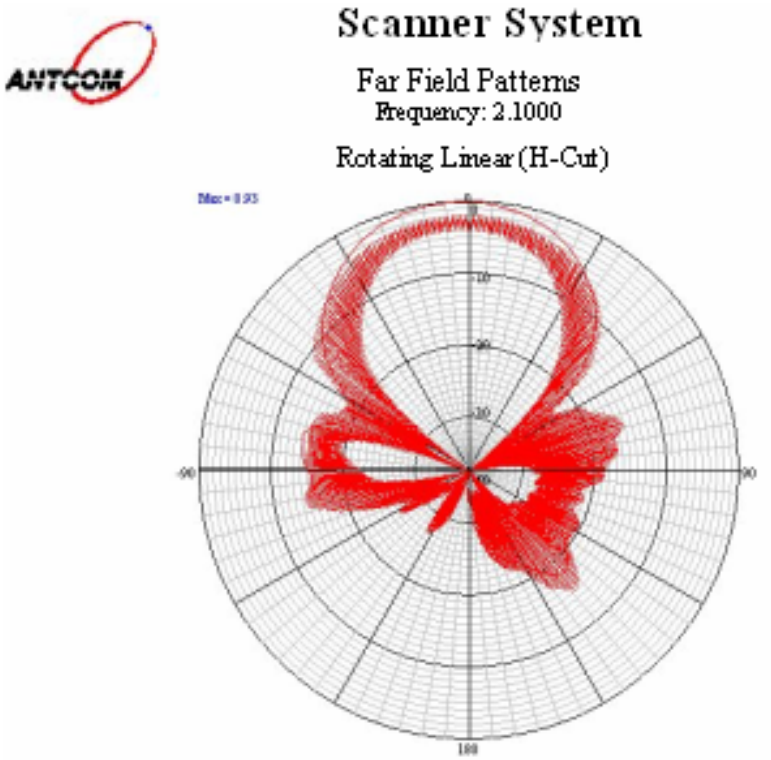

Fig. 4 b The AR results from experiment (H-Cut).

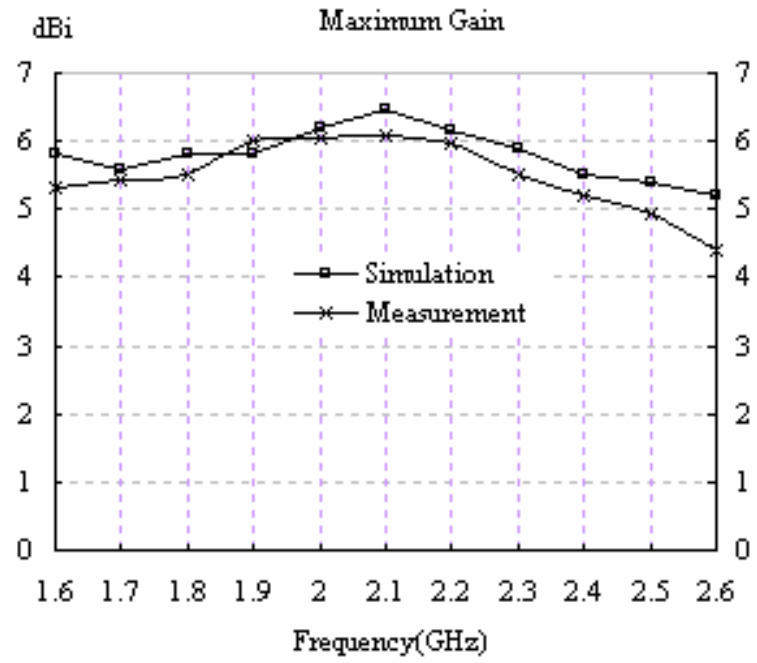

Fig. 5 The CPG result obtained from simulation and experiment.

ALGORITHMIC SYSTEM FOR IDENTIFYING BIRD RADIO-ECHO AND PLOTTING RADAR ORNITHOLOGICAL CHARTS

Leonid Dinevich, Yossi Leshem

George S. Wise Faculty of Natural Sciences, Dept. of Zoology, Tel-Aviv University, Ramat Aviv, 69978, Israel.

E-mail: dinevich@barak-online.net

Abstract

The territory of Israel is a route for major bird migration from Europe and partially from certain areas in Asia and Africa and back. During the period of intensive migration, the average density bird per a square kilometer may reach over 500 birds per a square kilometer of the air. These figures alongside with the fact the air over the country is saturated with aircraft makes it an urgent task to find solutions for prevention of disasters caused by aircraft/bird collisions. In the present paper, a new algorithm is proposed aimed at identifying bird radar echoes against the background of other reflectors.

The main idea underlying the new algorithm

In the course of the present study, additional echo characteristics have been found.

Fig. 1 (a,b) shows bird echo fields obtained by way of photographing the radar screen during horizontal scanning at a constant vertical angle, using the following two modes:

a) the camera shuttle was kept open during a single scan, duration 10 sec., vertical angle 3^0

b) the camera shuttle was kept open during 18 scans, duration 3 min., tilt angle 3^0 .

Fig. 1c) shows the same echo field after the digital data processing and data summation over 18 scans.

Comparative analysis of the three figures shows that the main common characteristic of bird echo is its specific movement, resulting in transformation of dotty radio-echo (fig. 1a) into streaks (fig. 1.b). The streaks are relatively straightforward (fig.1 b,c). The increments in the length of the streaks take place as the result of the echoes' forward movement from scan to scan. At the same time, the number of echo dots forming most streaks is smaller than the number of scans, hence the straightforwardness of streaks is disrupted by a change of direction. To sum up, bird echoes do move, and this movement has pronounced distinguishing characteristics.

We photographed the radar screen, the primary task being to find a simple way of selecting signals from birds on the photos. For this purpose, the camera shuttle was kept open during 1,5 minutes for each picture, with the help of a special valve and a timer. During this time interval, the radar beam, at the antenna scan rate of 6 revolutions per minute, performed 9 revolutions. The dotted signals from birds were converted into lines, forming a certain pattern of tracks, the length of such tracks corresponding to birds' flight velocities. The direction of bird flights was easily determined by the shift of dotted echo on the screen. Aiming the radar beam strictly to the north or to the south and registering the radio echo shifts within a preset time interval (1,5 minutes), we obtained both the velocity and the direction of bird flights. It was found that flight directions have a predominantly southern component in autumn and a northern component in spring. In rare cases, usually in those of non-migratory flights, these tracks have chaotic spatial orientation. Dotted echoes or area echoes that do not change their spatial position with time are not related to birds. Reflections from aircraft, due to their high velocities, are converted into dotted lines on the photos and could be easily identified. Fig. 1(a,b,c) shows dotted echo from birds, as well as tracks of both distinctly directed and chaotic movements of birds' echoes.

- The following data were obtained as a result of 200 experimental observations over bird echo movements both on the radar screen and the oscillograph (made both in the day light and at night). In a series of 8 scans (80 sec) at a fixed tilt angle within a 60-km radius, the radar registered moving bird echoes at a preset coordinate (a spot within

the scan area with coordinates X, Y, Z and dimensions determined by the radar resolution parameters). In 68% of cases, moving echoes were registered once, in 27% of cases twice, and in 5% of cases three times.

- A specially designed program enabled to analyze the structure of over 150 randomly selected echo streaks. All the streaks were obtained as a result of summing-up data over 8 scans. The angle was chosen with the goal of excluding the ground clutter echo as much as possible. The program enables to trace the formation of echo streaks from scan to scan. The results obtained show that in about 90% of cases, the echoes occurred twice at the same the same point during the 80-sec-long series of eight scans.

This result can be accounted for by both the character of birds' movements and the technical parameters of the radar system, with its short impulses and the narrow symmetric beam (Table.2).

Table 2. Resolutions parameters of the radar and the registration system

	Radar	Registration
Azimuth resolution	0.5^0; 1.5^0	0.176^0
Distance resolution	150 m	60 m

In contrast, the echoes from ground clutter, clouds and some atmospheric heterogeneities were usually registered as recurring at the same point and thus can be easily filtered out.

The only exception is weak signals with pronounced fluctuation reflected from porous clouds and precipitation. In case such "blinking" signals are relatively dense within a limited area (of about 2-10 km^2 in square and up to 2 km in height), they create an illusion of spatial movement. In some cases, such signals were registered as recurring at the same point twice during the eight scans, which is similar to the recurrence of bird echoes. However, subsequent echoes of these targets are not located along a direct line, but are rather scatted chaotically, thus forming chaotically directed vectors as opposed to those formed by echoes of migrating birds.

This characteristic is the basis for detecting the areas of these problematic echoes and is hereafter referred to as the-state-of-chaos coefficient..

To sum up, when we exclude all the echo that do not recur t the same point more than twice from the overall 8-scan data, we will "lose" echo of not more than 5-10% of birds. The remaining echoes are to be analyzed by the set of properties described above, first and foremost by the pattern of movement.

The principle underlying the system remains unchanged (Dinevich et al. 2004), while selection of bird echo is performed on the basis of the abovementioned properties and considerations.

The Scheme of the Algorithm

To sum up, the main stages of the algorithmic processing of radio-echo fields, described in detail in the preceding sections of the paper, are as follows:

summating the totality of radio-echo (that are above the noise level) over a prescribed number of scans

isolating each bird (bird group) echo against echoes from other reflectors on the basis of echo movement and specific parameters of this movement targetsculating flight velocity for each bird (bird group)

excluding false vectors by implementing a special analysis of vector fields on the basis of additional parameters

identifying, semi-automatically and promptly, individual target selected radio-echoes ("bird/non-bird") on the basis of the fluctuation parameter in halted antenna mode

Having completed the identification procedure, the algorithm plots ornithological and meteorological charts of various types.

Conclusions

- The study enabled to establish a set of radar characteristics and on this basis to develop an algorithm that enables to distinguish bird echo and perform on-line plotting of vector fields that represent birds' movement, including the height parameters.

- The technique of vector field plotting enables to classify birds, on the basis of their movement patterns, into four categories, among them birds flying with frequent shifts in flight direction (local birds), birds flying straightforwardly at steady velocity or at varying velocity, and those flying with repeating deviation from a straight line and variable velocity.
- Comprehensive charts plotted on the basis of the algorithm data enable to obtain diverse and relevant information on the ornithological situation within the area of 60-km radius from the radar position, including:

1. the total current quantity of birds in the air, specifically migrating birds
2. maximum and minimum flight velocity values
3. distribution of birds' mass throughout the height
4. the spectra of flight directions and velocities, including the sum direction vector
5. vector fields of bird movement juxtaposed with current meteorological status and local terrain
6. bird distribution by the flight pattern (the degree of straightforwardness and velocity steadiness)
7. data on clouds, precipitation and visually unobservable atmospheric inhomogeneities, including their evolution with time.

-Weak echoes with pronounced fluctuation, such as echoes from atomized clouds and precipitation, as well as from insects and atmospheric inhomogeneities, pose a major problem for the algorithm. However, in future the system will enable to apply additional properties, which will increase the identification reliability of echo of this type. Among the properties mentioned, there is the ratio of reflection coefficients on the two wavelengths, as well as polarization and fluctuation parameters of echoes obtained from various targets.

-The radar ornithological system described in the paper enables to perform real-time monitoring of global intercontinental migrations of large bird flocks by means of the network of radars, among them MRL-5, located in different countries and covering vast territories.

-The method of bird identification proposed in the study can be implemented in other types of high-grade potential coherent and incoherent radars whose antennas produce narrow-directivity beams.

REFERENCES

Dinevich L., Leshem Y., Pinsky M., Sterkin A., 2004. Detecting Birds and Estimating their Velocity Vectors by Means of MRL-5 Meteorological Radar. J. The RING 26, (2): 35-53.

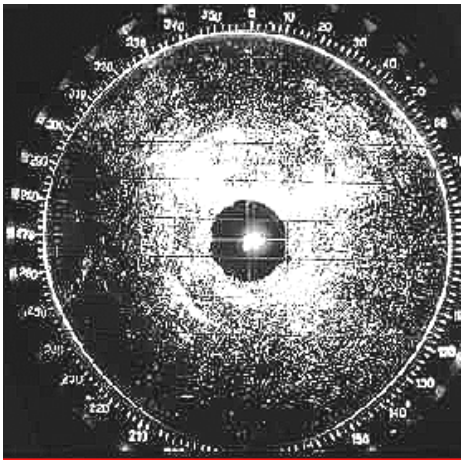

Fig.1a Photo of circular scan screen. Echoes are received within the range of the radar sensitivity. Single scan performed at nighttime. Exposure duration 10 sec. Tilt angle 3^0. Dot echoes are reflected from birds.

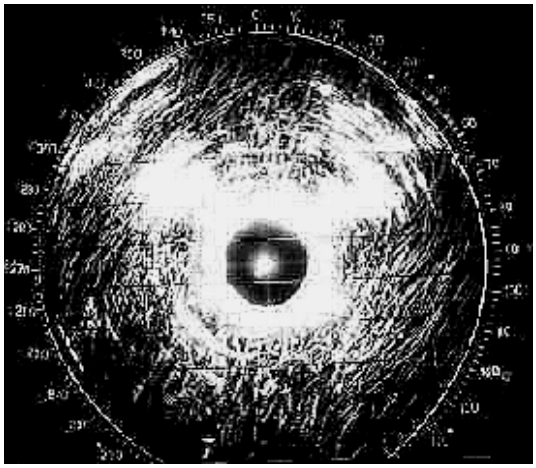

Fig. 1b. Radar screen photograph over a 18 scans (3-min exposure)

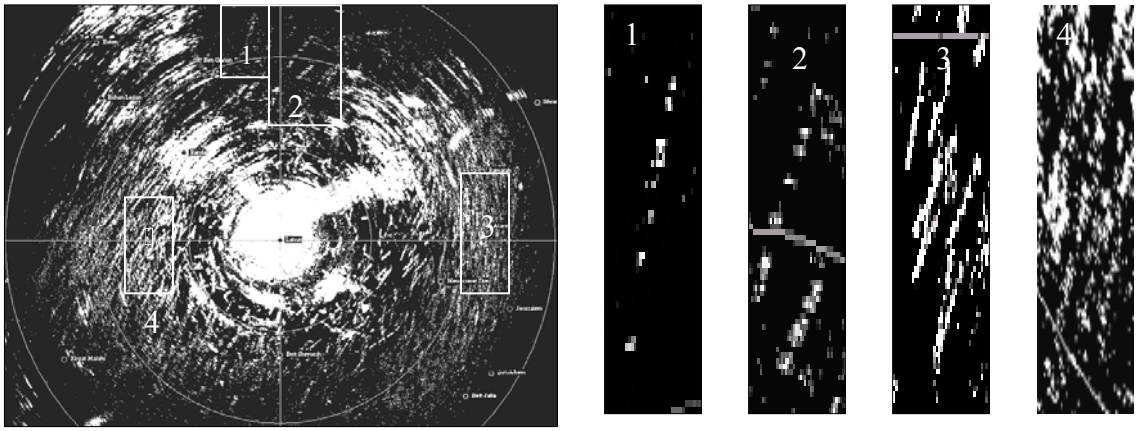

Fig. 1c Photo pf circular scan screen (the same as in Fig 1a) over 18 scans. Time interval between 1a) and 1 b) is 3 min. Tilt angle 3^0. Dot echo seen in 1 a) have transformed into tracks (bird flight trajectories). Flights directed towards the south. Lines formed by dotted echo represent bird flight tracks, other lines are echoes from hills. Fragments 1,2,3,4 distinctly show how dotted echoes from movement tracks.

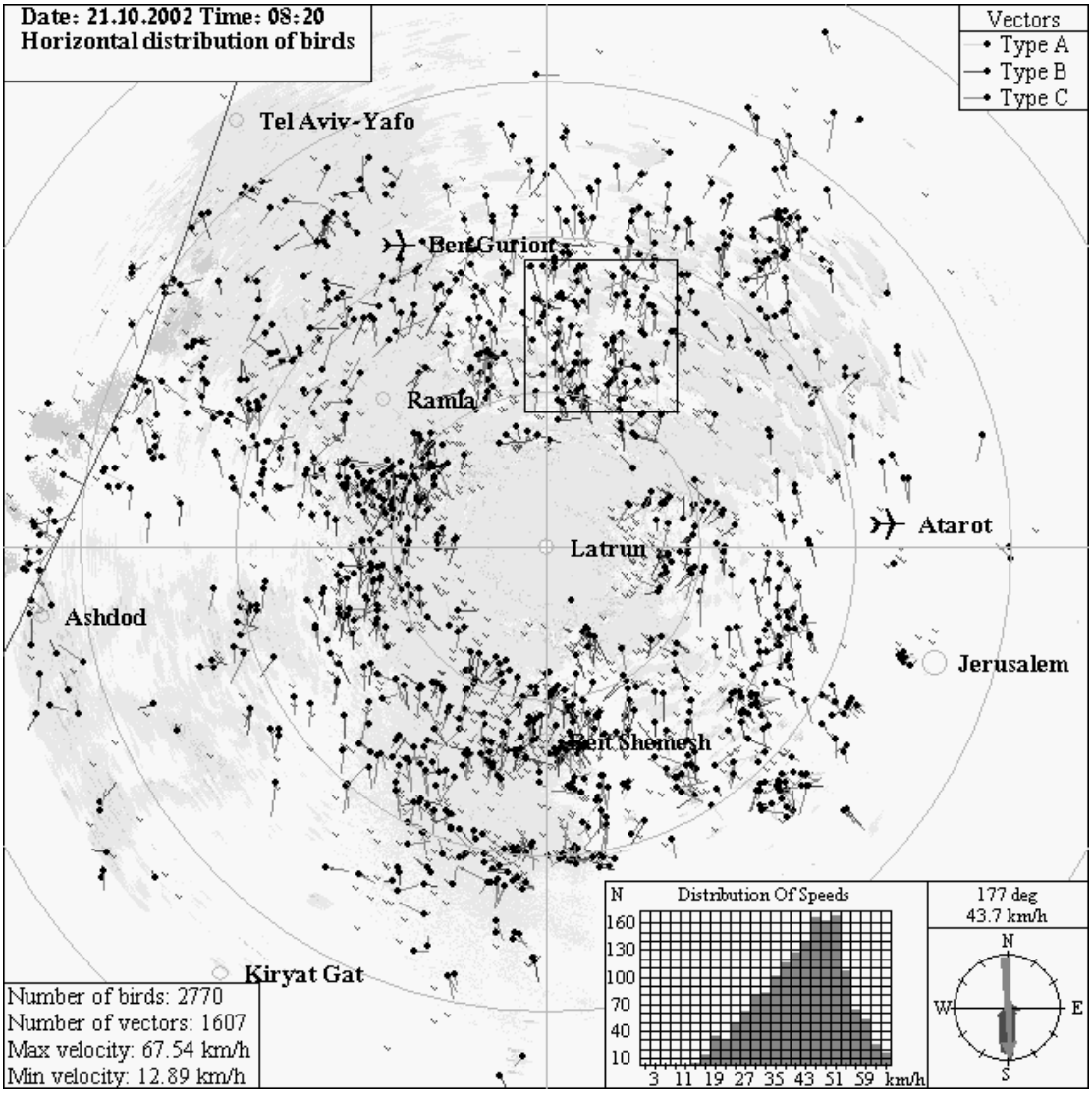

Fig. 2. Ornithological chart against the background of ground clutter and atmospheric formations.

Resonant Scattering by Layered Dielectric Structure with Weakly Kerr-Like Nonlinearity

V. V. Yatsyk
IRE Nat. Acad. of Sci. of Ukraine.

Abstract – Numerical analysis of the diffraction by a transversely non-homogeneous, isotropic, nonmagnetic, linearly polarized, weakly nonlinear layer and layered dielectric structures (with Kerr-like nonlinearity) is performed in the resonant frequency range when the parameter of cubic susceptibility takes positive and negative values. It is shown that as the excitation field intensity increases the diffraction characteristics acquire essentially different properties for positive and negative values of susceptibility. For a layered structure consisting of layers with positive and negative susceptibility of the enveloping medium the effects inherent to environments with positive and negative value of susceptibility are observed in certain areas of variation of the excitation field intensity.

1. The Nonlinear Problem

Let the time dependence be $\exp(-i\omega t)$, $\vec{E}(\vec{r})$ and $\vec{H}(\vec{r})$ complex amplitudes of an electromagnetic field. We consider a nonmagnetic, isotropic, transverse non-homogeneous, non-conducting, linearly polarized $\vec{E} = (E_x, 0, 0)$ and $\vec{H} = (0, H_y, H_z)$, with vector of polarization $\vec{P}^{(NL)} = \left(P_x^{(NL)}, 0, 0\right)$, and Kerr-like weakly nonlinearity $\varepsilon^{(NL)} << \varepsilon^{(L)}$ layered dielectric structure, see Fig. 1 and [1], [2]. Where $P_x^{(NL)} = \frac{3}{4}\chi^{(3)}_{xxxx}|E_x|^2 E_x$ component of a vector polarization, $\varepsilon = \varepsilon^{(L)} + \varepsilon^{(NL)}$ at $|z| \le 2\pi\delta$ is dielectric permeability of nonlinear structure, $\varepsilon^{(L)} = 1 + 4\pi\chi^{(1)}_{xx}(z)$, $\varepsilon^{(NL)} = 3\pi\chi^{(3)}_{xxxx}(z)|E_x|^2 = \alpha(z)|E_x|^2$, $\alpha(z) = 3\pi\chi^{(3)}_{xxxx}(z)$, $\chi^{(1)}_{xx}(z)$ and $\chi^{(3)}_{xxxx}(z)$ is the components of susceptibility tensor.

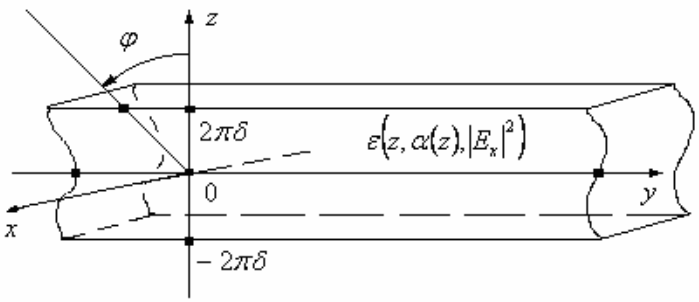

Figure 1: Weakly nonlinear dielectric layered structure.

The complete diffraction field $E_x(y,z) = E_x^{inc}(y,z) + E_x^{scat}(y,z)$ of a plane wave $E_x^{inc}(y,z) = a^{inc}\, exp[i(\phi y - \Gamma\cdot(z - 2\pi\delta))]$, $z > 2\pi\delta$ on the nonlinear dielectric layer (Fig. 1) satisfies such conditions of the problem:

$$\Delta\cdot\vec{E} + \frac{\omega^2}{c^2}\cdot\varepsilon^{(L)}(z)\cdot\vec{E} + \frac{4\pi\omega^2}{c^2}\cdot\vec{P}^{(NL)} \equiv \left(\Delta + \kappa^2\cdot\varepsilon\left(z,\alpha(z),|E_x|^2\right)\right)\cdot E_x(y,z) = 0, \qquad (1)$$

the generalized boundary conditions:

E_{tg} and H_{tg} are continuous at discontinuities $\varepsilon\left(z,\alpha(z)\cdot|E_x|^2\right)$;

$E_x(y,z)=U(z)\cdot exp(i\phi y)$, the condition of spatial quasihomogeneity along y; (2)

the condition of the radiation for scattered field:

$$E_x^{scat}(y,z)=\left\{\begin{matrix}a^{scat}\\ b^{scat}\end{matrix}\right\}\cdot e^{i(\phi y\pm\Gamma\cdot(z\mp 2\pi\delta))},\ z\begin{matrix}>\\<\end{matrix}\pm 2\pi\delta \tag{3}$$

Here: $\varepsilon\left(z,\alpha(z),|E_x|^2\right)=\begin{cases}1, & |z|>2\pi\delta\\ \varepsilon^{(L)}(z)+\alpha(z)\cdot|E_x|^2, & |z|\le 2\pi\delta\end{cases}$; $\Delta=\frac{\partial^2}{\partial y^2}+\frac{\partial^2}{\partial z^2}$; $\alpha(z)=3\pi\chi^{(3)}_{xxxx}(z)$;

$\Gamma=\left(\kappa^2-\phi^2\right)^{1/2}$; $\phi\equiv\kappa\cdot sin(\varphi)$; $|\varphi|<\pi/2$ (see Fig. 1); $\kappa=\omega/c\equiv 2\pi/\lambda$; $c=\left(\varepsilon_0\mu_0\right)^{-1/2}$, ε_0, μ_0 and λ length of the wave is the parameters of environment.

In this case the required of the solution of problem (1)-(3) are of kind:

$$E_x(y,z)=U(z)\cdot e^{i\phi y}=\begin{cases}a^{inc}\cdot e^{i(\phi y-\Gamma\cdot(z-2\pi\delta))} + a^{scat}\cdot e^{i(\phi y+\Gamma\cdot(z-2\pi\delta))}, & z>2\pi\delta,\\ U(z)\cdot e^{i\phi y}, & |z|\le 2\pi\delta,\\ b^{scat}\cdot e^{i(\phi y-\Gamma\cdot(z+2\pi\delta))}, & z<-2\pi\delta.\end{cases} \tag{4}$$

The nonlinear problem (1)-(3) is reduced to finding the solutions $U(z)\in L_2\left([-2\pi\delta,2\pi\delta]\right)$ (see (4)) of the non-homogeneous nonlinear integrated equation of the second kind [3]:

$$U(z)+\frac{i\kappa^2}{2\Gamma}\int_{-2\pi\delta}^{2\pi\delta}\exp\left(i\Gamma\cdot|z-z_0|\right)\left[1-\left(\varepsilon^{(L)}(z_0)+\alpha(z_0)|U(z_0)|^2\right)\right]U(z_0)dz_0=U^{inc}(z),\qquad |z|\le 2\pi\delta, \tag{5}$$

where $U^{inc}(z)=a^{inc}\,exp\left[-i\Gamma\cdot(z-2\pi\delta)\right]$ and $U(-2\pi\delta)=b^{scat}$, $U(2\pi\delta)=a^{inc}+a^{scat}$.

2. The Solution of the nonlinear integrated equation

The integrated equation (5) with application of the quadrature method is reduced to system of the nonlinear equations of the second kind [4].

$$\left(E-B\left(|U|^2\right)\right)\cdot U=U^{inc} \tag{6}$$

Here: $z_1=-2\pi\delta<z_2<...<z_n<...<z_N=2\pi\delta$; $U=\left\{U(z_n)\right\}_{n=1}^N$, $B\left(|U|^2\right)=\left\{A_m\cdot K_{nm}\left(|U|^2\right)\right\}_{n,m=1}^N$;

$K_{nm}\left(|U|^2\right)=\left(i\kappa^2/(2\Gamma)\right)\exp\left(i\cdot\Gamma|z_n-z_m|\right)\left[1-\left(\varepsilon^{(L)}(z_m)+\alpha(z_m)|U_m|^2\right)\right]$; $U^{inc}=\left\{a^{inc}\cdot e^{-i\cdot\Gamma\cdot(z_n-2\pi\delta)}\right\}_{n=1}^N$;

$E=\left\{\delta_n^m\right\}_{n,m=1}^N$; A_m are the numerical coefficients dictated by chosen quadrature form; δ_m^n is the Kronecker delta.

Solutions of the system (6) are carried out by the method of iterations:

$$\left\{\left(E-B\left(\left|\overset{(s-1)}{U}\right|^2\right)\right)\cdot\overset{(s)}{U}=U^{inc}\right\}_{s=1}^{S:\ \left\|\overset{(s)}{U}-\overset{(s-1)}{U}\right\|/\left\|\overset{(s)}{U}\right\|<\xi}. \tag{7}$$

3. Susceptibility and Effects Resonant Scattering of the Intensive Fields

Considering results of calculations, we shall use following designations for the factors describing a share of the reflected $R=\left|a^{scat}\right|^2/\left|a^{inc}\right|^2$ and last $T=\left|b^{scat}\right|^2/\left|a^{inc}\right|^2$ wave, that is factors of reflection and passage on intensity of a field of excitation, accordingly. And, at absence of losses in the environment, coefficients of reflection and transient on intensity of a field of excitation are connected by the equality $R+T=1$ representing the law of conservation of energy.

3.1 Intensity and Resonant Frequency

The effect of non-uniform shift of resonant frequency of the diffraction characteristics of nonlinear dielectric layer is found out at increase of intensity of inciting field [4] (see Fig. 2, at positive value of the susceptibility $\alpha = 0{,}01$, and also Fig. 3, at negative value of the susceptibility $\alpha = -0{,}01$).

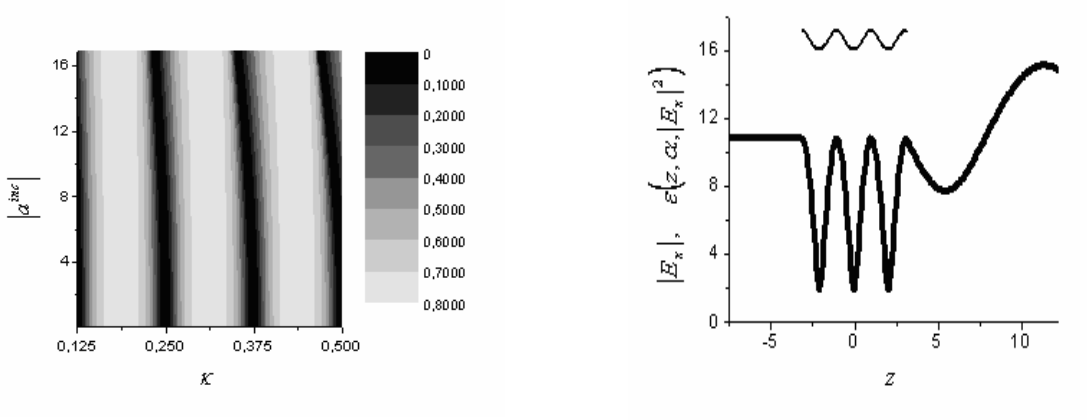

(a) (b)

Figure 2: Parameters of structure: $\delta = 0.5$; $\varphi = 45^0$; $\kappa = 0.375$; $\varepsilon^{(L)} = 16$, $\alpha = 0.01$; (a) The diagram of the reflection $R\left(\kappa, \left|a^{inc}\right|\right)$; (b) ——— $|E_x|$ and ——— $\varepsilon\left(z,\alpha,|E_x|^2\right)$ at $\left|a^{inc}\right| = 11.4$.

Growth of amplitude of the inciting field $\left|a^{inc}\right|$ results in change of the share of the reflected wave $R\left(\kappa, \left|a^{inc}\right|\right)$: reduction of value of resonant frequency with increase and reduction of a steepness of the diffraction characteristics before and after resonant frequency (Fig. 2, at $\alpha > 0$); increase of value of resonant frequency with reduction and increase of a steepness of the diffraction characteristics before and after resonant frequency (Fig. 3, at $\alpha < 0$).

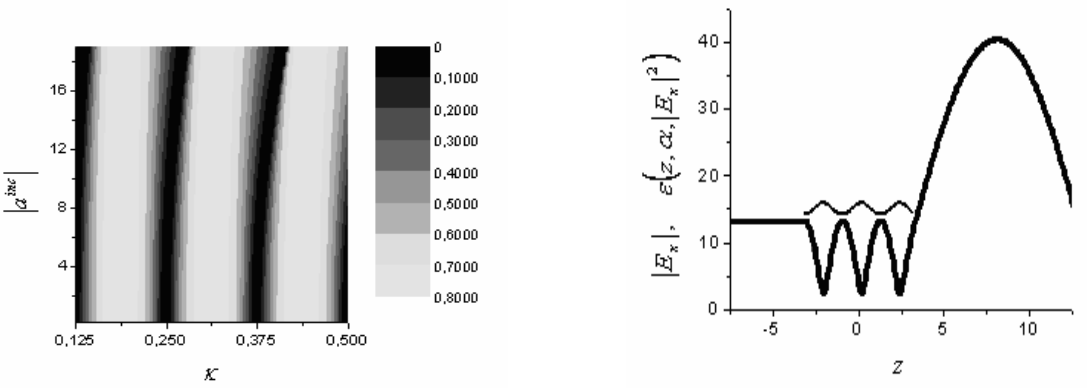

(a) (b)

Figure 3: Parameters of structure: $\delta = 0.5$; $\varphi = 45^0$; $\kappa = 0.375$; $\varepsilon^{(L)} = 16$, $\alpha = -0.01$; (a) The diagram of the reflection $R\left(\kappa, \left|a^{inc}\right|\right)$; (b) ——— $|E_x|$ and——— $\varepsilon\left(z,\alpha,|E_x|^2\right)$ at $\left|a^{inc}\right| = 22.4$.

3.2 Intensity and Angle

The effects: itself the channelling of a field – increase of the angle of the transparency of the nonlinear layer ($\alpha \neq 0$) when growth of intensity of the field (Fig. 4 (a), at positive value of the susceptibility, $\alpha > 0$); dechannelling of a field (Fig. 4 (b), at negative value of the susceptibility, $\alpha < 0$) are found out, [4].

The increase of the angle of a transparency with growth of intensity at positive value of the susceptibility $\alpha = 0{,}01$ is easy for tracking on Fig. 4 (a): $|a^{inc}| = 8$, $\varphi \approx 46^0$ and $|a^{inc}| = 11{,}4$, $\varphi \approx 85^0$.

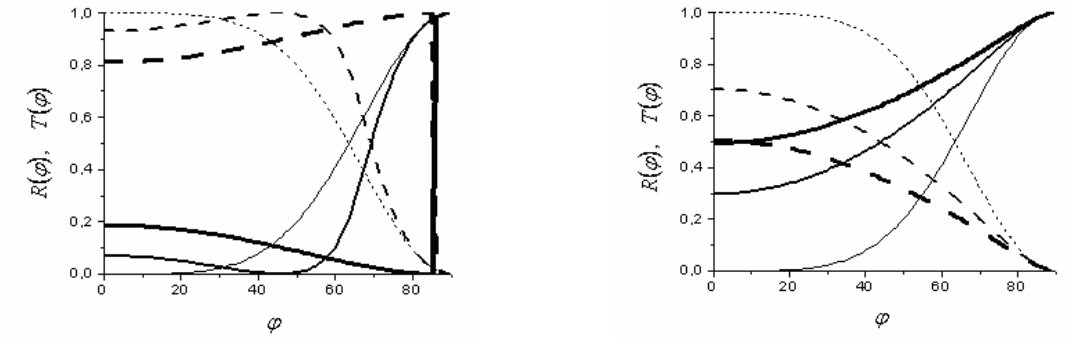

(a) (b)

Figure 4: Parameters: $\delta = 0.5$; $\kappa = 0.375$; $\varepsilon^{(L)} = 16$; (a) for $\alpha = 0.01$: —— $R(\varphi)$, ------ $T(\varphi)$ at $|a^{inc}| = 0.1$; —— $R(\varphi)$, - - - $T(\varphi)$ at $|a^{inc}| = 8$; ▬ $R(\varphi)$, ▬ ▬ $T(\varphi)$ at $|a^{inc}| = 11.4$; (b) for $\alpha = -0.01$: —— $R(\varphi)$, ------- $T(\varphi)$ at $|a^{inc}| = 0.1$; —— $R(\varphi)$, - - - $T(\varphi)$ at $|a^{inc}| = 8$; ▬ $R(\varphi)$, ▬ ▬ $T(\varphi)$ at $|a^{inc}| = 11.4$.

Let's consider diffraction characteristics of weakly nonlinear dielectric layered structure $\varepsilon\left(z, \alpha(z), |E_x|^2\right) = \left\{1, \text{ at } |z| > 2\pi\delta; \text{ and } \varepsilon^{(L)}(z) + \alpha(z) \cdot |E_x|^2, \text{ at } |z| \le 2\pi\delta\right\}$, with parameters

$$\left\{\varepsilon^{(L)}(z), \alpha(z)\right\} = \begin{cases} \left\{\varepsilon^{[1]} = 16,\ \alpha^{[1]} = \alpha_1\right\}, & z \in \left[-2\pi\delta, z_1 = -2\pi\delta \cdot \tau_1\right) \\ \left\{\varepsilon^{[2]} = a \cdot z + b,\ \alpha^{[2]} = \alpha_2\right\}, & z \in \left[z_1 = -2\pi\delta \cdot \tau_1,\ z_2 = 2\pi\delta \cdot \tau_2\right] \\ \left\{\varepsilon^{[3]} = 64,\ \alpha^{[2]} = \alpha_3\right\}, & z \in \left(z_2 = 2\pi\delta \cdot \tau_2,\ 2\pi\delta\right] \end{cases}; \quad \begin{array}{l} a = \dfrac{\varepsilon^{[3]} - \varepsilon^{[1]}}{z_2 - z_1}; \\ b = \varepsilon^{[1]} - a \cdot z_1; \\ \tau_1 = \tau_2 = 0. \end{array}$$

Growth of intensity of the inciting field results in change $R(\varphi)$ and $T(\varphi)$, see Fig. 5.

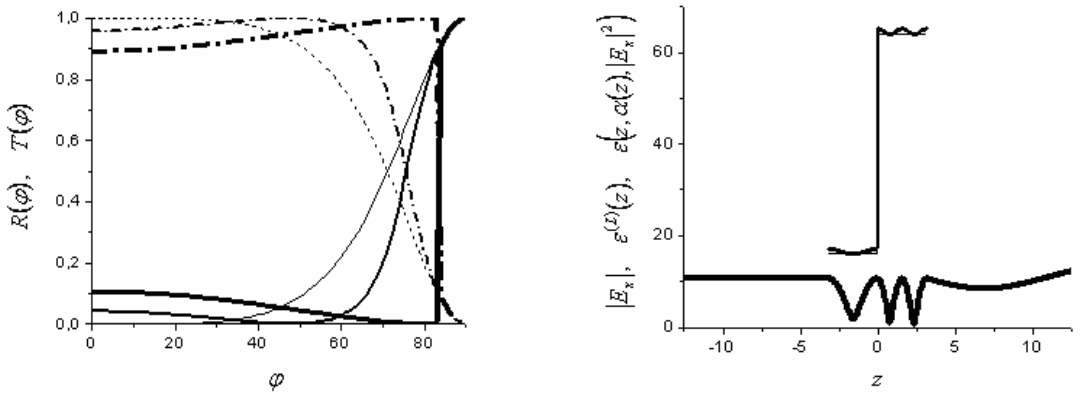

(a) (b)

Figure 5: Parameters of structure: $\delta = 0.5$; $\kappa = 0.25$; $\alpha_1 = \alpha_2 = \alpha_3 = 0.01$ and $\tau_1 = \tau_2 = 0$; (a) —— $R(\varphi)$, ------ $T(\varphi)$ at $|a^{inc}| = 0.1$; —— $R(\varphi)$, - - - $T(\varphi)$ at $|a^{inc}| = 8$; ▬ $R(\varphi)$, ▬ ▬ $T(\varphi)$ at $|a^{inc}| = 11$; (b) —— $\varepsilon^{(L)}(z)$, ▬ $|E_x|$ —— $\varepsilon\left(z, \alpha(z), |E_x|^2\right)$ at $|a^{inc}| = 11$, $\varphi = 45^0$.

The effect itself the channeling of a field (i.e. existence of angles $\varphi_{|a^{inc}|\geq 0} = \{\varphi \in [0, 90^0): R(\varphi) = 0\} \neq \{0\}$, the increase of angle of the transparency of the nonlinear layer when growth of intensity of the field, at positive values of the susceptibility, see Fig. 5 (a)), and also effect itself the channeling ($\varphi_{0\leq|a^{inc}|\leq 20} \neq \{0\}$) and de-channeling ($\varphi_{|a^{inc}|>20} = \{0\}$) of a field (at positive and negative values of the susceptibility of the dielectric layered structure, see Fig. 6 (a)) are found out. Here the symbol $\{0\}$ is empty set.

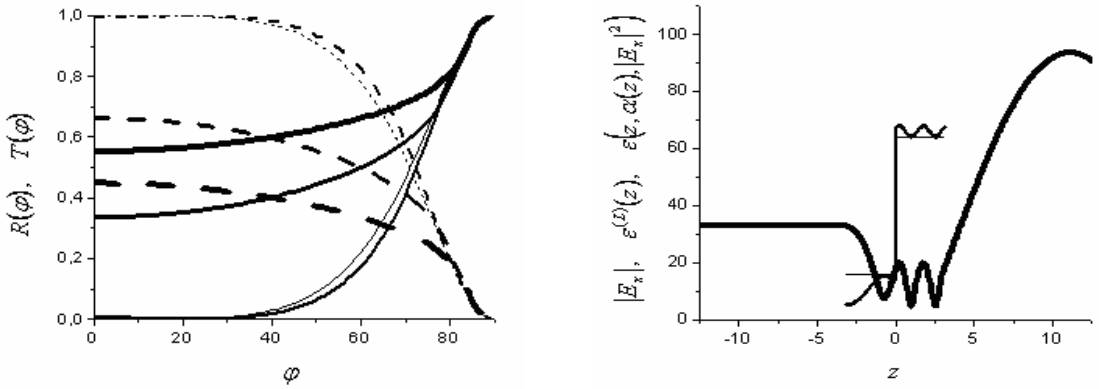

(a) (b)

Figure 6: Parameters of structure: $\delta = 0.5$; $\kappa = 0.25$; $\alpha_1 = -0.01$, $\alpha_2 = \alpha_3 = 0.01$ and $\tau_1 = \tau_2 = 0$;

(a) —— $R(\varphi)$, ----- $T(\varphi)$ at $|a^{inc}| = 0.1$; ——$R(\varphi)$, – – –$T(\varphi)$ at $|a^{inc}| = 20$; ——— $R(\varphi)$, – – $T(\varphi)$ at $|a^{inc}| = 40$; ——— $R(\varphi)$,– – $T(\varphi)$ at $|a^{inc}| = 52.5$.

(b) —— $\varepsilon^{(L)}(z)$, ——— $|E_x|$ —— $\varepsilon\left(z,\alpha(z),|E_x|^2\right)$ at $|a^{inc}| = 11$, $\varphi = 45^0$.

These effects (see Fig. 2 - Fig. 6) are connected to resonant properties of a nonlinear dielectric layer and caused by increase at positive value of the susceptibility or reduction at negative value of the susceptibility of a variation of dielectric permeability of a layer (its nonlinear components) when increase of intensity of a field of excitation of researched nonlinear object, see Fig. 2 (b), 3 (b), 5 (b), 6 (b).

4. Conclusion

The results of the numerical analysis are applied: at investigation of processes of wave self-influence; at the analysis of amplitude-phase dispersion of eigen oscillation-wave fields in the nonlinear objects; development of the approach of the description of evolutionary processes near to critical points of the amplitude-phase dispersion of nonlinear structure; at designing new selecting energy; transmitting, remembering devices; etc.

REFERENCES

1. Akhmediev N. N., Ankiewicz A., "Solitons," Moscow, Fizmatlit, 2003.
2. Schürmann H. W., Serov V. S., Shestopalov Yu. V., "TE-polarized waves guided by a lossless nonlinear three-layer structure", Physical Review E, vol. 58, no. 1, 1998, pp. 1040-1050.
3. Shestopalov V. P., Sirenko Yu. K., "Dynamic Theory of Gratings," Kiev, Naukova Dumka, 1989.
4. Yatsyk V. V., "The Numerical Simulations and Resonant Scattering of Intensive Electromagnetic Fields of Waves by Dielectric Layer with Kerr-Like Nonlinearity", E-print: Computational Physics, http://arxiv.org/pdf/physics/0412109, no. 12, 2004, pp. 1-11.

Analysis of Current Density Distribution Induced by ELF Magnetic Fields Utilizing Fast-Multipole Surface-Charge-Simulation Method for Voxel Data

Shoji Hamada and Tetsuo Kobayashi
Department of Electrical Engineering, Kyoto University, Japan

Abstract This paper describes an application of the FMM(fast multipole method[1])-SCM(surface charge simulation method) for voxel data[2] to analyses of current density distribution in a human model induced by 50Hz magnetic fields. The performance of this method is demonstrated by calculating the induced currents in the 'Taro'[3] licensed by NICT (National Institute of Information and Communications Technology). Taro models a Japanese adult male and is composed of 7,977,906, 2mm×2mm×2mm voxels. The required calculation time results in about six to seven hours on a 32bit, 3GHz, 2G-RAM, single Pentium IV, Windows PC.

1. Introduction

A variety of methods are practically utilized for calculating magnetically induced electric fields and currents in realistic high-resolution human voxel models. The most popular methods, such as SPFD, FDTD, FEM, FIT, and Impedance method, require $O(D^3)$ memory-capacity and operation-cost, when the number of voxels is about D^3. Although they are superior to $O(D^{4\sim6})$ cost of the conventional BEM, SCM, and MoM, increasing size of D causes intolerable cost increase. In order to overcome this problem, we had proposed the FMM-SCM for voxel data[2]. This method treats a square surface of a voxel that has different inside and outside conductivities as a surface element of the SCM that calculates three-dimensional Laplacian field. The main features of the method are as follows. (I) The diagonal form FMM provides $O(D^2)$ performance in the memory-capacity and operation-cost, when the number of voxels is about D^3. (II) The boundary equation integrated over each element strictly imposes the flux continuity, therefore the solution globally satisfies the Gauss' law. These features make it high-speed, high-capacity, and high-stability calculation method.

2. Basic Equations and Implementation of the FMM

The basic equations of magnetically induced, low-frequency, faint current in a human body are described in a lot of previous works[4]. By neglecting the effect of the permittivity, the induced electric field $\boldsymbol{E}$ and current density $\boldsymbol{J}$ satisfy following equations.

$$\boldsymbol{E} = -j\omega\{\boldsymbol{A} + \nabla\phi\} \quad , \quad \boldsymbol{J} = \sigma\boldsymbol{E} \quad , \quad \nabla^2\phi = 0 \tag{1}$$

where j is the imaginary unit, ω is the angular frequency of the given field source, $\boldsymbol{A}$ is the vector potential generated by the source, ϕ is an unknown scalar potential that satisfies the Laplace equation, and σ is the conductivity. The boundary equations are as follows.

$$\sigma_1\{\boldsymbol{A} + \nabla\phi_1\}\cdot\boldsymbol{n} = \sigma_2\{\boldsymbol{A} + \nabla\phi_2\}\cdot\boldsymbol{n} \quad , \quad \phi_1 = \phi_2 \tag{2}$$

where subscripts 1 and 2 denote the both sides of the boundary surface, and $\boldsymbol{n}$ means the unit normal vector of the surface. The SCM automatically satisfies the second equation of (2), therefore we consider only the first one of (2) in the following surface-integral form.

$$\sigma_1\int_{S_i}\nabla\phi_1\cdot\boldsymbol{n}dS - \sigma_2\int_{S_i}\nabla\phi_2\cdot\boldsymbol{n}dS = -(\sigma_1-\sigma_2)\int_{S_i}\boldsymbol{A}\cdot\boldsymbol{n}dS \quad , \quad i = 1\sim N \tag{3}$$

where S means the square surface of each element, subscript i denotes the element number, and N is the number of elements. This equation describes continuity of the flux flowing through the i-th element. The SCM expresses the ϕ and $\nabla\phi$ by superposing the Laplacian fields generated by the surface elements that have equivalent surface charges. The constant charge density x_i on the i-th element can be determined as the solution of a linear system $A\boldsymbol{x} = \boldsymbol{b}$ that is equivalent to (3) by utilizing an iterative solver, such as Bi-CGSTAB2[5].

In order to speed up the solver, we utilize the diagonal form FMM[1] by defining a cubic region composed of 4×4×4 voxels as a leaf-cell of the three-dimensional octal-tree structure. The FMM calculates the product $A\boldsymbol{x}$ as the sum of the 'near' part and the 'far' part. The contribution of x_j to $\left(\int_{S_i}\nabla\phi\cdot\boldsymbol{n}dS\right)^{\text{near}}$ is calculated by

Table 1: No. of tissues, conductivities (Sm^{-1}), and the numbers of voxels.

No.	Tissue	σ	voxels	No.	Tissue	σ	voxels	No.	Tissue	σ	voxels
1	Cerebellum	0.1	17320	20	Duodenum	0.5	1105	39	Trachea	0.35	3563
2	CSF	2.0	54200	21	Esophagus	0.5	860	40	Urine	0.7	40055
3	Cornea	0.4	25	22	Bile	1.4	944	44	Blood	0.7	148587
5	Vitreous Humor	1.5	2124	23	Gall Bladder	0.2	548	45	Cortical Bone	0.02	456228
6	Grey Matter	0.1	73362	24	Heart	0.1	50850	46	Marrow	0.06	509507
7	Hypothalamus	0.08	77	25	Kidney	0.1	37003	47	Cartilage	0.18	33015
8	Lens	0.25	73	26	Liver	0.07	143784	48	Fat (Mean)	0.04	1962602
9	Pineal Glands	0.08	20	27	Lung	0.14	412003	49	Muscle (Mean)	0.35	3193078
10	Pituitary	0.08	39	29	Pancreas	0.35	8288	50	Nerve	0.03	11340
11	Salivary Gland	0.35	8271	30	Prostate	0.4	4053	51	Skin	0.1	422953
12	Thalamus	0.08	2967	31	Small Intestine	0.5	40280	52	Tooth	0.02	3112
13	Tongue	0.3	11896	32	Spleen	0.1	17206	53	Ligament	0.3	18268
14	White Matter	0.06	76094	33	Stomach	0.5	22925	54	Contents of 31	0.35	32270
15	Adrenals	0.35	247	34	Contents of 33	0.35	8766	55	Diaphragm	0.35	7649
16	Bladder	0.2	7701	35	Tendon	0.3	7045	56	Seminal Vesicle	0.35	2739
18	Large Intestine	0.1	43411	36	Testis	0.35	14098	57	Cavernous Body	0.35	16268
19	Contents of 18	0.35	47188	38	Thyroid, Thymus	0.5	1899		Whole body		7977906

multiplying x_j by proportional coefficients between them. The calculation of $\left(\int_{S_i} \nabla\phi \cdot \boldsymbol{n} dS\right)^{\mathrm{far}}$ requires following processes. The field contribution by x_j in a leaf-cell is translated into the multipole-expansion coefficients M_n^m defined on the leaf-cell by multiplying x_j by proportional coefficients between them. The field contribution by local-expansion coefficients L_n^m defined on a leaf-cell is translated into the $\left(\int_{S_i} \nabla\phi \cdot \boldsymbol{n} dS\right)^{\mathrm{far}}$ in the leaf-cell by multiplying L_n^m by proportional coefficients between them. All these coefficients can be preliminarily calculated by numerical integrations in the form of (3), therefore no integration is needed during the FMM calculation. In addition, they depend only on the relative location between two elements or between an element and the center of an expansion, therefore the memory capacity required for storing these coefficients is only several Mbytes. All required M_n^m and L_n^m are calculated by the diagonal form FMM algorithm, where the upper limit of the n is set to ten.

3. Field at the Voxel Center and Field Smoothing near Boundaries

After solving $\boldsymbol{x}$, we can calculate $\int_S \boldsymbol{E} \cdot \boldsymbol{n} dS$ on the six inner surfaces of every voxel, which are denoted by $f^{\mathrm{x}+}$, $f^{\mathrm{x}-}$, $f^{\mathrm{y}+}$, $f^{\mathrm{y}-}$, $f^{\mathrm{z}+}$, and $f^{\mathrm{z}-}$. They yield a representative field at the center of the voxel as follows.

$$\boldsymbol{E}^{\mathrm{center}} \equiv \frac{f^{\mathrm{x}+} + f^{\mathrm{x}-}}{2S}\boldsymbol{i} + \frac{f^{\mathrm{y}+} + f^{\mathrm{y}-}}{2S}\boldsymbol{j} + \frac{f^{\mathrm{z}+} + f^{\mathrm{z}-}}{2S}\boldsymbol{k} \tag{4}$$

where S is the area of an element. It was shown that the $\boldsymbol{E}^{\mathrm{center}}$ represented induced fields with good accuracy except for those in the vicinity of the boundary[2]. However, sharp fluctuation of the $\boldsymbol{E}^{\mathrm{center}}$ in the vicinity of the boundary was observed owing to the lack of exact information of the boundary shape. This is a common problem shared by field calculation methods based on voxel models. Here, we add a smoothing process of the $\boldsymbol{E}^{\mathrm{center}}$ near boundary region. We pay attention to both a voxel V_0 that has conductivity σ_0 and field $\boldsymbol{E}_0^{\mathrm{center}}$ and its twenty-six ($3\times3\times3-1$) neighboring voxels $V_1 \sim V_{26}$ that have $\sigma_1 \sim \sigma_{26}$ and $\boldsymbol{E}_1^{\mathrm{center}} \sim \boldsymbol{E}_{26}^{\mathrm{center}}$. When all $\sigma_i (i = 1 \sim 26)$ are equal to σ_0, which implies V_0 locates far from boundaries, no smoothing process is carried out. When more than one $\sigma_i (i = 1 \sim 26)$ is not equal to σ_0, we replace the $\boldsymbol{E}_i^{\mathrm{center}}$ by the average of the fields set $\left\{\boldsymbol{E}_i^{\mathrm{center}}, i = 0 \sim 26 \text{ and } \sigma_i = \sigma_0\right\}$. We call this process as smoothing near boundaries.

4. NICT Taro Model and Applied Fields

Taro, a Japanese adult male whole body model, was developed by NICT, Kitasato Univ., Keio Univ., and Tokyo Metropolitan University[3]. He consists of 7,977,906 voxels except the air region around him, and the cubic voxel size is 2mm. Taro occupies the region of $0 \sim 516$mm in x, $0 \sim 270$mm in y, and $0 \sim 1732$mm in z. The gravity center is about (251.5, 122.5, 959.5) in mm. The tissues, conductivities, and the numbers of voxels are listed in Table 1. We can determine the locations of surface elements based on these data, and the number of the surface elements becomes 3,921,953.

We apply 50Hz homogeneous fields and 50Hz magnetic dipole fields to Taro. The applied homogeneous fields are $B\boldsymbol{i}$ (left-to-right), $B\boldsymbol{j}$ (back-to-front), and $B\boldsymbol{k}$ (foot-to-head), where B=1μT (peak). The magnetic dipole source fields are by $M\boldsymbol{i}$, $M\boldsymbol{j}$, and $M\boldsymbol{k}$, where M=0.5π μWb$\cdot$ m (peak), which are located at (251.5, 122.5+500,

Table 2: Calculation times, iterations, current densities (μAm^{-2}), and electric field strength (μVm^{-1}) in the whole body of Taro.

Case		Time	Iterations	Before smoothing near boundaries				After smoothing near boundaries			
				J_{max}	J_{ave}	E_{max}	E_{ave}	J_{max}	J_{ave}	E_{max}	E_{ave}
Uniform fields	$B\boldsymbol{i}$ (left-to-right)	6h 23min.	85	74.9	1.92	199	11.2	40.6	1.91	143	11.1
	$B\boldsymbol{j}$ (back-to-front)	5h 53min.	78	48.1	2.41	371	14.7	33.9	2.40	220	14.5
	$B\boldsymbol{k}$ (foot-to-head)	6h 06min.	81	40.9	1.56	188	9.90	28.6	1.55	166	9.79
Dipole source fields	$M\boldsymbol{i}$	6h 16min.	82	43.5	1.07	209	6.46	27.3	1.06	135	6.38
	$M\boldsymbol{j}$	6h 42min.	88	73.4	2.22	656	14.1	47.4	2.20	315	14.0
	$M\boldsymbol{k}$	6h 33min.	86	43.6	1.44	295	8.98	31.3	1.43	172	8.88

1398.5). It should be noted that, when the $M\boldsymbol{k}$ is located at (0, 0, 0), it generates 1μT magnetic field at (x, y, 0), where $\sqrt{x^2+y^2}$=500mm, and it generates 2μT magnetic field at (0, 0, z), where $|z|$=500mm.

5. Calculated Results

Table 2 show the calculation times, iterations, current densities J (μAm^{-2}), and electric field strength E (μVm^{-1}) in the whole body of Taro. The script 'max' and 'ave' stand for maximum and average value, respectively. It is shown that the calculation times are about six to seven hours in all cases. The significant part of the calculation time is occupied by the time required by the iterative solver. Therefore, the calculation time is almost proportional to the number of iterations, which is required to reduce the relative residual norms less than 10^{-7}. The statistical values listed in the table are qualitatively similar to those in [4]. Figs. 1 and 2 show the calculated current density distributions of these six cases, where a coronal slice is at y=137mm, a sagittal slice is at x=259mm, and horizontal slices are at z =1599, 1325, 1051, 777, 503, and 229mm. The gradation from black to white corresponds to the current density from $\log_{10}(J_{max} \times 0.01)$ to $\log_{10}(J_{max})$. Figs. 3 and 4 show z-layer-maximum, z-layer-averaged, tissue-maximum, and tissue-averaged current densities (μAm^{-2}) before and after the smoothing near boundaries. When we compare these results, we should be aware that the field by $M\boldsymbol{j}$ is 2μT and the others are 1μT at (251.5, 122.5, 1398.5). In Figs. 3 and 4, it is clearly observed that the smoothing process almost always reduces the maximum value, and it doesn't change the average value significantly. It is also observed that the current distributions induced by the dipole source fields are limited to the region nearby the dipole source, which explains the reduction of the whole-body-average values by the dipode source fields in the Table 2.

6. Conclusion

The performance of FMM(fast multipole method)-SCM(surface charge simulation method) for voxel data is successfully confirmed by calculating the induced currents in a Japanese adult male voxel model 'Taro' licensed by NICT. It is composed of 7,977,906, 2mm×2mm×2mm voxels, and is exposed to three kinds of homogeneous fields and three kinds of magnetic dipole source fields. It is shown that the required calculation time is about six to seven hours on a 32bit, 3GHz, 2G-RAM, single Pentium IV, Windows PC. These results demonstrate high-speed, high-capacity, and high-stability performance of the method.

REFERENCES

(1) L. Greengard, V. Rokhlin, "A new version of the fast multipole method for the Laplace equation in three dimensions," Acta Numerica, **6**, 229–269, 1997

(2) S. Hamada, T. Kobayashi, "Analysis of electric field induced by ELF magnetic field utilizing fast-multipole surface-charge-simulation method for voxel data," IEEJ Trans. FM, **126**, No. 5, 355–362, 2006

(3) T. Nagaoka, S. Watanabe, K. Sakurai, E. Kunieda, S. Watanabe, M. Taki, and Y. Yamanaka, "Development of realistic high-resolution whole-body voxel models of Japanese adult males and females of average height and weight, and application of models to radio-frequency electromagnetic-field dosimetry," Phys. Med. Biol. **49**, 1–15, 2004

(4) T. W. Dawson, K. Caputa, and M. A. Stuchly, "Influence of human model resolution on computed currents induced in organs by 60-Hz magnetic fields," Bioelectromagnetics, **18**, 478–490, 1997

(5) M. H. Gutknecht, "Variants of Bi-CGSTAB for matrices with complex spectrum," SIAM J. Sci. Comput., **14**, 1020–1033, 1993

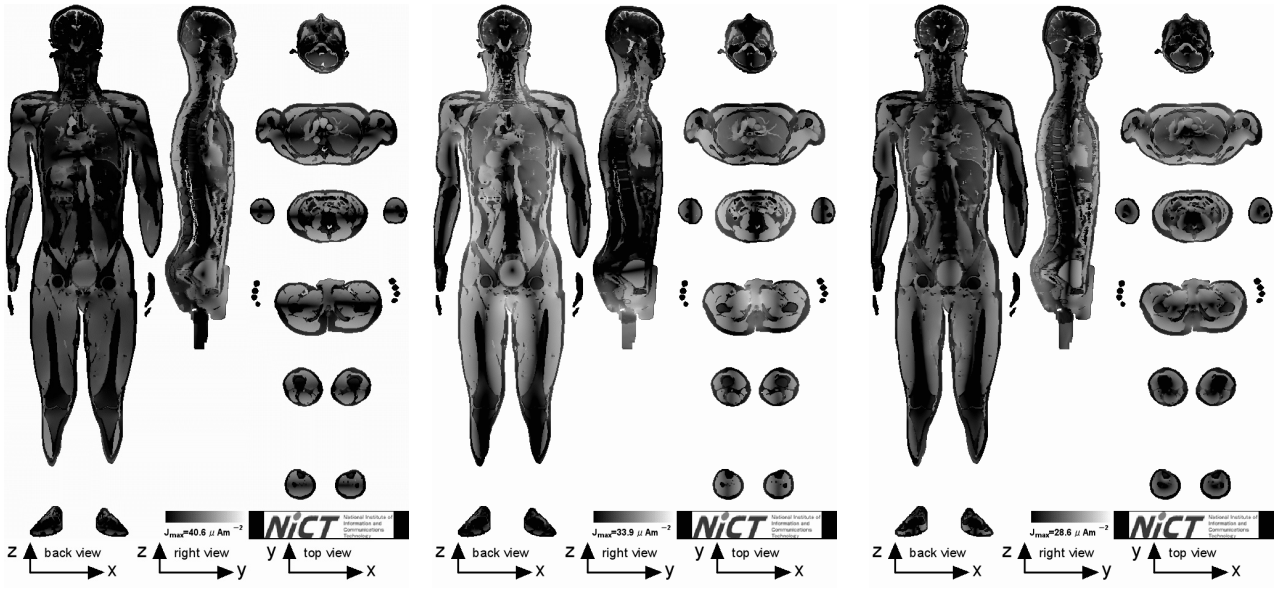

(i) Uniform $\boldsymbol{Bi}$ (left-to-right) (ii) Uniform $\boldsymbol{Bj}$ (back-to-front) (iii) Uniform $\boldsymbol{Bk}$ (foot-to-head)

Figure 1: Current density distributions induced by 1μT(peak), 50 Hz, uniform magnetic fields.

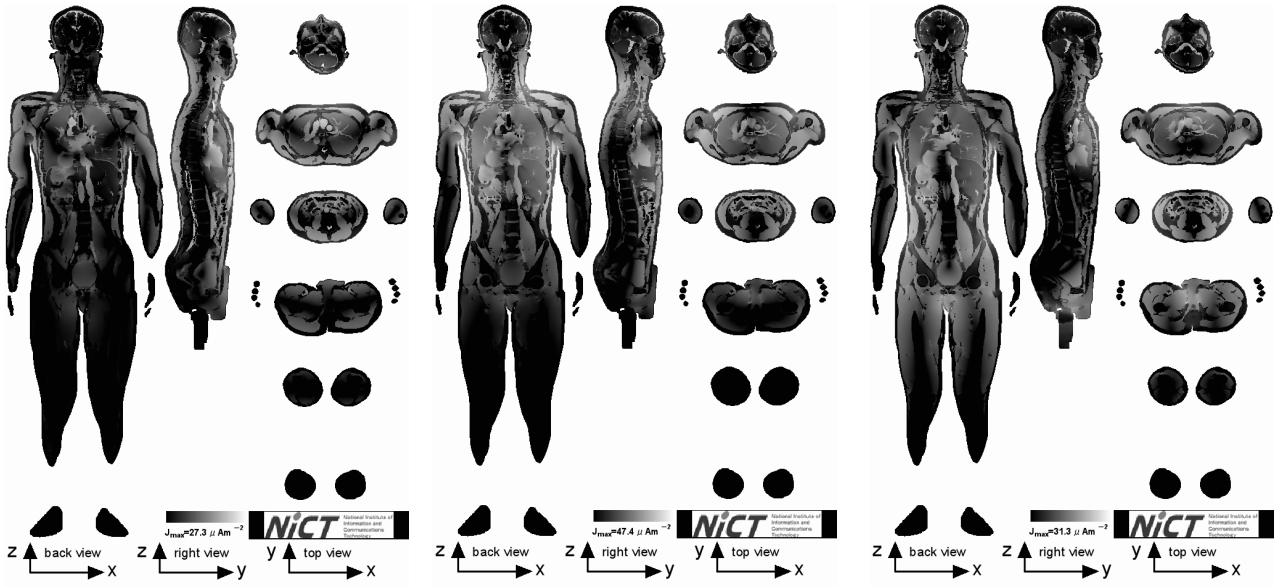

(i) Dipole $\boldsymbol{Mi}$ (ii) Dipole $\boldsymbol{Mj}$ (iii) Dipole $\boldsymbol{Mk}$

Figure 2: Current density distributions induced by 0.5π μWb·m(peak), 50 Hz dipole magnetic field sources.

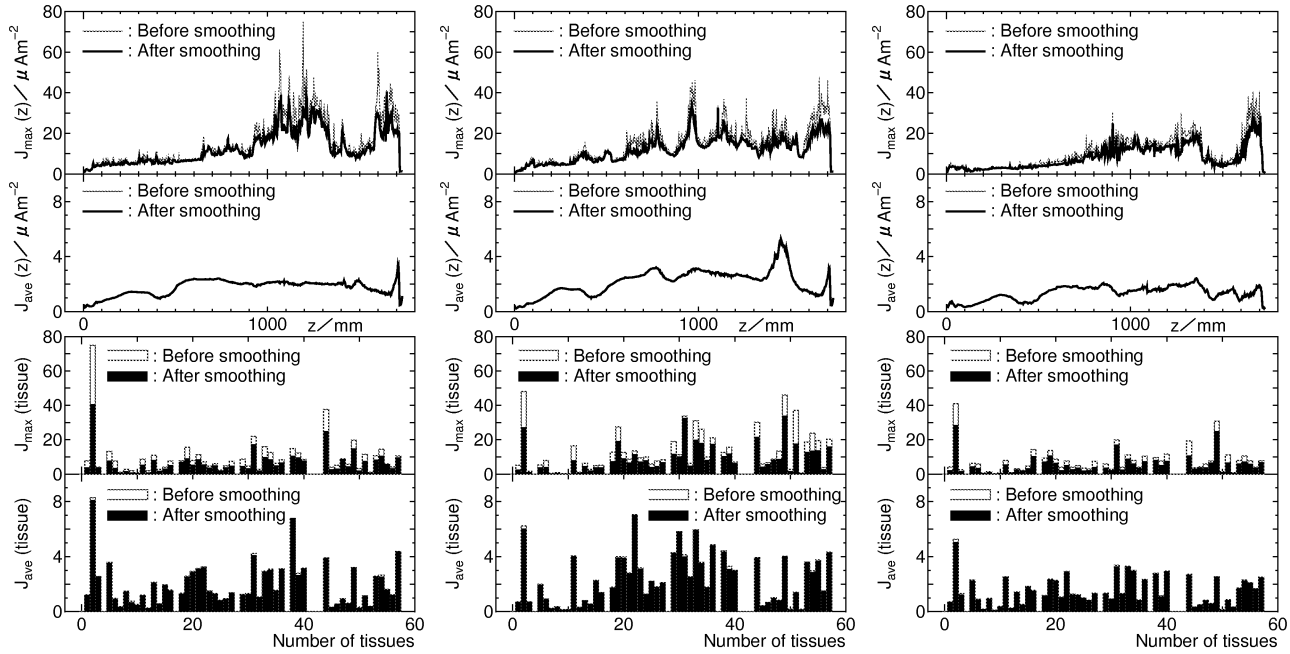

(i) Uniform $\boldsymbol{Bi}$ (left-to-right) (ii) Uniform $\boldsymbol{Bj}$ (back-to-front) (iii) Uniform $\boldsymbol{Bk}$ (foot-to-head)

Figure 3: Layer-maximum, layer-averaged, tissue-maximum, and tissue-averaged current densities (μAm^{-2}) induced by 1μT(peak), 50 Hz, uniform magnetic fields.

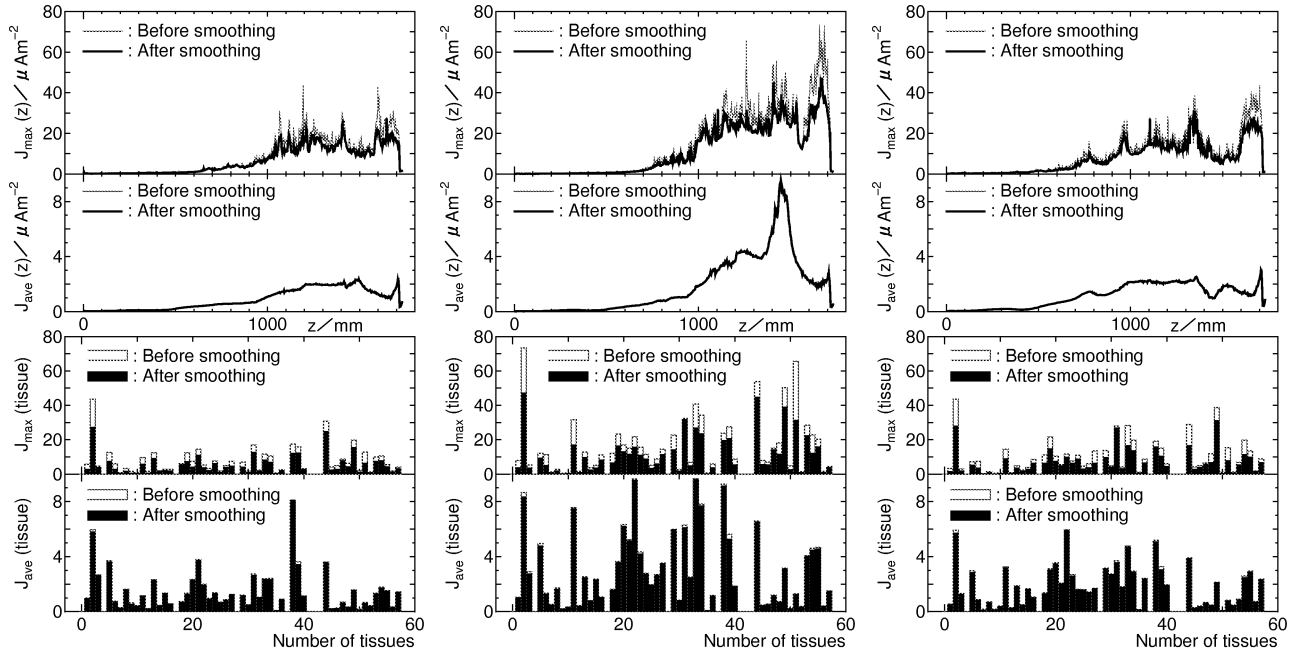

(i) Dipole $\boldsymbol{Mi}$ (ii) Dipole $\boldsymbol{Mj}$ (iii) Dipole $\boldsymbol{Mk}$

Figure 4: Layer-maximum, layer-averaged, tissue-maximum, and tissue-averaged current densities (μAm^{-2}) induced by 0.5π μWb·m(peak), 50 Hz dipole magnetic field sources.

CAVITY ANTENNA WITH PARTLY TRANSPARENT APERTURE FOR WIRELESS COMMUNICATIONS

N. I. Voytovich[(1)], A. V. Ershov[(1)], N. N. Repin[(2)], A. N. Sokolov[(3)]

[(1)]Design and Production of Radioequipment sub-faculty, Southern Ural State University, 76 Lenin Avenue, Chelyabinsk, 454080, Russia; E-mail: vni@chel.surnet.ru

[(2)]Nauchno-Issledovatelsky Institut po Izmeritelnoi Tekhnike, Open Corporation, 4 Vitebskaya Str., Chelyabinsk, 454080, Russia; E-mail: rnn17@mail.ru

[(3)]Radiophysics and electronics sub-faculty, Chelyabinsk State University, 129 Brat'ya Kashiriny Str., Chelyabinsk, 454021, Russia; E-mail: sokolov@csu.ru

ABSTRACT

The paper is devoted to the property analysis of a cavity antenna with a partially transparent wall. Cavity antenna with radiators in the form of rectangular openings on the cavity wide wall is excited by a stripline through the coupling opening bounded in perimeter by metal pin system shorting out the stripline screens. Cavity antenna has a so-called "short" structure (the distance between two wide walls of the cavity resonator is close to a half wave length) which allows to reach noticeable reduction of antenna dimensions. These advantages of cavity antennas with partly transparent aperture are attractive for external antennas designing for wireless communications.

INTRODUCTION

Cavity antennas with partly transparent aperture are known since the first part of the 20th century. Cavity antennas are more like three-dimensional cavity resonators. A basic electromagnetic mode H_{101} is excited inside the cavity. A multitude of small openings (slots or round holes) are made on one the metal cavity walls. Thus, the cavity antenna can also be considered as an antenna array. There is a critical review of the works on microwave cavity antennas in the [1]. It has been done since the 1950s for benefit of engineers and scientists in the fields of antennas and communication engineering. Known cavity antennas are excited by one a slot at the end of the waveguide. This paper presents cavity antennas with relatively big openings on one the metal cavity walls. Cavity antennas are excited by more than one of the slots. It is the author's opinion that cavity antenna is at an advantage. It has the selectivity, it has a good solidity, it has very simple excitation. These advantages of cavity antennas with partly transparent aperture are attractive for external antennas designing. Such antennas are good for high-speed wireless communication systems "point to point".

ANTENNA PHYSICAL ANALOGUE

Cavity antenna (fig.1,2) is a metal resonator 2 with dimensions a_2 x b_2 x H, the height H of which is close to half wavelength λ and cross sizes a_2 and b_2 are several λ. The resonator upper wide wall of thickness D arranged between the planes M_3 and M_4 has a system of K_0 radiating openings 5 with dimensions l_p x t_p ($p = 1,\ldots, K_0$) and separates the antenna from the half-space 3 by which an area external to the antenna is simulated. Through the coupling opening 4 with dimensions l_0 x t_0 in the low wall of thickness d arranged between the planes M_1 and M_2 the cavity antenna is excited by a stripline. Area 1 bounded by the stripline screens is considered as a transmission resonator with dimensions a_1 x b_1 x h, the height h of which is considerably less than λ. In middle of the region 1 ($z = h/2$) an infinitely thin strip of length L and width w is placed. Metal pins E_2 with radius ρ are arranged around the coupling opening 4 at points x_p, y_p ($p = 1,\ldots, K_2$, K_2 – pin number) and close the stripline screens (pins have not shown on fig.2). It is supposed that the strip width $w << \lambda$ and $\rho << \lambda$. An electromagnetic wave source is arranged on the transmission resonator side wall at the strip bottom. All cavity antenna and the stripline spaces are filled by a perfect dielectric and metal surfaces have infinite conductance.

STATEMENT AND SOLUTION OF ELECTRODYNAMIC PROBLEM

Within the scope of the antenna physical model a general electromagnetic problem is formed for a number of regions coupled electromagnetically through opening apertures. For the problem definition the method of equivalent currents is used which supposes that all regions are closed and structural components and opening apertures are taken into account

by the action of the corresponding equivalent currents. The equality to zero of tangential components of the electric field $\dot{\vec{E}}$ on the strip surface, the pins and the continuity of a tangential component of the magnetic field $\dot{\vec{H}}$ with transition from one region to another in the planes $M_1 - M_4$ (fig.1) are used.

As a result a system of integral equations is received relative to unknown distributions of electric currents on the strip $\dot{\vec{J}}^{E_1}$, the pins $\dot{\vec{J}}_q^{E_2}$ ($q = 1,\ldots, K_2$) and of magnetic currents on apertures of the coupling opening $\dot{\vec{J}}^{M_1}$, $\dot{\vec{J}}^{M_2}$ and radiating ones $\dot{\vec{J}}_q^{M_3}$, $\dot{\vec{J}}_q^{M_4}$ ($q = 1,\ldots, K_0$), in particular:

on the strip:
$$\dot{\vec{E}}_0^1\left\{\dot{\vec{J}}^{E_1}\right\}+\sum_{q=1}^{K_2}\dot{\vec{E}}_0^1\left\{\dot{\vec{J}}_q^{E_2}\right\}+\dot{\vec{E}}_0^1\left\{\dot{\vec{J}}^{M_1}\right\}=-\dot{\vec{E}}_0^s, \quad (1)$$

on the pins:
$$\dot{\vec{E}}_p^1\left\{\dot{\vec{J}}^{E_1}\right\}+\sum_{q=1}^{K_2}\dot{\vec{E}}_p^1\left\{\dot{\vec{J}}_q^{E_2}\right\}+\dot{\vec{E}}_p^1\left\{\dot{\vec{J}}^{M_1}\right\}=0,\ p=1,\ldots,K_2, \quad (2)$$

on the M_1:
$$\dot{\vec{H}}^1\left\{\dot{\vec{J}}^{E_1}\right\}+\sum_{q=1}^{K_2}\dot{\vec{H}}^1\left\{\dot{\vec{J}}_q^{E_2}\right\}+\dot{\vec{H}}^1\left\{\dot{\vec{J}}^{M_1}\right\}=\dot{\vec{H}}^4\left\{-\dot{\vec{J}}^{M_1}\right\}+\dot{\vec{H}}^4\left\{\dot{\vec{J}}^{M_2}\right\}, \quad (3)$$

on the M_2:
$$\dot{\vec{H}}^4\left\{-\dot{\vec{J}}^{M_1}\right\}+\dot{\vec{H}}^4\left\{\dot{\vec{J}}^{M_2}\right\}=\dot{\vec{H}}^2\left\{-\dot{\vec{J}}^{M_2}\right\}+\sum_{q=1}^{K_0}\dot{\vec{H}}^2\left\{\dot{\vec{J}}_q^{M_3}\right\}, \quad (4)$$

on the M_3:
$$\dot{\vec{H}}_p^2\left\{-\dot{\vec{J}}^{M_2}\right\}+\sum_{q=1}^{K_0}\dot{\vec{H}}_p^2\left\{\dot{\vec{J}}_q^{M_3}\right\}=\dot{\vec{H}}_p^{5p}\left\{-\dot{\vec{J}}_p^{M_3}\right\}+\dot{\vec{H}}_p^{5p}\left\{\dot{\vec{J}}_p^{M_4}\right\},\ p=1,\ldots,K_0, \quad (5)$$

on the M_4:
$$\dot{\vec{H}}_p^{5p}\left\{-\dot{\vec{J}}_p^{M_3}\right\}+\dot{\vec{H}}_p^{5p}\left\{\dot{\vec{J}}_p^{M_4}\right\}=\sum_{q=1}^{K_0}\dot{\vec{H}}_p^3\left\{-\dot{\vec{J}}_q^{M_4}\right\},\ p=1,\ldots,K_0, \quad (6)$$

$\dot{\vec{E}}_0^s$ – electric field intensity of outer source, the upper index of electric and magnetic field vectors indicating a region for which the corresponding characteristic is written; by "5*p*" *p*-th subregion of the fifth region is indicated.

Electric and magnetic fields are solved with Green tensor function usage. Galerkin method is used for the integral equation system solution. Fourier basis is used for definition of basic (test) functions on the strip and opening apertures. Then according to Galerkin method the procedure of integral equation system transformation into linear algebraic equation system is performed: $A \cdot I = V$, where I is a column of amplitude coefficients defining electric field on the strip, pins and magnetic field on opening apertures, V – a column of exciting voltage amplitudes (outer sources), A – a equivalent current interaction. As a result antenna numerical model is received. Standard approach to matrix equation solution is used.

NUMERICAL AND EXPERIMENTAL RESULTS

Numerical and experimental results have got for the antennas with one, two (fig. 3) and four (fig. 4) excited slots. The slots on fig. 3 have in-phase excitation. The antenna has got of linear polarization. The slots on fig. 4 have quadrature feed. The antenna has got of circular polarization. It is shown that the openings on the wide wall must be arranged so that the array spacing of the radiating openings placed in N number along each side of the resonator upper wide wall was equal to N-th part of this wall side length. In this case the directivity frequency response has maximum width. It is shown that for antenna excitation it is preferably to use two coupling openings arranged symmetrically at a distance of a quarter of the wide wall from the cavity center (fig.3). Antenna directivity graphs are given in fig. 5 in frequency range according to the resonator height H. Antenna ($a_2 = b_2$ =194 mm, a = 24.8 mm, K_0 = 8 x 8) is excited by two coupling openings. Directivity versus frequency relationship graphs (fig.5) is identical in the form to (tuned) circuit resonance curve. Maximum directivity is reached at the resonator height less than half wavelength. It is explained by the fact that the perforated wall has inductive character. With radiating openings dimension a_2, b_2 increase antenna resonance frequency decreases. With radiating openings dimension D increase directivity maximum shift to lower frequencies. That can be explained by the penetration of the field connected with the resonator into the region of radiating openings and outer space. There is a good matching of experimental patterns and calculated patterns obtained by presented approach (fig.6). Measured VSWR of the antenna with two excited slots is less than 1.34 for 8% frequency width (fig.7).

CONCLUSION

Physical, mathematical, numerical and calculated models of an antenna array are designed with elements in the form of radiating openings on the wide wall of a multimode metal resonator operating as a distributing device. As applied to cavity antenna-stripline system an electrodynamic problem is solved on excitation by electric and magnetic currents of a number of regions coupled by opening apertures.

The laws of cavity antenna patterns, directivity and polarization characteristic behavior are defined in frequency range depending on the dimensions of the cavity resonator and the perforated wall. There is a good matching of experimental and calculated patterns. Presented antennas are good as external antennas for high-speed wireless communication point to point systems.

REFERENCES

1. Kumar A. and Hristov H. D., *Microwave cavity antennas*, Artech House, Norwood, MA, 1989.

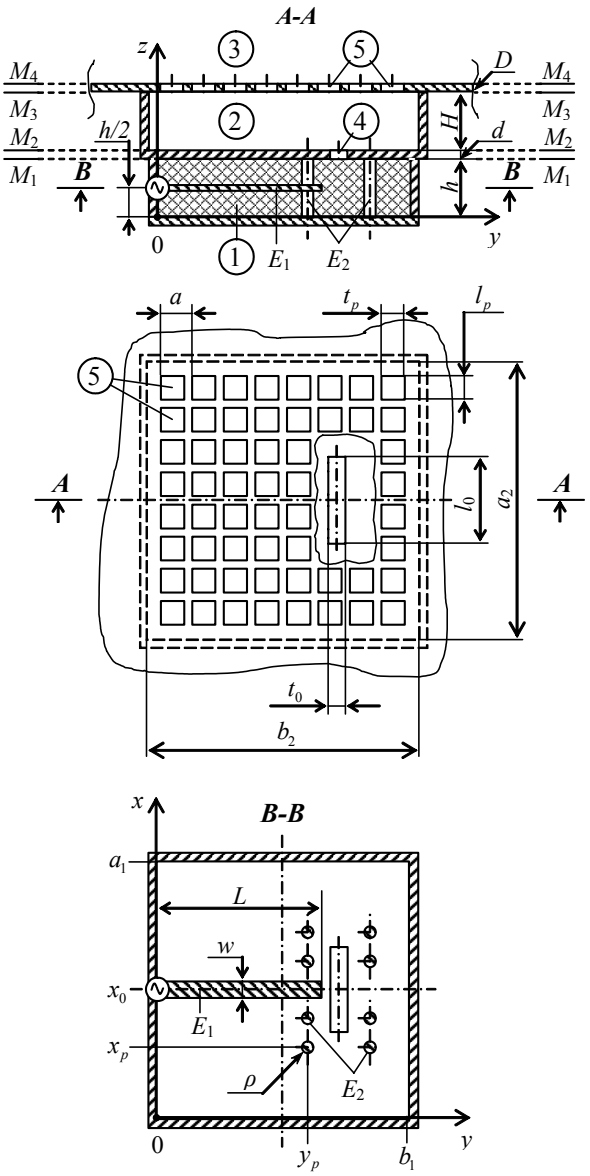

Figure1: Cavity antenna excited by a stripline.

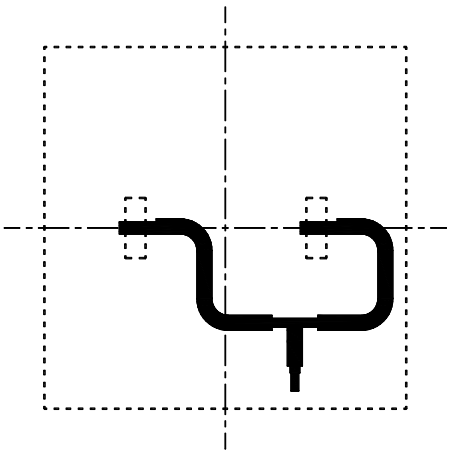

Figure 3: Power divider of the linear polarization antenna.

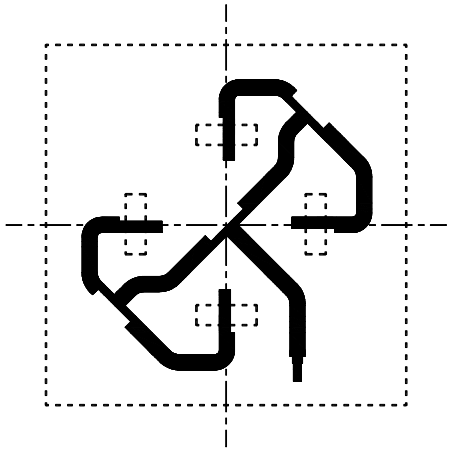

Figure 4: Power divider of the circular polarization antenna.

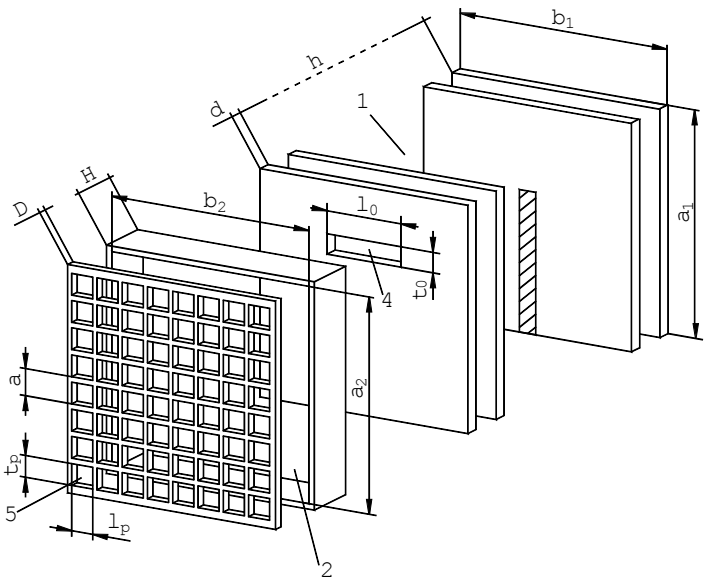

Figure 2: Cavity antenna with partly transparent aperture.

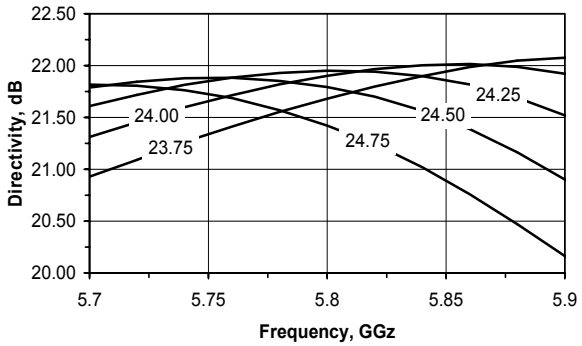

Figure 5: Cavity antenna directivity with different height of the resonator (mm).

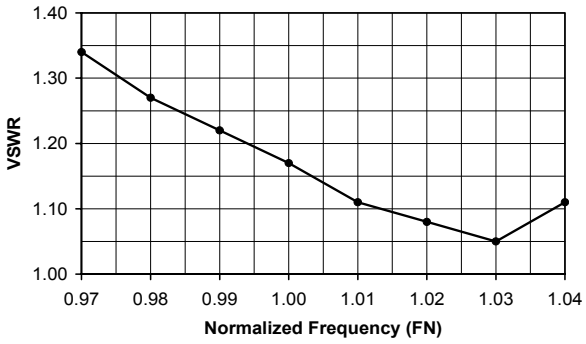

Figure 7: VSWR versus normalized frequency of antenna with one slot.

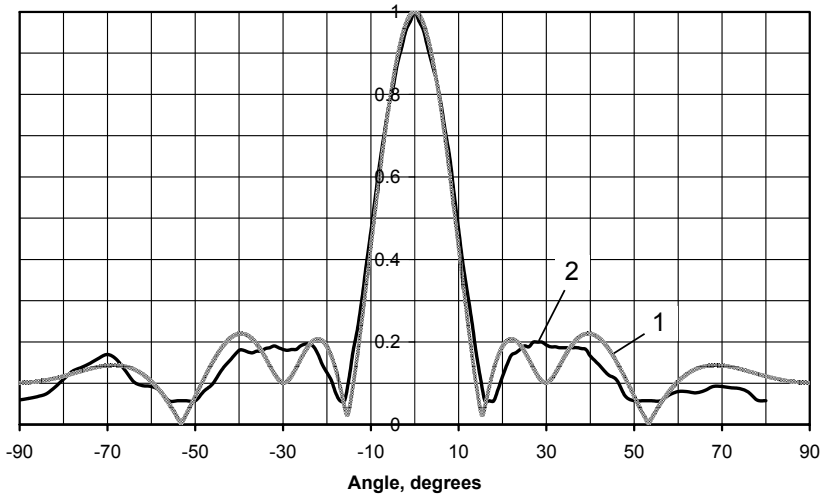

Figure 6: Calculated (1) and measured (2) patterns in *E*-plane.

Improvement of surface resistance property of ErBa2Cu3O7- films with BaTiO3

Y. Shingai
Kyushu University, CREST-JST, JSPS Research Fellow, JAPAN

M. Mukaida and R. Teranishi
Kyushu University, CREST-JST, JAPAN

K. Yamada and N. Mori
Kyushu University, JAPAN

A. Ichinose
Central Research Institute of Electric Power Industry, CREST-JST, JAPAN

R. Kita
Shizuoka University, CREST-JST, JAPAN

S. Horii
University of Tokyo, CREST-JST, JAPAN

Y. Yoshida
Nagoya University, CREST-JST, JAPAN

K. Matsumoto
Kyoto University, CREST-JST, JAPAN

T. Abe and A. Saito
Yamagata University, JAPAN

Abstract— We have improved surface resistance (R_S) properties of $ErBa_2Cu_3O_{7-\delta}$(ErBCO) films by using $BaTiO_3$(BTO) doping (BTO+ErBCO). The as-grown BTO+ErBCO films did not have enough carriers. We solve this problem by using O_3+O_2 as background gas during the growth of BTO+ErBCO films. Then, O_3+O_2 gas is useful to grow BTO+ErBCO films with superior superconducting properties. The R_S of a 2wt%BTO+ErBCO film is the lowest in BTO+ErBCO films grown in this study. This value is equal to that of a 1.5wt%BZO+ErBCO film. The microstructures of the 2wt%BTO+ErBCO film are observed by transmission electron microscopy (TEM). In the image, the BTO+ErBCO films did not have nanorods as the observed in BZO+ErBCO films against our expectation. However, the precipitates what BZO+ErBCO films do not have, are observed.

1. Introduction

$YBa_2Cu_3O_{7-\delta}$ (YBCO) has been studied among the 123 superconducting materials since the discovery of YBCO. Recently, $REBa_2Cu_3O_{7-\delta}$ (RE: rare earth elements) superconducting materials attract attentions as a substitution of the YBCO, because some REBCO materials have superior superconducting properties than YBCO. We have been focusing on $ErBa_2Cu_3O_{7-\delta}$ (ErBCO). Since this material has some advantages. For example, the ErBCO has a higher T_C than YBCO, without substitution problems between RE and Ba atoms, easy controlling of oxygen contents in a superconducting film and so on, We have reported that ErBCO films with $BaZrO_3$ (BZO) have low surface resistance.

In this study, we tried to fabricate ErBCO films with $BaTiO_3$ (BTO) doping. The BTO has the same crystal structure as BZO (perovskite structure). Then, it is expected that the BTO+ErBCO films have the similar micro-structure (we called nano-rod [1]) in the films and similar transport properties as the BZO+ErBCO films.

2. Experimental

Substrates used in this study were (100) $SrTiO_3$ (STO). ErBCO films were grown by pulsed ArF excimer laser deposition. Three types of sintered ErBCO ceramic with x wt% (x = 1.0, 2.0, 3.0) BTO were used as laser target in order to examine the effect of amount of BTO doping. The substrate was attached with silver paste to a rotating metal-substrate holder, which was heated by a lamp heater. The substrate temperature was monitored by a thermocouple and calibrated by an optical pyrometer.

During the ErBCO film growth, the background gas pressure was 400mTorr. The substrate temperature at the growth of the ErBCO films was 750 ^{O}C. The typical growth time of ErBCO films was 60min. After the growth, the ErBCO films were cooled down rapidly to room temperature in a background gas with increased atmospheric pressure. These conditions were optimized conditions of pure ErBCO films on STO substrates. Here, two type of gases were used as background gas, one was O_2, another was O_2(93%)+O_3(7%).

The preferred orientations of ErBCO films grown in this study were determined by X-ray $\theta/2\theta$ diffraction with Cu-kα radiation. The in-plane orientations of the ErBCO films were evaluated by X-ray φ-scan by using a (102) plane of ErBCO. The crystallinity of the grown ErBCO films was estimated by full width at the half maximum (FWHM) of a rocking curve using the (005) peak of the ErBCO films ($\delta\omega$). Lattice images and grain azimuth were observed by TEM pictures. The transport properties of the grown ErBCO films were obtained by a 4-probe method. The R_S at 38 GHz of the grown ErBCO films were measured by using a dielectric sapphire resonator in TE013 mode.

3. Results and Discussions

First of all, the BTO+ErBCO films were grown at optimized conditions in O_2 gas using the three targets with different BTO constituents. Crystallinity of grown films was characterized by using XRDθ/2θ and φ-scan. As a result, diffraction patterns and in-plane orientations of the films had not been affected by the amount of BTO doping, these films were *c*-axis oriented films with in-plane aligned However, no peaks corresponding to the BTO (002) were observed as reported in BZO+ErBCO films. Therefore, it was thought that BTO+ErBCO films have a different microstructure than what we expected.

Next, the ρ-T curves were observed for grown BTO+ErBCO films. ρ-T curves showed semi conductive characteristics with high resistivity. Furthermore, T_C was not confirmed above 77K. On the other hand, an as-grown pure ErBCO film has high T_C (=90.5K)[2]. As the origin of this phenomenon we thought that there are not enough carriers. Then, the *c*-axis length of grown BTO+ErBCO films were calculated by the resulr of X-ray θ/2θ diffraction pattern and using *N*-*R* function. All *c*-axis lengths of BTO+ErBCO films were longer than the *c*-axis of fully oxidized bulk ErBCO. From these results, it is necessary to dope oxygen in BTO+ErBCO films to supply carriers. Ozone(7%)+oxygen(93%) gas (O_3+O_2 gas) was used as background gas during the growth in order to improve oxygen contents of grown BTO+ErBCO films. Ozone gas had stronger oxygenation power compared to O_2 gas. Using O_3+O_2 gas as background gas at the BTO+ErBCO film growth, it was expected to dope enough oxygen into the films.

It was confirmed that all *c*-axis lengths of BTO+ErBCO films grown in O_3+O_2 gas were closer to the *c*-axis length of ErBCO bulk than BTO+ErBCO films grown in O_2 gas. Furthermore, ρ-T curves became metallic and T_C was increased to 86K. From these results, oxygen deficiency in BTO+ErBCO films was improved by using O_3+O_2 gas. From these results, usage of O_3+O_2 gas as background gas was useful for growing the BTO+ErBCO film with superior superconductivity.

The R_S-T (at 38GHz) properties of BTO+ErBCO films, a pure ErBCO film and a 1.5wt%BZO+ErBCO film (it is the best data we had) are showed in Fig.1. The R_S-T of the BTO+ErBCO film grown in O_2 gas has very large value compared to that of the BTO+ErBCO film grown in O_3+O_2 gas. Using O_3+O_2 gas as background gas is very important to fabricate BTO+ErBCO films having superior R_S properties. Furthermore, 2wt%BTO+ErBCO film grown in O_3+O_2 gas had low R_S compared to pure ErBCO, this R_S equals to R_S of 1.5wt%BZO+ErBCO films.

In these results, BTO doping into ErBCO film was very useful to fabricate the superconducting film with low R_S. Then, the optimized amount of BTO doping was 2wt% in these experiments.

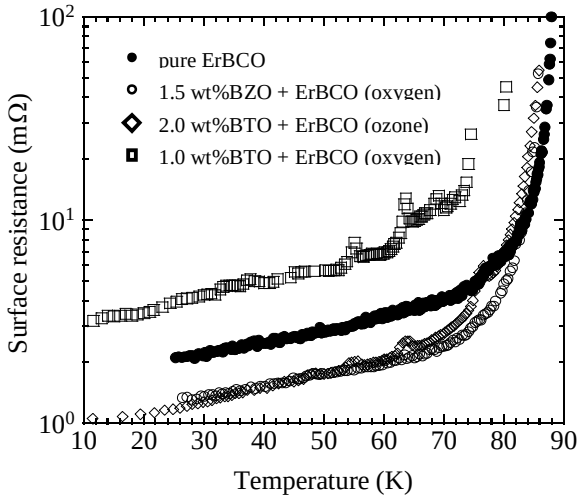

Fig. 1. The R_S properties of grown ErBCO films at different growth conditions (sort of target and background gas) respectively.

4. Conclusion

We have successfully improved R_S properties of ErBCO films using BTO doping. The as-grown BTO+ErBCO films did not have enough carriers. We solved this problem by using O_3+O_2 gas as background gas during the growth of BTO+ErBCO films. Then, O_3+O_2 gas is useful to fabricate superior BTO+ErBCO films. The R_S of a 2wt%BTO+ErBCO film was the lowest in BTO+ErBCO films grown in this study. This value was equal to that of a 1.5wt%BZO+ErBCO film. The microstructures of 2wt%BTO+ErBCO film were observed by TEM. In the TEM image, the BTO+ErBCO films did not have nanorods, as observed in BZO+ErBCO films against our expectation. However, the precipitates what BZO+ErBCO films did not have are observed. Now, we are going to investigate why R_S properties of ErBCO films are improved by BTO doping.

REFERENCES

[1]M. Mukaida, T. Horide, R. Kita, S. Horii, A. Ichinose, Y. Yoshida, O. Miura, K. Matsumoto, K. Yamada, N. Mori, Jpn. J. Appl. Phys. 44 L952 (2005)..

[2] T. Ohazama, M. Mukaida, A. Ichinose, K. Matsumoto, Y. Yoshida, S Horii, A. Saito, S. Ohshima, Physica C 412-414 1301 (2004).